



**HAL**  
open science

# Probing Lepton Flavour Universality through semitauonic $\Lambda_b$ decays using three-pions $\tau$ -lepton decays with the LHCb experiment at CERN

Victor Daussy-Renaudin

► **To cite this version:**

Victor Daussy-Renaudin. Probing Lepton Flavour Universality through semitauonic  $\Lambda_b$  decays using three-pions  $\tau$ -lepton decays with the LHCb experiment at CERN. High Energy Physics - Experiment [hep-ex]. Université Paris Saclay (COMUE), 2018. English. NNT : 2018SACL335 . tel-01907757

**HAL Id: tel-01907757**

**<https://theses.hal.science/tel-01907757>**

Submitted on 29 Oct 2018

**HAL** is a multi-disciplinary open access archive for the deposit and dissemination of scientific research documents, whether they are published or not. The documents may come from teaching and research institutions in France or abroad, or from public or private research centers.

L'archive ouverte pluridisciplinaire **HAL**, est destinée au dépôt et à la diffusion de documents scientifiques de niveau recherche, publiés ou non, émanant des établissements d'enseignement et de recherche français ou étrangers, des laboratoires publics ou privés.

# Probing Lepton Flavour Universality through semitauonic $\Lambda_b^0$ decays using three-pions $\tau$ -lepton decays with the LHCb experiment at CERN

Test de l'universalité de la saveur des leptons à travers l'étude des désintégrations semitauoniques de  $\Lambda_b^0$  avec les désintégrations en trois pions du lepton  $\tau$  dans l'expérience LHCb au CERN

Thèse de doctorat de l'Université Paris-Saclay  
préparée à l'Université Paris-Sud

Ecole doctorale n°576 Particules, Hadrons, Énergie, Noyau, Instrumentation, Imagerie,  
Cosmos et Simulation (PHENIICS)  
Spécialité de doctorat : Physique des particules

Thèse présentée et soutenue à Orsay, le 26 Septembre 2018, par

**VICTOR DAUSSY-RENAUDIN**

Composition du Jury :

Achille Stocchi Professeur (Université Paris-Sud (LAL))	Président
Francesco Forti Professeur (INFN Sezione di Pisa)	Rapporteur
Yannis Karyotakis Directeur de recherche (LAPP)	Rapporteur
Svjetlana Fajfer Professeure (University of Ljubljana)	Examinatrice
Patrick Owen Chercheur postdoctoral (University of Zurich)	Examineur
Guy Wormser Directeur de recherche (Université Paris-Sud (LAL))	Directeur de thèse

*À Mathilde.*

Que diable allait-il faire dans cette galère ?  
Molière, *Les Fourberies de Scapin*, Acte II, scène 7.



# Contents

Synthèse	9
Introduction	19
<b>1 The Standard Model of particle physics</b>	<b>21</b>
1.1 Particles, interactions and symmetries . . . . .	22
1.1.1 A world made of particles . . . . .	22
1.1.2 Overview of the fundamental interactions . . . . .	23
1.1.3 Symmetries . . . . .	25
1.2 The Standard Model . . . . .	28
1.2.1 Electroweak unification . . . . .	29
1.2.2 The Higgs Mechanism . . . . .	30
1.2.3 Quark mixing and CP violation . . . . .	32
1.2.4 Limits and unresolved issues . . . . .	34
<b>2 An introduction to semitauonic decays</b>	<b>37</b>
2.1 Lepton Flavour Universality . . . . .	38
2.1.1 $b \rightarrow sl^+\ell^-$ transitions . . . . .	39
2.1.2 $b \rightarrow c\tau\nu_\tau$ transitions in the Standard Model . . . . .	41
2.2 Current experimental status . . . . .	47
2.3 New Physics in semitauonic $b$ -decays . . . . .	48
<b>3 The LHCb detector</b>	<b>53</b>
3.1 The LHC . . . . .	53
3.2 The LHCb detector . . . . .	55
3.2.1 Tracking . . . . .	60
3.2.2 Particle identification . . . . .	66
3.3 The LHCb trigger . . . . .	76
3.3.1 L0 trigger . . . . .	76
3.3.2 High Level Trigger . . . . .	78
3.3.3 Trigger categories . . . . .	79
3.4 The LHCb software . . . . .	80

## CONTENTS

---

<b>4</b>	<b>Measurement of <math>\mathcal{R}(D^*)</math> using <math>\tau^- \rightarrow \pi^- \pi^+ \pi^- (\pi^0) \nu_\tau</math> decays</b>	<b>81</b>
4.1	Motivation and analysis strategy . . . . .	82
4.2	Event selection . . . . .	82
4.2.1	Event topology . . . . .	83
4.2.2	Isolation and partial reconstruction . . . . .	84
4.3	Study of the $D_s^+$ decays . . . . .	86
4.3.1	The $D_s^+$ decay model . . . . .	86
4.3.2	The $D_s^+$ control sample . . . . .	87
4.4	Fit model and results . . . . .	91
4.4.1	Fit model . . . . .	91
4.4.2	Signal and normalisation yields . . . . .	92
4.5	Systematics . . . . .	98
4.5.1	$\tau$ decay model . . . . .	98
4.5.2	Particle identification . . . . .	99
4.5.3	Summary of systematic uncertainties . . . . .	103
4.6	$\mathcal{R}(D^*)$ result . . . . .	103
<b>5</b>	<b>Measurements of <math>\mathcal{B}(\Lambda_b^0 \rightarrow \Lambda_c^+ \tau^- \bar{\nu}_\tau)</math> and <math>\mathcal{R}(\Lambda_c^+)</math></b>	<b>107</b>
5.1	Analysis method . . . . .	109
5.1.1	Definition of the measurement . . . . .	109
5.1.2	Possible normalisation procedures . . . . .	110
5.1.3	Background channels classification . . . . .	112
5.1.4	Determination of the signal yield . . . . .	114
5.2	Data and simulation samples . . . . .	114
5.2.1	Data samples . . . . .	114
5.2.2	Simulation samples . . . . .	114
5.3	Selection of the events . . . . .	115
5.3.1	Online selection . . . . .	116
5.3.2	Offline preselection . . . . .	116
5.3.3	Event topology . . . . .	119
5.3.4	Additional cuts . . . . .	120
5.3.5	Selection of the normalisation events . . . . .	126
5.3.6	$\Lambda_c^+$ background removed using sideband subtraction . . . . .	126
5.3.7	$\Lambda_c^*$ feed-down . . . . .	129
5.4	Isolation tools . . . . .	130
5.4.1	Charged particles isolation using a BDT . . . . .	131
5.4.2	Neutrals isolation . . . . .	135
5.5	Reconstruction techniques . . . . .	139
5.5.1	Reconstructing $\Lambda_b^0 \rightarrow \Lambda_c^+ \tau^- \bar{\nu}_\tau$ events . . . . .	139
5.5.2	Signal reconstruction results using simulation samples . . . . .	140
5.5.3	Partial reconstruction of $\Lambda_b^0 \rightarrow \Lambda_c^+ D_s^-$ events . . . . .	141
5.6	Estimation of the efficiencies . . . . .	149
5.6.1	Trigger efficiencies . . . . .	149
5.6.2	Stripping efficiencies . . . . .	154
5.6.3	Selection efficiencies . . . . .	156
5.7	Description and performances of the BDT . . . . .	157

---

5.7.1	Introduction on Boosted Decision Trees for event classification . . .	157
5.7.2	Definition of a Boosted Decision Tree algorithm . . . . .	158
5.7.3	Description of the BDT . . . . .	158
5.7.4	Validation of the BDT . . . . .	165
5.8	Determination of the normalisation yield . . . . .	168
5.8.1	Normalisation using the $\Lambda_b^0 \rightarrow \Lambda_c^+ \pi^- \pi^+ \pi^-$ exclusive peak . . . . .	168
5.9	Double-charm backgrounds . . . . .	175
5.9.1	Determination of the $\Lambda_b^0 \rightarrow \Lambda_c^+ D_s^- X$ background composition on data . . . . .	175
5.9.2	Data-driven control samples . . . . .	177
5.10	Extraction of the signal yield . . . . .	182
5.10.1	The fit model . . . . .	182
5.10.2	Computation of the constrained parameters of the fit . . . . .	183
5.10.3	Fit results . . . . .	186
5.10.4	Evidence of the observation of $\Lambda_b^0 \rightarrow \Lambda_c^+ \tau \nu_\tau$ decay . . . . .	188
5.11	Systematics . . . . .	189
5.11.1	$\tau$ decay model . . . . .	189
5.11.2	Systematics related to the fitting procedure . . . . .	189
5.11.3	Efficiencies, selection and trigger . . . . .	192
5.11.4	Normalisation channel . . . . .	192
5.11.5	$\Lambda_c^*$ feed-down . . . . .	193
5.11.6	Simulation statistics . . . . .	193
5.11.7	Systematics uncertainties summary . . . . .	193
5.12	Results . . . . .	194
5.12.1	Results regarding $\mathcal{R}(\Lambda_c)$ . . . . .	194
5.12.2	Observation of the decay $\Lambda_b^0 \rightarrow \Lambda_c^+ \tau^- \bar{\nu}_\tau$ . . . . .	194
5.12.3	Prospects . . . . .	194
	<b>Conclusion</b>	<b>197</b>
	<b>Bibliography</b>	<b>198</b>
	<b>Acknowledgements</b>	<b>209</b>

## CONTENTS

---

# Synthèse

Le travail réalisé dans le cadre de cette thèse consiste en l'étude de deux désintégrations,  $B^0 \rightarrow D^{*-} \tau^+ \nu_\tau$  et  $\Lambda_b^0 \rightarrow \Lambda_c^+ \tau^- \bar{\nu}_\tau$ , dites semitaoniques, en utilisant la reconstruction du lepton  $\tau$  en trois pions chargés. Le diagramme de Feynman de la transition  $b \rightarrow c \tau \nu_\tau$  est donné en Fig. 1. Les rapports de branchements de ces deux désintégrations permettent de construire les observables suivantes

$$\mathcal{R}(D^*) = \frac{\mathcal{B}(B^0 \rightarrow D^{*-} \tau^+ \nu_\tau)}{\mathcal{B}(B^0 \rightarrow D^{*-} \mu^+ \nu_\mu)}$$

$$\mathcal{R}(\Lambda_c) = \frac{\mathcal{B}(\Lambda_b^0 \rightarrow \Lambda_c^+ \tau^- \bar{\nu}_\tau)}{\mathcal{B}(\Lambda_b^0 \rightarrow \Lambda_c^+ \mu^- \bar{\nu}_\mu)}$$

permettant de tester l'universalité de la saveur des leptons dans le cadre du Modèle Standard, soit l'égalité des couplages des trois familles de leptons ( $e$ ,  $\mu$  et  $\tau$ ) aux bosons  $Z$  et  $W$ .

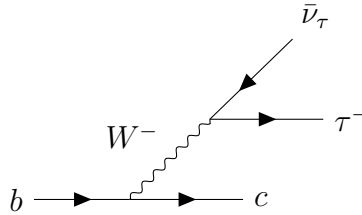


Figure 1 – Un diagramme en arbre pour la transition  $b \rightarrow c \tau \bar{\nu}_\tau$ .

Cette étude est motivée par un désaccord de l'ordre de  $3.78 \sigma$  entre la combinaison des mesures expérimentales  $\mathcal{R}(D)$  et  $\mathcal{R}(D^*)$  et les prédictions théoriques illustré en Fig. 2. Ceci pourrait être l'indication d'une contribution de Nouvelle Physique (NP) dans ces phénomènes décrit par le Modèle Standard.

Afin de mieux comprendre cette problématique, une courte introduction du Modèle Standard est présentée en chapitre 1. Les principaux éléments du modèle, comme l'importance des symétries, le mécanisme de Higgs et la matrice CKM, sont décrits. Une discussion sur les limites de ce modèle clôt ce chapitre.

Les prédictions théoriques de  $\mathcal{R}(D)$  et  $\mathcal{R}(\Lambda_c)$  sont discutées en profondeur dans le chapitre 2. Les désintégrations semitaoniques consistent en un hadron comportant un

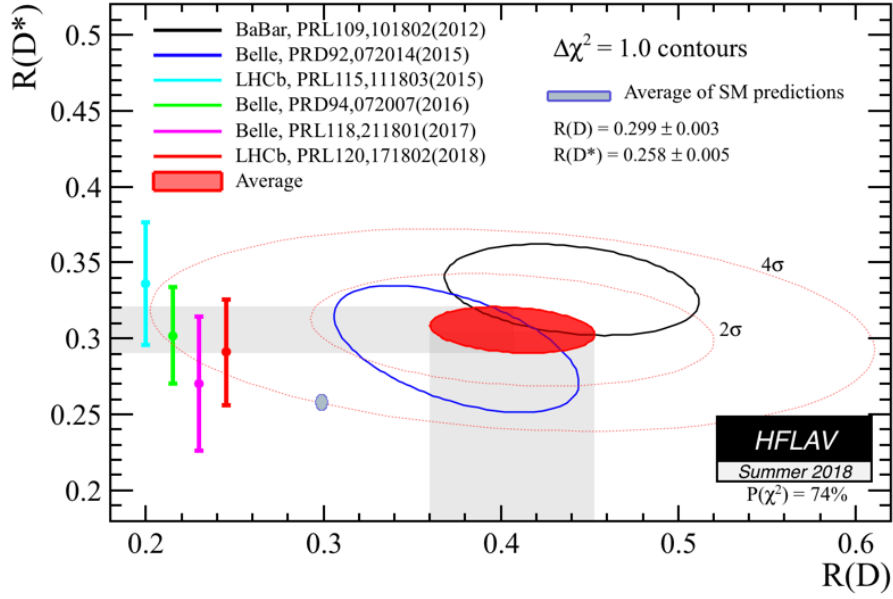


Figure 2 – Situation actuelle des mesures de  $\mathcal{R}(D)$  et  $\mathcal{R}(D^*)$ . Figure provenant de Réf. [1].

quark  $b$  ( $B^0$  ou  $\Lambda_b^0$ ) se désintégrant en un lepton  $\tau$  et un hadron contenant un quark  $c$  ( $D^{*-}$  ou  $\Lambda_c^+$ ). Afin d’avoir une prédiction précise concernant l’universalité de la saveur des leptons, les effets concernant la partie hadronique de la désintégration doivent être correctement évalués afin d’être sensible à une potentielle contribution de Nouvelle Physique. Le calcul des ratios  $\mathcal{R}(D^*)$  et  $\mathcal{R}(\Lambda_c)$  et des facteurs de formes hadroniques associés est discuté en détail et conduit aux prédictions suivantes

$$\mathcal{R}(D^*)_{SM} = 0.258 \pm 0.005 [1] \text{ et } \mathcal{R}(\Lambda_c)_{SM} = 0.3328 \pm 0.0074 \pm 0.0070 [2].$$

Une revue des différentes mesures publiées concernant les désintégrations semitaoniques est présentée ainsi qu’une étude de la sensibilité de la désintégration  $\Lambda_b^0 \rightarrow \Lambda_c^+ \tau^- \bar{\nu}_\tau$  aux contributions de Nouvelle Physique. En Fig. 3 sont présentés deux possibles diagrammes de Nouvelle Physique faisant intervenir un nouveau boson ( $W'$ ), un boson de Higgs chargé ( $H^\pm$ ) ou un Leptoquark (LQ).

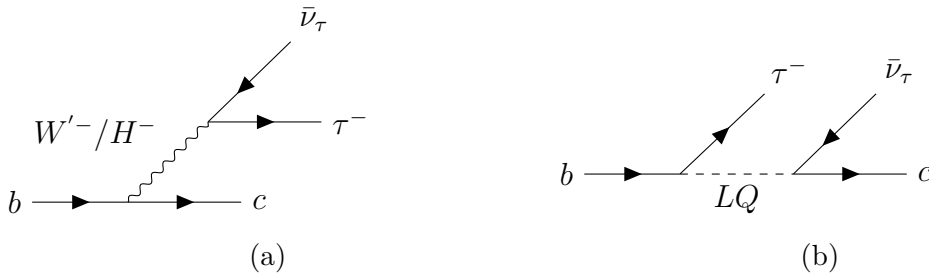


Figure 3 – Exemples de contributions de Nouvelle Physique avec des diagrammes de Feynman incluant un  $W'^- / H^-$  (a) ou un Leptoquark (b).

Le détecteur LHCb est actuellement le détecteur permettant l’étude du plus grand nombre de désintégrations semitaoniques et l’unique possibilité pour analyser la désintégration

$\Lambda_b^0 \rightarrow \Lambda_c^+ \tau^- \bar{\nu}_\tau$ . Installé le long du Large Hadron Collider (LHC) au CERN près de Genève, ce détecteur est un spectromètre à un bras couvrant la région  $2 < \eta < 5$  en pseudo-rapacité. Cette géométrie particulière est optimisée pour la détection de hadrons contenant un quark  $b$ , en effet les paires  $b\bar{b}$  sont principalement produites dans les collisions proton-proton du LHC dans deux cônes étroits vers l'arrière et vers l'avant par rapport au point de collision.

Le fonctionnement du détecteur LHCb est décrit dans le chapitre 3 et une vue schématique est présentée en Fig. 4. Il est constitué d'un détecteur de vertex (Vertex Locator ou VELO), de trajectographes et de détecteurs à effet Cherenkov (RICH1 et RICH2) placés à la fois en amont et en aval de l'aimant, de deux calorimètres électromagnétique et hadronique et de cinq chambres à muons. Le détecteur est complété par un système de déclenchement électronique et informatique permettant de sélectionner et enregistrer les collisions les plus intéressantes pour les analyses de physique. Ses excellentes performances tout particulièrement concernant la résolution sur la position des vertex et l'identification des particules ont rendu possible l'étude des désintégrations semitaoniques avec la reconstruction en trois pions du  $\tau$ .

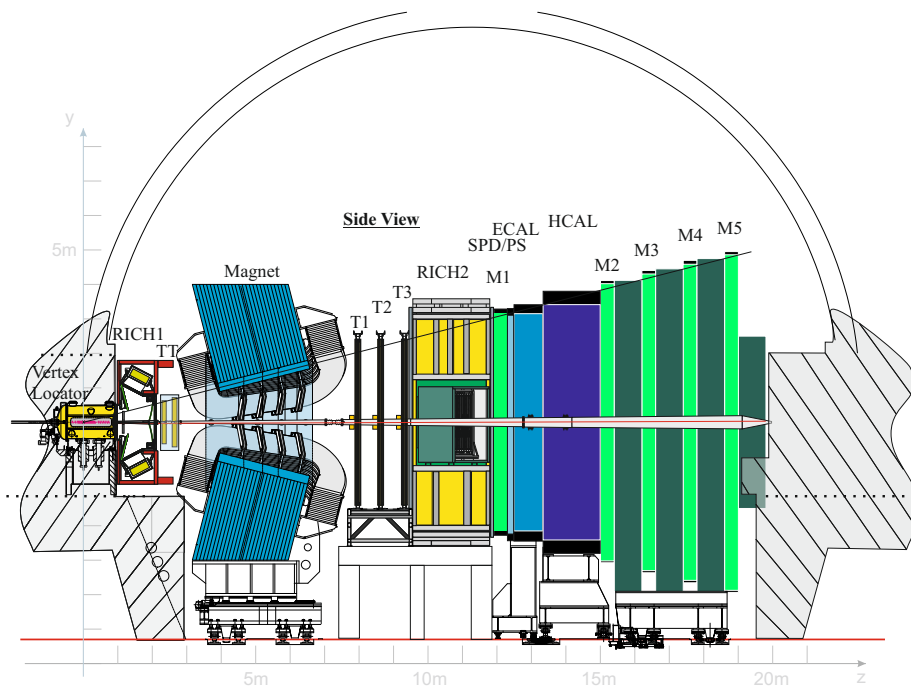


Figure 4 – Vue de profil du détecteur LHCb.

Les analyses effectuées sur les données collectées par le détecteur LHCb concernent principalement les mesures de précision dans le domaine de la physique des saveurs lourdes, soit les désintégrations de hadrons comportant un quark  $b$  ou  $c$ .

Les analyses présentées dans cette thèse sont basées sur l'étude des données collectées en 2011 et 2012, période décrite comme étant le Run1 du LHC, à une énergie dans le centre de masse de respectivement 7 et 8 TeV correspondant à une luminosité intégrée de  $3 \text{ fb}^{-1}$ .

Ces analyses sont les premières à utiliser une nouvelle technique de reconstruction du lepton  $\tau$  utilisant la désintégration  $\tau^- \rightarrow \pi^- \pi^+ \pi^- (\pi^0) \nu_\tau$ , permettant une nouvelle mesure de  $\mathcal{R}(D^*)$  avec des systématiques différentes par rapport à la première mesure utilisant la désintégration muonique du  $\tau$ ,  $\tau^- \rightarrow \mu^- \bar{\nu}_\mu \nu_\tau$  et la première étude de la désintégration  $\Lambda_b^0 \rightarrow \Lambda_c^+ \tau^- \bar{\nu}_\tau$ .

L'utilisation de ce mode de reconstruction hadronique du  $\tau$  est rendu possible par l'application d'une coupure de sélection sur la topologie de l'événement en conservant uniquement les événements où le  $\tau$  se trouve en aval du hadron contenant un quark  $c$  ( $D^{*-}$  ou  $\Lambda_c^+$ ). Les topologies des désintégrations  $B^0 \rightarrow D^{*-} \tau^+ \nu_\tau$  et  $\Lambda_b^0 \rightarrow \Lambda_c^+ \tau^- \bar{\nu}_\tau$  sont reportées en Fig. 5 avec les coupures effectuées pour les deux analyses indiquées. Ces coupures permettent de rejeter avec une excellente efficacité les événements du type  $B^0 \rightarrow D^{*-} \pi^+ \pi^- \pi^+ N$  et  $\Lambda_b^0 \rightarrow \Lambda_c^+ \pi^- \pi^+ \pi^- X$ , où  $X$  indique une ou plusieurs particules, qui sont initialement en bien plus grand nombre que le signal recherché.

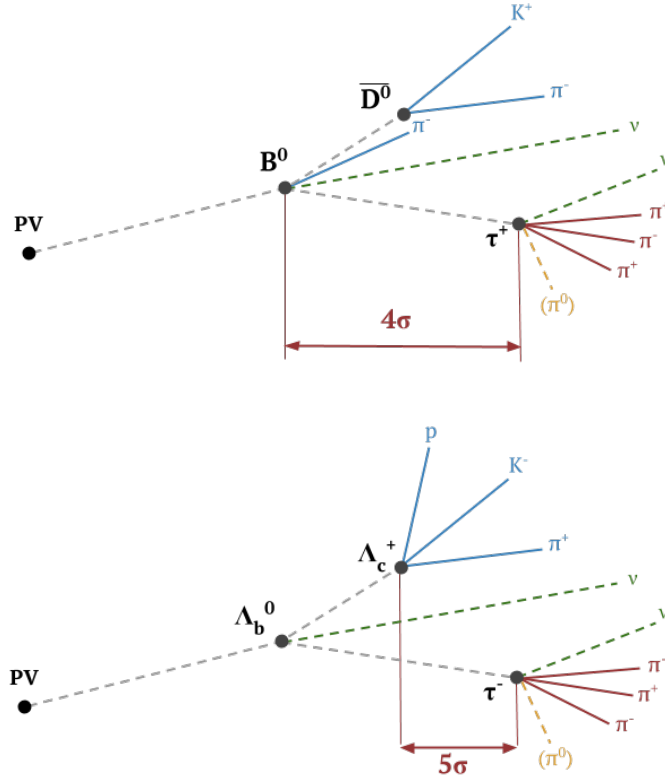


Figure 5 – Topologies des désintégrations  $B^0 \rightarrow D^{*-} \tau^+ \nu_\tau$  et  $\Lambda_b^0 \rightarrow \Lambda_c^+ \tau^- \bar{\nu}_\tau$ , le vertex du  $D^{*-}$  n'est pas représenté sur premier schéma car il est confondu avec celui du  $B^0$ . Les coupures appliquées pour les analyses  $\mathcal{R}(D^*)$  et  $\mathcal{R}(\Lambda_c)$  sont reportées sur les deux schémas.

L'analyse de la désintégration  $B^0 \rightarrow D^{*-} \tau^+ \nu_\tau$  menant à la mesure de  $\mathcal{R}(D^*)$  est détaillée dans le chapitre 4 avec une attention plus marquée sur les éléments de l'analyse qui sont aussi utilisés pour la mesure de  $\mathcal{R}(\Lambda_c)$ . Ainsi, l'étude des désintégrations doublement charmées,  $B^0 \rightarrow D^{*-} DX$ , est décrite en détail, tout particulièrement la sélection des événements, le modèle de désintégration du  $D_s^+$  et la procédure d'extraction du nombre

d'événements pour le signal recherché. Le modèle du  $D_s^-$ , le bruit de fond le plus important après la réjection des événements du type  $B^0 \rightarrow D^{*-} \pi^+ \pi^- \pi^+ X$ , est présenté en Fig. 6. Les distributions de plusieurs variables permettant de décrire les désintégrations du  $D_s^-$  sont ajustées sur un lot d'événements extraits des données enrichis en événements  $D_s^-$  ce qui permet de corriger les données de simulation et améliorer la modélisation de ce bruit de fond.

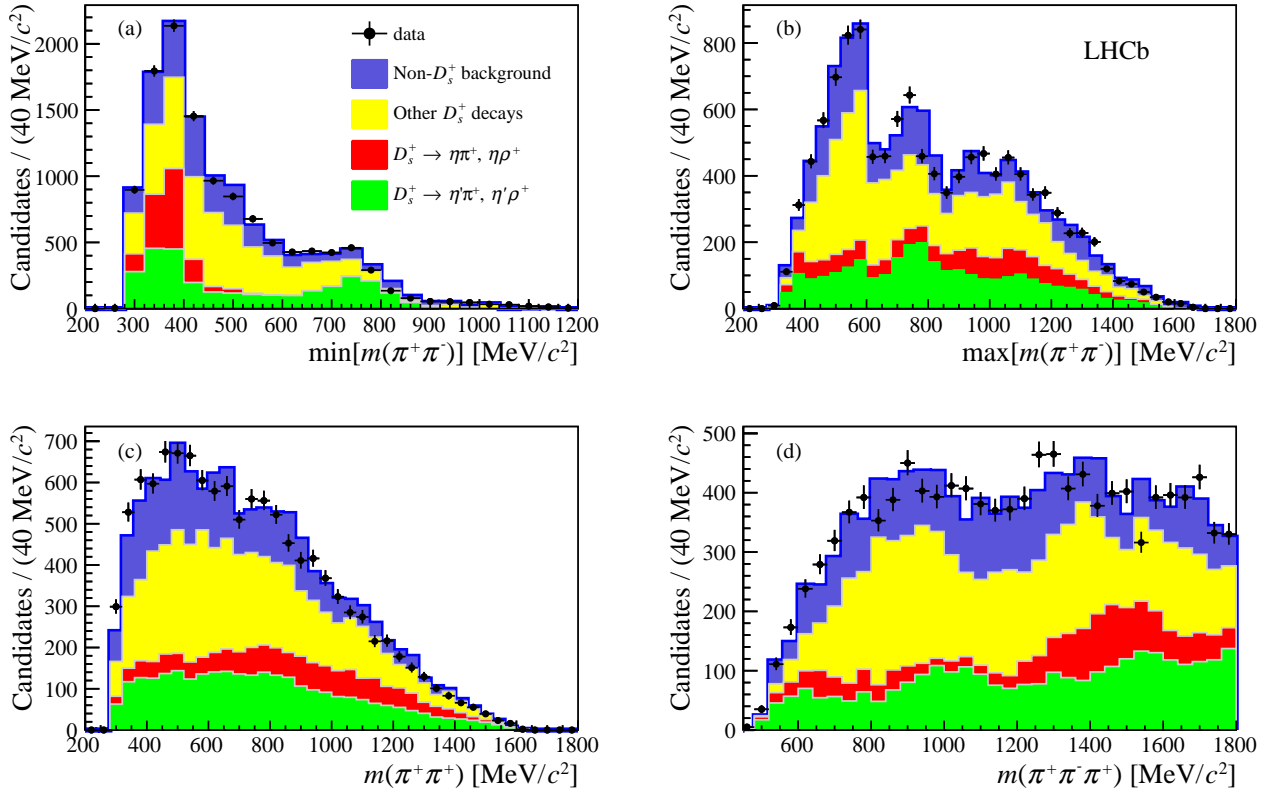


Figure 6 – Distributions des variables  $\min[m(\pi^+\pi^-)]$  (a),  $\max[m(\pi^+\pi^-)]$  (b),  $m(\pi^+\pi^+)$  (c) et  $m(\pi^+\pi^-\pi^+)$  (d) pour un lot de données enrichi en désintégrations  $B \rightarrow D^{*-} D_s^+(X)$ . Les différents composants de l'ajustement effectué correspondent aux désintégrations de  $D_s^+$  comprenant un  $\eta$  (rouge) ou un  $\eta'$  (vert) dans l'état final, d'autres désintégrations de  $D_s^+$  (jaune) et des bruits de fond issus de désintégrations d'autres particules que le  $D_s^+$ . Figure provenant de la Réf. [3].

Afin d'extraire le nombre d'événements signal, un ajustement sur les données est effectué simultanément sur le temps de vie du  $\tau$ , l'impulsion transférée  $q^2$  et le score du BDT. Les résultats de l'ajustement sont projetés sur ces trois variables en Fig. 11.

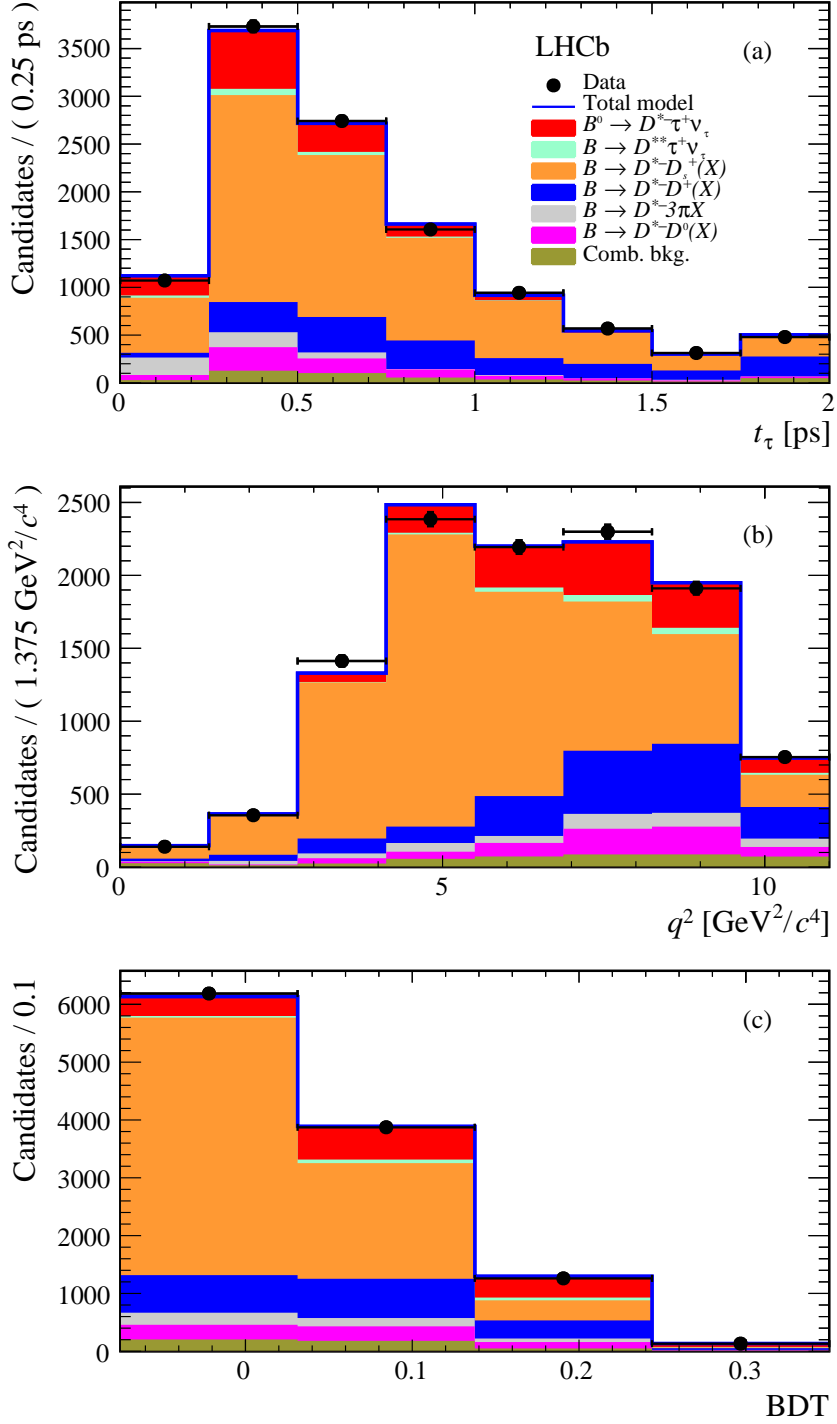


Figure 7 – Projections du fit pour  $\mathcal{R}(D^*)$  sur les distributions de la durée de vie du  $\tau$  (a), du  $q^2$  (b) et du score du BDT (c). Figure provenant de Réf. [3].

Il est ainsi possible de calculer  $\mathcal{R}(D^*)$  et le rapport de branchement  $\mathcal{B}(B^0 \rightarrow D^{*-} \tau^+ \nu_\tau)$  en utilisant les valeurs des rapports de branchement des désintégrations  $B^0 \rightarrow D^{*-} \pi^+ \pi^- \pi^+$  et  $B^0 \rightarrow D^{*-} \mu^+ \nu_\mu$  données respectivement par la moyenne des mesures présentées dans Réf. [4, 5, 6] et par le PDG [7]. Les résultats pour  $\mathcal{B}(B^0 \rightarrow D^{*-} \tau^+ \nu_\tau)$  et  $\mathcal{R}(D^*)$  sont

$$\mathcal{B}(B^0 \rightarrow D^{*-} \tau^+ \nu_\tau) = (1.42 \pm 0.094 \text{ (stat)} \pm 0.129 \text{ (syst)} \pm 0.054) \times 10^{-2}$$

$$\mathcal{R}(D^*) = 0.291 \pm 0.019 \text{ (stat)} \pm 0.026 \text{ (syst)} \pm 0.013 \text{ (ext)}$$

où la première incertitude est statistique, la deuxième est systématique et la troisième provient des incertitudes associées aux rapports de branchements des désintégrations  $B^0 \rightarrow D^{*-} \pi^+ \pi^- \pi^+$  et  $B^0 \rightarrow D^{*-} \mu^+ \nu_\mu$ . Le résultat est en accord avec la prédiction du Modèle Standard [1] à une déviation standard près et permet d'améliorer la précision de la moyenne mondiale de  $\mathcal{R}(D^*)$  et renforce légèrement le désaccord avec la prédiction théorique grâce à sa très bonne précision. Ce travail a fait l'objet de deux publications, Réf [8] et Réf [3].

L'analyse de la désintégration  $\Lambda_b^0 \rightarrow \Lambda_c^+ \tau^- \bar{\nu}_\tau$  est présentée en détail dans le chapitre 5. La stratégie de l'analyse, héritée de l'analyse  $\mathcal{R}(D^*)$ , consiste à mesurer  $\mathcal{K}(\Lambda_c^+)$ , défini par

$$\mathcal{K}(\Lambda_c^+) = \frac{\mathcal{B}(\Lambda_b^0 \rightarrow \Lambda_c^+ \tau^- \bar{\nu}_\tau)}{\mathcal{B}(\Lambda_b^0 \rightarrow \Lambda_c^+ \pi^- \pi^+ \pi^-)} = \frac{N_{sig}}{N_{norm}} \times \frac{\epsilon_{norm}}{\epsilon_{sig}} \times \frac{1}{\mathcal{B}(\tau^- \rightarrow \pi^- \pi^+ \pi^- (\pi^0) \nu_\tau)} \quad (1)$$

où  $N_{sig}$  et  $N_{norm}$  désignent respectivement les nombres d'événements des catégories signal et normalisation,  $\epsilon_{sig}$  et  $\epsilon_{norm}$  leur efficacités associées et  $\mathcal{B}(\tau^- \rightarrow \pi^- \pi^+ \pi^- (\pi^0) \nu_\tau)$  la somme des rapports de branchement des désintégrations  $\tau \rightarrow 3\pi \nu_\tau$  et  $\tau \rightarrow 3\pi \pi^0 \nu_\tau$ .

Il existe ensuite plusieurs méthodes possibles pour calculer  $\mathcal{R}(\Lambda_c)$  à partir de  $\mathcal{K}(\Lambda_c)$ .

Afin d'extraire le signal, une coupure sur la topologie de l'événement est appliquée comme décrit dans la Fig. 5 et un premier BDT (Arbre de Décision Boosté) est entraîné sur les variables d'isolation afin de mieux rejeter les événements de bruit de fond avec des traces supplémentaires par rapport à celles utilisées pour construire le candidat signal, la distribution du score de ce BDT est visible en Fig. 8.

Plusieurs outils sont ensuite utilisés afin de rejeter et contraindre le bruit de fond venant des désintégration doublement charmées comme la reconstruction partielle des événements, permettant de calculer les variables  $q^2$  et temps de vie du  $\tau$ , et une correction des fractions des différentes catégories de désintégrations  $\Lambda_b^0 \rightarrow \Lambda_c^+ D_s^- X$  en ajustant la distribution de la masse  $\Lambda_c^+ 3\pi$  des données comme montré en Fig. 9.

Un deuxième BDT est ensuite entraîné et optimisé pour différencier les événements de type signal de ceux venant de désintégrations doublement charmées. La distribution en sortie du BDT est montré Fig. 10.

Finalement, un ajustement simultané des variables  $q^2$ , temps de vie du  $\tau$  et BDT est réalisé, les projections du résultat de l'ajustement pour ces trois variables est présenté Fig. 11, ainsi que l'estimation des incertitudes statistiques et systématiques associées. Le même ajustement est aussi appliqué dans l'hypothèse où aucun événement signal est

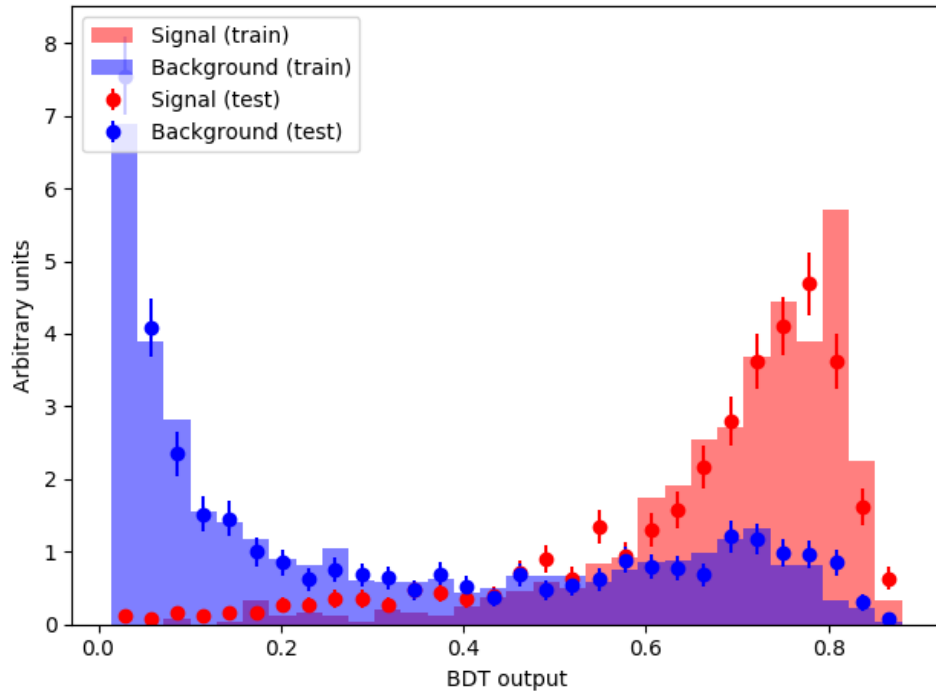


Figure 8 – Distribution du score du BDT d'isolation pour des événements isolés (rouge) et non isolés (bleu) pour les lots de données d'entraînement et de test.

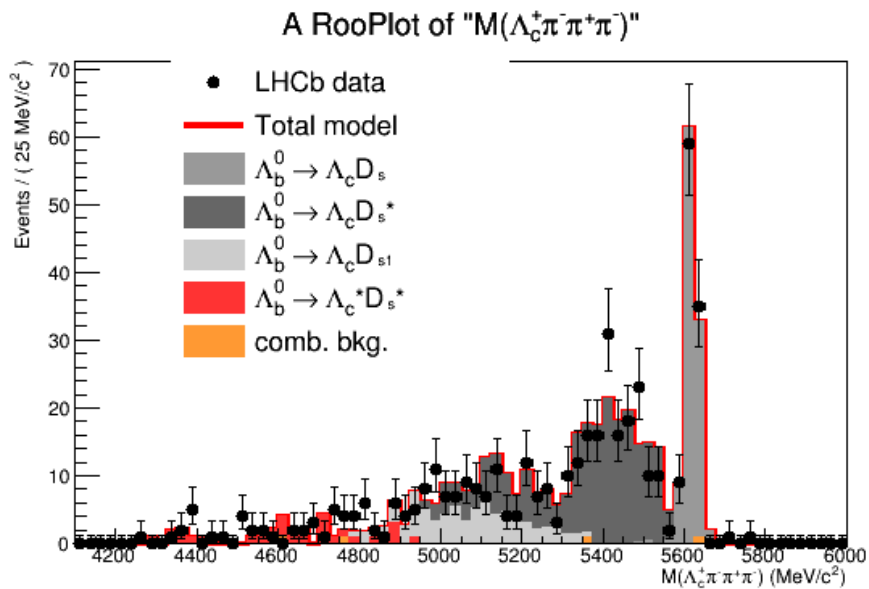


Figure 9 – Ajustement de la distribution de la masse  $m(\Lambda_c^+ 3\pi)$  pour extraire les fractions des différents désintégrations  $\Lambda_b^0 \rightarrow \Lambda_c^+ D_s^- X$ .

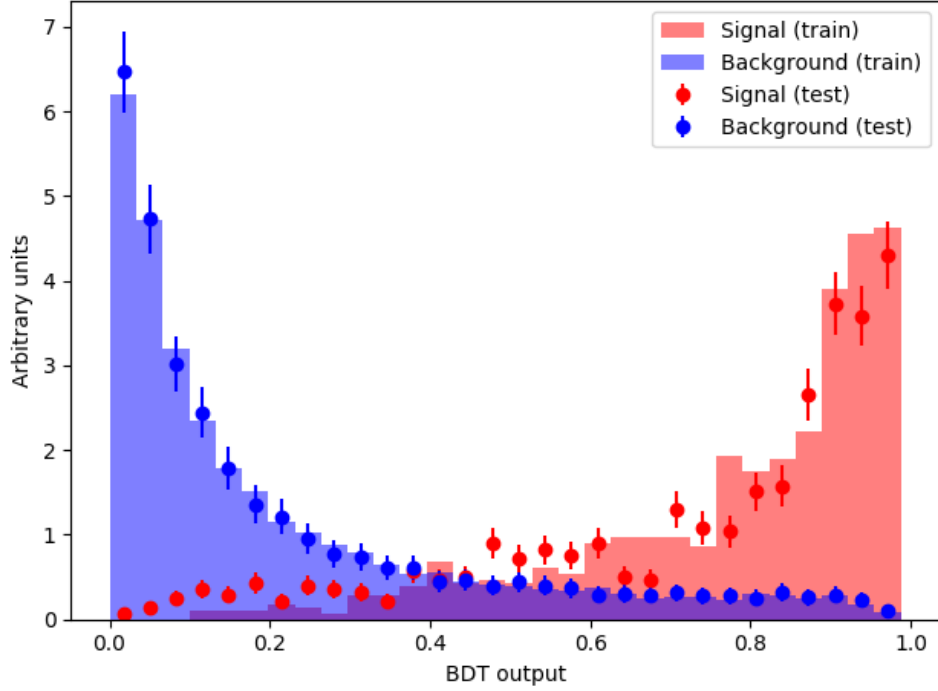


Figure 10 – Distribution du score du BDT pour les événements de type signal (rouge) et bruit de fond (bleu) pour les lots de données d’entraînement et de test.

présent et la différence de  $\chi^2$  permet de déterminer l’observation de la désintégration  $\Lambda_b^0 \rightarrow \Lambda_c^+ \tau^- \bar{\nu}_\tau$  avec une importance statistique de  $5.7\sigma$ , et ce pour la première fois.

La connaissance des nombres d’événements signal et normalisation ainsi que les incertitudes associées permet de reporter la mesure de  $\mathcal{R}(\Lambda_c)$  suivante:

$$\mathcal{R}(\Lambda_c^+) = \frac{\mathcal{B}(\Lambda_b^0 \rightarrow \Lambda_c^+ \tau^- \bar{\nu}_\tau)}{\mathcal{B}(\Lambda_b^0 \rightarrow \Lambda_c^+ \mu^- \bar{\nu}_\mu)} = XXX \times (1 \pm 0.105(\text{stat}) \pm 0.162(\text{syst}) \pm 0.12(\text{ext})) \quad (2)$$

où la valeur centrale est pour le moment inconnue mais qui fera bientôt l’objet d’une publication de la collaboration LHCb.

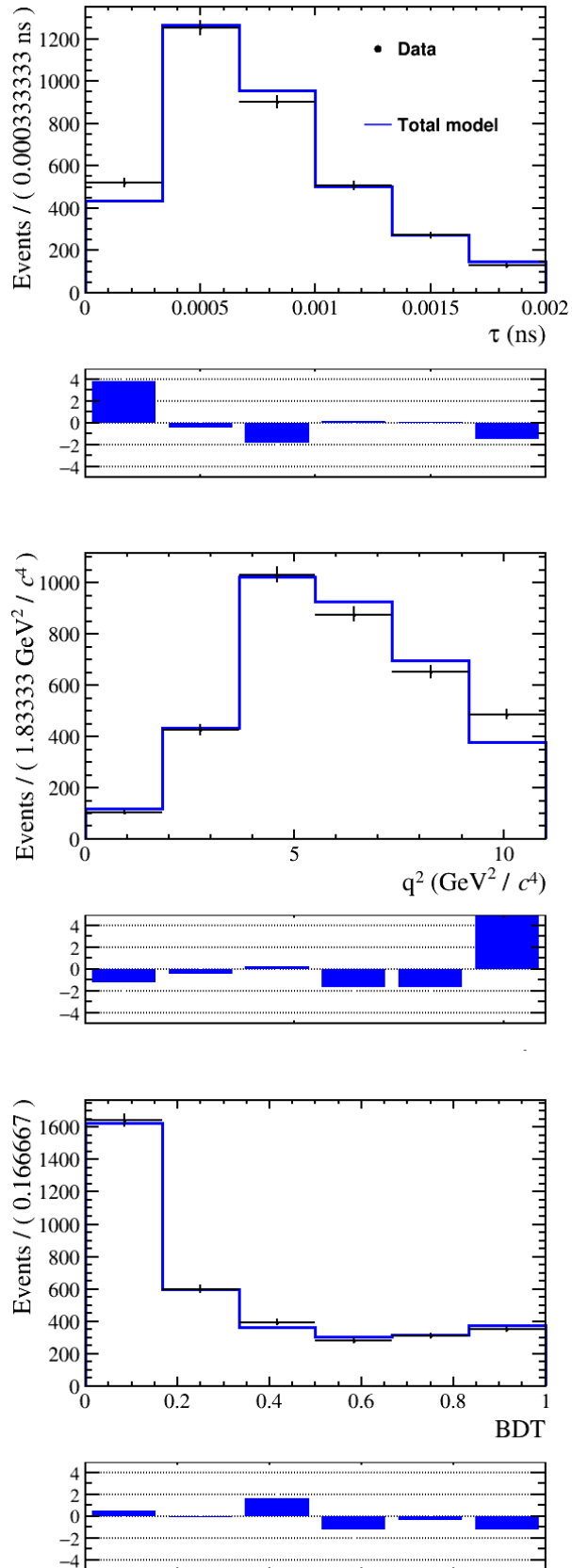


Figure 11 – Projections du fit pour  $\mathcal{R}(\Lambda_c)$  sur les distributions de la durée de vie du  $\tau$  (a), du  $q^2$  (b) et du score du BDT (c).

# Introduction

The Standard Model of particle physics is the model describing the elementary constituents of matter and the fundamental interactions. Since its discovery in the 70's, the SM have been extensively tested by experiments installed at  $pp$  colliders such as Tevatron and LHC or  $e^+e^-$  experiments as Belle and BaBar. The discovery of the Higgs boson by ATLAS and CMS experiments was the last remaining part to complete the model. Nevertheless, several open questions are still remaining, which motivates the search for New Physics effects. Both the SM and its limitations are discussed in Chap. 1.

The work presented in this thesis is focused on testing Lepton Flavour Universality through the measurements of  $b \rightarrow c\tau\nu_\tau$  transitions. An overview on how to test Lepton Flavour Universality is presented in Chapter 2 discussing both theoretical and experimental aspects. By measuring SM processes with precise theoretical predictions and control over the uncertainties related to the hadronic part of the process, it is possible to look for potential New Physics contributions. The experimental status is also described with a current World Average of the combination of  $\mathcal{R}(D)$  and  $\mathcal{R}(D^*)$  measurements which is in tension with the SM predictions at the level of  $3.78\sigma$ . It is therefore crucial to gain precision on these measurements and add new modes such as  $\Lambda_b^0 \rightarrow \Lambda_c^+ \tau \bar{\nu}_\tau$  to demonstrate New Physics effects or constrain New Physics models.

With  $pp$  collisions recorded by the LHCb detector, a wide range of  $B$  hadrons can be studied to strengthen the experimental status of semitauonic measurements. Its performances regarding vertex measurements of  $B$  hadrons and or particle identification are of great use for the analyses presented. A description of the LHCb detector is thus provided in Chapter 3.

A novel technique was used in LHCb to measure  $\mathcal{R}(D^*)$  by relying upon the  $\tau$  reconstruction using three pions decays. This analysis is presented in Chapter 4, focusing on its main features such as the study of vertex displacement to reject background, partial reconstruction techniques and a fit to a data sample enriched in  $D_s^+$  events to model its decay into three pions. The signal extraction using a 3D templates-based fit, the systematic uncertainties associated to the result, with a particular focus on the one related to particle identification efficiency, is also described. The impact of this novel result on the current experimental status is then discussed.

Finally, the description of the analysis to measure both  $\mathcal{B}(\Lambda_b^0 \rightarrow \Lambda_c^+ \tau \bar{\nu}_\tau)$  and  $\mathcal{R}(\Lambda_c)$  is

---

provided in Chapter 5. This analysis is using both tools developed for the  $\mathcal{R}(D^*)$  hadronic measurement and new improvements which correspond to the main work performed for this thesis. The results obtained using the LHCb Run1 dataset ( $3 \text{ fb}^{-1}$  collected at centre-of-mass energies of 7 and 8 TeV) are presented.

# The Standard Model of particle physics

## Contents

---

<b>1.1</b>	<b>Particles, interactions and symmetries . . . . .</b>	<b>22</b>
1.1.1	A world made of particles . . . . .	22
1.1.2	Overview of the fundamental interactions . . . . .	23
1.1.3	Symmetries . . . . .	25
<b>1.2</b>	<b>The Standard Model . . . . .</b>	<b>28</b>
1.2.1	Electroweak unification . . . . .	29
1.2.2	The Higgs Mechanism . . . . .	30
1.2.3	Quark mixing and CP violation . . . . .	32
1.2.4	Limits and unresolved issues . . . . .	34

---

On the 27<sup>th</sup> of April 1900, Lord Kelvin gave a lecture titled ‘Nineteenth-Century Clouds over the Dynamical Theory of Heat and Light’ at the Royal Institution, presenting two problems yet to be resolved at that time. The first problem concerned the description of the movement of matter through aether, which was thought as the medium needed for the propagation of light, even if the latest results of the Michelson-Morley experiment were not conclusive on its existence. The second problem was related to the Law of Equipartition, a theorem in statistical mechanics connecting the average energy of a system to its number of degrees of freedom. The measured heat capacity of gases were in disagreement with the theoretical predictions using such theorem.

These ‘two dark clouds’ led to the discovery of two major theories of the XX<sup>th</sup> century: Special Relativity and Quantum Mechanics. The generalisation of the former is the modern theory describing all phenomena involving Gravitation, the General Relativity and refinements to the latter during the whole XX<sup>th</sup> century are embedded in a theory describing all the known fundamental interactions, except the Gravitation, in the so called Standard Model (SM) of Particle Physics.

This Chapter presents an overview of the Standard Model with a brief summary of its history and the description of its main components.

## 1.1 Particles, interactions and symmetries

### 1.1.1 A world made of particles

The electron is the first elementary particle discovered by Joseph Thomson in 1897 and as the list of discoveries and the studies of the properties of such objects expanded, the need of a classification grew. To classify particles, one needs firstly to know its spin, the intrinsic angular momentum. If the spin is an integer, the particle is called a boson and will follow the Bose-Einstein statistics and the Klein-Gordon equation will be used for its description. One important property is the ability of bosons to be all in the same energy state whereas particles with a half-integer spin, called fermions, need to respect the Pauli exclusion principles: two fermions cannot be in the same energy state, they are thus described by the Fermi-Dirac statistics and their dynamics is described by the Dirac equation.

In the Standard Model, the elementary fermions are called quarks and leptons. In this context, elementary means that no experiment has yet been able to find substructures in these particles and up to now, these are known as the smallest building blocks of matter. They are two types of leptons, both divided in three groups, often called ‘families’, depending on their ‘lepton flavour’: charged leptons (electron ( $e$ ), muon ( $\mu$ ) and tau ( $\tau$ )) and neutral ones, the neutrinos ( $\nu_e$ ,  $\nu_\mu$  and  $\nu_\tau$ ). Quarks are both carrying electrical and colour charged and an additional quantum number called *flavour*, all described in the next sections. Thus, six versions of quarks exist called up ( $u$ ), down ( $d$ ), strange ( $s$ ), charmed ( $c$ ), beauty ( $b$ ) and top ( $t$ ). It should be noted that the number of fermions within the SM is not constrained, a fourth family of quark can be conceived even if no experimental proof should suggest so.

If quarks and leptons are the elementary constituents of matter, elementary bosons are the force carriers responsible for the fundamental interactions. The photon ( $\gamma$ ) is the carrier of the electromagnetic interaction, gluons ( $g$ ) transmit the strong one and the weak interaction is described by three bosons: two charged ones ( $W^+$ ,  $W^-$ ) and a neutral one ( $Z^0$ ). There is another fundamental boson called the Higgs boson ( $H$ ) responsible for the masses of the elementary particles, it will be described in more depth in Section 1.2.2.

For each of these particles, an alternate version sharing the same mass but with the opposite charge exists: the anti-particle, they are denoted using a bar, for instance, the  $b$  anti-quark symbol is  $\bar{b}$ . Some particles are their own anti-particle such as the photon.

In addition to these elementary particles, there are also combination of quarks and anti-quarks called hadrons. They are divided in two categories, mesons formed usually by a quark and an anti-quark and baryons made either from three quarks or three anti-quarks even if more exotic forms of both mesons and baryons can exist. It has to be noted that

the spin of a hadron depends on its constituents and thus mesons are bosons and baryons are fermions.

### 1.1.2 Overview of the fundamental interactions

In addition to identify fundamental particles, ones also needs to characterise interactions allowing two particles to alter the dynamics of each other. Up to now, four fundamental interactions are known: gravitation, electromagnetic, strong and weak interactions. Tab 1.1 presents a summary of the main characteristics of each fundamental interaction.

Being the weakest of the fundamental interactions is not the only peculiarity of the gravitation. It is described by General Relativity which is not a Quantum Field Theory contrary to the theories describing the other interactions and the graviton, which is thought as the fundamental boson carrying gravitation is a hypothetical particle. A theory able to describe the four fundamental interactions in a single framework is yet to be found. Luckily, the masses of all the particles and its tiny relative strength make gravitation completely negligible for Particle Physics. The remaining interactions, strong, weak and electromagnetic are the only ones considered in Particle Physics, in the 70s, their unification in a common theory, called the Standard Model (SM), has been a major breakthrough.

interaction	relative strength	model	messenger	charge	range [m]
strong	1	QCD	gluons	colour	$10^{-15}$
electromagnetic	$10^{-2}$	QED	photon	electric charge	$\infty$
weak	$10^{-5}$	(*)	$W^\pm$ & $Z^0$	flavour	$10^{-17}$
gravitation	$10^{-42}$	GR	graviton (?)	mass	$\infty$

Table 1.1 – Main characteristics of the four known fundamental interactions.

#### Electromagnetic interaction

All charged particles, quarks and charged leptons ( $e$ ,  $\mu$  and  $\tau$ ) are sensitive to the electromagnetic interaction. This interaction is carried by the photon, a massless and electrically neutral particle and conserves both lepton number and quark flavour, which forbid a photon to couple to two quarks or leptons of different type. The typical decay time of a particle through an electromagnetic process is  $10^{-20}$  s.

The theory describing this interaction is called Quantum Electrodynamics (QED) and was conjointly developed by Feynman [9], Schwinger [10] and Tomonaga [11] in the late 40's. The renormalisation, or how to deal with infinite integrals in a perturbative computation, was invented and successfully applied to QED. Due to the renormalisation, the theory is described by a running coupling factor  $\alpha$ , its value depends on the energy of the process considered, which value decreases as the energy becomes lower. Its asymptotic value, describing a situation where photons and charged particles are no longer interacting, is known historically as the fine structure constant and is equal to:

$$\alpha = \frac{e^2}{4\pi\epsilon_0\hbar c} \approx \frac{1}{137}$$

where  $e$  is the electric charge of the electron and  $\epsilon_0$  the permittivity of the vacuum.

### Strong interaction

The strong interaction governs the interaction of the quarks as these particles carry a charge of ‘colour’. The particles transmitting the colour charge are known as gluons and as they carry themselves a colour charge, they are thus also capable of strongly interacting.

The colour charge can take three different values denoted as red, blue and green, and in the same manner as negative electric charges, anti-colour charges exist in the three corresponding versions. To obtain a neutral colour charge, one needs to combine the three different (anti-)colour charges. The strong interaction is characterised by a  $SU(3)$  symmetry group which leads to 8 different types of gluons, each carrying both a colour and an anti-colour charge. The typical decay time of a particle strongly interacting is  $10^{-23}$  s.

The theory describing the strong interaction is known as Quantum Chromodynamics (QCD) with strong contributions from Gell-Mann [12] for the concept of colour charge and from Gross, Politzer, Wilczek ([13] and [14]) for the discovery of asymptotic freedom. The behaviour of the running factor is opposite with respect to QED, it becomes very small at high energies and increases at low energies forbidding perturbative computations at such energies.

Its main features are:

- Asymptotic freedom: The interaction between quarks decreases as the energy increases and the distance between them diminishes.
- Confinement: quarks interact stronger as the distance between them increases.

Confinement leads to the impossibility for quarks to be observed individually, they need to group to form colourless objects known as hadrons. Two categories exist depending on the value of the baryon number ( $B$ ), which is a quantum number conserved by each interaction:

- if  $B = 0$ , the hadron is known as a meson and consists usually in a quark anti-quark pair ( $q\bar{q}$ ) even if other arrangements are possible such as tetraquarks ( $q\bar{q}q\bar{q}$ ) as detected in Ref. [15]
- if  $B = 1$ , the particle is a baryon and consists in most cases in a triplet of (anti-)quarks ( $qqq$  or  $\bar{q}\bar{q}\bar{q}$ ) even if other possibilities exist such as pentaquarks ( $qqqq\bar{q}$ ) as observed in Ref. [16].

In the context of increasing distance between two quarks, the strength of the interaction becomes so high and the energy stored in it so large that new particles are created to form new hadrons in a process referred to as hadronisation. Hadronisation is used to describe jets occurring in hadronic collisions.

Another quantum number is also defined to describe the strong interaction, the isospin ( $I$ ) which is constructed in analogy with the spin and relies on  $SU(N)$  symmetry group where  $N$  is the number of quarks involved<sup>1</sup>. For instance, both neutron and proton belong

---

<sup>1</sup>The isospin is not an exact symmetry of the strong interaction as for instance there is a mass

to the same isospin doublet ( $I = \frac{1}{2}$ ) of  $SU(2)$  but the projection on its third component, denoted as  $I_3$ , is  $+\frac{1}{2}$  for the proton and  $-\frac{1}{2}$  for the neutron.

### Weak interaction

As both quarks and leptons carry a flavour charge, they can interact through weak interaction. The typical decay time through weak interaction is  $10^{-8}$  s and the interaction is carried by  $W^\pm$  bosons for charged currents and  $Z$  boson for neutral ones. These bosons are massive with

$$m_W = 80.379 \pm 0.012 \text{ GeV}/c^2$$

and

$$m_Z = 91.1876 \pm 0.0021 \text{ GeV}/c^2$$

according to PDG [7].

The modern description of weak processes is performed within the electroweak unification model proposed by Glashow [17], Salam [18] and Weinberg [19], described in Sec. 1.2.1. The bosons of this theory are massless but are given masses through the spontaneous symmetry breaking of the electroweak gauge symmetry using the Higgs mechanism described in Sec. 1.2.2.

Historically, Fermi was the first to introduce in 1932 a theory in Ref. [20] to describe weak interactions using a point interaction to understand nuclear  $\beta$ -decays with neutron decaying in protons through the  $n \rightarrow pe^-\bar{\nu}_e$  process. The model was then modified to reflect the symmetry breaking happening in weak decays as described in the next section.

### 1.1.3 Symmetries

Studying symmetries of a system have always been of a great help for scientists as it helps to set the frame in order to solve it. With a spherical system, one knows that the description of this system will be far simpler using spherical coordinates.

The equation of motion of a physical system can be embedded in a mathematical object called a Lagrangian ( $\mathcal{L}$ ) and the knowledge of which transformation keeps the system invariant helps to constrain which mathematical expression the Lagrangian can take.

Emmy Noether, a German mathematician, took symmetries to a deeper level by her demonstration in 1915 [21] of the theorem now named after her stating that each symmetry can be associated to a conservation law. If a system is invariant under some symmetry, some intrinsic quantity of this system is conserved. Some examples of symmetries and their conserved quantity are given in Tab. 1.2.

In quantum field theory (QFT), a symmetry is described by an operator that needs to let invariant the vacuum, the physical observables and the action of the Lagrangian

---

difference between the neutron and the proton. Yet this approximate symmetry is particularly useful to study light hadrons.

Symmetry	Conserved quantity
Time translation	Energy
Space translation	Momentum
Rotation	Angular momentum

Table 1.2 – Examples of symmetry and their conserved quantity.

describing the theory defined as:

$$\mathcal{S} = \int d^4x \mathcal{L}(t, \vec{x})$$

In addition to continuous symmetries such as space and times translations, several discrete symmetries are important to describe the Standard Model Lagrangian.

The first three discrete symmetries to consider are called Charged conjugation (C), Parity (P) and Time reversal (T). A given particle of spatial coordinate  $\vec{x}$  and time coordinate  $t$  is transformed under each of these symmetries as follows:

- C: If the charged conjugation is applied, the particle becomes its own anti-particle with same mass and spin but opposite quantum numbers such as the electric charge ( $e^- \rightarrow e^+$ )
- P: Parity transforms the spatial coordinate  $\vec{x}$  into  $-\vec{x}$
- T: Time reversal converts the time coordinate  $t$  into  $-t$

Two combinations of these symmetries are also considered, the conjugation of C and P known as CP and the conjugation of the three symmetries referred as CPT.

By construction, any quantum field theory is invariant under the CPT symmetry, which is also known as the CPT theorem. One of its implications that can be experimentally studied is that both a particle and its anti-particle share the same mass, and the most accurate results come from the mass difference of  $K^0$  and  $\bar{K}^0$  known to be less than  $10^{-18}$  as discussed in [22].

If the CPT symmetry cannot be violated within the QFT framework, both C, P, CP and T can be as long the different violations compensate to conserve CPT. Both strong and electromagnetic interactions are invariant under these transformations whereas weak interaction was found to violate both C, P and CP symmetries<sup>2</sup>.

Before the 50's, Parity was always considered as an implicit symmetry of any interaction without experimental proof. However, the  $\tau - \theta$  puzzle led to a change of perspective on this subject. Two particles  $\tau$ , not to be confused with the  $\tau$  lepton discovered later during the 70's, and  $\theta$  were measured to have the same mass and quantum numbers but opposite parity as seen in the following decays:

$$\theta^+ \rightarrow \pi^+ \pi^0 \quad (P = +1)$$

---

<sup>2</sup>As CPT remains conserved, T is also broken but it is much more difficult to study experimentally, the evidence of its violation was nevertheless observed by the BaBar collaboration in Ref. [23].

## 1.1. PARTICLES, INTERACTIONS AND SYMMETRIES

---

$$\tau^+ \rightarrow \pi^+ \pi^0 \pi^0 \quad (P = -1)$$

In Ref. [24], Lee and Yang proposed as an alternate explanation that  $\theta$  and  $\tau$  were indeed the same particle with one of the decay process breaking the conservation of the parity. They thus proposed to study parity violation in weak decays.

C.S Wu and her group were then able to demonstrate the violation of the parity in weak transitions by studying  $\beta$ -decays of Cobalt nuclei:

$${}^{60}\text{Co} \rightarrow {}^{60}\text{Ni}^* e^- \bar{\nu}_e$$

Using an external magnetic field, the nuclear spin of the Cobalt nuclei were aligned. If parity were to be conserved, no preferred direction of emission of the electron should exist. Electrons were measured to be preferentially emitted backwards with respect to the direction of the nuclear spin, which clearly proved the breaking of the parity symmetry by the weak interaction.

Furthermore, it was demonstrated in 1958 by Goldhaber *et al.* in Ref. [25] that neutrinos have negative helicity. The helicity of a particle is the projection of the spin onto its momentum:

$$h = \frac{\vec{S} \cdot \vec{p}}{|\vec{p}|}$$

For massless particles, a negative helicity means a left-handed particle whereas a positive helicity corresponds to a right-handed one. As neutrinos can be considered massless to a large extent, this means that only left-handed neutrinos and right-handed anti-neutrinos exist, which is the proof of the violation of the charge conjugation symmetry by the weak interaction.

Finally, Cronin and Fitch observed in Ref. [26] the violation of the CP symmetry in neutral kaons decays. As neutral kaons are oscillating, a  $K^0$  can become a  $\bar{K}^0$ , the particles observed experimentally are not  $K^0$  and  $\bar{K}^0$  but linear combinations of the two which will be referred as  $K_s^0$  and  $K_L^0$ . If the weak interaction is invariant under the CP symmetry, these observable states should identify to the CP eigenstates  $K_1$  and  $K_2$  defined as follows:

$$\begin{aligned} |K_1\rangle &= \frac{|K^0\rangle - |\bar{K}^0\rangle}{\sqrt{2}} \\ |K_2\rangle &= \frac{|K^0\rangle + |\bar{K}^0\rangle}{\sqrt{2}} \end{aligned} \tag{1.1}$$

such as  $CP|K_1\rangle = |K_1\rangle$  and  $CP|K_2\rangle = -|K_2\rangle$  with  $K_s^0 = K_1$  and  $K_L^0 = K_2$  if CP is conserved.

Due to their respective parity,  $K_1$  can decay into two pions whereas  $K_2$  decays into three pions. Because of the difference in available phase space, the decay time of  $K_1$  is much shorter than  $K_2$ . This decay time difference implies that a  $K^0$  beam is only composed of  $K_2$  mesons after some time as all the  $K_1$  mesons already disintegrated.

Cronin and Fitch reported decays of the  $K_L^0$  state into two pions, meaning that the observed particles, the weak eigenstates, do not match with the CP ones. In fact, one can introduce  $\epsilon$  to take into account the effect of CP violation, with  $\epsilon = 2.24 \times 10^{-3}$  [22], to describe the weak eigenstates as:

$$|K_S^0\rangle = \frac{1}{\sqrt{1+|\epsilon|^2}}(|K_1\rangle + \epsilon|K_2\rangle)$$

$$|K_L^0\rangle = \frac{1}{\sqrt{1+|\epsilon|^2}}(|K_2\rangle + \epsilon|K_1\rangle)$$

The description of the CP violation in the Standard Model is further discussed in Sec. 1.2.3.

As a summary, Tab. 1.3 presents all the fundamental interactions described by the Standard Model and with invariance status under the different discussed symmetries. In addition to the quantum numbers discussed in this section, there are also the lepton number (L), +1 for leptons and  $-1$  for anti-leptons, also conserved by each of the three interactions and the quark flavour, one for each of the six types of quarks, conserved only by strong and electromagnetic interactions. The flavour of a quark can change under a weak process, with for instance a  $b$  becoming a  $c$ , and is described in Sec. 1.2.3.

Symmetry or quantum number	Strong int.	Electromagnetic int.	Weak int.
CPT	✓	✓	✓
P	✓	✓	X
C	✓	✓	X
CP or T	✓	✓	X
Q (electric charge)	✓	✓	✓
B (Baryon number)	✓	✓	✓
L (Lepton number)	✓	✓	✓
flavour	✓	✓	X
I (Isospin)	✓	X	X
J (Total angular momentum)	✓	✓	✓

Table 1.3 – Summary of invariance under symmetries and conservation of quantum numbers for each of the three fundamental interactions of the Standard Model.

## 1.2 The Standard Model

The Standard Model is the quantum field theory describing both electromagnetic, weak and strong interactions, it is then built to be invariant under  $U(1)_Y \times SU(2)_L \times SU(3)_C$  gauge invariance where  $SU(3)_C$  is the gauge invariance of QCD and  $C$  denotes the colour charge and  $U(1)_Y \times SU(2)_L$  is the electroweak gauge invariance discussed in Sec. 1.2.1 with  $Y$  denoting the hypercharge and  $L$  the weak isospin.

The Lagrangian of the Standard Model can be expressed as:

$$\mathcal{L}_{SM} = \sum_{\text{gauge bosons}} -\frac{1}{4}F^{\mu\nu}F_{\mu\nu} + \sum_{\text{fermions}} \bar{\psi}(\gamma^\mu D_\mu)\psi + \mathcal{L}_Y + (D_\mu\Phi)^\dagger(D^\mu\Phi) - V(\Phi) \quad (1.2)$$

where  $\psi$  denotes fermion fields,  $\Phi$  the Higgs doublet and  $F^{\mu\nu}$  the gauge bosons fields. The first two terms of the SM Lagrangian describe the kinematics of both gauge bosons and fermions, the third is the Yukawa Lagrangian ( $\mathcal{L}_Y$ ) describing the mechanism through which the fermions acquire a mass as discussed in Sec. 1.2.3 and the last term is the Higgs Lagrangian described in Sec. 1.2.2 responsible for the mass of the gauge bosons  $W$  and  $Z$ .

The covariant derivative  $D_\mu$  in Eq. 1.2 can be expressed as:

$$D_\mu = \partial_\mu + ig'B_\mu Y + ig\frac{\vec{\tau}}{2} \cdot \vec{W}^\mu + ig_3\frac{\lambda_a}{2}G_a^\mu \quad (1.3)$$

where  $g$ ,  $g'$  and  $g_3$  are respectively the electroweak and strong coupling constants with  $B^\mu$ ,  $W^\mu$  and  $G^\mu$  being the gauge bosons fields.  $\vec{\tau}$  denotes the Pauli matrices,  $\lambda_a$  are the 8 generators of the  $SU(3)$  colour group corresponding to the 8 gluons of QCD and  $Y$  is the weak hypercharge related to the electric charge  $Q$  and the third component of the weak isospin by the formula:

$$Y = 2(Q - T_3)$$

The covariant derivative introduces the couplings of the gauge bosons to the fermions.

In the following of this section, right-handed singlets ( $\psi_R$ ) and left-handed doublets ( $\psi_L$ ) of particles will also be used to respect the  $U(1)_Y \times SU(2)_L$  structure of the electroweak interaction. These two objects are defined as follows:

$$\psi_R = \{\ell^-, u_{R\alpha}, d_{R\alpha}\}, \quad \psi_L = \left\{ \begin{pmatrix} \nu_\ell \\ \ell^- \end{pmatrix}_L, \begin{pmatrix} u_\alpha \\ d_\alpha \end{pmatrix}_L \right\} \quad (1.4)$$

where  $\ell^-$  denotes a charged lepton,  $u$  and  $d$  refer respectively to an up-type quark ( $u$ ,  $c$  or  $t$ ) or a down-type quark ( $d$ ,  $s$  or  $b$ ) and  $\alpha$  is the index taking into account the colour charge.

The next sections are meant to describe the electroweak interactions, the Higgs field and flavour structure of the Standard Model as it will be used to describe the semitauonic decays in Chap. 2.

### 1.2.1 Electroweak unification

Due to the parity violation of the weak interactions, the weak interaction is invariant under a  $SU(2)_L$  gauge symmetry where  $L$  denotes the weak isospin. Fermions are then described as left-handed doublets of the weak isospin  $I = \frac{1}{2}$  and right-handed singlets with  $I = 0$ .

In 1967, Glashow [17], Weinberg [19] and Salam [18] proposed a model to unify both electromagnetic and weak interactions in an electroweak interaction conserving the  $U(1)_Y \times SU(2)_L$  invariance. Two new covariant derivatives have to be written:

$$D_{\mu,L} = \partial_\mu + ig \frac{\sigma_i}{2} W_\mu^i + ig' \frac{Y}{2} B_\mu \quad (1.5)$$

$$D_{\mu,R} = \partial_\mu + ig' \frac{Y}{2} B_\mu \quad (1.6)$$

where  $g$  and  $g'$  are respectively the coupling constants of the  $SU(2)_L$  and  $U(1)_Y$  gauge invariances. The electroweak part of the SM Lagrangian can thus be written as:

$$\mathcal{L}_{EW} = i\bar{\psi}_L \gamma^\mu D_{\mu,L} \psi_L + i\bar{\psi}_R \gamma^\mu D_{\mu,R} \psi_R - \frac{1}{4} W_{\mu\nu}^i W_i^{\mu\nu} - \frac{1}{4} B_{\mu\nu} B^{\mu\nu} \quad (1.7)$$

The physical bosons,  $\gamma$ ,  $Z^0$  and  $W^\pm$  are then described by the following fields:

$$A_\mu = B_\mu \cos \theta_W + W_\mu^3 \sin \theta_W \quad (1.8)$$

$$Z_\mu = -B_\mu \sin \theta_W + W_\mu^3 \cos \theta_W \quad (1.9)$$

$$W_\mu^\pm = \frac{1}{\sqrt{2}} (W_\mu^1 \mp iW_\mu^2) \quad (1.10)$$

with  $\theta_W$  being the Weinberg or weak mixing angle.

The electromagnetic coupling constant can then be expressed as:

$$\alpha = g \sin \theta_W = g' \cos \theta_W \quad (1.11)$$

## 1.2.2 The Higgs Mechanism

To describe the mass of the fermions, the easiest solution would be to add a mass term expressed as  $m\bar{\psi}\psi$  for all of the fermions in  $\mathcal{L}_{SM}$ . Unfortunately, such term is not invariant as it can be rewritten using left-handed ( $\psi_L$ ) and right-handed projections ( $\psi_R$ ) and terms as  $m\bar{\psi}_R\psi_L$  and  $m\bar{\psi}_L\psi_R$  appear which are not invariant as the  $U(1)_Y \times SU(2)_L$  treats differently left and right-handed particles.

The mechanism to add masses in the Lagrangian of SM relies on the concept of spontaneous symmetry breaking which means that although the Lagrangian itself is invariant under a symmetry, the vacuum expectation does not. This is achieved by the Brout–Englert–Higgs mechanism developed in 1964 by three independent groups of researchers, Brout and Englert in Ref. [27], Higgs in Ref. [28, 29] and Hagen, Guralnik and Kibble in Ref. [30]. This mechanism allows to introduce masses for both gauge bosons and fermions through their couplings with a new particle, the Higgs boson. The couplings

of the fermions to the Higgs boson will be specifically discussed in Sec. 1.2.3 with the Yukawa Lagrangian and the CKM matrix.

The Higgs potential from Eq. 1.2 is defined as:

$$V(\Phi^\dagger\Phi) = \lambda(\Phi^\dagger\Phi)^2 - \mu^2\phi^\dagger\Phi + \frac{\mu^4}{4\lambda} \quad (1.12)$$

where  $\Phi$ , the Higgs doublet can be expressed as:

$$\Phi = \begin{pmatrix} \phi^+ \\ \phi^0 \end{pmatrix} \quad (1.13)$$

with  $\phi^+$  and  $\phi^0$  being two complex scalar fields.  $\mu$  is the Higgs mass parameter and  $\lambda$  describes the Higgs self coupling.

If  $\mu^2 > 0$ , the minimum of the potential is at  $\Phi^\dagger\Phi = 0$  where  $\mathcal{L}_{SM}$  is invariant under the  $U(1)_Y \times SU(2)_L$  symmetry but if  $\mu^2 < 0$ , the minimum of  $\Phi$  is at:

$$\Phi^\dagger\Phi = \frac{-\mu^2}{2\lambda} \quad (1.14)$$

which is a point where the SM Lagrangian is not invariant under the electroweak gauge symmetry. Due to quantum fluctuations, even if the Higgs field is at point where the electroweak symmetry is conserved, this is not stable and  $\Phi$  has an expectation value in the vacuum of:

$$\langle |\Phi| \rangle = \sqrt{\frac{-\mu^2}{2\lambda}} = \frac{\nu}{\sqrt{2}} \quad (1.15)$$

The parameter  $\nu$  is referred as the vacuum expectation value and its value is  $\nu \approx 246$  GeV [7] which defines the electroweak scale where the electroweak symmetry is broken.

As the expression of the ground state can change through gauge transformation, the expression of  $\Phi$  is set using the so-called *unitary gauge* and expressed as follows:

$$\Phi = \frac{1}{\sqrt{2}} \begin{pmatrix} 0 \\ \nu + H \end{pmatrix} \quad (1.16)$$

which defines  $H$ , the Higgs boson.

With the expression of  $\Phi$  defined in Eq. 1.16, one can then expand the kinetic term  $((D_\mu\Phi)^\dagger(D^\mu\Phi))$  present in the expression of the Higgs potential in Eq. 1.12 using the expression of the covariant derivative in Eq. 1.3 to create the mass terms for the gauge bosons. The masses are then expressed as follows:

$$m_A = 0 \quad (1.17)$$

$$m_Z = \frac{\nu}{2} \sqrt{g^2 + g'^2} \quad (1.18)$$

$$m_W = \frac{g\nu}{2} = m_Z \cos \theta_W \quad (1.19)$$

And the mass of the Higgs boson itself is defined as:

$$m_H = \sqrt{2\lambda\nu^2} \quad (1.20)$$

As  $\lambda$  is a free parameter of the SM, there is no prediction for the mass of the Higgs boson. After an intensive search at the LEP collider, the construction and operation of the LHC allowed for ATLAS [31] and CMS collaborations [32] to announce the 4<sup>th</sup> of July 2012 the detection of a new boson with a mass of 125 GeV/ $c^2$  to be compatible with the Higgs boson of the Standard Model. The quantum numbers of this particle have also been studied and the measurement presented in Ref. [33] with a spin of 0 and a positive parity are in agreement with the SP predictions for the Higgs boson.

In the next section, the Yukawa Lagrangian to describe the fermion masses is discussed in addition to the mixing of the quarks and the CKM matrix.

### 1.2.3 Quark mixing and CP violation

Charged lepton and quark masses are described by a Yukawa Lagrangian which reduces an interaction to the Higgs boson to a mass term. The masses of the fermions are then proportional to their couplings to the Higgs often referred as the Yukawa couplings.

The Yukawa interaction for a charged lepton can be written as:

$$\mathcal{L}_Y^\ell = -g_\ell(\bar{\ell}_L\Phi\ell_R + \bar{\ell}_R\Phi^\dagger\ell_L) \quad (1.21)$$

Taking the vacuum expectation value of the Higgs field, it then becomes:

$$\mathcal{L}_Y^\ell = -\frac{1}{\sqrt{2}}g_\ell(\bar{\ell}_L\ell_R + \bar{\ell}_R\ell_L) = -\frac{1}{\sqrt{2}}g_\ell\bar{\ell}\ell \quad (1.22)$$

which identifies with a mass term with

$$m_\ell = \frac{1}{\sqrt{2}}g_\ell\nu \quad (1.23)$$

For quarks, the situation is similar with the Yukawa Lagrangian being expressed as:

$$\mathcal{L}_Y = -(g_{ij}^u\bar{q}_{Li}\tilde{\Phi}u_{Rj} + g_{ij}^d\bar{q}_{Li}\Phi d_{Rj} + h.c.) \quad (1.24)$$

with  $g_{ij}^i$  the coupling constants of the Higgs fields ( $\Phi$ ,  $\tilde{\Phi} = i\tau^2\Phi^*$ ) to the quarks doublets defined as:

$$q_{Li} = \begin{pmatrix} u_{Li} \\ d_{Li} \end{pmatrix}, \quad u_{Ri} = \begin{pmatrix} u_{Ri} \\ 0 \end{pmatrix}, \quad d_{Ri} = \begin{pmatrix} 0 \\ d_{Ri} \end{pmatrix}. \quad (1.25)$$

The indices  $i j$  both indicate one of the three generations of quarks ( $(u, d)$ ,  $(c, s)$  and  $(t, b)$ ) and h.c. refers to the hermitian conjugate of the expression placed upstream.

The quark Yukawa Lagrangian can then be written using mass matrices in the unitary gauge as follows:

$$\mathcal{L}_Y = -\bar{u}_{Li}m_{ij}^u u_{Rj} - \bar{d}_{Li}m_{ij}^d d_{Rj} + h.c. \quad (1.26)$$

with  $m_{ij}^u$  and  $m_{ij}^d$  being respectively the up and down quarks mass matrices.

As the quark flavour is not conserved in weak interactions with a charged current, these mass matrices are not directly diagonal. As the weak states in Eq. 1.26 do not correspond to the mass states, the mass matrices need to be diagonalised, which correspond to a rotation of the quarks from the weak states to the mass ones.

By introducing four unitary matrices  $V_{L,R}^{u,d}$ , one can retrieve the diagonalised mass matrices  $m_\alpha$ :

$$m_\alpha^u = \begin{pmatrix} m_u & 0 & 0 \\ 0 & m_d & 0 \\ 0 & 0 & m_t \end{pmatrix} \quad (1.27)$$

$$m_\alpha^d = \begin{pmatrix} m_d & 0 & 0 \\ 0 & m_s & 0 \\ 0 & 0 & m_b \end{pmatrix} \quad (1.28)$$

It has to be noted that the mass range, and therefore the Yukawa couplings one, spreads on five orders of magnitude with no explanation within the SM. It is known as the *hierarchy problem*.

The charged current part of the weak Lagrangian becomes using the mass eigenstates:

$$\mathcal{L}_{CC} = \frac{ig'}{\sqrt{2}} \left\{ W_\mu^+ \bar{u}_{Li} [V_L^u V_L^{d\dagger}] \gamma^\mu d_{Lj} + W_\mu^- \bar{d}_{Li} [V_L^d V_L^{u\dagger}] \gamma^\mu u_{Lj} \right\} \quad (1.29)$$

which defines the Cabbibo-Kobayashi-Maskawa (CKM) matrix [34]:

$$V_{CKM} = V_L^u V_L^{d\dagger} \quad (1.30)$$

Through the CKM matrix, one can relate the weak eigenstates ( $d, s, b$ ) to the mass eigenstates ( $d', s', b'$ ) as follows:

$$\begin{pmatrix} d' \\ s' \\ b' \end{pmatrix} = V_{CKM} \begin{pmatrix} d \\ s \\ b \end{pmatrix} = \begin{pmatrix} V_{ud} & V_{us} & V_{ub} \\ V_{cd} & V_{cs} & V_{cb} \\ V_{td} & V_{ts} & V_{tb} \end{pmatrix} \begin{pmatrix} d \\ s \\ b \end{pmatrix} \quad (1.31)$$

The CKM matrix is often expressed using the Wolfenstein parametrisation [35] by an expansion in power of  $\lambda$  ( $\lambda = V_{us}$ ):

$$V_{CKM} = \begin{pmatrix} 1 - \lambda^2/2 & \lambda & A\lambda^3(\rho - i\eta) \\ -\lambda & 1 - \lambda^2/2 & A\lambda^2 \\ A\lambda^3(1 - \rho - i\eta) & -A\lambda^2 & 1 \end{pmatrix} + \mathcal{O}(\lambda^4) \quad (1.32)$$

One of the most important features of the CKM matrix is the existence of two complex elements as seen in Eq. 1.32 which account for the CP violation measured experimentally and discussed earlier in Sec. 1.1.3.

Through the CKM matrix, the Standard Model presents a particular flavour structure with non-zero off-diagonal terms and complex terms accounting for CP violation. There is no reason for a NP model to respect this structure which motivates precise measurements of the CKM matrix and consistency tests as any deviation could indicate a NP contribution.

### 1.2.4 Limits and unresolved issues

The Standard Model has been since its creation a very successful theory able to cope with the many experimental studies developed for instance at the LEP, the Tevatron or at the LHC. For instance, the various analysis testing the CP violation using  $B$  mesons decays show no clear deviation from the SM predictions [36].

Yet, several unexplained phenomena motivate the search of a more accurate model of the fundamental interactions. These open questions fall in two categories, observed phenomena not accounted for by the Standard Model or theoretical problems within the framework of the SM.

Among the observations not accounted by the SM are the existence of dark matter, detected through its gravitational effects as seen for instance in the dynamics of galaxies as discussed in Ref [37], or the presence of dark energy which can be measured using the Cosmological Microwave Background with the latests measurements performed by the Planck collaboration [38].

Within the Standard Model, several open questions still remain. For instance, a CP violating term can be added in the QCD dynamics but its phase is currently constrained by the measurements of the neutron electric dipole moment to be less than  $10^{-9}$  with no theoretical argument in the SM to constrain its value to zero, which might indicate a NP mechanism able to do so. The broad range of the Yukawa couplings, from  $\mathcal{O}(10^{-5})$  for the light quarks to 1 for the top quark, is also an open question which is also often referred as the *hierarchy problem*. Yukawa couplings are free parameters of the SM and no mechanism exists to set their relative strength.

The current cosmological model describe an early universe with an equal amount of matter and antimatter, yet the observable universe is now only composed of matter. To understand this matter-antimatter asymmetry, Sakharov identified in Ref. [39] three conditions for an interaction to produce matter and antimatter at different rates including the violation of the CP symmetry. Even though the SM includes CP violation through weak interactions, the CP violation phase of the CKM matrix is far lower than required to explain the asymmetry alone. Other sources of CP violation are required, for instance in the leptonic sector, to explain the matter-antimatter asymmetry.

Hence, several searches effects of New Physics models are ongoing. Both searches of direct observation of decays of new particles, also referred as *direct searches* and studies of NP

contributions within SM processes, through loops or additional Feynman diagrams, denoted as *indirect searches* are currently performed. In the next chapter, indirect searches related to Lepton Universality are discussed.



# An introduction to semitauonic decays

## Contents

---

<b>2.1 Lepton Flavour Universality . . . . .</b>	<b>38</b>
2.1.1 $b \rightarrow s\ell^+\ell^-$ transitions . . . . .	39
2.1.2 $b \rightarrow c\tau\nu_\tau$ transitions in the Standard Model . . . . .	41
<b>2.2 Current experimental status . . . . .</b>	<b>47</b>
<b>2.3 New Physics in semitauonic <math>b</math>-decays . . . . .</b>	<b>48</b>

---

The Standard Model has remained for years a robust model passing each experimental test. All direct searches of New Physics particles in  $pp$  collisions at the LHC have been unsuccessful for now.

Indirect searches of New Physics rely on precise measurements of SM processes with high sensitivity to NP contributions. The rare decay mode of  $B_s^0 \rightarrow \mu^+\mu^-$  is for instance one of the ‘golden modes’ of such searches with its very low and precise SM expectation and high enhancement if any charged Higgs exists. Its measurement, in Ref. [40], found to be compatible with SM expectation allowed to put stringent constraints on a wide range of NP models.

Semitauonic decays of  $b$ -hadrons are a topic with experimental measurements in tension with the predictions of the Standard Model. Could this disagreement with the SM be the first cracks of the model?

This chapter proposes a short introduction on the subject of Lepton Flavour Universality (LFU) tests on both theoretical and experimental aspects. A detailed review of the current picture of the semitauonic measurements is also provided. Finally, a short discussion on New Physics using a model-independent approach, some NP models and direct searches of such particles ends this chapter.

## 2.1 Lepton Flavour Universality

The two electroweak gauge bosons of the Standard Model,  $Z$  and  $W$ , have equal couplings to the three leptons flavours, which is often referred as Lepton Flavour Universality (LFU). This also means that the three leptons,  $e$ ,  $\mu$  and  $\tau$  are equivalent in every process up to phase space and helicity effects.

Lepton Flavour Universality was precisely tested during the LEP era with for instance the ratio of partial decay rates of the  $Z$  boson going to  $\mu^+\mu^-$  and  $e^+e^-$  measured [41] to be:

$$\frac{\Gamma(Z \rightarrow \mu^+\mu^-)}{\Gamma(Z \rightarrow e^+e^-)} = 1.0009 \pm 0.0028$$

But measurements at tree level in  $b \rightarrow c\tau\nu_\tau$  transitions and at loop level in  $b \rightarrow sl^+\ell^-$  decays have shown potential disagreement with SM expectations.

Such processes are described by an effective Hamiltonian where contributions from electromagnetic, strong and weak interactions can be factorised depending on their respective energy scale. The low energy part of the process is way below the mass of the  $b$  and related to soft gluons described by matrix elements related, this is the hadronic part. On another side, the short-distance contributions, with a typical energy range of the order of the mass of the electroweak bosons, are related to the leptonic part.

Lepton Flavour Universality, or its potential breaking, only concerns the leptonic part but the uncertainties coming from the description of the hadronic matrix elements could hide these processes if they are not well under control.

To properly describe the hadronic currents [2], several theoretical tools can be used such as Heavy Quark Effective Theory (HQET) and Lattice QCD. HQET [42] is an approximation of QCD at an intermediate energy scale, in the same manner as the Fermi theory is able to describe weak decays at low energy. Hard gluons are not considered and integrated which leads to an effective Hamiltonian with a new feature: the spin-flavour symmetry. Several setup can be used to compute the form factors, two different parametrisations will be discussed in the following.

Lattice QCD is a non-perturbative approach discretising space and time on a grid. One can retrieve the physical quantities when the lattice-spacing is extrapolated to zero. Lattice QCD computations are very important as they do not rely on experimental inputs and can provide non-perturbative computations of observables.

To further minimise the impact of the description of the hadrons in the result, analyses tend to rely on ratios of decays rates of two different leptons which allows to only consider a residual uncertainty as the hadronic form factors uncertainty is shared in both cases and suppressed in the ratio.

With SM uncertainties kept as low as possible, any New Physics contributions with specific couplings depending on the leptonic flavour, such as couplings depending on the mass of the lepton, could change the value of such ratios and being the first step to a theory beyond the Standard Model.

2.1.1  $b \rightarrow sl^+\ell^-$  transitions

Decays of the type  $b \rightarrow sl^+\ell^-$  are flavour-changing neutral currents (FCNC) transitions that can only occur through loop diagrams in the SM. As the CKM matrix is close to be diagonal, FCNC processes are rare processes in the SM whereas any NP model without such flavour suppression could have noticeable effects.

Such decays are good candidates for looking for New Physics effects as hadronic effects are well controlled and further reduced by measuring ratios and NP contributions can occur both within loops or new tree diagrams.

Some of the SM leading order diagrams are shown in Fig. 2.1 and examples of potential NP contributions are shown in Fig. 2.2.

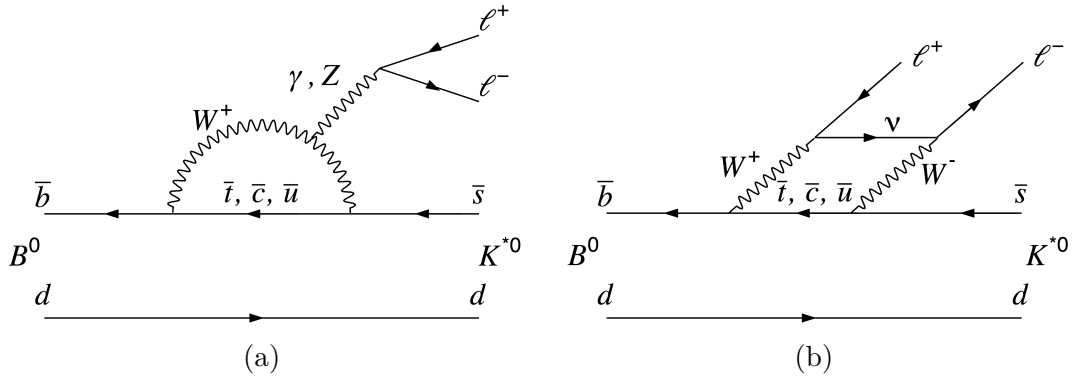


Figure 2.1 – Standard Model penguin (a) and box (b) diagrams for the  $B^0 \rightarrow K^{*0}l^+\ell^-$  decay.

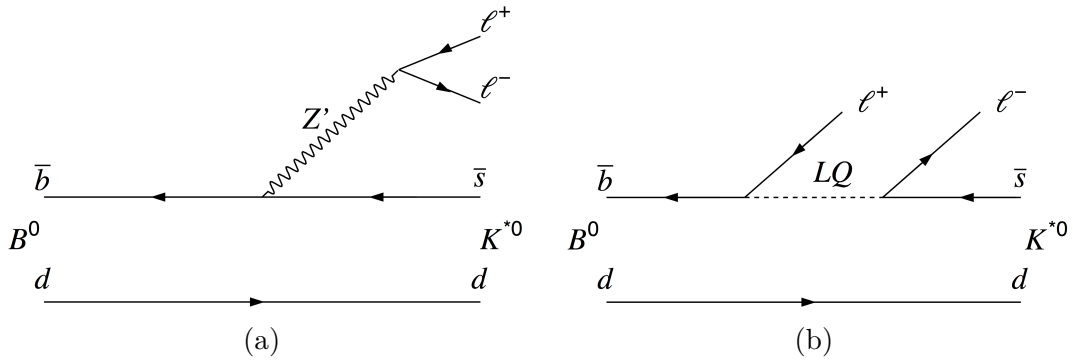


Figure 2.2 – Potential New Physics diagrams, with an additional  $Z'$  boson (a) and a Leptoquark (b) for the  $B^0 \rightarrow K^{*0}l^+\ell^-$  decay.

The two ratios  $R_K$  and  $R_{K^{*0}}$  are particularly interesting to study  $b \rightarrow sl^+\ell^-$ , they are defined as follows:

$$R_K = \frac{\int_{q_{\min}^2}^{q_{\max}^2} \frac{d\mathcal{B}(B^+ \rightarrow K^+ \mu^+ \mu^-)}{dq^2} dq^2}{\int_{q_{\min}^2}^{q_{\max}^2} \frac{d\mathcal{B}(B^+ \rightarrow K^+ e^+ e^-)}{dq^2} dq^2} \quad (2.1)$$

$$R_{K^{*0}} = \frac{\int_{q_{\min}^2}^{q_{\max}^2} \frac{d\mathcal{B}(B^0 \rightarrow K^{*0} \mu^+ \mu^-)}{dq^2} dq^2}{\int_{q_{\min}^2}^{q_{\max}^2} \frac{d\mathcal{B}(B^0 \rightarrow K^{*0} e^+ e^-)}{dq^2} dq^2} \quad (2.2)$$

Due to the large cancellations of hadronic uncertainties in the ratios, the SM expectations of such ratios are very precise with for instance  $R_K$  being equal to 1 at the  $10^{-4}$  level [43], making them excellent probes to potential NP effects.

The value measured of  $R_K$  by LHCb using Run1 data in the  $[1, 6] \text{ GeV}^2/c^4$   $q^2$  region is  $R_K = 0.745_{-0.074}^{+0.090}(\text{stat}) \pm 0.036(\text{syst})$  [44] and is consistent with the SM at the level of 2.6 standard deviations. The comparison between SM and measurements of  $R_K$  performed by BaBar, Belle and LHCb is shown in Fig. 2.3, with the LHCb measurement being the most precise of all three.

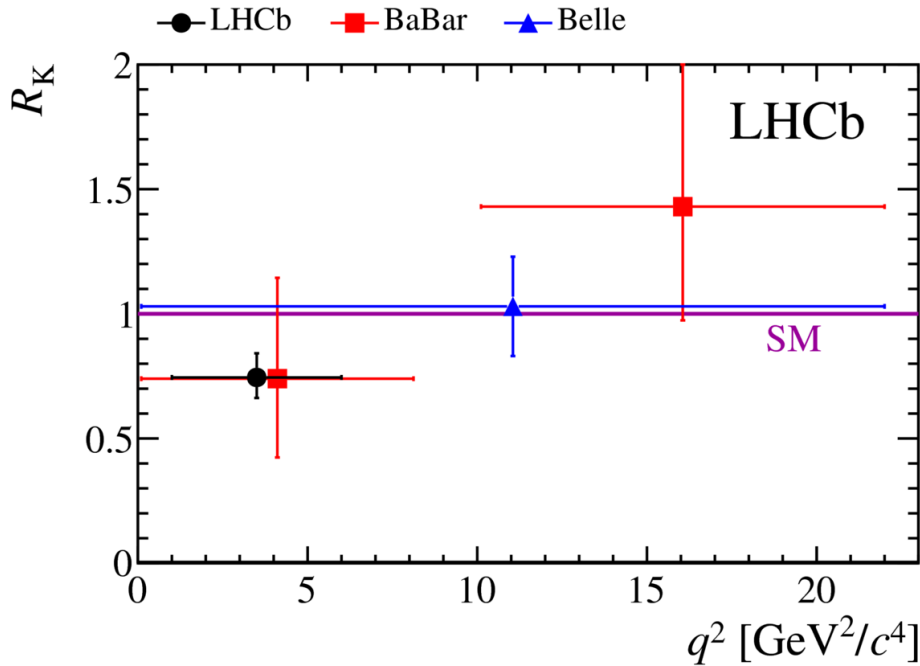


Figure 2.3 – Measurement of  $R_K$  performed by BaBar [45], Belle [46] and LHCb [44] compared to the SM expectation. Picture taken from Ref. [44].

$R_{K^{*0}}$  was also measured using Run1 data in two bins of  $q^2$ :  $0.045 < q^2 < 1.1 \text{ GeV}^2/c^4$  and  $1.1 < q^2 < 6.0 \text{ GeV}^2/c^4$  with the results shown in Ref. [47] being:

$$R_{K^{*0}} = 0.66_{-0.07}^{+0.11}(\text{stat}) \pm 0.03(\text{syst}) \text{ for } 0.045 < q^2 < 1.1 \text{ GeV}^2/c^4$$

$$R_{K^{*0}} = 0.69_{-0.07}^{+0.11}(\text{stat}) \pm 0.05(\text{syst}) \text{ for } 1.1 < q^2 < 6.0 \text{ GeV}^2/c^4$$

<sup>1</sup>In this context  $q^2$  is the squared momentum transferred to the dilepton system, which is also  $m_{\ell^+\ell^-}^2$ .

The deviation from the SM expectation is respectively at the level of  $2.1 - 2.3\sigma$  and  $2.4 - 2.5\sigma$  for the first and second bins. The LHCb measurement and the different available SM predictions and the comparison with the measurements performed at the B factories are respectively shown in Fig. 2.4a and in Fig. 2.4b.

There is an ongoing effort to study more  $b \rightarrow s\ell^+\ell^-$  decays to better understand this disagreement with SM expectations and better discriminate between potential NP models.

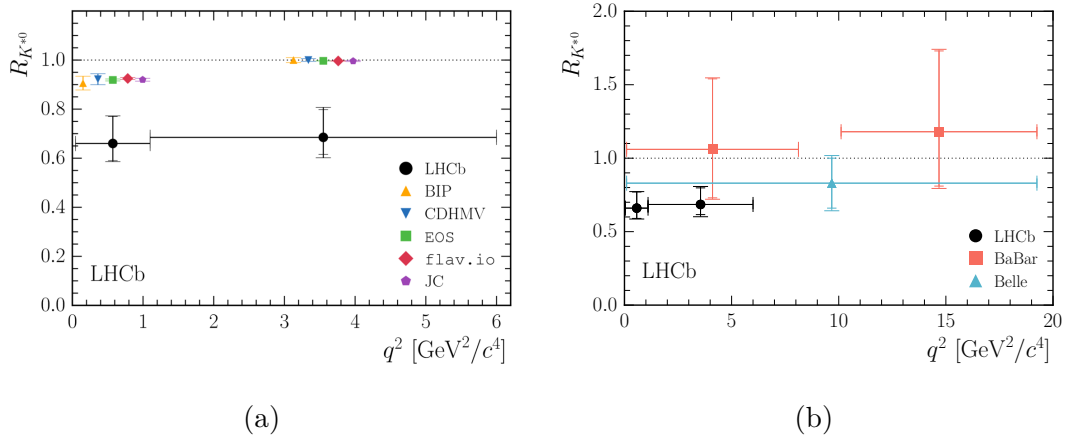


Figure 2.4 –  $R_{K^{*0}}$  measurement for the LHCb Run1 data in bins of  $q^2$  with the different available SM predictions (a) and compared to the measurements of BaBar [45] and Belle [46] in (b). Pictures taken from Ref. [47].

### 2.1.2 $b \rightarrow c\tau\nu_\tau$ transitions in the Standard Model

In the Standard Model,  $b \rightarrow c\ell\nu$  processes occur through tree-level diagrams, as seen in Fig. 2.5, and only differ through the mass of the lepton ( $\ell = e, \mu, \tau$ ). All NP models adding couplings to the leptons proportional to their mass would preferentially couple to the  $\tau$ . Hence, precise predictions of semitauonic processes within the SM are crucial to probe NP contributions.

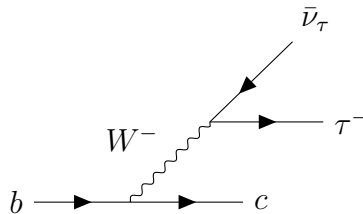


Figure 2.5 – A tree-level diagram of the  $b \rightarrow c\tau\bar{\nu}_\tau$  transition.

In order to reduce the uncertainty introduced by hadronic effects, similarly to  $b \rightarrow s\ell^+\ell^-$  transitions, ratios of branching fractions are introduced as follows:

$$\mathcal{R}(H_b) = \frac{\mathcal{B}(H_b \rightarrow H_c\tau\nu_\tau)}{\mathcal{B}(H_b \rightarrow H_c\mu\nu_\mu)} \quad (2.3)$$

The computation of such ratio is performed within the Heavy Quark Effective Theory (HQET) framework [42] developed in the 90's to describe transitions of heavy quarks ( $b$  or  $c$ ) to light ones. One great success of this framework was the computation of the  $\Lambda_b^0$  lifetime as seen in Ref. [48].

Heavy and light quarks refer to the comparison of the mass of the quarks with the energy scale of confinement in QCD,  $\Lambda_{QCD} \sim 0.2 \text{ GeV}$ . As the quarks masses are arranged as follows:

$$m_u, m_d, m_s < \Lambda_{QCD} \ll m_c, m_b, m_t$$

the first ones are light quarks and the latter are heavy ones. The top quark is not taken into account in the following as it does not hadronise.

In HQET, the mass of the heavy quark,  $m_Q$ , is considered as infinite. In that limit, a heavy hadron composed of a heavy quark and its complex cloud of light quarks and gluons can be approximated to a heavy quark at rest surrounding by light constituents, light quarks and soft gluons, only affected by the colour charge of the heavy quark.

This means that changing the heavy quark by another with only different flavour or spin does not affect the dynamics of the system as long as the colour charge and the velocity  $v$  stay the same, which is known as the spin-flavour symmetry.

With such a symmetry,  $B \rightarrow D^{(*)}$  Form Factors are only described by the Isgur-Wise function as follows:

$$\langle D(v') | \bar{c}_{v'} \gamma^\mu b_v | \bar{B}(v) \rangle \propto \xi(v \cdot v') (v + v')^\mu \quad (2.4)$$

where  $\xi$  is the Isgur-Wise function and  $v \cdot v'$ , also referred as  $w$ , is the recoil variable.  $\xi$  only depends on  $B$  and  $D$  velocities, hence no dependence on the masses.

The construction of the HQET effective Lagrangian is discussed in detail in Ref. [42], it can be shortly summarized as an expansion of the QCD Lagrangian in powers of  $1/m_Q$ .

Following Ref. [49], the effective Hamiltonian considered for  $b \rightarrow c \tau \nu_\tau$  to compute both  $\mathcal{R}(D^*)$  and  $\mathcal{R}(\Lambda_c)$  within the SM can be written as:

$$\mathcal{H}_{eff} = \frac{4G_F V_{cb}}{\sqrt{2}} (\bar{c} \gamma_\mu P_L b) (\bar{\tau} P_L \nu_\tau) + h.c. \quad (2.5)$$

where  $G_F$  is the Fermi constant measured to be  $G_F = 1.1662787 \times 10^{-5} \text{ GeV}^{-2}$ ,  $V_{cb}$  is the CKM matrix element and  $P_L$  and  $P_R$  are helicity operators defined as:

$$P_L = \frac{1 - \gamma^5}{2}$$

$$P_R = \frac{1 + \gamma^5}{2}$$

Both  $\mathcal{R}(D^*)$  and  $\mathcal{R}(\Lambda_c)$  computations using this effective Hamiltonian are presented in the following sections.

2.1.2.1  $\mathcal{R}(D)$  and  $\mathcal{R}(D^*)$  in the Standard Model

$\mathcal{R}(D^*)$  is defined as:

$$\mathcal{R}(D^*) = \frac{\mathcal{B}(B^0 \rightarrow D^{*-} \tau^+ \nu_\tau)}{\mathcal{B}(B^0 \rightarrow D^{*-} \mu^+ \nu_\mu)} \quad (2.6)$$

The detailed computation can be found in Ref. [49], its main steps are reported in the following of this section. Using the effective Hamiltonian given in Eq. 2.5, the differential decay rate of  $B^0 \rightarrow D^{*-} \ell^+ \nu$  can be written as:

$$\begin{aligned} \frac{d^2\Gamma_\ell}{dq^2 d\cos\theta} = & \frac{G_F^2 |V_{cb}|^2 |\mathbf{p}| q^2}{256\pi^3 m_B^2} \left(1 - \frac{m_\ell^2}{q^2}\right)^2 \times \\ & \left[ (1 - \cos\theta)^2 |H_{++}|^2 + (1 + \cos\theta)^2 |H_{--}|^2 + 2\sin^2\theta |H_{00}|^2 + \right. \\ & \left. \frac{m_\ell^2}{q^2} \left( (\sin^2\theta (|H_{++}|^2 + |H_{--}|^2) + 2|H_{0t} - H_{00}\cos\theta|^2) \right) \right] \end{aligned} \quad (2.7)$$

where  $q^2$  is the transferred momentum to the  $\ell - \nu$  system,  $q^2 = (p_B - p_{D^*})^2$  and  $\theta$  is the angle between the  $D^*$  and the lepton in the  $\ell - \nu$  rest frame.  $H_{xx'}$  are the helicity amplitudes defined as:

$$\begin{aligned} H_{\pm\pm}^{\text{SM}}(q^2) &= (m_B + m_{D^*}) A_1(q^2) \mp \frac{2m_B}{m_B + m_{D^*}} |\mathbf{p}| V(q^2), \\ H_{00}^{\text{SM}}(q^2) &= \frac{1}{2m_{D^*} \sqrt{q^2}} \left[ (m_B^2 - m_{D^*}^2 - q^2)(m_B + m_{D^*}) A_1(q^2) - \frac{4m_B^2 |\mathbf{p}|^2}{m_B + m_{D^*}} A_2(q^2) \right], \\ H_{0t}^{\text{SM}}(q^2) &= \frac{2m_B |\mathbf{p}|}{\sqrt{q^2}} A_0(q^2). \end{aligned} \quad (2.8)$$

Three axial ( $A_0(q^2)$ ,  $A_1(q^2)$ ,  $A_2(q^2)$ ) and one vector ( $V(q^2)$ ) hadronic form factors intervene in the helicity amplitudes. They can be expressed using the following hadronic matrix elements as:

$$\langle D^*(p_{D^*}, \epsilon_\alpha) | \bar{c} \gamma_\mu b | B(p_B) \rangle = \frac{2iV(q^2)}{m_B + m_{D^*}} \epsilon_{\mu\nu\alpha\beta} \epsilon^{*\nu} p_B^\alpha p_{D^*}^\beta, \quad (2.9a)$$

$$\begin{aligned} \langle D^*(p_{D^*}, \epsilon_\alpha) | \bar{c} \gamma_\mu \gamma_5 b | B(p_B) \rangle &= 2m_{D^*} A_0(q^2) \frac{\epsilon^* \cdot q}{q^2} q_\mu + (m_B + m_{D^*}) A_1(q^2) \left( \epsilon_\mu^* - \frac{\epsilon^* \cdot q}{q^2} q_\mu \right) \\ &\quad - A_2(q^2) \frac{\epsilon^* \cdot q}{m_B + m_{D^*}} \left( (p_B + p_{D^*})_\mu - \frac{m_B^2 - m_{D^*}^2}{q^2} q_\mu \right) \end{aligned} \quad (2.9b)$$

Integrating Eq. 2.7 over  $\theta^2$ , gives the decay rate for  $B^0 \rightarrow D^{*-}\ell^+\nu$  as follows:

$$\frac{d\Gamma_\ell}{dq^2} = \frac{G_F^2 |V_{cb}|^2 |\mathbf{P}| q^2}{96\pi^3 m_B^2} \left(1 - \frac{m_\ell^2}{q^2}\right)^2 \left[ (|H_{++}|^2 + |H_{--}|^2 + |H_{00}|^2) \left(1 + \frac{m_\ell^2}{2q^2}\right) + \frac{3}{2} \frac{m_\ell^2}{q^2} |H_{0t}|^2 \right] \quad (2.10)$$

To make a prediction on the value of  $\mathcal{R}(D^*)$ , form factors need to be computed within the HQET framework.

The recoil variable  $w$  can be expressed in this context as:

$$w = v_B \cdot v_{D^*} = \frac{m_B^2 + m_{D^*}^2 - q^2}{2m_B m_{D^*}} \quad (2.11)$$

The  $B \rightarrow D^*$  transition can be expressed by a universal form factor:

$$h_{A_1}(w) = A_1(q^2) \frac{1}{M} \frac{2}{w+1} \quad (2.12)$$

where  $M$  is defined as

$$M = \frac{2\sqrt{m_B m_{D^*}}}{(m_B + m_{D^*})}$$

And the  $R_1$ ,  $R_2$  and  $R_0$  ratios as follows:

$$\begin{aligned} A_0(q^2) &= \frac{R_0(w)}{M} h_{A_1}(w), \\ A_2(q^2) &= \frac{R_2(w)}{M} h_{A_1}(w), \\ V(q^2) &= \frac{R_1(w)}{M} h_{A_1}(w), \end{aligned} \quad (2.13)$$

In the heavy quark limit, the variation of these factors as a function of  $w$  is driven by:

$$\begin{aligned} h_{A_1}(w) &= h_{A_1}(1)[1 - 8\rho^2 z + (53\rho^2 - 15)z^2 - (231\rho^2 - 91)z^3], \\ R_1(w) &= R_1(1) - 0.12(w-1) + 0.05(w-1)^2, \\ R_2(w) &= R_2(1) + 0.11(w-1) - 0.06(w-1)^2, \\ R_0(w) &= R_0(1) - 0.11(w-1) + 0.01(w-1)^2, \end{aligned} \quad (2.14)$$

where

$$z = \frac{\sqrt{w+1} - \sqrt{2}}{\sqrt{w+1} + \sqrt{2}}$$

The first three relations come from Ref. [50] and the latter is coming from Ref. [49]. These relations described above are known as the CLN parametrisation.

---

<sup>2</sup>Experimentally, it can be very hard to define  $\theta$  as it is defined in the  $\ell - \nu$  rest-frame, with the neutrino being undetected in LHCb.

The values of each of these factors at zero recoil,  $w = 1$ , are free parameters as  $\rho^2$ . As  $h_{A_1}(1)$  is present in each hadronic current,  $\mathcal{R}(D^*)$  does not depend on it. Three other parameters were measured using  $B^0 \rightarrow D^* \ell \nu$  decays in Ref. [51]:

$$\rho^2 = 1.401 \pm 0.033 \quad (2.15)$$

$$R_1(1) = 1.401 \pm 0.033 \quad (2.16)$$

$$R_2(1) = 0.854 \pm 0.020 \quad (2.17)$$

$R_0(1)$  was not measured as these decays are not sensitive to this parameter as it only enters in the helicity suppressed amplitude  $H_{0t}$ . It is evaluated with leading order corrections to be  $R_0(1) = 1.14$  and a 10% uncertainty is assigned to take into account higher order corrections.

The ratio of decay rate for both  $\tau$  and  $\ell$ ,  $\ell$  being either  $e$  or  $\mu$ , is given using Eq. 2.10 as a function of  $q^2$  as follows:

$$R_{D^*}(q^2) = \frac{d\Gamma_\tau/dq^2}{d\Gamma_\ell/dq^2} = \left(1 - \frac{m_\tau^2}{q^2}\right)^2 \left[ \left(1 + \frac{m_\tau^2}{2q^2}\right) + \frac{3m_\tau^2}{2q^2} \frac{|H_{0t}(q^2)|^2}{|H_{++}(q^2)|^2 + |H_{-}(q^2)|^2 + |H_{00}(q^2)|^2} \right] \quad (2.18)$$

By integrating over  $q^2$  and using the form factors discussed above, the SM expectation for  $\mathcal{R}(D^*)$  is found to be

$$\mathcal{R}_{SM}(D^*) = 0.252(3)$$

Recently, the Belle collaboration released a new analysis of the  $B^0 \rightarrow D^* \ell \nu$  decay mode with the unfolded  $q^2$  spectrum [52]. This new information was used in new calculations of both  $\mathcal{R}(D)$  and  $\mathcal{R}(D^*)$ . In addition, not only the CLN parametrisation of the form factors is used but also the BGL one, described in Ref. [53]. The BGL parametrisation relies on the Taylor expansion of the form factors around  $z = 0$ , such as a generic form factor  $F$  can be written as:

$$F(z) = \frac{1}{P(z)\phi(z)} \sum_{n=0}^N a_n z^n \quad (2.19)$$

where  $P(z)$  is called the Blaschke factor and depends on the number of  $B_c$  states above the  $BD$  pair production threshold and  $\phi$  phase space factors.  $N$  is the maximal power considered in the expansion, usually 2 as  $z^3 \sim 10^{-4}$ .

Using these new inputs, several computations of  $\mathcal{R}(D^*)$  were performed, in good agreement with Ref. [49], with different treatment of the errors. Additional data and Lattice QCD calculations, especially Lattice QCD  $B \rightarrow D^*$  form factors at non zero recoil, are needed to solve this disagreement. For the moment, the average of all the available new predictions of  $\mathcal{R}(D^*)$  is considered for the comparison with the experimental measurements performed by HFLAV [1]. The available predictions are presented in Tab. 2.1, with the average being:

$$\mathcal{R}(D^*) = 0.258 \pm 0.005$$

Table 2.1 – Available  $\mathcal{R}(D^*)$  predictions using the new  $B \rightarrow D^* \ell \nu$  dataset released by the Belle Collaboration [52].

Reference	$\mathcal{R}(D^*)$
F.Bernlochner, Z.Ligeti, M.Papucci, D.Robinson [54]	$0.257 \pm 0.003$
D.Bigi, P.Gambino, S.Schacht [55]	$0.260 \pm 0.008$
S.Jaiswal, S.Nandi, S.K.Patra [56]	$0.257 \pm 0.005$
Average	$0.258 \pm 0.005$

$\mathcal{R}(D)$  is computed with a very similar logic and using the form factors measurements from BaBar [57] and Belle [58] and Lattice calculations inputs ([59] and [60]), the value of  $\mathcal{R}(D)$  is expected to be in Ref. [61]:

$$\mathcal{R}(D) = 0.299 \pm 0.003$$

### 2.1.2.2 $\mathcal{R}(\Lambda_c)$ in the SM

In the same manner as  $\mathcal{R}(D)$  and  $\mathcal{R}(D^*)$ ,  $\mathcal{R}(\Lambda_c)$  is defined as:

$$\mathcal{R}(\Lambda_c) = \frac{\mathcal{B}(\Lambda_b^0 \rightarrow \Lambda_c^+ \tau^- \bar{\nu}_\tau)}{\mathcal{B}(\Lambda_b^0 \rightarrow \Lambda_c^+ \mu^- \bar{\nu}_\mu)} \quad (2.20)$$

The computation of the form factors of  $\Lambda_b^0 \rightarrow \Lambda_c^+$  processes using Lattice QCD and the SM expectation of  $\mathcal{R}(\Lambda_c)$  are performed in Ref. [2].

To do so, the decay rate of  $\Lambda_b^0 \rightarrow \Lambda_c^+ \ell^- \nu$  is expressed using the same effective Hamiltonian as for  $\mathcal{R}(D^*)$ <sup>3</sup>:

$$\begin{aligned} \frac{d\Gamma}{dq^2} &= \frac{G_F^2 |V_{cb}|^2 \sqrt{s_+ s_-}}{768 \pi^3 m_{\Lambda_b}^3} \left(1 - \frac{m_\ell^2}{q^2}\right)^2 \\ &\times \left\{ 4 (m_\ell^2 + 2q^2) (s_+ g_\perp^2 + s_- f_\perp^2) \right. \\ &\quad + 2 \frac{m_\ell^2 + 2q^2}{q^2} \left( s_+ [(m_{\Lambda_b} - m_{\Lambda_c^+}) g_+]^2 + s_- [(m_{\Lambda_b} + m_{\Lambda_c^+}) f_+]^2 \right) \\ &\quad \left. + \frac{6m_\ell^2}{q^2} \left( s_+ [(m_{\Lambda_b} - m_{\Lambda_c^+}) f_0]^2 + s_- [(m_{\Lambda_b} + m_{\Lambda_c^+}) g_0]^2 \right) \right\}, \quad (2.21) \end{aligned}$$

where  $s_\pm = (m_{\Lambda_b^0} \pm m_{\Lambda_c^+})^2 - q^2$  and  $f_0, f_\perp, f_+, g_0, g_\perp$  and  $g_+$  are the six form factors describing  $\Lambda_b^0 \rightarrow \Lambda_c^+$  transitions evaluated on the Lattice.

With such framework, the value of  $\mathcal{R}(\Lambda_c)$  is expected to be:

$$\mathcal{R}(\Lambda_c) = 0.3328 \pm 0.0074 \pm 0.0070$$

where the first uncertainty is statistical and the latter is systematic.

<sup>3</sup>This calculation is adapted from Ref. [2] using only the SM components.

## 2.2 Current experimental status

Measurements of  $\mathcal{R}(D)$  and  $\mathcal{R}(D^*)$  rely either on the reconstruction of the  $\tau$  using its muonic decay,  $\tau \rightarrow \mu\nu_\mu\nu_\tau$ , or using a hadronic decay such as  $\tau^- \rightarrow \pi^-\pi^+\pi^-(\pi^0)\nu_\tau$ <sup>4</sup> or  $\tau^- \rightarrow \pi^-/\rho^-\nu_\tau$ .

Using the muonic channel allows for a straightforward normalisation as the final state ( $D^{(*)}\mu$ ) is the same for both  $B^0 \rightarrow D^{(*)}\tau\nu_\tau$  and  $B^0 \rightarrow D^{(*)}\mu\nu_\mu$ . This channel allows for a high statistics sample but it can be quite hard to differentiate a muon coming from a tau decay from another muon directly coming from a  $D$  meson decaying semileptonically.

Using a hadronic decay, especially with three pions, allows to reconstruct the  $\tau$  vertex and access the internal dynamics of the three pions, this will be discussed in Sec. 5.9.

Both B-factories, BaBar and Belle, and LHCb measured  $\mathcal{R}(D)$  and  $\mathcal{R}(D^*)$ . BaBar and Belle both use tagging techniques to fully reconstruct the signal candidate. Both  $e^+e^-$  colliders, PEP-II and KEKB for respectively BaBar and Belle, are operating at an energy in the centre-of-mass frame of 10.58 GeV corresponding to the  $\Upsilon(4S)$  resonance. This resonance almost only decays in a pair of two  $B$  mesons, either  $B^0\bar{B}^0$  or  $B^-B^+$ , meaning that the  $B$  production consists in  $e^+e^- \rightarrow \Upsilon(4S) \rightarrow B\bar{B}$ .

The presence of only two  $B$  mesons allow to fully reconstruct one of them, known as the tagged  $B$  and labelled as  $B_{tag}$ , which gives access to the full kinematics of the other  $B$  meson of the event, the signal candidate ( $B_{sig}$ ). In published measurements of  $\mathcal{R}(D)$  and  $\mathcal{R}(D^*)$ , BaBar used the reconstruction of the  $B_{tag}$  using several hadronic modes, known as the *hadronic tag*, and Belle used in addition the semileptonic  $B \rightarrow D^*\ell\nu$  decay to select signal candidates, which is referred as the *semileptonic tag*.

The BaBar collaboration published first the combined measurement of  $\mathcal{R}(D)$  and  $\mathcal{R}(D^*)$  using the hadronic tag [62], [63]. Belle also published a combined measurement of  $\mathcal{R}(D)$  and  $\mathcal{R}(D^*)$  using the hadronic technique in Ref. [64] and also measured  $\mathcal{R}(D^*)$  and the  $\tau$  polarisation reconstructing the  $\tau$  in both  $\tau \rightarrow \pi\nu$  and  $\tau \rightarrow \rho\nu$  using the semileptonic tag [65], [66].

The LHCb experiment also published the  $\mathcal{R}(D^*)$  measurement reconstructing the  $\tau$  in  $\tau^- \rightarrow \mu^-\bar{\nu}_\mu\nu_\tau$  in Ref. [67] and using the three-prong hadronic decay channels  $\tau \rightarrow 3\pi(\pi^0)\nu_\tau$  in Ref. [3] and in Ref. [8].

To experimentally extract  $\mathcal{R}(D^*)$ , using the muonic decay of the  $\tau$ , a fit on the three most discriminating variables to distinguish muons coming from a  $\tau$  decay from muons coming from semileptonic decays of  $D^{(**,*)}$  is used with templates extracted from simulation samples to model the different background sources. The three variables are:

- $E_\mu^*$ : the energy of the muon in the  $B$  centre-of-mass frame
- $m_{miss}^2$ : the missing mass squared defined as  $(p_B^\mu - p_D^\mu - p_\mu^\mu)^2$
- $q^2$ : the squared four momentum transferred to the  $\tau - \nu_\tau$  system,  $(p_B^\mu - p_D^\mu)^2$

<sup>4</sup>In the following, the three charged pions coming from a tau will be labelled as  $3\pi$ .

The results of the fit to the LHCb Run1 dataset are shown in Fig. 2.6 as a function of  $m_{miss}^2$  and  $E_\mu^*$  in bins of  $q^2$ .

The analysis of the measurement of  $\mathcal{R}(D^*)$  using the hadronic decay of the  $\tau$  will be discussed in more details in Chap. 4.

The different measurements, their combination and the average of the current available SM predictions is shown in Fig. 2.7. The average value of  $\mathcal{R}(D)$  is estimated to be

$$\mathcal{R}(D) = 0.407 \pm 0.039 \pm 0.024$$

and the one for  $\mathcal{R}(D^*)$  is

$$\mathcal{R}(D^*) = 0.306 \pm 0.013 \pm 0.007$$

Both  $\mathcal{R}(D)$  and  $\mathcal{R}(D^*)$  are above the SM expectation at the level of respectively 2.3 and  $3.0\sigma$ . Combined, the discrepancy is at the level of  $3.78\sigma$  using the average of the available SM predictions or  $3.62\sigma$  if only comparing at the SM prediction with the higher uncertainty [55].

In addition to semitauonic measurements of  $B^0$  or  $B^+$  decays involving either  $D$  or  $D^*$ , LHCb has also access to a wide range of hadronisation. The measurement of  $\mathcal{R}(J/\psi)$  defined as:

$$\mathcal{R}(J/\psi) = \frac{\mathcal{B}(B_c^+ \rightarrow J/\psi \tau^+ \nu_\tau)}{\mathcal{B}(B_c^+ \rightarrow J/\psi \mu^+ \nu_\mu)} \quad (2.22)$$

was also performed for the first time and published in Ref. [68]. The value of  $\mathcal{R}(J/\psi)$  is measured to be

$$\mathcal{R}(J/\psi) = 0.71 \pm 0.17 \pm 0.18$$

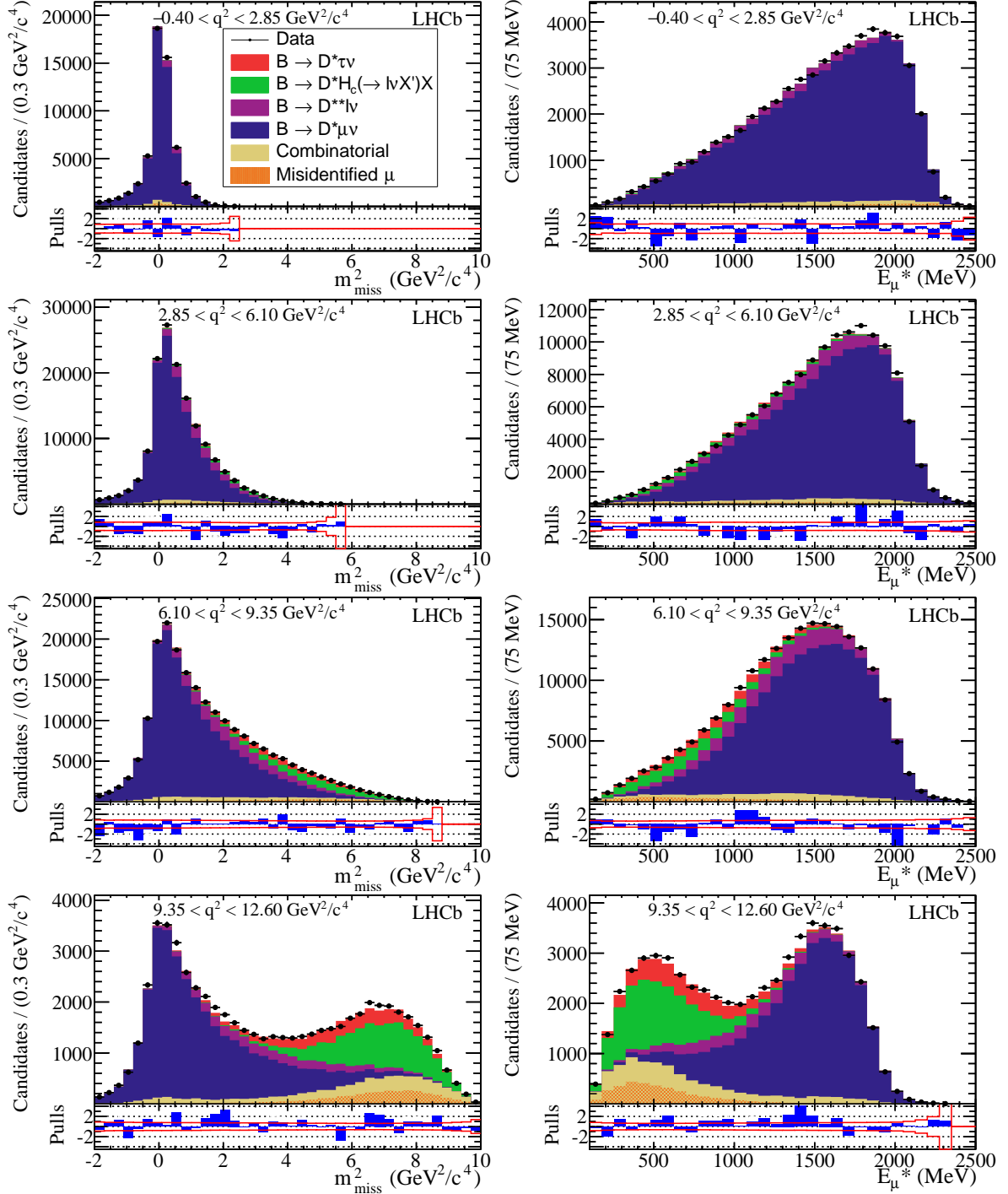
where the first uncertainty is statistical and the second is systematic. Its value is  $2\sigma$  above the SM prediction, expected to be in the range [0.25, 0.28].

In addition to  $\mathcal{R}(J/\psi)$  and  $\mathcal{R}(\Lambda_c)$ , presented in Chap. 5, other semileptonic modes are investigated such decays of the  $\Lambda_b^0$  baryon in excited  $\Lambda_c^+$  states or  $B_s^0$  decays into  $D_s^+$  and its excited states.

## 2.3 New Physics in semitauonic $b$ -decays

To study NP effects in semitauonic decays in a model-independent way, the SM effective Hamiltonian can be expanded with new operators as follows:

$$\begin{aligned} \mathcal{H}_{eff} = & \frac{4G_F V_{cb}}{\sqrt{2}} \left\{ \left[ \bar{c} \gamma_\mu P_L b + g_L \bar{c} \gamma_\mu P_L b + g_R \bar{c} \gamma_\mu P_R b \right] \bar{\tau} \gamma^\mu P_L \nu_\tau \right. \\ & \left. + 2 \left[ g_S \bar{c} b + g_P \bar{c} \gamma_5 b \right] \bar{\tau} P_L \nu_\tau + \left[ g_T \bar{c} \sigma^{\mu\nu} P_L b \right] \bar{\tau} \sigma_{\mu\nu} P_L \nu_\tau + h.c. \right\}, \end{aligned} \quad (2.23)$$


 Figure 2.6 – Fit results as a function of  $m_{miss}^2$  and  $E_{\mu}^*$  in bins of  $q^2$ . Figure taken from Ref. [67].

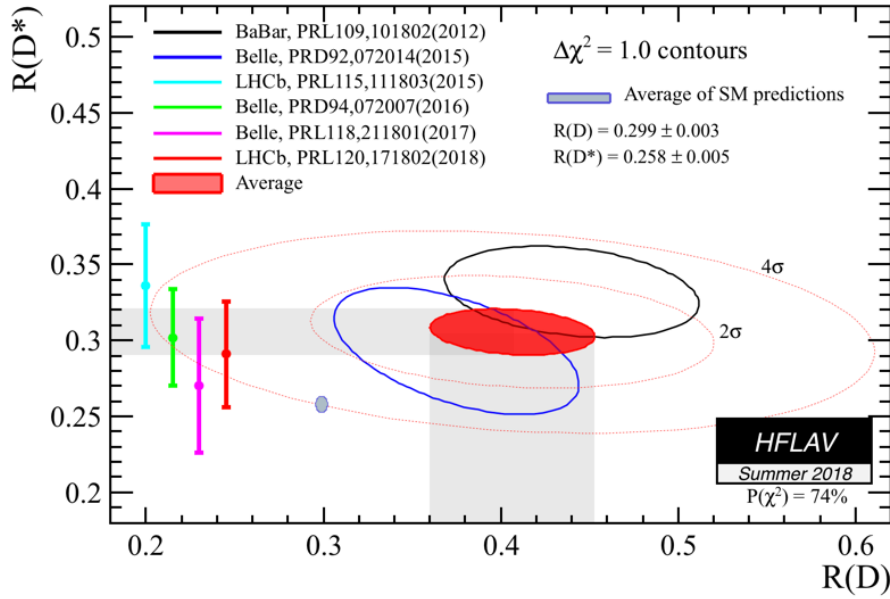


Figure 2.7 – Current status of the combination of both  $\mathcal{R}(D)$  and  $\mathcal{R}(D^*)$  measurements. Figure taken from Ref. [1].

where  $g_L$ ,  $g_R$ ,  $g_S$ ,  $g_P$  and  $g_T$  are NP contributions corresponding to vector and pseudovector ( $g_L$  and  $g_R$ )<sup>5</sup>, scalar ( $g_S$ ), pseudoscalar ( $g_P$ ) and tensor ( $g_T$ ) operators. The SM effective Hamiltonian can be retrieved by setting all these coupling constants to zero.

Decay rates and ratios such as  $\mathcal{R}(D)$ ,  $\mathcal{R}(D^*)$ ,  $\mathcal{R}(\Lambda_c)$  are computed with such Hamiltonian extended with NP operators, see for instance Ref. [70] for  $B \rightarrow D^* \tau \nu_\tau$  and Ref. [71] for  $\Lambda_b^0 \rightarrow \Lambda_c^+ \tau^- \bar{\nu}_\tau$ .

It is important to note that the different decays processes do not have the same sensitivity for all coupling constants. The  $B \rightarrow D \tau \nu_\tau$  is sensitive to the scalar coupling  $g_S$  with no sensitivity to the pseudoscalar one  $g_P$  whereas the situation is the opposite for  $B \rightarrow D^* \tau \nu_\tau$ .

The analysis performed in Ref. [71] for the  $\Lambda_b^0 \rightarrow \Lambda_c^+ \tau^- \bar{\nu}_\tau$  process shows that constraints from this mode on the NP couplings are complementary with the mesonic ones. Constraining the values of the  $\mathcal{R}(D)$  and  $\mathcal{R}(D^*)$  observables to be within  $3\sigma$  to their experimental value and the  $B_c^+$  lifetime<sup>6</sup> by requiring  $\mathcal{B}(B_c^+ \rightarrow \tau^+ \nu_\tau)$  to be less than 30%, the computation of both  $\mathcal{R}(\Lambda_c)$  and  $\mathcal{R}(\Lambda_c)^{Ratio}$  defined as:

$$\mathcal{R}(\Lambda_c)^{Ratio} = \frac{\mathcal{R}(\Lambda_c)}{\mathcal{R}(\Lambda_c)^{SM}}$$

is performed with one coupling left free and the other set to zero. The results are shown in Tab. 2.2 extracted from Ref. [71]. This shows how  $\mathcal{R}(\Lambda_c)$  can be both higher, up to +58% in the only  $g_T$  case, or lower, till -6% when only considering  $g_S$ , than its SM expectation depending on the NP coupling considered even after constraining both  $\mathcal{R}(D)$

<sup>5</sup>Some papers such as Ref. [69] use axial  $g_A = 1 - g_L + g_R$  and vector  $g_V = g_L + g_R$  coupling constants.

<sup>6</sup>The value of  $\tau_{B_c^+}$  adds a strong constraint on the parameter  $g_P$

### 2.3. NEW PHYSICS IN SEMITAUONIC $B$ -DECAYS

Coupling	$R(\Lambda_c^+)_{\max}$	$R_{\Lambda_c^+_{\max}}^{Ratio}$	coupling value	$R(\Lambda_c^+)_{\min}$	$R_{\Lambda_c^+_{\min}}^{Ratio}$	coupling value
$g_S$ only	0.405	1.217	0.363	0.314	0.942	-1.14
$g_P$ only	0.354	1.062	0.658	0.337	1.014	0.168
$g_L$ only	0.495	1.486	$0.094 + 0.538i$	0.340	1.022	$-0.070 + 0.395i$
$g_R$ only	0.525	1.576	$0.085 + 0.793i$	0.336	1.009	-0.012
$g_T$ only	0.526	1.581	0.428	0.338	1.015	-0.005

Table 2.2 – The maximum and minimum values of  $\mathcal{R}(\Lambda_c)$  and  $\mathcal{R}(\Lambda_c)^{Ratio}$  allowed by the mesonic constraints for each NP coupling constant with the corresponding values of the coupling constants. Table extracted from Ref. [71].

and  $\mathcal{R}(D^*)$ . This works strongly motivates the measurement of  $\mathcal{R}(\Lambda_c)$  as it adds new constraints on the possible NP scenarios.

In addition to  $\mathcal{R}(\Lambda_c)$ , other variables are proposed such as the forward-backward asymmetry defined as:

$$A_{FB}(q^2) = \frac{\int_0^1 (d^2\Gamma/dq^2 d\cos\theta_\tau) d\cos\theta_\tau - \int_{-1}^0 (d^2\Gamma/dq^2 d\cos\theta_\tau) d\cos\theta_\tau}{d\Gamma/dq^2}, \quad (2.24)$$

A study of  $\mathcal{R}(D^*)$  or  $\mathcal{R}(\Lambda_c)$  in bins of  $q^2$  would also be beneficial as the shape of the  $q^2$  distribution can be modified by NP contributions.

In Ref. [70], an in depth study of the angular analysis of  $B \rightarrow D^{(*)}\ell\nu$  is performed adding new variables sensitive to NP contributions. Assuming NP contributions only with the  $\tau$ , the extraction of these angular variables from the analysis of the  $B^0 \rightarrow D^{(*)}\tau\nu$  would help to distinguish between the different NP models available.

In addition to the study of model-independent NP contributions, several models are proposed to add new couplings to the  $\tau$  lepton. For instance, an extended Higgs sector with a charged Higgs is a good candidate as the coupling to the lepton is proportional to the mass of the lepton. The effect of a  $H^\pm$  boson in semitauonic  $B$  decays was first studied in Ref. [72]. The Two-Higgs double model (2HDM) of type II was highly disfavoured by the BaBar measurement of  $\mathcal{R}(D)$  and  $\mathcal{R}(D^*)$  [62] but other models with a charged Higgs can still be considered.

Other models, such as Leptoquarks or  $W'$ , are also studied as they could give a comprehensive picture for both  $b \rightarrow s\ell^+\ell^-$  and  $b \rightarrow c\tau\nu_\tau$  transitions. As the former process happen at the loop level whereas the latter are tree level decays, it is not obvious that the scale of New Physics is the same in both cases. Examples of potential new diagrams are shown in Fig. 2.8.

In Ref. [71], several leptoquark models are studied. Depending on the quantum numbers of the leptoquark considered, the expected value of  $\mathcal{R}(\Lambda_c)$  could be 20% to 80% higher than the SM one which indicates a good sensitivity of the  $\mathcal{R}(\Lambda_c)$  in this context.

A  $W'$  [73] model would for instance add a tree level diagram for the  $b \rightarrow s\ell^+\ell^-$  with a  $Z'$  boson and a tree level diagram with a  $W'$  for  $b \rightarrow c\tau\nu_\tau$  with non-universal couplings to leptons.

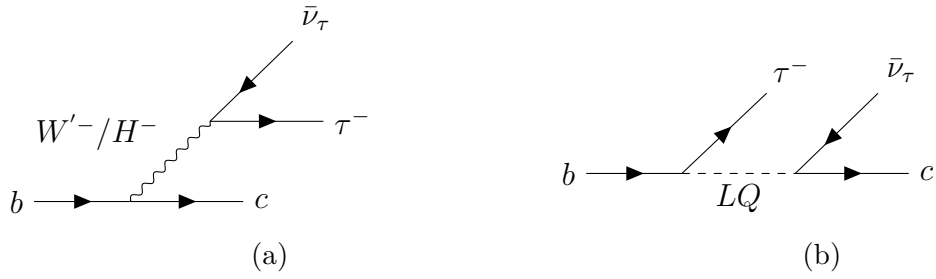


Figure 2.8 – Examples of potential new NP contributions with  $W'^{-}/H^{-}$  (a) and Leptoquark (b) diagrams.

These new particles, whether they are charged Higgs, new  $W'/Z'$  bosons or Leptoquarks are also searched for in direct searches of NP in both ATLAS and CMS experiments. For the time being and with the current datasets, there is no evidence of such particles and the parameters space of these models is decreasing as new exclusion limits are set. The ATLAS Run1 data has been studied for the process  $gb \rightarrow H^{\pm}(\rightarrow tb)t$  with no excess found. A search for high-mass resonances decaying to  $\tau\nu_{\tau}$  is also performed in Ref. [74] and a  $W'$  boson with a mass lower than 3.7 TeV is excluded.

# The LHCb detector

## Contents

---

<b>3.1 The LHC</b> . . . . .	<b>53</b>
<b>3.2 The LHCb detector</b> . . . . .	<b>55</b>
3.2.1 Tracking . . . . .	60
3.2.2 Particle identification . . . . .	66
<b>3.3 The LHCb trigger</b> . . . . .	<b>76</b>
3.3.1 L0 trigger . . . . .	76
3.3.2 High Level Trigger . . . . .	78
3.3.3 Trigger categories . . . . .	79
<b>3.4 The LHCb software</b> . . . . .	<b>80</b>

---

Data used in the analyses presented in Chap. 4 and Chap. 5 were collected by the LHCb detector, one of the main experiments installed along the Large Hadron Collider (LHC) at CERN. This chapter aims at introducing the LHC and the main elements of the LHCb detector, its trigger system and the software framework used to handle the data collected.

## 3.1 The LHC

The CERN (European Organisation for Nuclear Research) is a vast laboratory located on both sides of the border between France and Switzerland, near Geneva. The Large Hadron Collider (LHC) is the main accelerator of the CERN accelerator complex, and the world largest proton accelerator and collider. It is build in a tunnel located at 100 meters below the surface with a circumference of 27 kilometres. This tunnel was carved from 1985 to 1988 to build the Large Electron Positron Collider (LEP) which was operated from 1989 to 2000.

Both heavy ion (especially Pb ions) and proton beams can be accelerated by the LHC. Only proton beams will be described in the following although both proton-lead and

lead-lead collisions can be recorded which allows the study of many QCD processes such as the quark-gluon plasma.

In order to accelerate protons, a chain of smaller accelerators is used, as shown in Fig. 3.1. Atoms of a bottle of hydrogen are first excited to eject the electrons and obtaining protons which are then injected in a linear accelerator (LINAC2) which accelerates protons to 50 MeV and create a bunched beam: instead of a continuous stream of protons, protons are packed in bunches. The proton beam is then further accelerated by three circular accelerators, the BOOSTER up to 1.4 GeV, the Proton Synchrotron (PS) with a maximal energy of 25 GeV and the Super Proton Synchrotron (SPS) finally accelerates the beam to 450 GeV. The beam is then injected in the LHC clockwise and counter-clockwise.

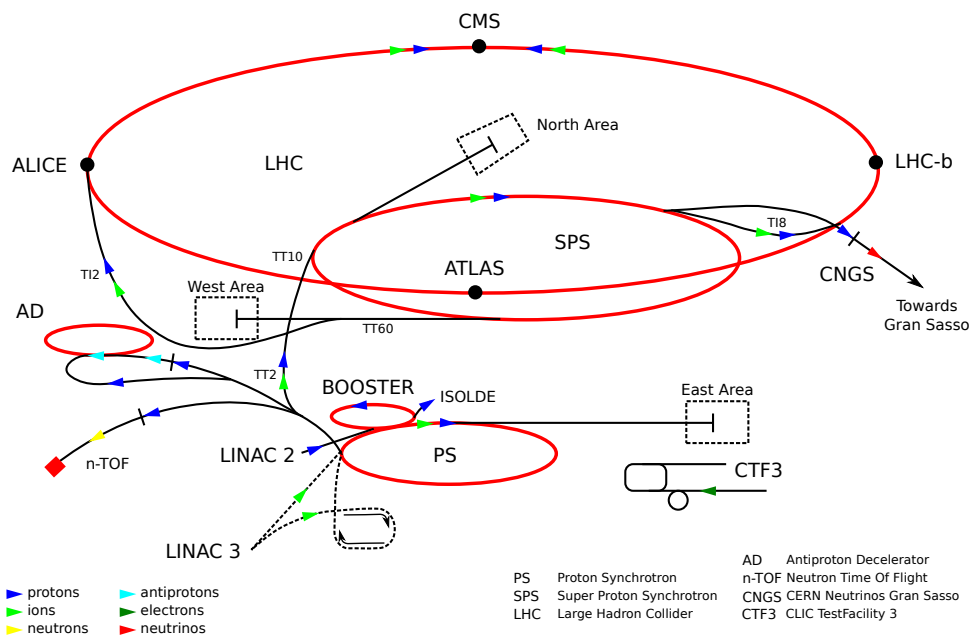


Figure 3.1 – The CERN accelerator complex.

To accelerate the protons, the LHC contains 16 Radiofrequency (RF) cavities which allow to accelerate proton beams up to 6.5 TeV. To keep the beam on its circular orbit, 1232 superconductive dipole magnets made of a niobium-titanium alloy are placed along the accelerator. Using a helium cooling system, these dipoles are kept at a temperature of 1.9 K and provide a powerful 8.3 T magnetic field. In addition to the dipole magnets required for the bending of particles, 392 quadrupole magnets are also placed in the LHC to provide stabilisation and focus to the beams.

The two beams of the LHC cross each other in 4 different locations along the ring called Interaction Points (IPs) where the collision occurs. Bunches of  $\sim 10^{11}$  protons cross each other at a frequency of 40 MHz. Each of the 4 main experiments – ALICE, ATLAS, CMS and LHCb – is installed at one of these points.

The complete list of detectors along the LHC is as follows:

- ALICE [75]: the purpose of this detector is the study of heavy ion collisions using both a Time Projecting Chamber (TPC) and a forward spectrometer.

- ATLAS [76] and CMS [77] : the two general purpose experiments of the LHC build to search for the Higgs boson, which they discovered in 2012 as shown in [31] and [32]. These two experiments are also looking for direct signals of phenomena beyond the Standard Models and put limits on several New Physics models as cited in [78] or [79] in addition to precise measurements of the SM.
- LHCb [80]: A single-arm forward spectrometer focusing on Flavour Physics. Its various sub-detectors are shown in Fig. 3.5 and it will be described thoroughly in the next section.
- LHCf [81]: This experiment is dedicated to study the particle production relevant for cosmic rays physics and will help to construct better modelisation of such processes. A recent overview of the measurements achieved by this experiment is shown in [82].
- TOTEM [83]: This detector was built to measure elastic, inelastic and total proton-proton cross sections. More information can be found in [84].
- MoEDAL [85]: An experiment located close to the LHCb detector dedicated to the search for the magnetic monopole and other phenomena beyond the Standard Model. Using data collected in 2015 and 2016, this experiment puts the most stringent limits on the existence of magnetic monopole [86].

In the following of this chapter, I will focus on the specificities of the LHCb detector.

## 3.2 The LHCb detector

The LHCb detector is a single-arm forward spectrometer purposely built for precise measurements in flavour physics. The core physics program of LHCb consists in precise measurements of the CKM matrix and its Unitary Triangle, such as the  $\gamma$  angle, the study of potential CP-violation in processes involving hadrons containing either b or c quarks and precise measurements of Standard Model processes hunting for any deviation with the SM expectations which could indicate the presence of New Physics contributions.

Compared to both ATLAS and CMS which have an angular coverage close to  $4\pi$  steradians and run at the nominal luminosity provided by the LHC ( $10^{34} \text{ cm}^{-2}\text{s}^{-1}$ ), LHCb was designed with different purposes. The angular coverage of the LHCb detector is indeed 10 to 300 (250) mrad in the bending (non-bending) plane. Using the pseudorapidity  $\eta$ , defined as  $\eta = -\ln[\tan(\frac{\theta}{2})]$  with  $\theta$  being the angle between a particle momentum and the beam axis, this angular coverage is equivalent to a region  $2 < \eta < 5$ . The geometry of the detector was chosen as simulation studies pointed that at high energies,  $b\bar{b}$  pairs are mainly produced in two backward and forward narrow cones around the collision point as shown in Fig. 3.2.

In addition to its particular acceptance, the detector also operates at a constant luminosity two orders of magnitude lower than the nominal one by adjusting the transversal beam overlap, as illustrated in Fig. 3.3. At this luminosity value, the average number of

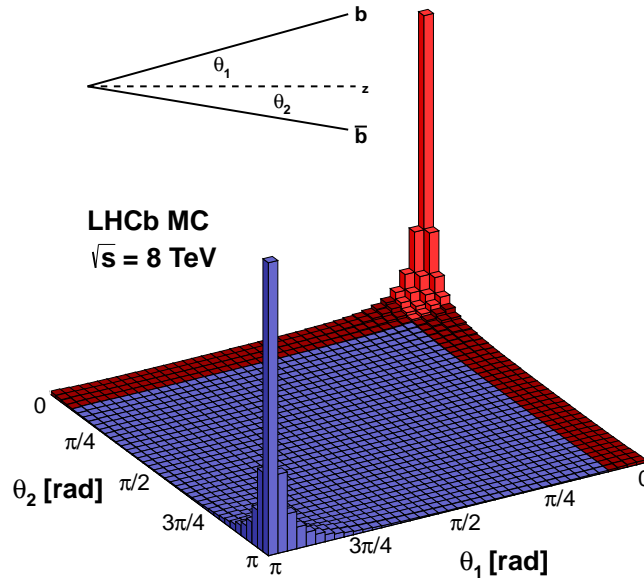


Figure 3.2 – Polar angles of  $b$  and  $\bar{b}$  correlations in proton-proton collisions obtained from a PYTHIA simulation at a centre-of-mass energy of 8 TeV. The LHCb acceptance is shown in red.

interactions per bunch crossing (also referred as pile-up) is close to 1<sup>1</sup>.

This particular luminosity tune with a low number of pile-up is required to keep the detector performances optimal as a  $B$  vertex has to be associated unambiguously to a primary vertex. Algorithms used both in the reconstruction and in the data processing take also advantage of this low number of primary vertices.

The integrated luminosity is presented in Fig. 3.4, the datasets collected in 2011 and 2012 are also known as the Run1 dataset and is used in both Chapters 4 and 5. Data collected from 2015 to 2018 form the Run2 dataset.

The system of coordinates used to describe the detector can be summarised as:

- the interaction is taken as the origin
- the  $x$ -axis and  $y$ -axis are perpendicular and pointing respectively from the interaction point to the outside of the LHC ring and upwards with a tilt of 3.601 mrad with respect to the vertical axis.
- the  $z$ -axis is supported by the beam direction directed from the interaction point to the LHCb detector.

This definition gives a right-handed Cartesian system of coordinates. To compute the transverse kinematical variables such as  $E_T$  or  $p_T$ , the transverse plane is defined as the  $(x-y)$  plane.

<sup>1</sup>As a reference, pile-up in ATLAS or CMS is above 20.

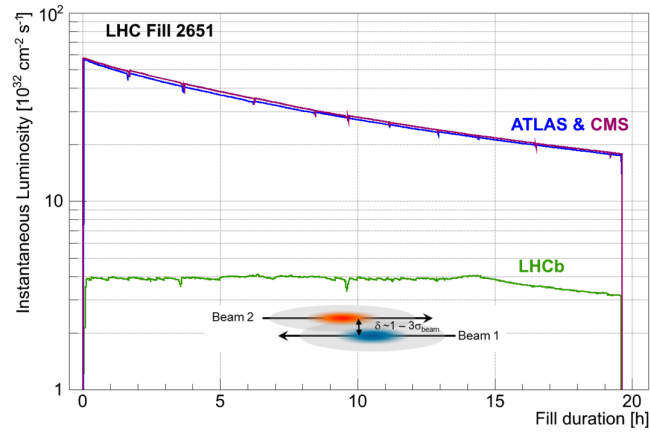


Figure 3.3 – Instantaneous luminosity in ATLAS, CMS and LHCb detectors during LHC fill 2651. The luminosity is kept stable in the LHCb detector by adjusting the transversal beam overlap. Figure taken from [87]

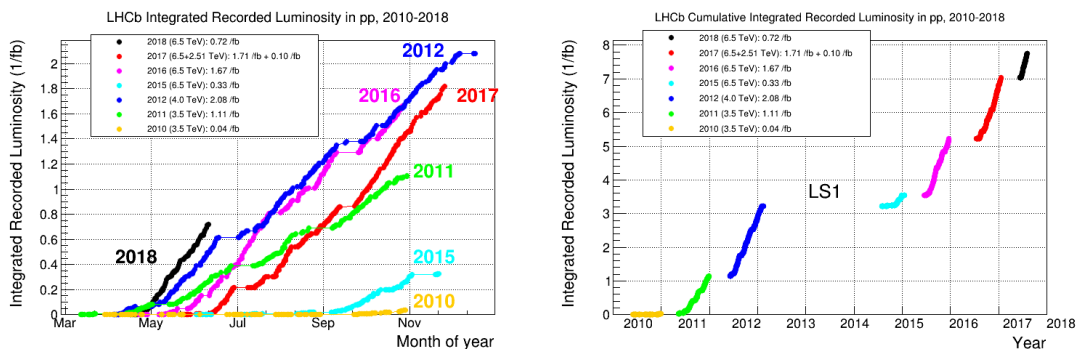


Figure 3.4 – Integrated luminosity collected from 2010 to May 2018.

## CHAPTER 3. THE LHCb DETECTOR

---

Concerning the bending of the trajectories of charged particles, the magnet is such that the bending plane is the (x-z) plane and the non-bending plane is the (y-z) one, which is used to show the LHCb detector in Fig. 3.5.

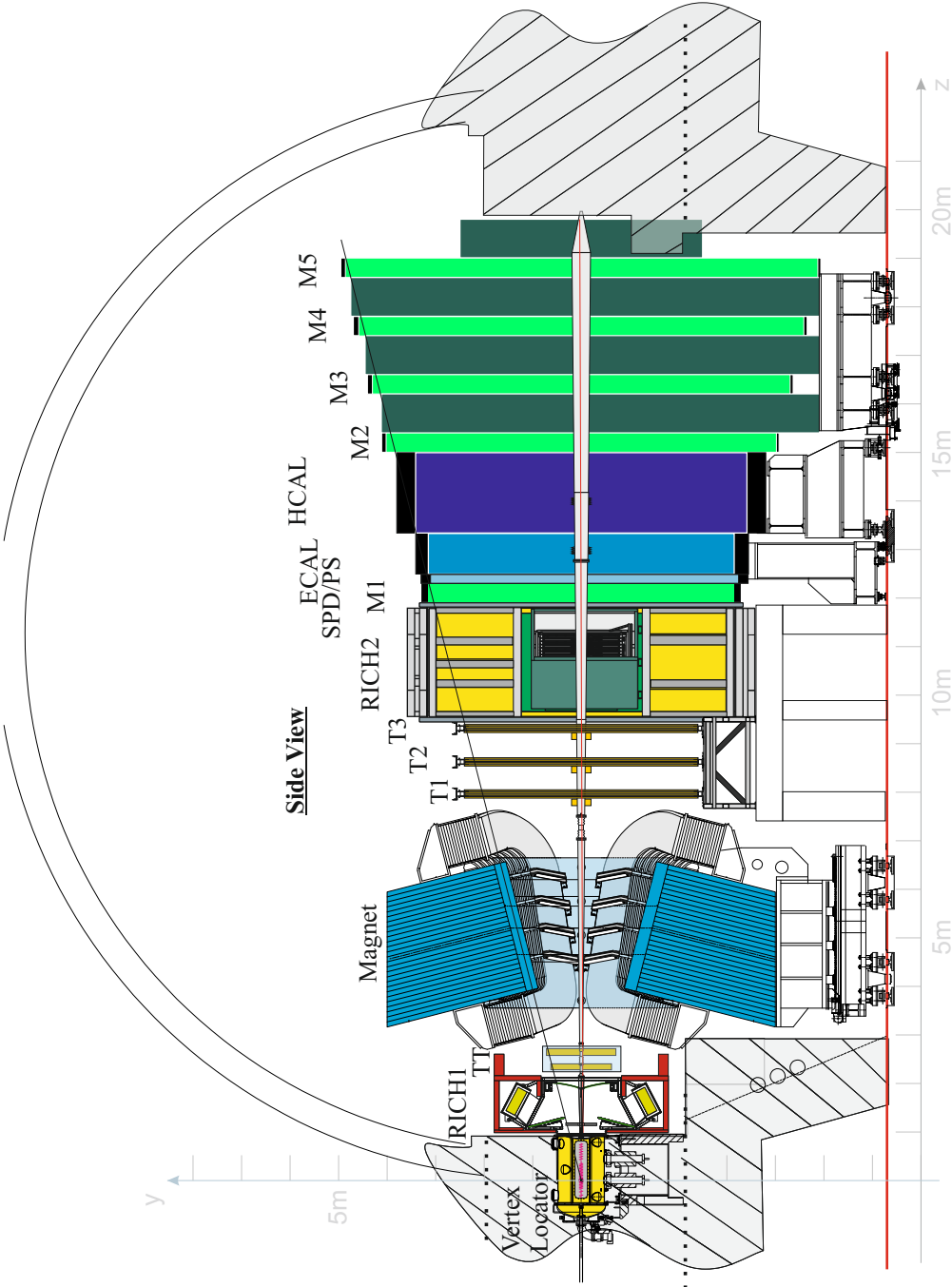


Figure 3.5 – The LHCb detector and its different sub-detectors.

### 3.2.1 Tracking

A tracking system is designed to reconstruct the tracks of particles from hits collected by various detectors. Using a magnet to bend the charged particles trajectories, it is also possible to access the momentum of these particles. In LHCb, the tracking is performed by the VERtEX LOcator (VELO) surrounding the interaction point where the two beams are crossing and tracking stations place upstream (TT) and downstream (T1, T2 and T3) of the magnet.

#### 3.2.1.1 The Vertex Locator

Surrounding the interaction point, the VELO aims to provide precise location of primary vertices (PV). Excellent performances on the spatial resolution of the PV position are crucial for a wide range of analyses from the measurement of CP parameters to lifetime measurements of B and D hadrons and also for computations performed by the HLT system. The event topology cut used in the semitauonic analyses discussed in this document would also not be possible without the excellent performances of the VELO detector.

The VELO is composed of silicon sensors placed along the beam pipe as shown in Fig. 3.6. During data taking, the sensors are positioned only at 8 mm from the beam centre which is smaller than the beam radius during injection. To prevent the detector to be damaged, the VELO is built in two disjoint halves that can remained in an open position during the beam injection. As soon as the beam is stable, the two halves switch to the closed position. The modules on the two halves are not aligned, a 1.5 cm displacement is set in order to allow the two halves to overlap in closed position and ensuring full azimuthal coverage. The two VELO positions are described at the bottom of Fig. 3.6.

Each of the two halves of the detector contains 21 stations made of both a R-sensor and a  $\phi$ -sensor to measure respectively the radial distance to the beam axis and the azimuthal coordinate of the trajectory of a charged particle. The position of the module along the beam line is taken as the value of the third coordinate.

Two additional modules, referred as ‘VETO system’ in Fig. 3.6, are also present upstream of the interaction point to detect particles moving backwards from the LHCb detector. The number of such tracks, is used in the hardware trigger to reject events with too many multiple interactions. Both types of sensors are made of 2,048 silicon strips each, their layout is shown in Fig. 3.7. Their external radius is 42 mm and the internal one is 8 mm. For R-modules, the strips are divided in 45 quadrants and are concentric with an inner pitch of 38  $\mu\text{m}$  and growing linearly with the radius up to a pitch size of 102  $\mu\text{m}$  at the outer edge.  $\phi$ -sensors are made of straight strips divided in inner and outer region of the sensor with a pitch size between 36  $\mu\text{m}$  and 97  $\mu\text{m}$ . The distance between two stations is set to ensure that each particle will pass through at least three stations.

The VELO is placed in a vacuum container protected from beam radiation by an RF Aluminium foil, which also reduces RF interferences.

The performances of the VELO concerning the primary vertex spatial resolution are shown in Fig. 3.8 for 2012 data as a function of the number of tracks used to reconstruct

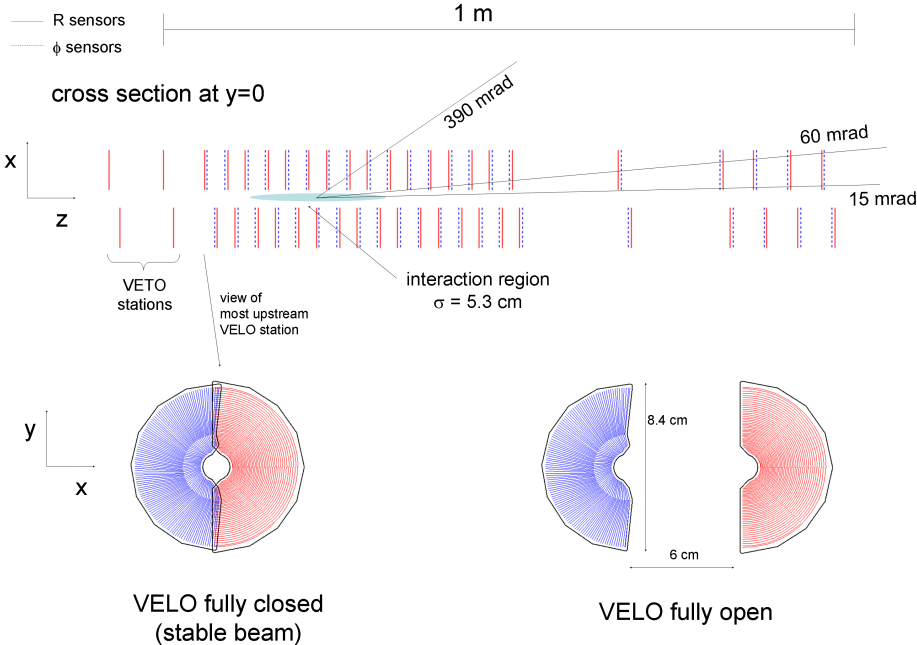


Figure 3.6 – Overview of the VELO detector. The positions of the silicon sensors are shown in the  $(x,y)$  plane at  $y = 0$  and the two schemes at the bottom present the ‘open’ and ‘closed’ positions.

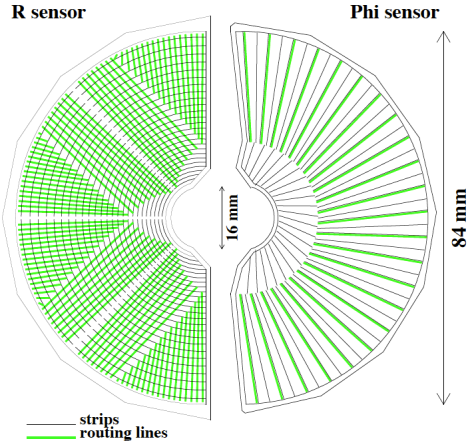


Figure 3.7 – Layouts of R-type and  $\phi$  type sensors.

the PV. Similar performances were achieved for events containing two or three PVs and during 2011 data taking.

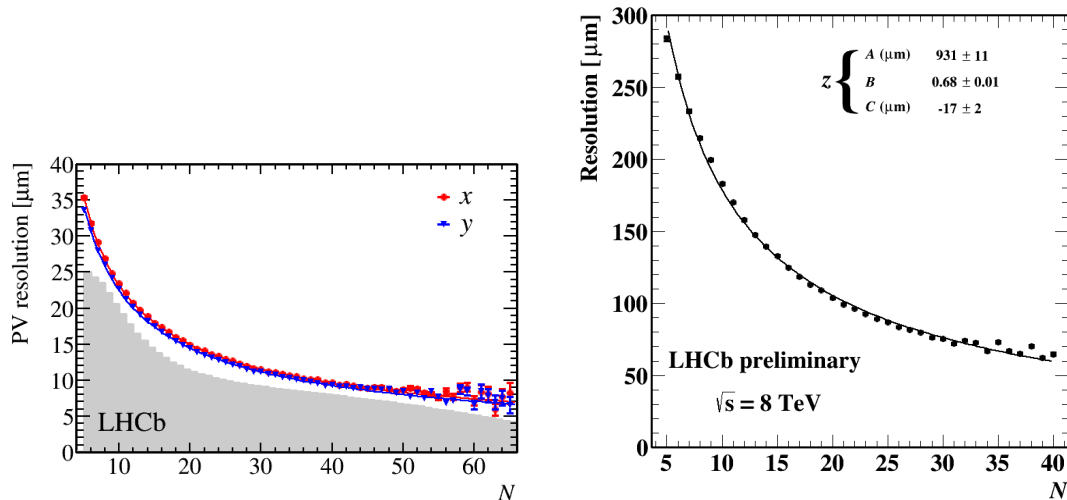


Figure 3.8 – Primary vertex resolution for 2012 data along  $x$  and  $y$  axes (left) and  $z$  axis (right) as a function of the number of tracks used to reconstruct the PV for events containing a single PV.

### 3.2.1.2 The Magnet

The LHCb detector uses a warm dipole magnet with the layout shown in Fig. 3.9 to bend the charged particles in the  $(x-z)$  plane to measure their momentum. The magnet integrated magnetic field is approximately 4Tm. It is made of two identical coils of conical saddle shape placed mirror-symmetrically to each other in the magnet yoke.

The non-uniformity of the magnetic field was measured to be about 1%. The left-right systematic uncertainties due to these detector non-uniformities are kept under control by reversing often the polarity of the field during data taking. Each year of data taking consists then of two roughly equal size datasets labelled as ‘MagUp’ and ‘MagDown’ to both study and reduce potential asymmetries which could lead to systematic uncertainties in analyses.

### 3.2.1.3 Tracking stations

Tracking stations are based on two different technologies, silicon strip based detectors fast enough for its information to be processed by the trigger system and well-suited for high occupancy areas and drift tubes in region with lower occupancy to cover the full angular acceptance.

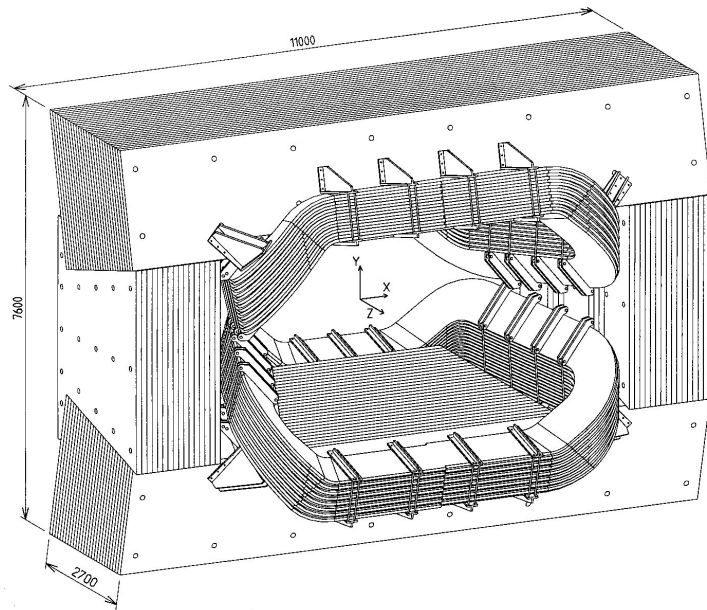


Figure 3.9 – Layout of the LHCb magnet.

### Tracker Turicensis and Inner Tracker

The Tracker Turicensis (TT), or Trigger Tracker, is with the Inner Tracker the two components of the Silicon Tracker (ST).

The TT is composed of two stations (TTa and TTb) placed after the RICH1 and upstream of the dipole magnet. Each station is made of two layers of silicon strip sensors and the two stations have a gap of 27 cm between them. The four stations composing the TT are tilted respectively by 0, 5,  $-5$  and 0 along the  $z$ -axis. This configuration is referred as an  $x - u - v - x$  configuration as both the first and the last stations provide a measurement along the  $x$ -axis whereas the combination of measurements in the second and the third stations gives the position of the track with respect to the  $y$ -axis.

Each sensor, the rectangles in Fig. 3.10a, of the TT is 9.44 cm high and 9.64 cm wide with a thickness of  $500 \mu\text{m}$ . Assembled, they cover a surface of  $8.4\text{m}^2$  in the  $(x - y)$  plane making the TT 150 cm wide and 130 cm high to have a full coverage of the acceptance. Due to the pitch size of  $183 \mu\text{m}$  for each silicon strip, the detector is able to achieve a hit resolution of  $\sim 50 \mu\text{m}$  with a hit efficiency well above 99%.

The Inner Tracker is placed downstream of the dipole magnet covering the inner region, where the highest occupancy is expected, of each of the three stations, T1, T2 and T3. As the TT, sensors of the IT are also arranged in the  $(x - u - v - x)$  configuration in each station with a width of 7.6 cm, a height of 11.0 cm and a thickness of  $320 \mu\text{m}$  or  $410 \mu\text{m}$ .

The sensors are grouped in four boxes displaced in a cross-shaped pattern around the beam pipe with overlap between them to ensure both full coverage and easier alignment.

Both TT and IT are placed in opaque boxes and also thermally and electrically insulated. To both reduce radiation damages and keep a low noise rate, boxes are equipped with a

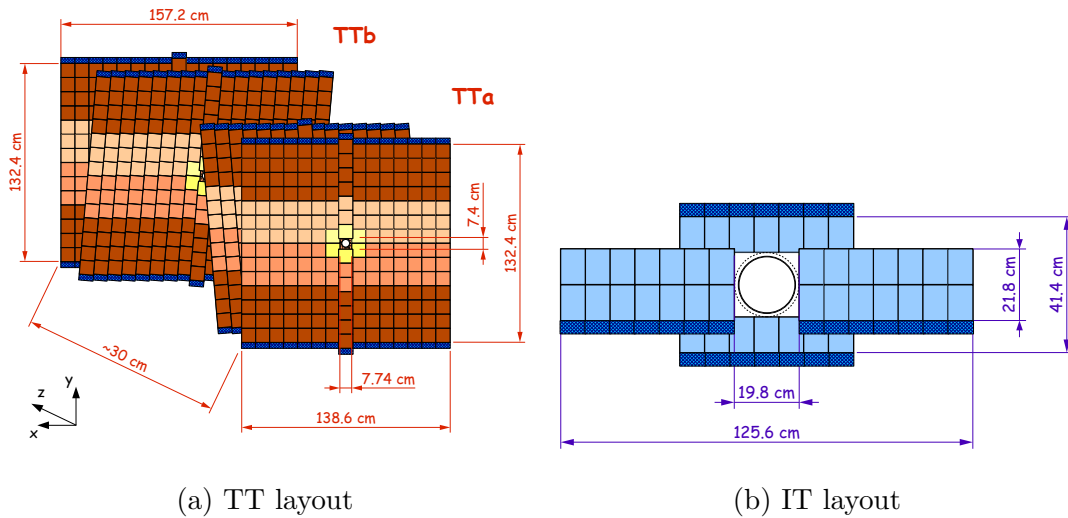


Figure 3.10 – The two components of the Silicon Tracker, including the TT (a) and IT (b).

cooling system maintaining each of the detectors at a temperature of  $5^{\circ}\text{C}$ .

## Outer Tracker

The Outer Tracker (OT), shown in Fig. 3.11, covers the outermost region of each of the T1, T2 and T3 tracking stations to complete the IT and achieve full angular coverage. As for the IT, the three stations of the OT are composed of layers arranged in the  $(x-u-v-x)$  configuration. Instead of silicon strips, each station is composed of two staggered layers of drift tubes. Each tube has an inner (outer) diameter of 4.9 mm (5.0 mm) and is filled with a gas mixture of Argon (70%),  $\text{CO}_2$  (28.5%) and  $\text{O}_2$  (1.5%) to have a drift time less than 50 ns and a spatial resolution of  $200\ \mu\text{m}$ .

## Tracking performances

Tracks leaving hits in both the VELO and tracking stations give the best performances in terms of momentum resolution. Such tracks are referred as ‘long tracks’ and are the most used for physics analyses, including the semitauonic analyses discussed in this document. In addition to this type of tracks, several other categories can be defined as shown in Fig. 3.12 with ‘downstream tracks’ leaving no hits in the VELO, which are very useful for the reconstruction of long-lived particles such as  $K_S^0$  and  $\Lambda$ .

Tracking performances were measured in [87] for the data taking period between 2010 and 2012. The momentum resolution is measured to be  $\sim 0.4\%$  at  $5\ \text{GeV}/c$  up to  $0.6\%$  at  $100\ \text{GeV}/c$  as shown in Fig. 3.13a and the track reconstruction efficiency, shown in Fig. 3.13b, is above 96% in both 2011 and 2012 data taking periods.

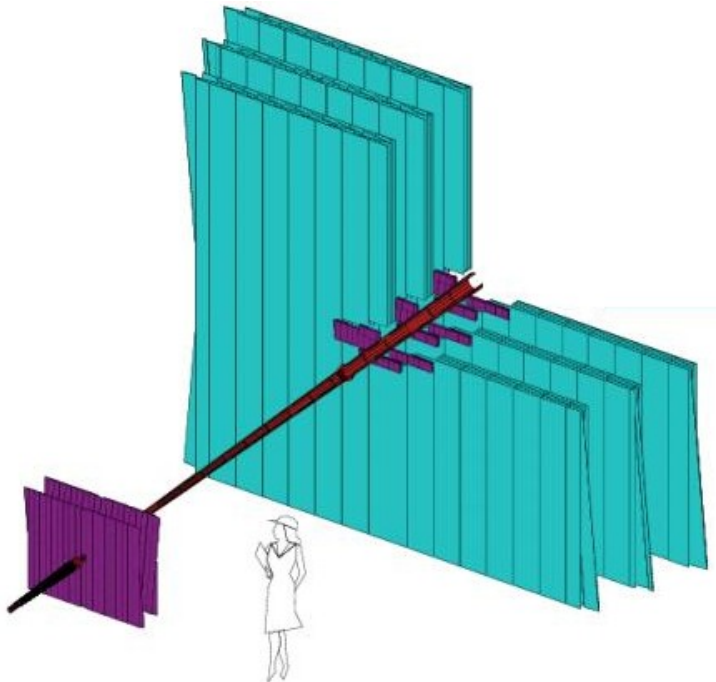


Figure 3.11 – Tracking stations of the LHCb detector. Both TT and IT are coloured in violet and the OT is shown in cyan.

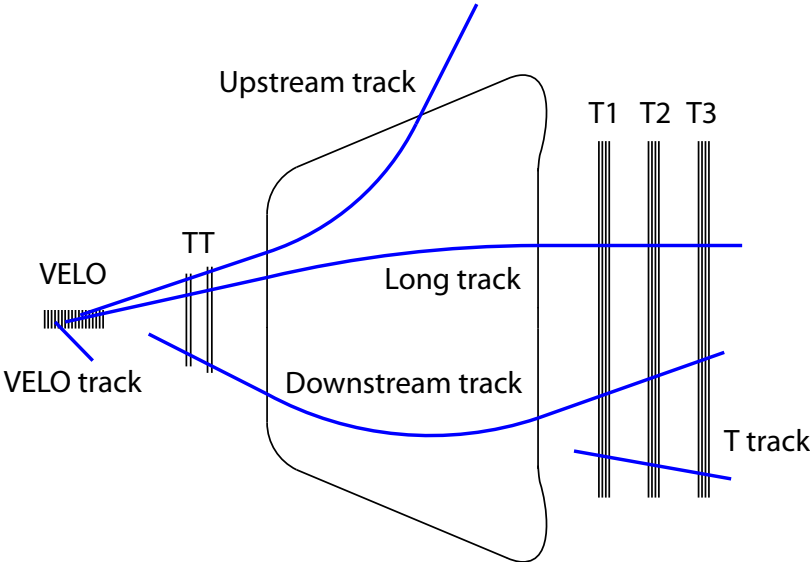


Figure 3.12 – Scheme of the different types of tracks in the LHCb detector.

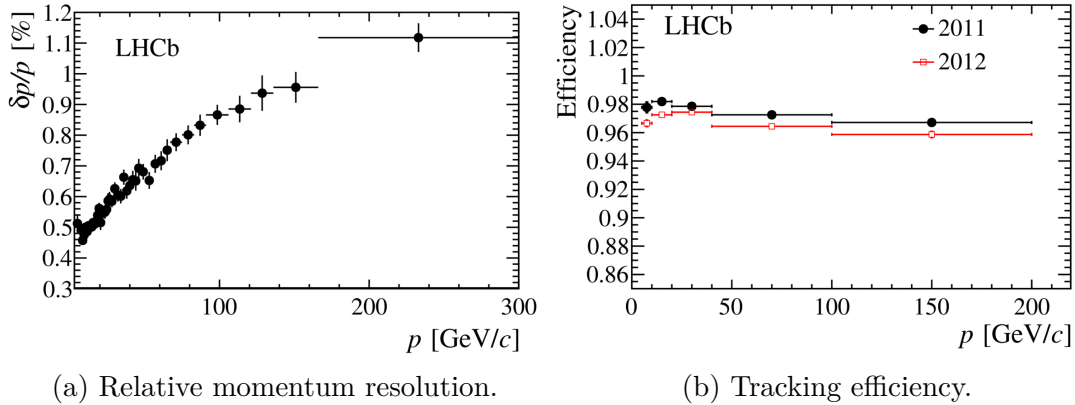


Figure 3.13 – Relative momentum resolution for long tracks (a) and tracking efficiency (b) as a function of the momentum.

## 3.2.2 Particle identification

Excellent particle identification (PID) performances are required by numerous analyses in the LHCb collaboration. PID performances rely on the use of the two RICH detectors, the two calorimeters and the muon chambers. The main features of these detectors are reported in this section and the description of the PID variables used in analyses are also discussed.

### 3.2.2.1 The RICH detectors

The two RICH detectors, for Ring Imaging CHerenkov, both rely on the Cherenkov effect. A particle propagating through a material, referred in the following as a radiator with a refractive index  $n$ , faster than the speed of light in this medium emits photons in a cone of aperture  $\theta$  around its direction of propagation. The value of  $\theta$  is directly related to the velocity of the particle ( $\beta = v/c$ ) through the formula:

$$\cos \theta = \frac{1}{n\beta} \quad (3.1)$$

As the tracking system provides the momentum estimation, the measurement of  $\theta$  gives access to the velocity of the particle and thus to its mass. The indication of the mass of the particle is then enough to identify it. This allows to distinguish pions from kaons with excellent performances throughout the whole momentum range of  $B$  and  $D$  mesons, typically from 1 GeV/c to 100 GeV/c.

To cover this momentum range, two RICH detectors are installed and filled with two different type of radiators. The RICH1 detector is placed upstream of the magnet between the VELO and the TT and is filled with  $C_4F_{10}$ <sup>2</sup> to cover the momentum range between

<sup>2</sup>During Run1, a layer of silica aerogel was also placed in the RICH1 targeting specifically the particles with lowest momentum. It was removed before Run2 due to its limited performances and to permit the same reconstruction both online and offline.

1 GeV to 60 GeV/ $c$ .

The RICH2 detector, located after the tracking stations, is filled with  $\text{CF}_4$  to cover the momentum range from 15 GeV/ $c$  up to more than 100 GeV/ $c$  and contrary to the RICH1 detector covering the full angular acceptance, the RICH2 only covers the 12 mrad – 120(100) mrad range in the bending (non-bending) plane corresponding to the acceptance of the high- $p_T$  tracks. The side view of each detector is shown in Fig. 3.14. The momentum coverage of both detectors is shown in Fig. 3.15 with an example of a RICH1 event display.

To limit the material budget, the two detectors are equipped of a mirror system guiding the light outside of the LHCb acceptance to be collected by Hybrid Photon Detectors (HPDs). As particles are travelling through the RICH1 mirrors, they are made of carbon fibre reinforced with polymer (CFRP) whereas RICH2 mirrors are made of glass as it is located downstream of the tracking system.

To limit the noise coming from the magnetic field, HPDs are placed in iron boxes to provide magnetic shielding.

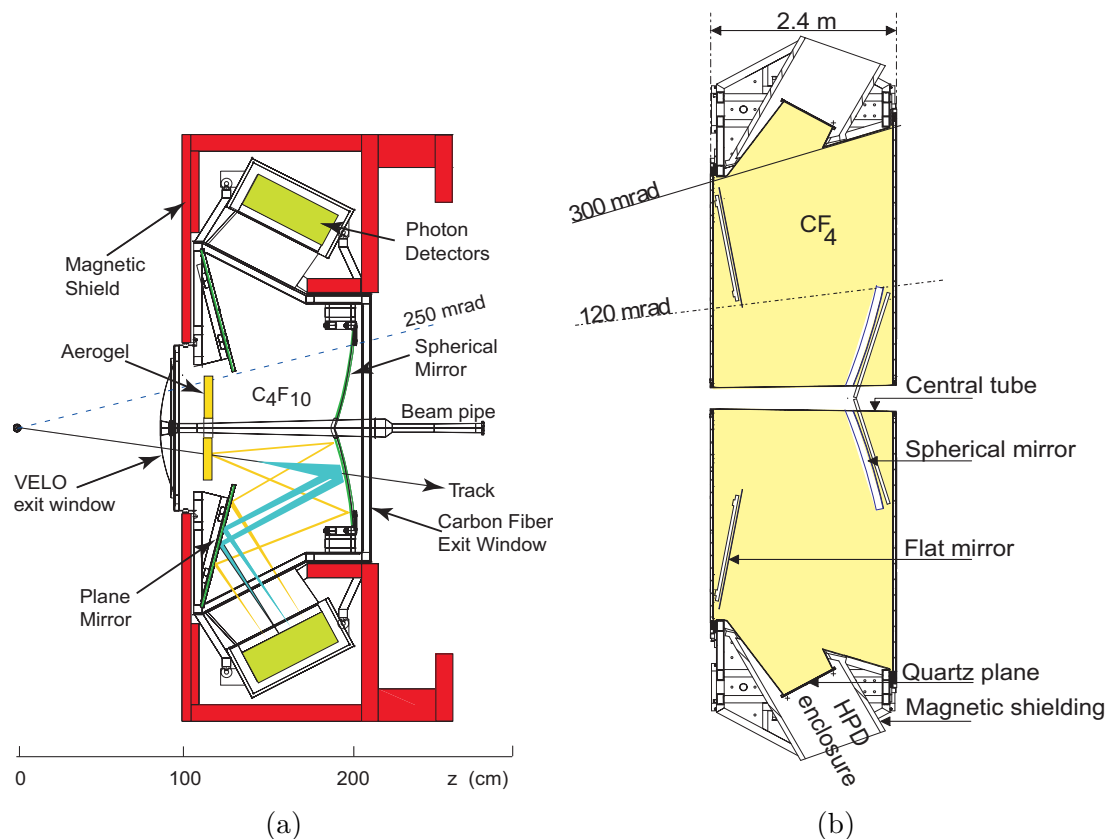


Figure 3.14 – Schematic side views of RICH1 (a) and RICH2 (b) detectors.

### 3.2.2.2 Calorimeter system

The Calorimeter system provides several important information:

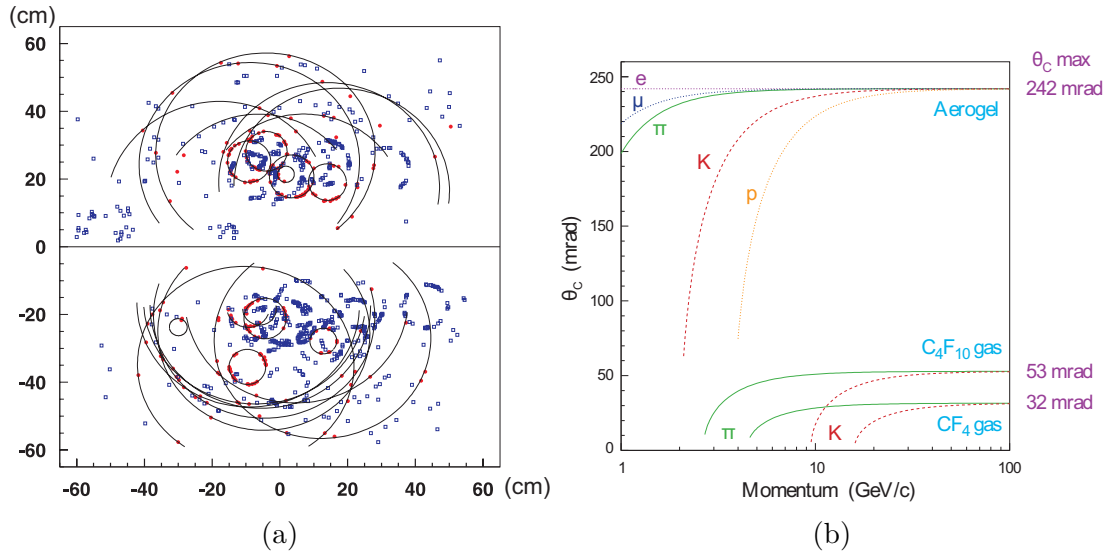


Figure 3.15 – Typical RICH1 event display with the photon rings is presented in (a) and the momentum coverage of both  $C_4F_{10}$  (RICH1) and  $CF_4$  (RICH2) is shown in (b).

- Identification of  $e^\pm$ ,  $\gamma$  and  $\pi^0$  particles and the measurement of their energy and position
- Provide additional PID information for charged hadrons
- fast measurement of  $E_T$  to be used by the hardware trigger

The Calorimeter system is composed in increasing of a Scintillator Pad Detector (SPD), a Preshower (PS), an electromagnetic calorimeter (ECAL) and a hadronic one (HCAL). The geometry of each sub-system is such than the whole angular acceptance is covered by the calorimeter system.

An illustration of the segmentation of the calorimeter system is shown in Fig. 3.17. In addition, the typical shower profile for both electrons, photons and charged hadronic particles used for particle identification is also presented. Charged particles deposit some energy in the SPD and electromagnetic showers are initiated in the lead layer placed between SPD and PS detectors. The full electromagnetic development happens in the ECAL and hadronic showers mostly develop in the HCAL, with a potential initial energy deposit located at the end of the ECAL.

As the expected particle flux varies by two orders of magnitude between the region surrounding the beam pipe and the outermost region, different segmentation schemes were engineered. They are both presented in Fig. 3.16. Both SPD, PS and ECAL detectors are divided in three inner, middle and outer regions whereas the HCAL is only divided in two inner and outer regions. To have the best shower separation in the high occupancy region, the width of a cell of the inner section (40.4 mm) is very comparable to the Moliere radius of the ECAL ( $\sim 36$  mm).

### SPD and PS

Both SPD and PS are two 15 mm thick scintillator pads spaced from one another by

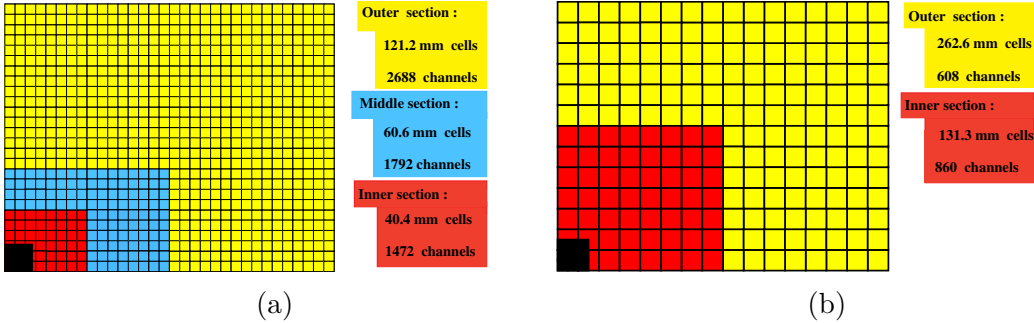


Figure 3.16 – Segmentations used for SPD, PS and ECAL detectors (a) and the one used for the HCAL detector (b).

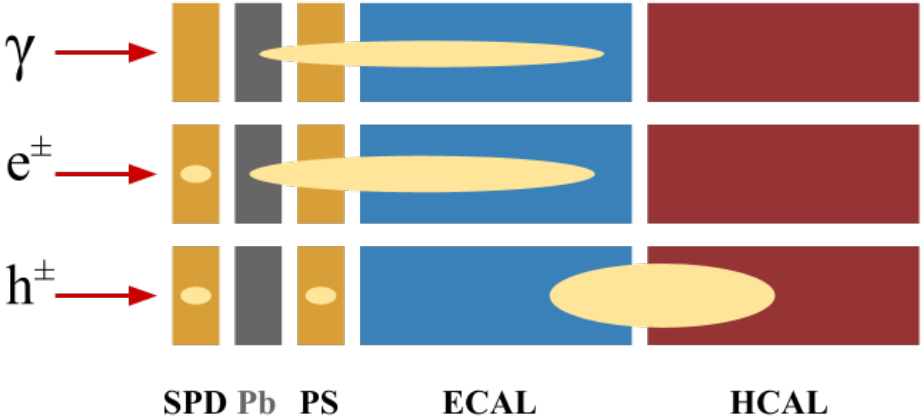


Figure 3.17 – Schematic side view of the different sub-detectors of the LHCb calorimeter system. Typical electromagnetic and hadronic showers are displayed.

56 mm, with an active surface 7.6 m wide and 6.2 m high. A layer of lead material is placed in between the two detectors.

This lead layer is equivalent to  $2.5 X_0$  and  $\sim 0.06\lambda_I$ ,  $X_0$  and  $\lambda_I$  being respectively the electromagnetic and hadronic interaction lengths.

In such configuration, electromagnetic showers of photons and electrons are initiated in the lead layer while hadronic showers will be initiated downstream of the ECAL. These particles created in showers will then initiate scintillating light in the plastic layers collected by wavelength-shifting (WLS) fibres. This light is then transmitted and collected by photomultiplier tubes (PMT).

The SPD is used to distinguish electrons from photons as the latter don't create energy deposit upstream of the lead layer. The number of hits on the surface of the SPD, shortened as nSPDHits, is also a measurement of the charged particles multiplicity in an event. As the multiplicity is hard to model in simulation, nSPDHits is used in both analyses described in Chapters 4 and 5 to reweight simulation samples.

The combination of electromagnetic measurement in both SPD and ECAL provides a longitudinal segmentation used to distinguish electromagnetic showers from interactions of charged pions with the calorimeter material.

## ECAL and HCAL

Both ECAL and HCAL are made of alternatively assembled layer of plastic scintillator and absorber. The ECAL uses lead as absorber while iron layers are used in the HCAL.

The ECAL is placed at 12.5 m of the interaction point and is 7.8 m wide and 6.3 m high to cover fully covering the LHCb angular acceptance. This sampling calorimeter is composed alternatively of layers of scintillating plastic and lead tiles crossed by WLS fibres. The layout of an ECAL cell is shown in Fig. 3.18a, with its 66 lead layers 2 mm thick and the 67 layers of 4 mm thick plastic scintillator. This ensemble of layers is equivalent to  $\sim 25X_0$ , to fully contain the electromagnetic showers created by high energy electrons and photons.

The HCAL is located downstream of the ECAL at 13.3 m from the interaction point and its dimensions are 8.4 m  $\times$  6.8 m. It is also a sampling calorimeter made of scintillating tiles parallel to the beam axis with iron as absorber in between two scintillator layers as shown in Fig. 3.18b. Due to space limitations and the limited resolution required, this design only covers  $5.6\lambda_I$ .

The HCAL can be self-calibrated as it embeds a  $^{137}\text{Cs}$   $\gamma$  source that can travel within steel tube placed at the centre of all tiles. This system is used to measure the ageing of the detector and tune the gains to keep a constant trigger rate. The calibration of the ECAL relies on  $\pi^0 \rightarrow \gamma\gamma$  decays with calibration constants for each cells of the ECAL tuned by performing fits to the invariant  $\pi^0$  mass distribution.

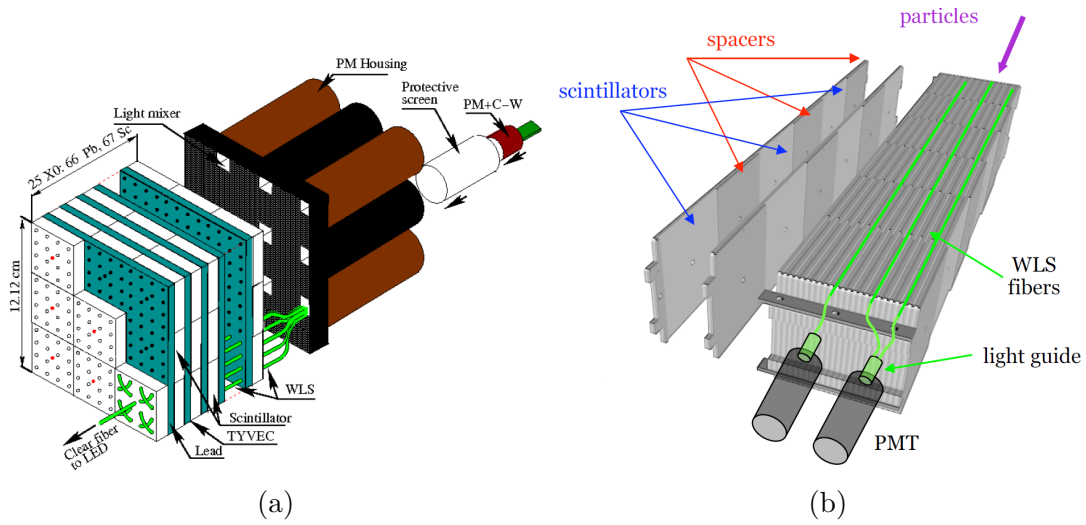


Figure 3.18 – Layout of both inner electromagnetic (a) and hadronic (b) cells.

The resolution of a calorimeter can be described by the formula:

$$\frac{\sigma_E}{E} = \frac{a}{\sqrt{E}} \oplus b \oplus \frac{c}{E} \quad (3.2)$$

The first, second and third terms are referred as *stochastic*, *constant* and *noise* terms which are respectively related to the fluctuation of the light collection of a shower, the non uniformity of the calorimeter and the electric noise.

ECAL and HCAL were designed to reach a design resolution of:

$$\frac{\sigma_E^{ECAL}}{E} = \frac{10\%}{\sqrt{E}} \oplus 1\% \quad (3.3)$$

$$\frac{\sigma_E^{HCAL}}{E} = \frac{65\%}{\sqrt{E}} \oplus 9\% \quad (3.4)$$

These resolutions are required for the calorimeter information to be used at the trigger level.

Using test beams [88], the ECAL energy resolution was measured to be:

$$\frac{\sigma_E^{ECAL}}{E} = \frac{(9.4 \pm 0.2)\%}{\sqrt{E}} \oplus (0.83 \pm 0.02)\% \quad (3.5)$$

The HCAL resolution was also determined in [89] to be:

$$\frac{\sigma_E^{HCAL}}{E} = \frac{(69 \pm 5)\%}{\sqrt{E}} \oplus (9 \pm 2)\% \quad (3.6)$$

### 3.2.2.3 The Muon system

The Muon system is designed to both identify muons for offline analyses and trigger on high- $p_T$  muons.

To do so, it is composed of five stations, M1, located in between the RICH2 and ECAL detectors, and M2 to M5, placed at the downstream end of the LHCb detector, covering the full angular acceptance. Particles are identified as muons if they leave one hit per station and the positions of the hits are used to measure its  $p_T$ .

To only allow muons to propagate through all of the stations, M2-M5 chambers are also separated by iron absorbers 80 cm thick. Including the calorimeter system the total interaction length is  $20\lambda_I$ , meaning that most muons are contained by this system as they need to have an momentum above 6 GeV/ $c$  to cross all the stations. The whole muon system with its iron absorbers along the  $z$ -axis is shown in Fig. 3.19b.

These stations are each arranged in four quadrants, each one is composed of 4 regions (R1-R4) of increasing granularity. The layout of a quadrant is presented in Fig. 3.19a with the disposition of the different regions also shown.

All regions are made of multi-wire proportional chambers (MWPC) except for the inner region of the M1 stations (R1) where triple Gas Electron Multiplier (GEM) are installed to cope with the higher particle flux causing a faster ageing. Both GEM detectors and MWPC are filled with a gas mixture composed of Ar/CO<sub>2</sub>/CF<sub>4</sub> and the proportions are set to gather the information in a 20 ns time window to be able to use it in the hardware trigger system.

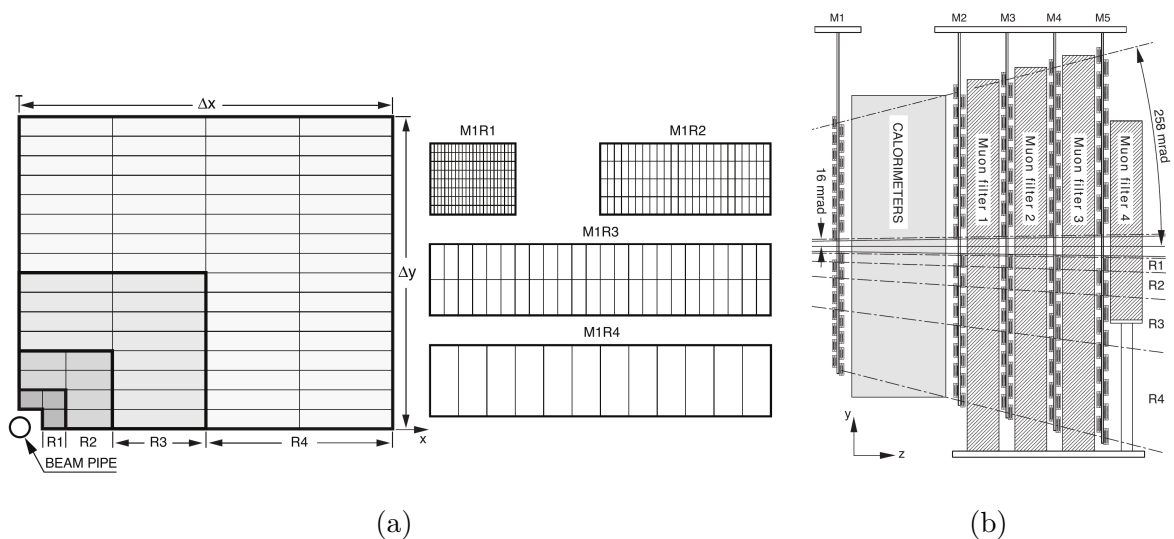


Figure 3.19 – The 4 regions of a muon quadrant with the different granularity (a) and the side view on the muon system (b).

### 3.2.2.4 PID variables and performances

Information gathered by the tracking system, the two RICH detectors, the calorimeter system and the muons chambers are combined by dedicated algorithm to provide a particle hypothesis for a given track.

The hadron identification relies on the calorimeter system as shown in Fig. 3.17, and is further refined to separate between  $\pi$  and  $K$  using the two RICH detectors.  $\gamma/e^\pm$  separation uses the combination information provided by SPD, PS and ECAL detectors and  $\mu$  are selected using the muons stations, the RICH information is also used to identify electrons and muons.

Two different methods are used to provide particle identification variables in offline analyses, a likelihood-based technique and another using a Machine Learning algorithm.

The likelihood of each sub-system, measuring the probability of a given track to be identified as particle  $h$  according to this sub-system, are combined according to the following formula:

$$\mathcal{L}(h) = \mathcal{L}^{RICH}(h) \times \mathcal{L}^{CALO}(\text{non } e) \times \mathcal{L}^{MUON}(\text{non } \mu) \quad (3.7)$$

where  $\mathcal{L}^{CALO}(\text{non } e)$  and  $\mathcal{L}^{MUON}(\text{non } \mu)$  are respectively the likelihood given by the calorimeter system for a given track to not be identified as an electron, and the likelihood provided by the muon system for the track to be discarded as a muon.

To compare particle hypotheses to the  $\pi$  one, the difference of the log-likelihood are computed as follows:

$$PID_h = \ln \mathcal{L}(h) - \ln \mathcal{L}(\pi) = \ln \frac{\mathcal{L}(h)}{\mathcal{L}(\pi)} \quad (3.8)$$

where  $h$  stands for either  $p$ ,  $K$ ,  $\pi$ ,  $e$  or  $\mu$  hypotheses.

The LHCb PID performances for the Run1 data taking period are excellent with for instance,  $PID_K > 0$  giving an average  $K$  efficiency ( $K \rightarrow K$ ) of 95% and a  $\pi$  misidentification ( $\pi \rightarrow K$ ) of 5%.

A Neural Network (NN) algorithm is also used to further optimise particle identification performances. The PID information is combined in such algorithm and trained separately for each type of particle to be identified with simulation samples. The output of each Neural Network, called ProbNN, is a probability of a given track to be identified as the particle associated with this particular Neural Network. There are then  $ProbNN(K, e, \pi, p, \mu, ghost)$  variables to be used in offline analyses.

Such variables are able to take into account correlations between different  $PID_h$  variables and the different sub-detectors resulting in better performances than  $PID_h$  as illustrated in Fig. 3.21 for both  $\mu$  and  $p$ .

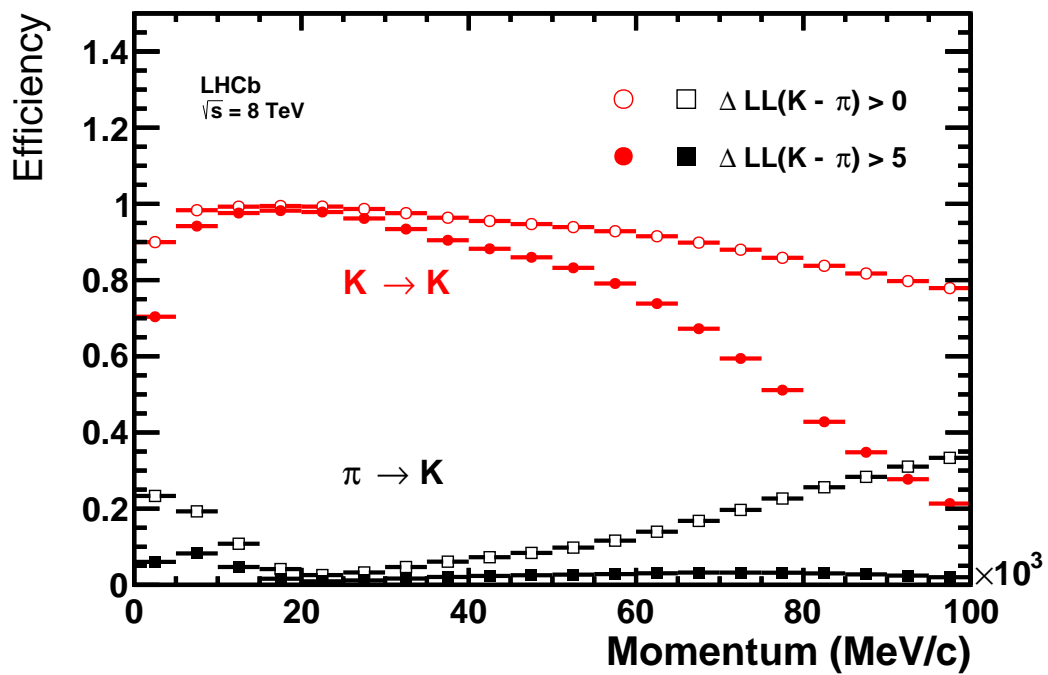
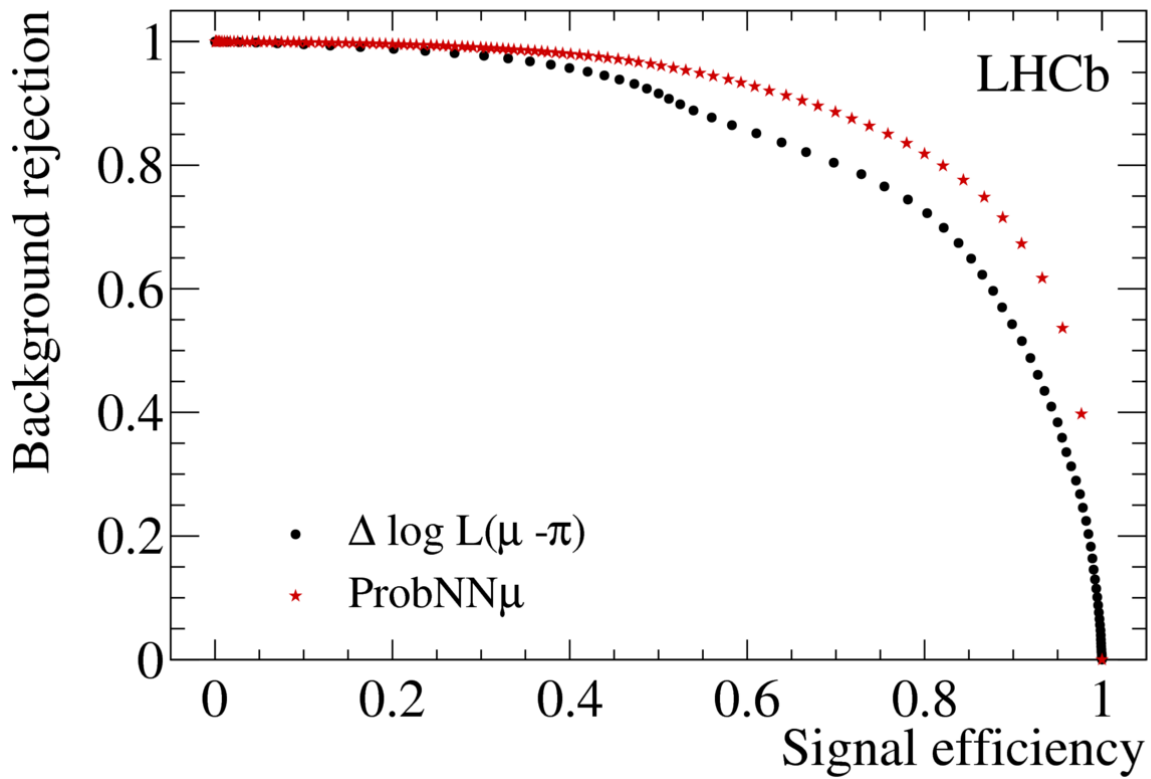
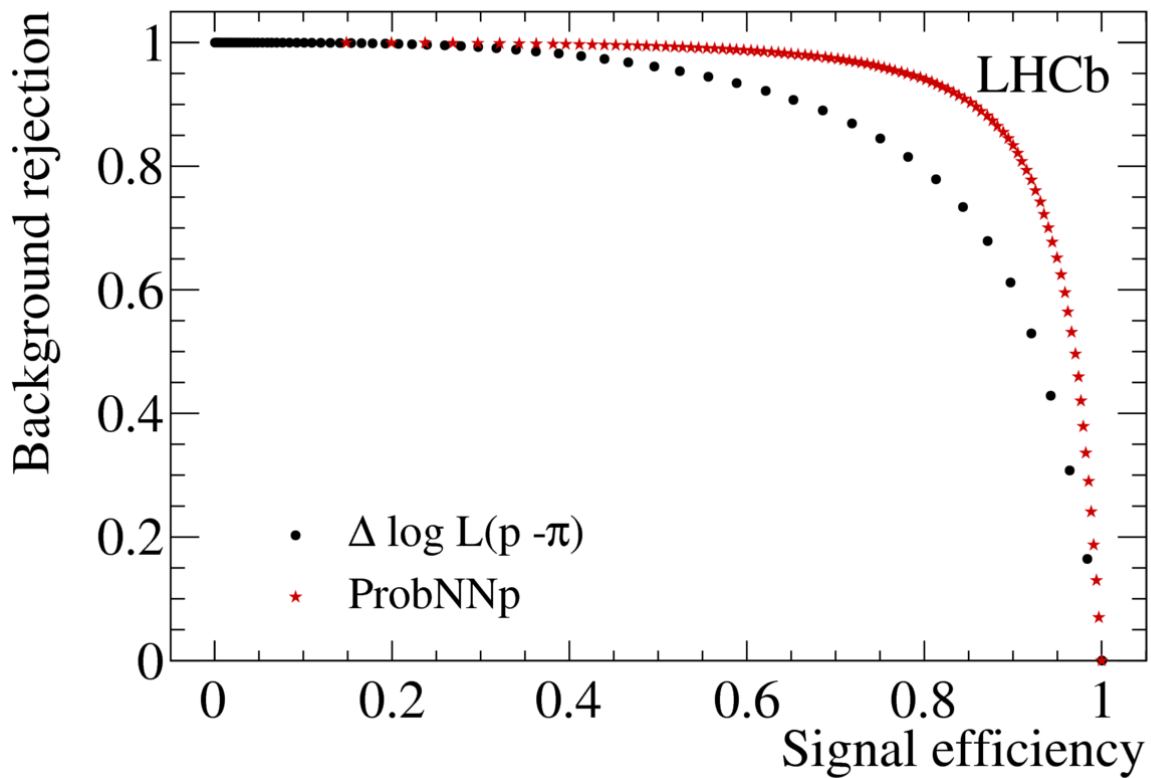


Figure 3.20 – PID performances for Kaons during 2012 data taking.  $K$  efficiency ( $K \rightarrow K$ ) and  $\pi$  misidentification ( $\pi \rightarrow \pi$ ) for two different PIDK selection, PIDK  $> 0$  with open markers and PIDK  $> 5$  with filled ones. Figure taken from [87].



(a)



(b)

Figure 3.21 – Comparison between PID $h$  ( $\Delta \ln \mathcal{L}(h - \pi)$ ) and ProbNN $h$  variables for both  $p$  and  $\mu$ . Figure taken from [87].

### 3.3 The LHCb trigger

With a bunch crossing frequency of 40 MHz at the LHC, the rate of bunch crossings containing visible interactions in the LHCb detector is 10 MHz, which is too high to store everything for offline analyses. In addition, at a luminosity of  $2 \times 10^{32} \text{ cm}^{-2} \text{ s}^{-1}$ <sup>3</sup>, 100 kHz of  $b\bar{b}$  pairs are expected with only 15% of them with at least one  $B$  hadron with all decay products within the LHCb acceptance.

A trigger system was then designed to reduce the event rate to 5 kHz to be written on storage and to select specifically events containing  $b$  or  $c$  hadrons and reject events only containing light flavoured hadrons.

The LHCb trigger system is divided in two levels, a hardware trigger, referred as Level-0 (L0), and a software based one called High Level Trigger (HLT). The Run1 trigger system can be seen in Fig. 3.22a.

The L0 trigger is designed to select high- $p_T$  or high- $E_T$  candidates using the information provided by the VELO pile-up system, the calorimeter and the muon system. Its fast electronics is able to process these information at 40 MHz and reduces the event rate to 1 MHz.

A frequency of 1 MHz is low enough for the whole detector can be read-out and this information is then used by the HLT. The HLT is a software running on the Event Filter Farm (EFF), using the whole detector information in its reconstruction algorithm executed asynchronously. In 2012, 20% of the events accepted by the L0 trigger were deferred to disk to be processed by the HLT in between LHC fills. With such strategy, the EFF resources were used in a more efficient way.

It has to be noted that during Run1, the reconstruction performed in the HLT was different from the offline one as no real-time calibration or alignment information were used in the trigger reconstruction and some simplifications were made to the reconstruction algorithms to fulfil the timing constraints.

A great achievement for the Run2 data taking was the implementation of real-time alignment and calibration during data taking. This leads to reconstructed events stored after the trigger to be much closer to offline ones. The Run2 trigger scheme with the real-time calibration of the detector is shown in Fig. 3.22b. The output rate of the trigger is also higher than in Run1 due to an increase of the available CPU and storage resources.

#### 3.3.1 L0 trigger

Dedicated fast read-out electronics in the VELO pile-up, calorimeter and muon stations allows to process the L0 trigger at the same 40 MHz rate as the bunch crossings. To preferentially select  $b$  or  $c$  candidates, the L0 system relies on the fact that heavy flavoured hadrons have higher masses than light ones hence their decay products have on average,

---

<sup>3</sup>During Run1, the nominal luminosity was  $4 \times 10^{32} \text{ cm}^{-2} \text{ s}^{-1}$

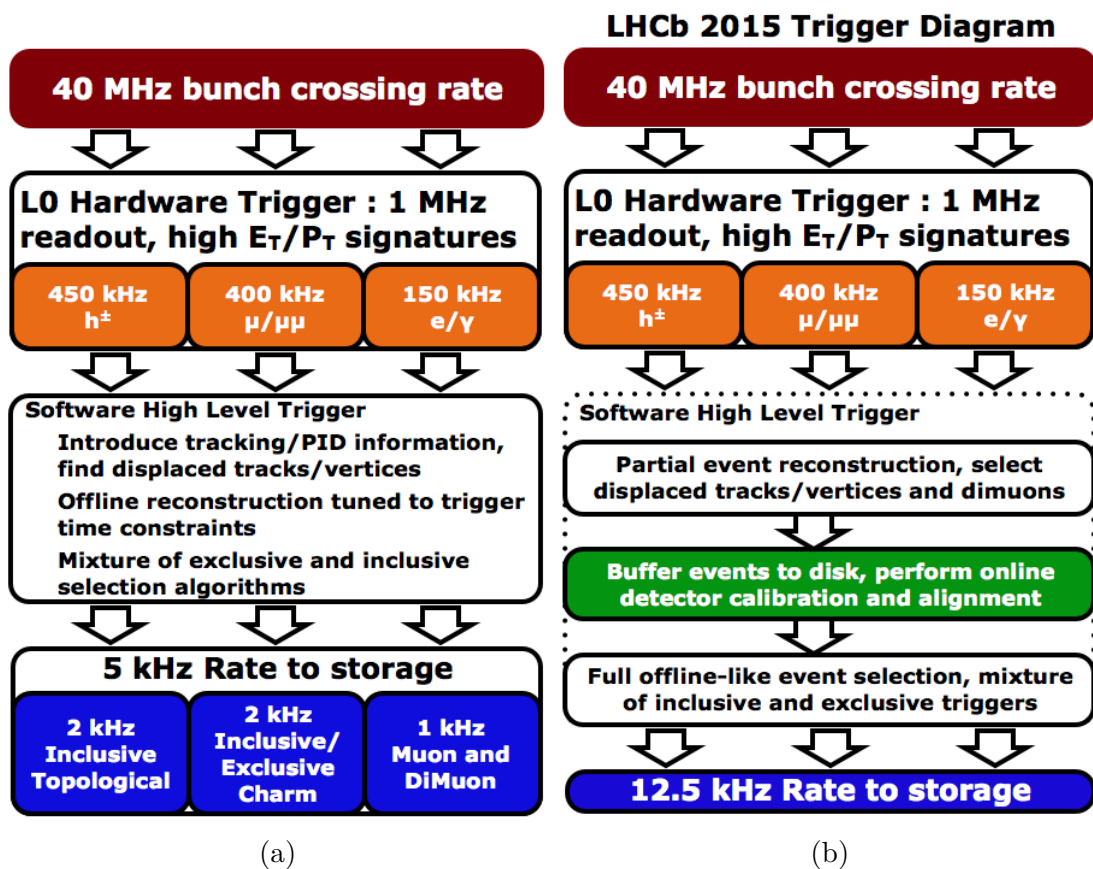


Figure 3.22 – Schematic view of the LHCb trigger for Run1 (a) and Run2 (b).

higher transverse momentum ( $p_T$ ) and energy ( $E_T$ ). The L0 trigger relies on three units: L0-Calorimeter, L0-Muon and L0-PileUp.

The L0-Calorimeter collects information from SPD, PS, ECAL and HCAL.  $E_T$  clusters composed of  $2 \times 2$  cells are computed to create L0Hadron, L0Electron and L0Photon candidates. A L0Hadron candidate corresponds to the highest HCAL  $E_T$  cluster taking into account the energy deposit in the corresponding ECAL cluster. To create a L0Photon candidate, one needs to select the highest  $E_T$  cluster in the ECAL with 1 or 2 hits in the corresponding region of the PS and no hit in the cells of the same region of the SPD. L0Electron candidates are based on the same logic than the one for L0Photon ones except that at least one hit in the corresponding cell of the SPD is required. A cut on the number of hits in the SPD is also set to remove events with multiplicity too high to be further processed by the HLT in a reasonable time.

The event is then triggered if the  $E_T$  of the candidate is higher than a particular threshold. All thresholds, for both L0 and HLT, discussed in this section are stored in the Trigger Configuration Key (TCK), which is preloaded before each LHC fill. Typical values of the L0 thresholds during Run1 are given in Tab. 3.1.

The L0Muon system tracks the two highest  $p_T$  in each quadrant of the muon stations. The eight candidates are then compared to both the single highest  $p_T$  threshold or the two highest  $p_T$  candidates one to either create L0Muon or L0DiMuon candidates.

The L0-PileUp system is used to reject events with multiple interactions and provides a luminosity measurement using the four most upstream sensors of the VELO as described in Sec. 3.2.1.1.

The L0 Decision Unit (DU) finally proceeds to the combination of the information provided by the three sub-systems as a logical OR to create the global L0 trigger decision. The time window for the L0 system between the  $p$  collision and the delivery of its decision is set to 4  $\mu$ s taking into account the delays coming from both electronics and cable transmission and the time needed by the particles to travel through the whole detector.

L0 decision line	$p_T$ or $E_T$		SPD multiplicity
	2011	2012	2011 and 2012
L0Muon	1.48 GeV/ $c$	1.76 GeV/ $c$	600
L0DiMuon $p_{T_1} \times p_{T_2}$	(1.30 GeV/ $c$ ) <sup>2</sup>	(1.60 GeV/ $c$ ) <sup>2</sup>	900
L0Hadron	3.50 GeV	3.70 GeV	600
L0Electron	2.50 GeV	3.00 GeV	600
L0Photon	2.50 GeV	3.00 GeV	600

Table 3.1 – Typical L0 cuts used in Run1. The table is adapted from [87].

### 3.3.2 High Level Trigger

As the HLT is a software-based trigger running on the EFF, it is highly flexible, which is important to cope with the experiment needs and the analysis algorithms development. If in theory the full reconstruction could be run in the HLT, due to the limited resources

available in the EFF, it is using first a partial reconstruction to better optimise the event rejection and keep the processing of an event in the HLT within  $\sim 30$  ms

### HLT1

The HLT is divided in two stages, the first one, referred as HLT1, is only using a partial reconstruction of an event. VELO tracks are reconstructed and primary vertices are identified. The reconstruction of the tracks is only using VELO tracks with either a high impact parameter (IP)<sup>4</sup> or be associated with a muon track. Several HLT1 dedicated selections, called Hlt1 lines, are running to match the analyses criteria.

For instance semitauonic analyses discussed in Chap. 4 and Chap. 5 both rely on the `Hlt1TrackAllL0` line. This Hlt1 line is looking for at least one track with an IP higher than 0.1 mm with respect to each PV and a  $p_T$  higher than 1.6 GeV/ $c$ .

The HLT1 system is able to reduce the 1 MHz rate taken as an input from the L0 to  $\sim 80$  kHz which is low enough to perform a full event reconstruction in the second stage of the HLT, the HLT2 system.

### HLT2

A complete event reconstruction is performed at the HLT2 level and both exclusive decays modes and inclusive ones are selected and stored.

For instance, the events used in the  $\mathcal{R}(\Lambda_c)$  analysis described in Chap. 5 are either selected by an exclusive line dedicated to  $B \rightarrow Dh\bar{h}h$  events, where  $h$  stands for either  $\pi$  or  $K$ , an inclusive line searching for a  $\Lambda_c^+$  decay in the event or topological lines reconstructing a  $B$  hadron decay in two, three or four charged particles.

These topological trigger lines, `Hlt2Topo(2,3,4)BodyBBDT`, are using Bonsai Boosted Decision Trees (BBDT), to trigger on partially reconstructed  $b$  hadron decays. Details on its implementation can be found in [90] and [91]. The list of all Hlt2 lines used during Run1 data taking is also detailed in [92].

During Run2, the EFF resources increased with an output rate of 12.5 kHz instead of 5 kHz during Run1 and a time window of 650 ms to process the Hlt2 trigger step instead of 150 ms. These additional resources allowed the implementation of both calibration and alignment of the different sub-detectors within the HLT trigger reducing the differences between online and offline reconstruction. Physics measurements were even made possible taking directly the trigger output, thanks to the ‘turbo stream’ described in [93], which was a real gain for charm physics measurements.

### 3.3.3 Trigger categories

Events selected by the trigger system can be classified in two non-mutually exclusive categories:

---

<sup>4</sup>The Impact Parameter of a track with respect to a vertex is the shortest distance between the two. A track with a high IP with respect to the primary vertices is likely to come from a  $B$  decay.

- **TOS**: Trigger On Signal, at least one of the objects composing the signal candidate was used in the trigger decision
- **TIS**: Trigger Independent of Signal, the trigger decision rely on objects not associated with the signal candidate

Events belonging to both categories, referred as TIS & TOS, can be used to assess the trigger efficiency of the offline selection candidates only relying on data samples as described in [94].

If the number of TIS, TOS and TIS & TOS events are labelled  $N^{TOS}$ ,  $N^{TIS}$  and  $N^{TISTOS}$ , one can then define the TIS and TOS trigger efficiencies as follows:

$$\epsilon^{TIS} = \frac{N^{TISTOS}}{N^{TOS}} \quad (3.9)$$

$$\epsilon^{TOS} = \frac{N^{TISTOS}}{N^{TIS}} \quad (3.10)$$

These efficiencies are discussed in more details in Sec. 5.6.

## 3.4 The LHCb software

The LHCb software relies on a general C++ framework called Gaudi [95] which every application uses. Raw data are processed using the Moore application which runs the HLT application and the full offline reconstruction is performed within the Brunel software whose output is stored in Data Summary Tape (DST) file format.

As running each analysis on these files would be extremely tedious, loose preselections are splitting the dataset into several streams, composed of several lines each dedicated to a specific decay channel. This loose preselection is called the Stripping step with its stripping streams and lines. More details on the stripping lines used in the  $\mathcal{R}(\Lambda_c)$  are shown in Sec. 5.3.2. To collect all events selected by a given stripping selection, the DaVinci application needs to be used and its output is stored as a ROOT [96] TTree.

The Monte-Carlo (MC) simulation samples are produced using the Gauss application [97], relying on the PYTHIA [98] package to generate  $pp$  collision with the  $B$  hadron decays modelled by EVTGEN [99] and the final state radiations taken care of by PHOTOS [100].

The detector response is generated using the Geant4 toolkit [101]. To process simulation samples as close as possible to real data, the detector response is then digitised by the Boole application to emulate raw data. MC samples are then processed using the same tools as real raw data.

# Measurement of $\mathcal{R}(D^*)$ using $\tau^- \rightarrow \pi^- \pi^+ \pi^- (\pi^0) \nu_\tau$ decays

## Contents

---

<b>4.1 Motivation and analysis strategy . . . . .</b>	<b>82</b>
<b>4.2 Event selection . . . . .</b>	<b>82</b>
4.2.1 Event topology . . . . .	83
4.2.2 Isolation and partial reconstruction . . . . .	84
<b>4.3 Study of the <math>D_s^+</math> decays . . . . .</b>	<b>86</b>
4.3.1 The $D_s^+$ decay model . . . . .	86
4.3.2 The $D_s^+$ control sample . . . . .	87
<b>4.4 Fit model and results . . . . .</b>	<b>91</b>
4.4.1 Fit model . . . . .	91
4.4.2 Signal and normalisation yields . . . . .	92
<b>4.5 Systematics . . . . .</b>	<b>98</b>
4.5.1 $\tau$ decay model . . . . .	98
4.5.2 Particle identification . . . . .	99
4.5.3 Summary of systematic uncertainties . . . . .	103
<b>4.6 <math>\mathcal{R}(D^*)</math> result . . . . .</b>	<b>103</b>

---

This chapter presents a summary of the measurement of  $\mathcal{R}(D^*)$  performed using the  $\tau^- \rightarrow \pi^- \pi^+ \pi^- (\pi^0) \nu_\tau$  mode to reconstruct the  $\tau$ .

In addition to a short description of the main steps of the analysis, its results used in the  $\mathcal{R}(\Lambda_c)$ , presented in Chap. 5, are discussed in more details such as the  $D_s^-$  decay model and some systematics related to the  $\tau$  physical description. Finally, the work performed to correct the simulation/data disagreement related to particle identification is presented in details. More on this analysis can be found in Ref. [3] and Ref. [8].

## 4.1 Motivation and analysis strategy

As discussed in Chap. 2, the current combination of  $\mathcal{R}(D)$  and  $\mathcal{R}(D^*)$  measurements is in tension with the SM expectation at the level of  $3.78\sigma$ . A measurement of  $\mathcal{R}(D^*)$  with the hadronic  $\tau$  reconstruction in three charged pions allows to use a dataset with very low correlations with respect to the measurement performed using the muonic decay of the  $\tau$  [67] with a very different set of systematic uncertainties. It also allows to isolate a sample with both high statistics and high purity using the particular characteristics of the hadronic  $\tau$  decay such as:

- the presence of only one neutrino in the decay chain
- the  $\tau$  vertex is reconstructed using the tracks of the three charged pions items the internal dynamics of the  $3\pi$  system

To measure  $\mathcal{R}(D^*)$ , the analysis is performed using the Run1 dataset collected by the LHCb detector. The signal yield ( $N_{sig}$ ) is extracted using a 3D template based fit described in Sec. 4.4 and compared to the normalisation yield ( $N_{norm}$ ), with the normalisation channel chosen to be  $B^0 \rightarrow D^{*-} 3\pi$  due to its visible final state being identical to the signal one.

The measured quantity can be defined as follows:

$$\mathcal{K}(D^{*-}) \equiv \frac{\mathcal{B}(B^0 \rightarrow D^{*-} \tau^+ \nu_\tau)}{\mathcal{B}(B^0 \rightarrow D^{*-} 3\pi)} = \frac{N_{sig}}{N_{norm}} \frac{\epsilon_{norm}}{\epsilon_{sig}} \frac{1}{\mathcal{B}(\tau^+ \rightarrow 3\pi \bar{\nu}_\tau) + \mathcal{B}(\tau^+ \rightarrow 3\pi \pi^0 \bar{\nu}_\tau)}, \quad (4.1)$$

with  $\epsilon_{sig}$  and  $\epsilon_{norm}$  being respectively the normalisation and signal efficiencies. The  $B^0 \rightarrow D^{*-} \tau^+ \nu_\tau$  branching fraction is then obtained as:

$$\mathcal{B}(B^0 \rightarrow D^{*-} \tau^+ \nu_\tau) = \mathcal{K}(D^{*-}) \times \mathcal{B}(B^0 \rightarrow D^{*-} 3\pi)$$

where  $\mathcal{B}(B^0 \rightarrow D^{*-} 3\pi)$  is the average of the measurements presented in Ref. [4, 5, 6]. The value of  $\mathcal{R}(D^*)$  is finally obtained using  $\mathcal{B}(B^0 \rightarrow D^{*-} \mu^+ \nu_\mu)$  from Ref. [1].

The event selection is described in Sec. 4.2, its main features such as the event topology cut or the isolation techniques are described. Sec. 4.3 presents a detailed analysis of the  $D_s^-$  decays as they are useful both in  $\mathcal{R}(D)$  and  $\mathcal{R}(\Lambda_c)$  analyses.

The fit model, its parameters and the corresponding results are shown in Sec. 4.4 and a detailed description of the associated systematics is presented in Sec. 4.5. In particular, the reweighting procedure for the particle identification variables and the computation of the related systematic uncertainty is discussed in Sec. 4.5.2.

## 4.2 Event selection

The event selection is designed to remove two categories of background:

- $B^0 \rightarrow D^{*-} 3\pi X$  events, also referred as *prompt* background, through the use of a cut on the event topology

- $B^0 \rightarrow D^{*-}D(X)$  where  $D$  can be either  $D_s^+$ ,  $D^0$  or  $D^+$  using a Boosted Decision Tree (BDT) algorithm, this background is denoted as *double charm* in Tab. 4.1

Dedicated cuts to reject combinatorial background are also added such as asking for a good quality  $3\pi$  vertex or rejecting tracks coming from the PV by requiring high  $IP_{\chi^2}(PV)$ . The list of selection cuts is given in Tab. 4.1, the cut on the distance between  $B^0$  and  $3\pi$  vertices along the  $z$ -axis is discussed in Sec. 4.2.1. More details on the definition of the variables used to define the event selection can be found in Sec. 5.3.2.

Variable	Requirement	Targeted background
$[z(3\pi) - z(B^0)]/\sigma_{(z(3\pi)-z(B^0))}$	$> 4$	prompt
$p_T(\pi)$ , $\pi$ from $3\pi$	$> 250 \text{ MeV}/c$	all
$3\pi$ vertex $\chi^2$	$< 10$	combinatorial
$IP_{\chi^2}(\pi)$ , $\pi$ from $3\pi$	$> 15$	combinatorial
$IP_{\chi^2}(\bar{D}^0)$	$> 10$	charm
$[z(3\pi) - z(PV)]/\sigma_{(z(3\pi)-z(PV))}$	$> 10$	charm
$r_{3\pi}$	$\in [0.2, 5.0] \text{ mm}$	spurious $3\pi$
$PV(\bar{D}^0)$	$= PV(3\pi)$	charm/combinatorial
number of $B^0$ candidates	$= 1$	all
$\Delta m \equiv m(D^{*-}) - m(\bar{D}^0)$	$\in [143, 148] \text{ MeV}/c^2$	combinatorial

Table 4.1 – List of the selection cuts with the different background categories defined in the text. Table adapted from [3].

It has to be noted that normalisation events are selected with a very similar set of cuts with the difference that the cut on the displacement of vertices used is:

$$vtx_z 3\pi - vtx_z(D^0) < 4\sigma$$

and no cut is required on the output of the BDT discussed in the following of this section.

### 4.2.1 Event topology

The removal of prompt background events relies on the requirement of a displacement between  $B^0$  and  $3\pi$  vertices as only a particle with a significant lifetime, such as a  $\tau$  or a  $D$  meson, can create it.

By asking a displacement  $\Delta z$  defined as:

$$\Delta z = vtx_z(3\pi) - vtx_z(B^0)$$

to be higher than 4 times its significance  $\sigma_{\Delta z}$ , where  $\sigma_{\Delta z}$  is defined as:

$$\sigma_{\Delta z} = \sqrt{vtx_z(B^0)_{err} \oplus vtx_z(3\pi)_{err}}$$

the number of prompt events is reduced by three orders of magnitude in the analysis as shown in Fig. 4.1. The vertical line defining the cut on the event topology used in this analysis and the dominance of double charm events of the form  $D^*D X$  is clearly visible

with the prompt background becoming quite negligible in comparison. The similarities of the distribution of  $\Delta z / \sigma_{\Delta z}$  for both double charm and signal events should also be noted as it motivates the use of other techniques to remove the double charm background component, which are described in the following.

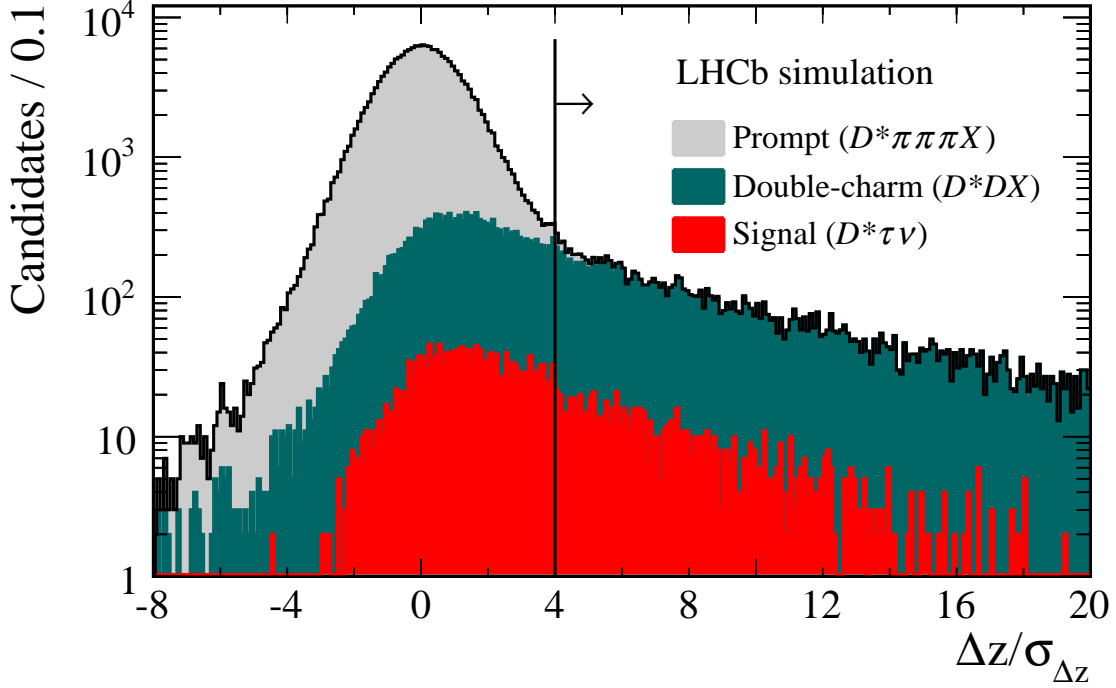


Figure 4.1 – Distribution of the distance between the  $B^0$  vertex and the  $3\pi$  vertex along the  $z$ -axis divided by its uncertainty, obtained using simulation. The vertical line shows the  $4\sigma$  requirement used in the analysis to reject the prompt background component. Figure taken from Ref. [3].

## 4.2.2 Isolation and partial reconstruction

In addition to the cuts defined in the event selection, the rejection of background, especially double charm events, relies on:

- the use of partial reconstruction
- isolation techniques to remove events with extra-tracks found among the charged tracks originating from the decay of the other  $B$  of the event and compatible with one of the vertices of the decay chain of the signal candidate. Deposits of energy compatible with neutral particles are also looked for in the calorimeter system.
- a BDT algorithm trained on  $D^{*-}D_s^+$  and signal samples to further reject  $D^{*-}D_s^+$  events.

The partial reconstruction technique will not be discussed in this chapter as the same strategy is applied for the  $\mathcal{R}(\Lambda_c)$  analysis with the whole implementation discussed in Sec. 5.5.

Double-charm decays can involve extra-particles not used to create the decay chain of the signal candidate. Both deposits of neutral energy and tracks in the event can be looked for and if found to be compatible with either one of the vertices present in the decay chain, these events can be tagged as non-isolated and rejected.

The same variables for neutral isolation are considered in Sec. 5.4, only the treatment of charged isolation is different between  $\mathcal{R}(D^*)$  and  $\mathcal{R}(\Lambda_c)$  analyses. A BDT-based approach is used in the  $\mathcal{R}(\Lambda_c)$  analysis with a cut on the output of the algorithm to reject non-isolated events whereas, for  $\mathcal{R}(D^*)$ , tracks not coming from the PV ( $IP_{\chi^2}(PV) > 4$ ) but compatible with either the  $3\pi$  or  $B^0$  vertices ( $IP_{\chi^2}(3\pi) < 25$  or  $IP_{\chi^2}(B^0) < 25$ ) are searched for and any event found with such track is referred as non-isolated and vetoed.

The exhaustive list of the variables used to train the BDT can be found in Ref. [102], which is very similar to the list of variables used for the  $\mathcal{R}(\Lambda_c)$  analysis defined in Sec. 5.7. All variables belong to one of the following categories:

- partial reconstruction variables such as the reconstructed  $B^0$  momentum or the reconstructed energy of the neutrino
- neutral and charge isolation variables such as the sum of neutral energy in a cone around the  $3\pi$  line of flight
- variables related to the internal dynamics of the three pions such as the minimum of the mass of the two  $\pi^-\pi^+$  pairs
- kinematic variables as the energy of the  $3\pi$  system or the  $B^0$  mass

The BDT is trained on both signal and  $D^*D$  simulation samples and the distribution of its output is shown in Fig. 4.2, where the background refers to  $D^*D$  events.

The requirement of the BDT output to be greater than -0.075, as shown by a vertical line in Fig. 4.2, is used as it was found to be the cut minimising the statistical uncertainty of the fit result used to extract the signal yield.

By construction of the BDT, the number of signal events in the sample defined by a BDT score lower than -0.075 is low whereas this dataset is enriched in  $D_s^+$  decays. This is very useful as this sample is used to fit the  $D_s^+$  decay model described in Sec. 4.3 to extract the different components of the  $D_s^+ \rightarrow 3\pi X$  decays.

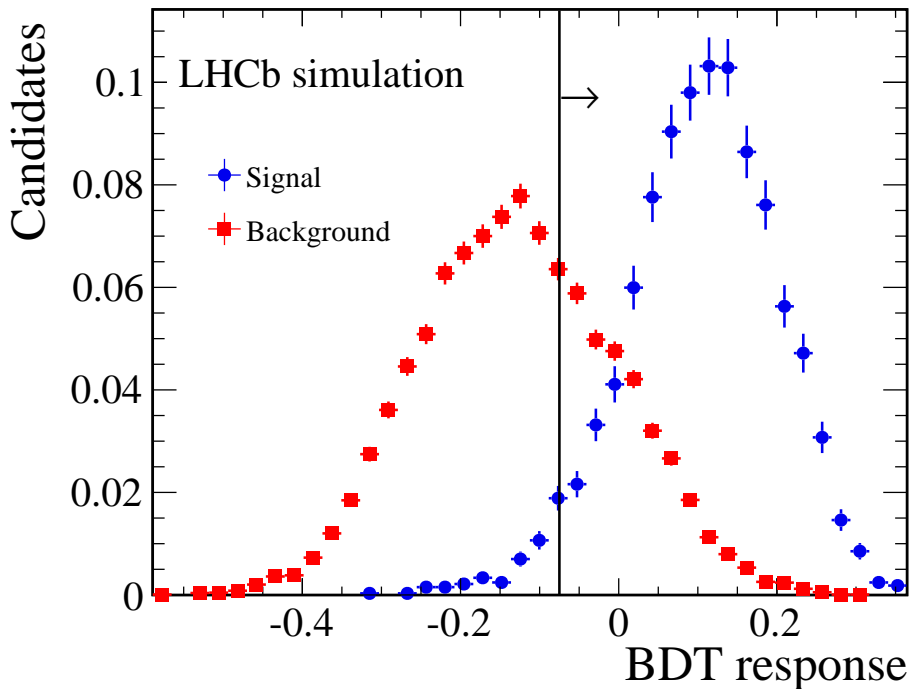


Figure 4.2 – Distribution of the BDT response on the signal and background simulated samples. Figure taken from Ref. [3].

### 4.3 Study of the $D_s^+$ decays

As the fit described in Sec. 4.4 is based on templates for each background component extracted from simulation samples, it is crucial to check the agreement between simulation and data samples for each background category. I will concentrate on the study of  $D_s^+$  decays as they are the dominant contribution throughout the double charm decays. The study of both  $D^0$  and  $D^+$  samples can be found in Ref. [3] for the  $\mathcal{R}(D^*)$  analysis and is discussed in Sec. 5.9 for the  $\mathcal{R}(\Lambda_c)$  one.

#### 4.3.1 The $D_s^+$ decay model

The motivation to know as precisely as possible the relative contributions of the different components of the  $D_s^+$  decays into three pions comes from its dominant contribution in the background and the large branching fraction of the  $D_s^+$  decaying inclusively into three pions. To have a satisfactory background modeling, it is thus crucial to have as much control as possible on the  $D_s^+$  component.

Decays of  $\tau$  into three pions happen through the  $a_1(1260)^+$  resonance decaying into  $\rho^0 \pi^+$  [103].  $D_s^+$  decays involving a  $\rho^0$  are due to  $\eta' \rightarrow \rho^0 \gamma$ . It is thus crucial to precisely know the amount of  $D_s^+$  decays involving a  $\eta'$ .

Besides the inclusive branching fraction of  $D_s^+$  decaying into three pions is roughly 15 times larger than  $\mathcal{B}(D_s^+ \rightarrow \pi^+ \pi^- \pi^+)$  due to contributions of several particles such as

$K_s^0$ ,  $\eta$ ,  $\eta'$ ,  $\phi$  and  $\omega$ , denoted as  $R$  in the following. If most of the decays of the type  $D_s^+ \rightarrow R\pi^+$  are precisely known, this is not always the case for decays such as  $D_s^+ \rightarrow R(\rightarrow \pi^+\pi^-X)\pi^+\pi^0$  or  $D_s^+ \rightarrow R3\pi$ .

To determine the  $D_s^+ \rightarrow 3\pi X$  model, a fit is performed on the Run1 dataset with the requirement to have a BDT score lower than  $-0.075$  to have an enriched  $D_s^+$  sample. The fit is simultaneously performed on the distributions of  $\min[m(\pi^+\pi^-)]$ ,  $\max[m(\pi^+\pi^-)]$ ,  $m(\pi^+\pi^+)$  and  $m(3\pi)$  using templates extracted from dedicated simulation samples with the following components:

- $D_s^+$  decays where at least one pion originates from the decay of an  $\eta$  meson, the  $D_s^+ \rightarrow \eta\pi^+$  and  $D_s^+ \rightarrow \eta\rho^+$  components are taken into account in this category.
- $D_s^+$  decays where, with the same logic used in the category above, an  $\eta'$  meson is present.
- $D_s^+$  decays where at least one pion originates from an intermediate resonance other than  $\eta$  or  $\eta'$ ; these are then further divided into  $R\pi^+$  and  $R\rho^+$  final states.
- Other  $D_s^+$  decays, without any intermediate resonance involved in the  $3\pi$  decay; these are then subdivided into  $K^03\pi$ ,  $\eta3\pi$ ,  $\eta'3\pi$ ,  $\omega3\pi$ ,  $\phi3\pi$ ,  $\tau^+(\rightarrow 3\pi(N)\bar{\nu}_\tau)\nu_\tau$ , and  $3\pi$  non resonant final states,  $X_{nr}$ . For the  $D_s^+ \rightarrow \tau^+\nu_\tau$  decay,  $N$  denotes any potential extra neutral particle.

The fit results are shown in Fig. 4.3 with an overall good agreement between the fit and the data. The fit parameters and the corrections to be applied to simulation samples are shown in Tab. 4.2. These corrections are both applied on the templates used in the  $\mathcal{R}(D^*)$  fit and the one used in the  $\mathcal{R}(\Lambda_c)$  analysis.

### 4.3.2 The $D_s^+$ control sample

The events present in the exclusive peak of  $D_s^+ \rightarrow 3\pi$  provide a pure sample of  $B^0 \rightarrow D^{*-}D_s^+X$  decays which can be used to validate the modelling of the simulation sample by performing a fit to the  $D^{*-}3\pi$  mass distribution.

The fit model, and its probability density function denoted as  $\mathcal{P}$ , is described as follows:

$$\mathcal{P} = f_{\text{c.b.}} \mathcal{P}_{\text{c.b.}} + \frac{(1 - f_{\text{c.b.}})}{k} \sum_j f_j \mathcal{P}_j \quad (4.2)$$

where  $i, j = \{D_s^{*+}; D_s^+; D_{s0}^{*+}; D_{s1}^+; D_s^+X; (D_s^+X)_s\}$  and  $k = \sum_i f_i$ .

The shapes of each component of the fit is extracted from simulation samples of decays of  $D_s^+$  and its excited states. The fit to the  $D^{*-}3\pi$  mass distribution is shown in Fig. 4.4 and also its projections on  $q^2$ ,  $t_\tau$  and the output of the BDT which are the variables used in the fit to extract the signal yield.

The same control sample is used for the  $\mathcal{R}(\Lambda_c)$  analysis and is discussed in Sec. 5.9.

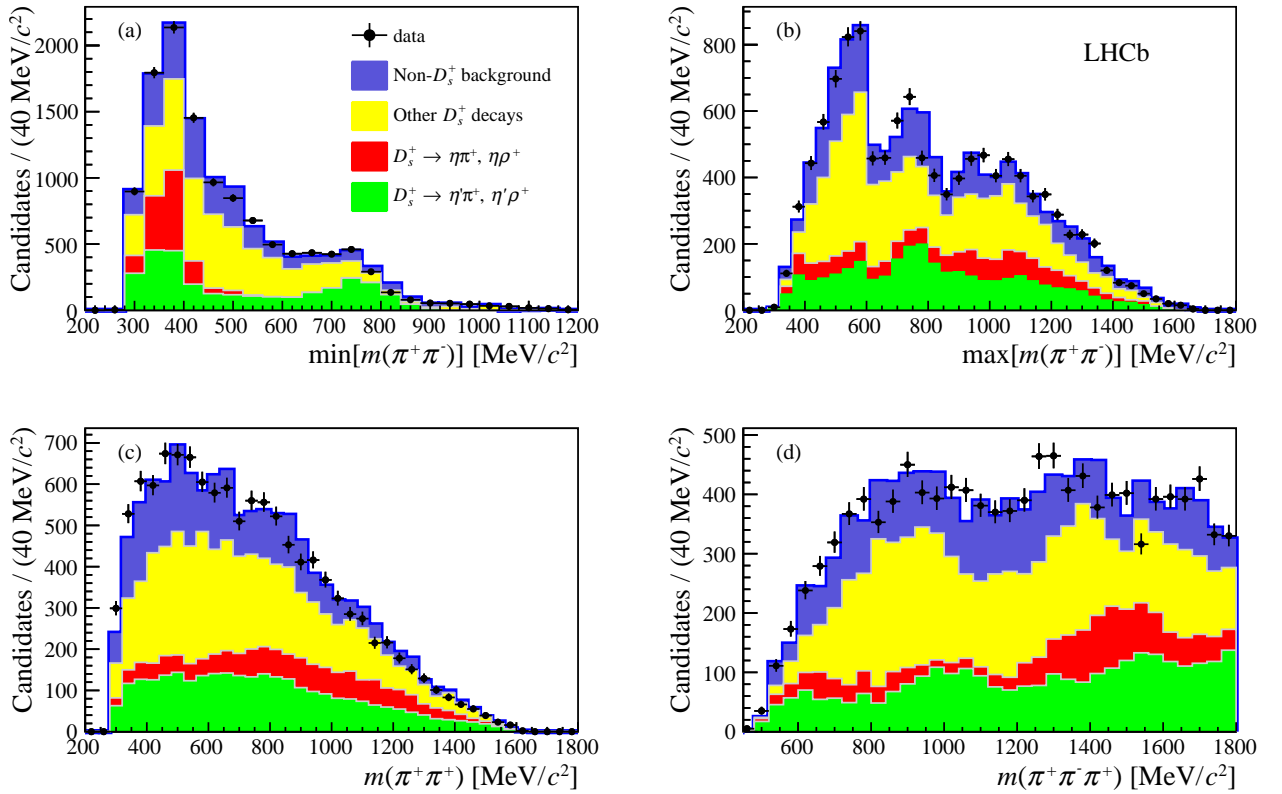


Figure 4.3 – Distributions of (a)  $\min[m(\pi^+\pi^-)]$ , (b)  $\max[m(\pi^+\pi^-)]$ , (c)  $m(\pi^+\pi^+)$ , (d)  $m(\pi^+\pi^-\pi^+)$  for a sample enriched in  $B \rightarrow D^{*-} D_s^+(X)$  decays, obtained by requiring the BDT output below a certain threshold. The different fit components correspond to  $D_s^+$  decays with (red)  $\eta$  or (green)  $\eta'$  in the final state, (yellow) all the other considered  $D_s^+$  decays, and (blue) backgrounds originating from decays not involving the  $D_s^+$  meson. Figure taken from Ref. [3].

$D_s^+$ decay	Relative contribution	Correction to simulation
$\eta\pi^+(X)$	$0.156 \pm 0.010$	
$\eta\rho^+$	$0.109 \pm 0.016$	$0.88 \pm 0.13$
$\eta\pi^+$	$0.047 \pm 0.014$	$0.75 \pm 0.23$
$\eta'\pi^+(X)$	$0.317 \pm 0.015$	
$\eta'\rho^+$	$0.179 \pm 0.016$	$0.710 \pm 0.063$
$\eta'\pi^+$	$0.138 \pm 0.015$	$0.808 \pm 0.088$
$\phi\pi^+(X), \omega\pi^+(X)$	$0.206 \pm 0.02$	
$\phi\rho^+, \omega\rho^+$	$0.043 \pm 0.022$	$0.28 \pm 0.14$
$\phi\pi^+, \omega\pi^+$	$0.163 \pm 0.021$	$1.588 \pm 0.208$
$\eta 3\pi$	$0.104 \pm 0.021$	$1.81 \pm 0.36$
$\eta' 3\pi$	$0.0835 \pm 0.0102$	$5.39 \pm 0.66$
$\omega 3\pi$	$0.0415 \pm 0.0122$	$5.19 \pm 1.53$
$K^0 3\pi$	$0.0204 \pm 0.0139$	$1.0 \pm 0.7$
$\phi 3\pi$	0.0141	0.97
$\tau^+(\rightarrow 3\pi(N)\bar{\nu}_\tau)\nu_\tau$	0.0135	0.97
$X_{nr} 3\pi$	$0.038 \pm 0.005$	$6.69 \pm 0.94$

Table 4.2 – Results of the fit to the  $D_s^+$  decay model. The relative contribution of each decay and the correction to be applied to the simulation are reported in the second and third columns, respectively. Table extracted from Ref. [3].

Parameter	Simulation	Fit	Ratio
$f_{c.b.}$	—	0.014	—
$f_{D_s^+}$	0.54	$0.594 \pm 0.041$	$1.10 \pm 0.08$
$f_{D_{s0}^{*+}}$	0.08	$0.000^{+0.040}_{-0.000}$	$0.00^{+0.50}_{-0.00}$
$f_{D_{s1}^+}$	0.39	$0.365 \pm 0.053$	$0.94 \pm 0.14$
$f_{D_s^+ X}$	0.22	$0.416 \pm 0.069$	$1.89 \pm 0.31$
$f_{(D_s^+ X)_s}$	0.23	$0.093 \pm 0.027$	$0.40 \pm 0.12$

Table 4.3 – Relative fractions of the various components obtained from the fit to the  $B \rightarrow D^{*-} D_s^+(X)$  control sample. The values to produce the simulation samples and the ratio of these two fraction for each component of the fit is also shown. Table from Ref. [3].

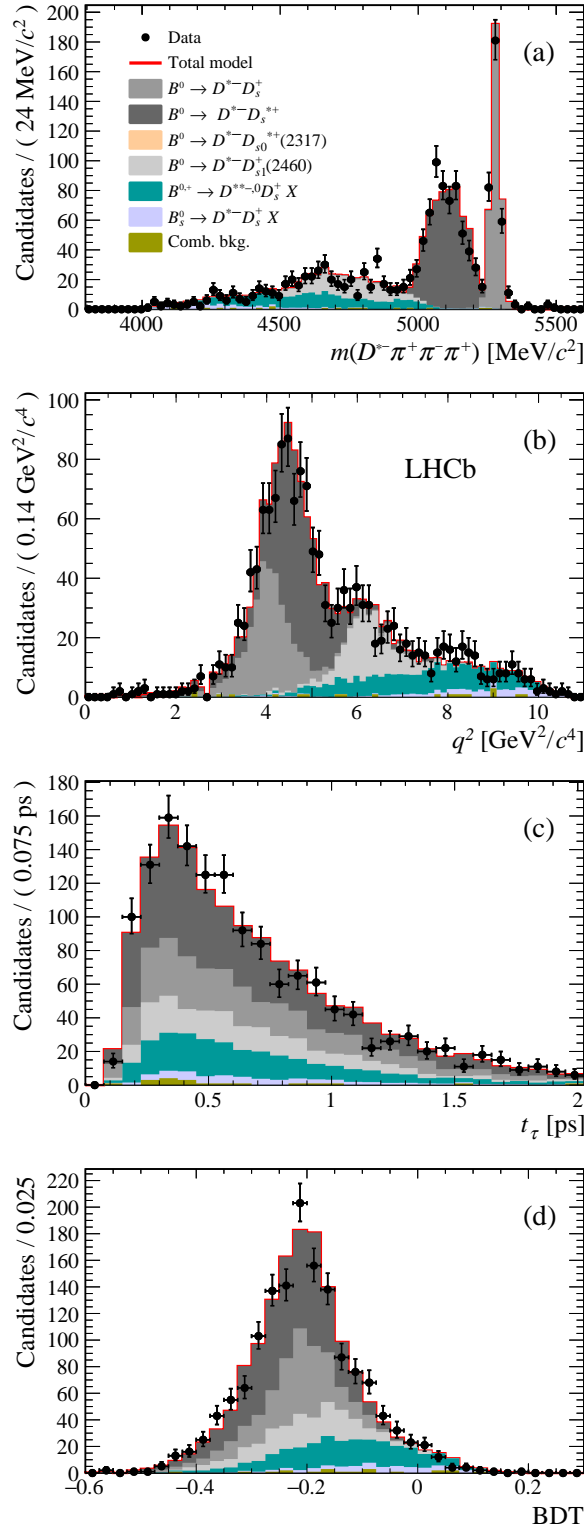


Figure 4.4 – Results from the fit to data for candidates containing a  $D^{*-} D_s^+$  pair, where  $D_s^+ \rightarrow 3\pi$ . The fit components are described in the legend. The figures correspond to the fit projection on (a)  $m(D^* 3\pi)$ , (b)  $q^2$ , (c)  $3\pi$  decay time  $t_\tau$  and (d) BDT output distributions, the variables used the 3D fit to extract the signal yield. Figures taken from Ref. [3].

## 4.4 Fit model and results

To extract the signal yield, a fit is performed on  $q^2$ , the  $\tau$  decay time and the output of the BDT. The same strategy is also used for the  $\mathcal{R}(\Lambda_c)$  analysis as described in Sec. 5.10.

### 4.4.1 Fit model

The fit is based on templates extracted from simulation samples. The binning scheme is defined with 8 bins for the  $q^2$  distribution, 8 bins in  $t_\tau$  and 4 bins to describe the output of the BDT. Tab. 4.4 presents the different templates used in the fit and the relative normalisation for each of them.

The different parameters entering in the normalisation are:

- $N_{\text{sig}}$  is the parameter of interest of the fit, it is left free and accounts for the signal yield.
- $f_{\tau \rightarrow 3\pi\nu}$  is the fraction of  $\tau^+ \rightarrow 3\pi\bar{\nu}_\tau$  signal candidates with respect to the sum of the  $\tau^+ \rightarrow 3\pi\bar{\nu}_\tau$  and  $\tau^+ \rightarrow 3\pi\pi^0\bar{\nu}_\tau$  components. This parameter is fixed to 0.78, according to the different branching fractions and efficiencies of the two modes.
- $f_{D^{**}\tau\nu}$ , fixed to 0.11, is the ratio of the yield of  $B \rightarrow D^{**}\tau^+\nu_\tau$  decay candidates to the signal decays to take into account the  $D^{**}$  feed-down. This yield is computed assuming that the ratio of the decay rates lies between the ratio of available phase space (0.18) and the predictions found in Ref. [104] (0.06), and taking into account the relative efficiencies of the different channels.
- $N_{D^0}^{\text{sv}}$  is the yield of  $B \rightarrow D^{*-}D^0X$  decays where the three pions have a common origin and share the same vertex (SV) as the  $D^0$  vertex. The  $D^0 \rightarrow K^+\pi^-\pi^+\pi^-$  ( $\pi^0$ ) decays are reconstructed by recovering a charged kaon pointing to the  $3\pi$  vertex in non-isolated events. The exclusive  $D^0 \rightarrow K^+\pi^-\pi^+\pi^-$  peak is used to apply a 5% Gaussian constraint to this parameter, which reflects the uncertainty on the estimation of the efficiency in finding the additional kaon.
- $f_{D^0}^{v_1v_2}$  is the ratio of  $B \rightarrow D^{*-}D^0X$  decays where at least one pion originates from the  $D^0$  vertex and the other pion(s) from a different vertex, normalized to  $N_{D^0}^{\text{sv}}$ .
- $f_{D^+}$  is the ratio of  $B \rightarrow D^{*-}D^+X$  decays with respect to those containing a  $D_s^+$  meson.
- $N_{D_s}$  is the yield of events involving a  $D_s^+$ . The parameters  $f_{D_s^+}$ ,  $f_{D_s^{*+}}$ ,  $f_{D_{s1}^+}$ ,  $f_{D_s^+X}$ ,  $f_{(D_s^+X)_s}$  and  $k = \sum_i f_i$ , are defined in Sec. 4.3.
- $N_{B \rightarrow D^{*-}3\pi X}$  is the yield of prompt  $B \rightarrow D^{*-}3\pi X$  events where the three pions come from the  $B$  vertex. This value is constrained by using the observed ratio between  $B^0 \rightarrow D^{*-}3\pi$  exclusive and  $B \rightarrow D^{*-}3\pi X$  inclusive decays, corrected for efficiency.
- $N_{B_1B_2}$  is the number of combinatorial background events where the  $D^{*-}$  and the  $3\pi$  system come from different  $B$  decays. Its yield is fixed by scaling it using the wrong-sign stripping line in the region  $m(D^{*-}\pi^-\pi^+\pi^-) > 5.1 \text{ GeV}/c^2$ .

- $N_{\text{not}D^*}$  is the combinatorial background yield with a fake  $D^{*-}$ . Its value is fixed by using the number of events in the  $\bar{D}^0$  mass sidebands of the  $D^{*-} \rightarrow \bar{D}^0 \pi^-$  decay.

Fit component	Normalisation
$B^0 \rightarrow D^{*-} \tau^+ (\rightarrow 3\pi \bar{\nu}_\tau) \nu_\tau$	$N_{\text{sig}} \times f_{\tau \rightarrow 3\pi \nu}$
$B^0 \rightarrow D^{*-} \tau^+ (\rightarrow 3\pi \pi^0 \bar{\nu}_\tau) \nu_\tau$	$N_{\text{sig}} \times (1 - f_{\tau \rightarrow 3\pi \nu})$
$B \rightarrow D^{**} \tau^+ \nu_\tau$	$N_{\text{sig}} \times f_{D^{**} \tau \nu}$
$B \rightarrow D^{*-} D^+ X$	$f_{D^+} \times N_{D_s}$
$B \rightarrow D^{*-} D^0 X$ different vertices	$f_{D^0}^{v_1 v_2} \times N_{D^0}^{\text{sv}}$
$B \rightarrow D^{*-} D^0 X$ same vertex	$N_{D^0}^{\text{sv}}$
$B^0 \rightarrow D^{*-} D_s^+$	$N_{D_s} \times f_{D_s^+} / k$
$B^0 \rightarrow D^{*-} D_s^{*+}$	$N_{D_s} \times 1/k$
$B^0 \rightarrow D^{*-} D_{s0}^* (2317)^+$	$N_{D_s} \times f_{D_{s0}^*} / k$
$B^0 \rightarrow D^{*-} D_{s1} (2460)^+$	$N_{D_s} \times f_{D_{s1}^+} / k$
$B^{0,+} \rightarrow D^{**} D_s^+ X$	$N_{D_s} \times f_{D_s^+ X} / k$
$B_s^0 \rightarrow D^{*-} D_s^+ X$	$N_{D_s} \times f_{(D_s^+ X)_s} / k$
$B \rightarrow D^{*-} 3\pi X$	$N_{B \rightarrow D^* 3\pi X}$
B1B2 combinatorics	$N_{B1B2}$
Combinatoric $D^{*-}$	$N_{\text{not}D^*}$

Table 4.4 – Summary of fit components and their corresponding normalisation parameters. The first three components correspond to parameters related to the signal.

#### 4.4.2 Signal and normalisation yields

The fit results are presented in both Tab. 4.5 for the detailed description of all the parameters and their values and in Figures 4.5 and 4.6 to see the projections of the fit on the three variables  $q^2$ ,  $t_\tau$  and the output of the BDT. The signal yield is measured to be

$$N_{\text{sig}} = 1273 \pm 85$$

after correcting of  $-3\%$  due to a fit bias related to the limited statistics in simulation samples leading to several empty bins. The correction is estimated using smoothed templates produced using a Kernel Density Estimator technique [105].

Taking into account the statistical uncertainty coming from the simulation samples, the chi-square is estimated to be  $\chi^2 = 1.15$ .

The statistical uncertainty is retrieved by performing a second fit with the parameters describing the shapes of the different  $D_s^+$  contributions and the fraction of  $D^0$  with pions coming from two different vertices ( $f_{D^0}^{v_1 v_2}$ ) fixed to their values found by the nominal fit.

The normalisation yield is extracted from a fit to the  $D^{*-} 3\pi$  mass distribution using the dedicated selection for the normalisation sample. The background component is described by an exponential and a sum of a Gaussian and a Crystal Ball [106] is used for the  $B^0 \rightarrow D^{*-} 3\pi$  peak.

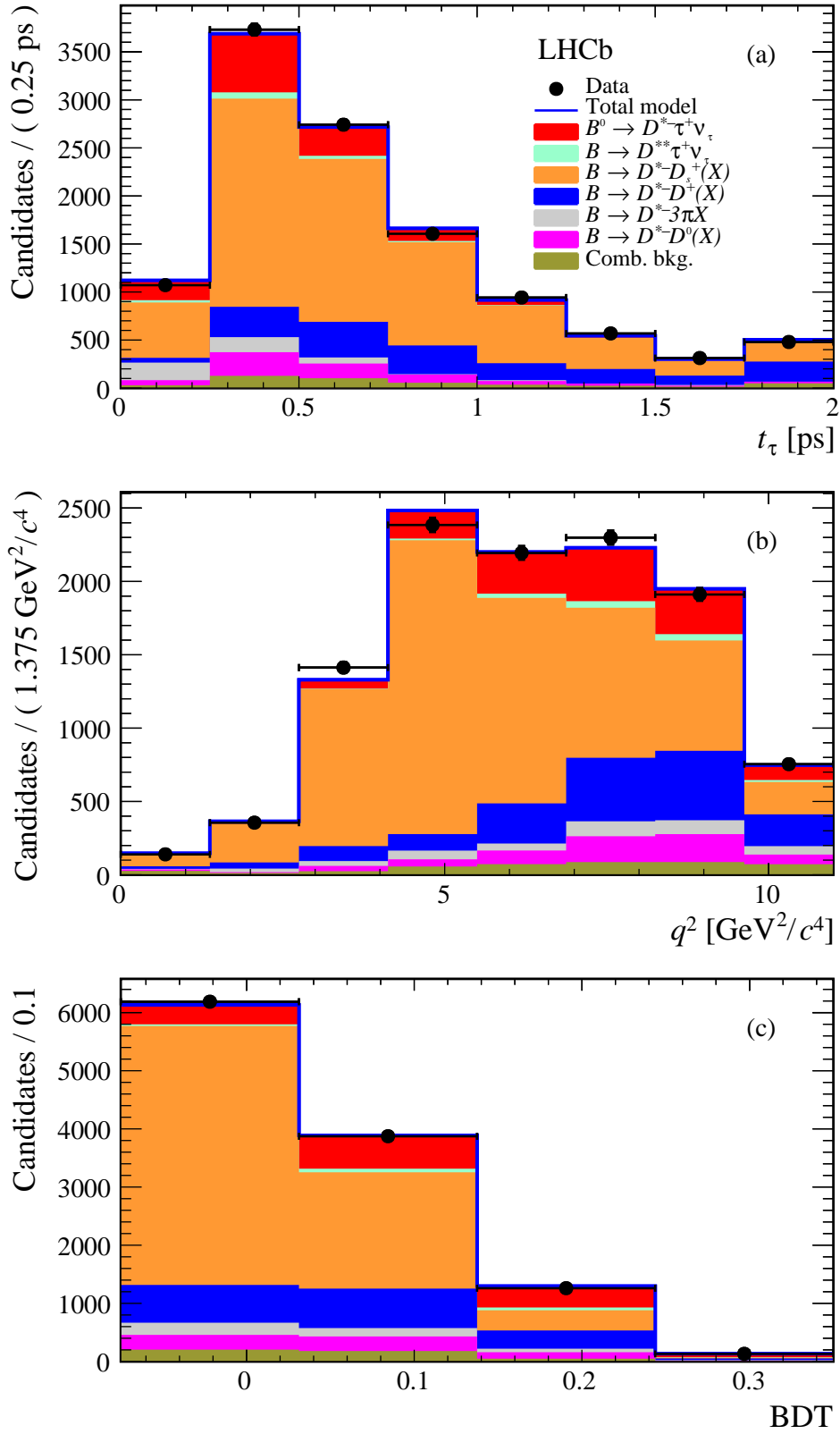


Figure 4.5 – Projections of the fit on the (a)  $\tau$  decay time, (b)  $q^2$  and (c) BDT output distributions. The fit components are described in the legend. Figures taken from Ref. [3].

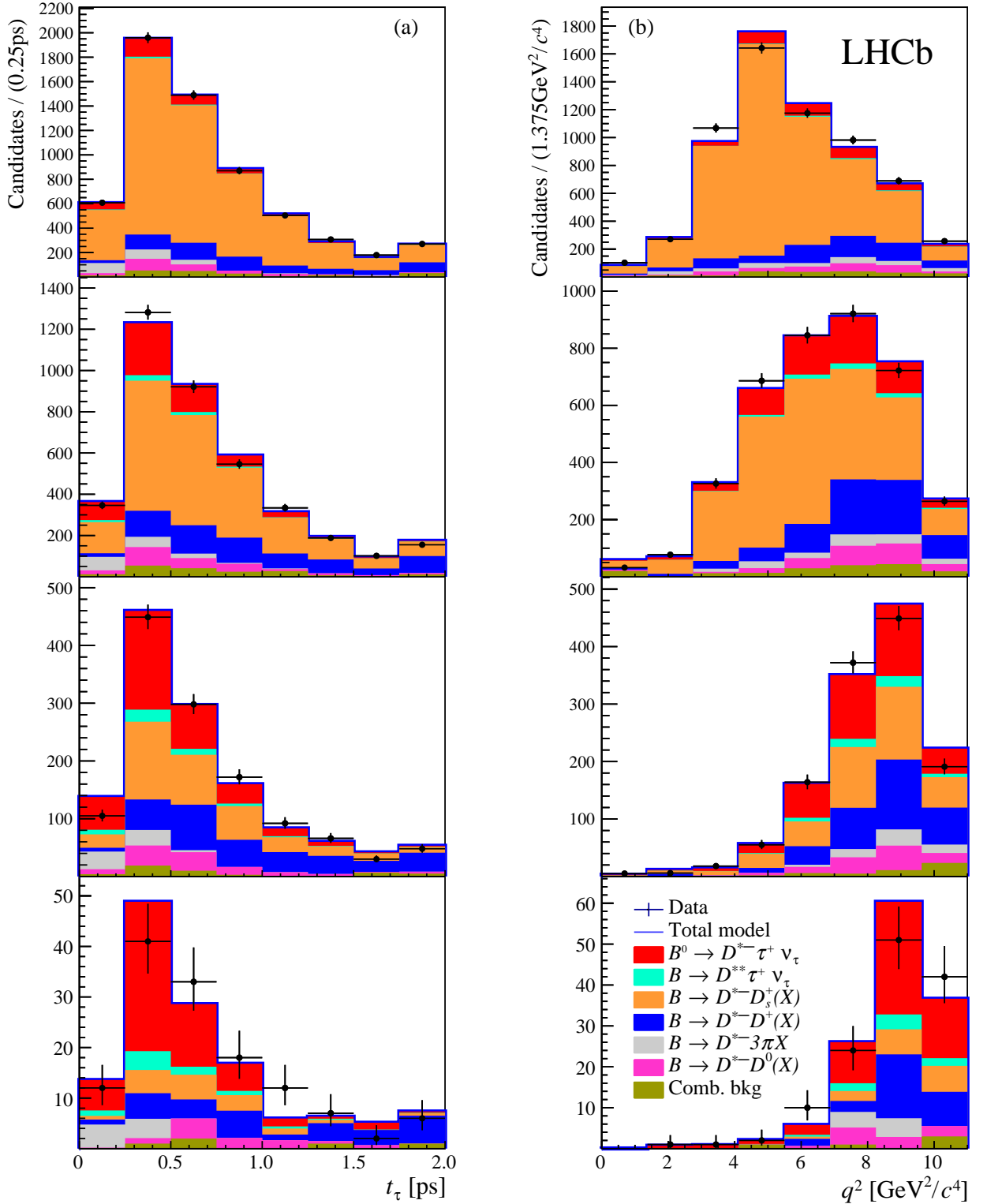


Figure 4.6 – Distributions of (a)  $t_\tau$  and (b)  $q^2$  in four different BDT bins, with increasing values of the BDT score from top to bottom. The fit components are described in the legend. Figures taken from Ref. [3].

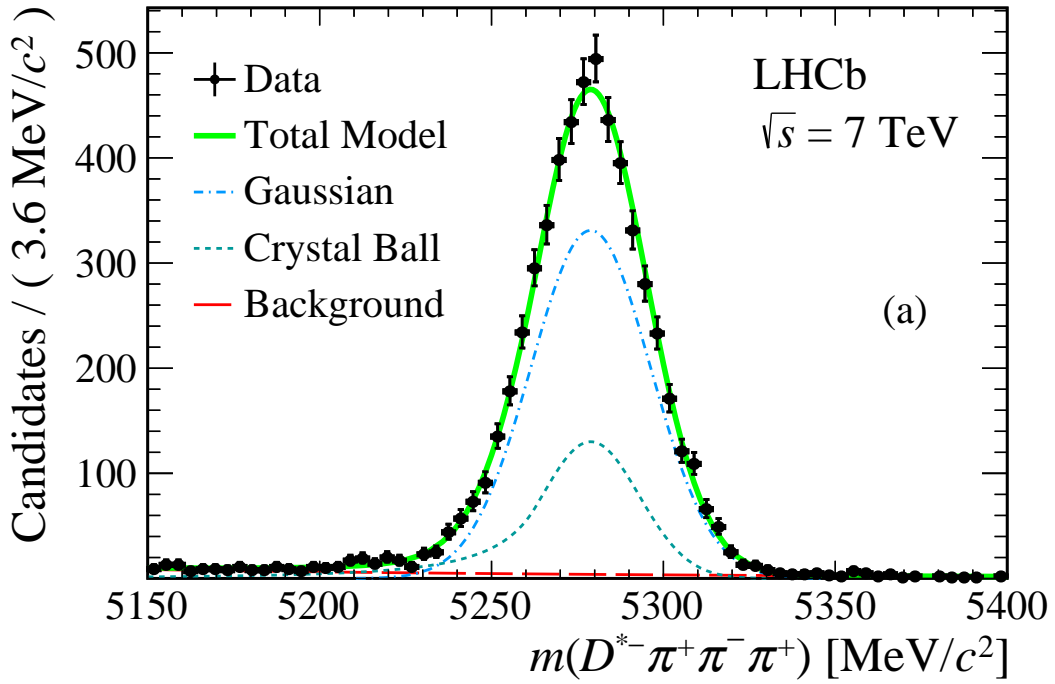
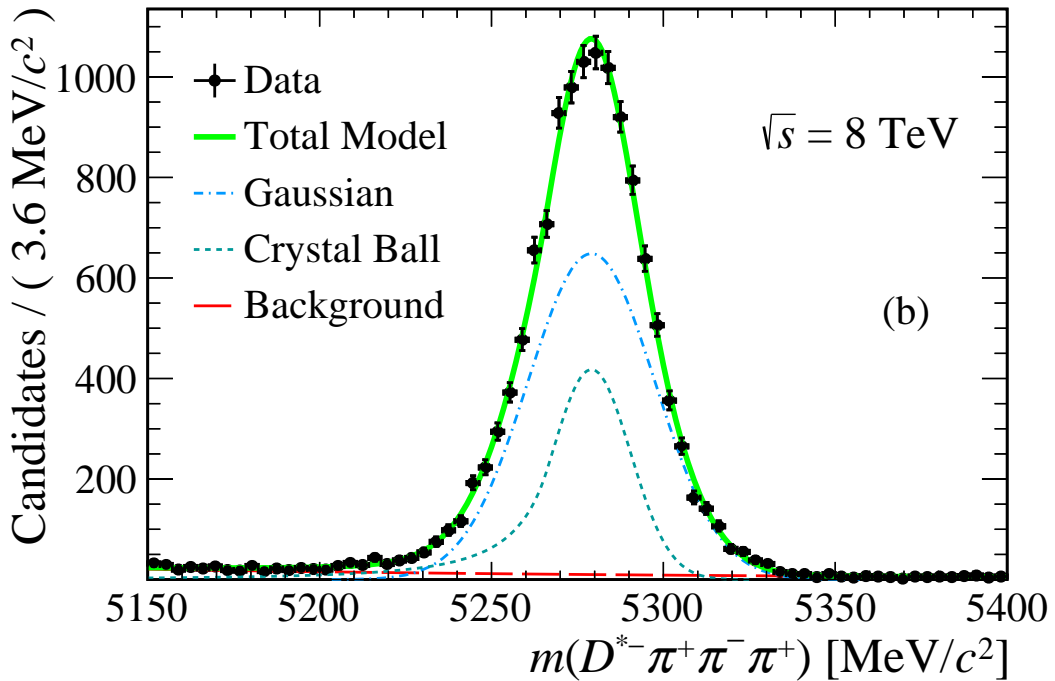
(a)  $\sqrt{s} = 7 \text{ TeV}$ , 2011 dataset(b)  $\sqrt{s} = 8 \text{ TeV}$ , 2012 dataset

Figure 4.7 – Fit to the  $m(D^{*-}3\pi)$  distribution after the full selection for both 2011 (a) and 2012 (b) data samples. Figures from Ref. [3].

Parameter	Fit result	Constraint
$N_{\text{sig}}$	$1296 \pm 86$	
$f_{\tau \rightarrow 3\pi\nu}$	0.78	0.78 (fixed)
$f_{D^{**}\tau\nu}$	0.11	0.11 (fixed)
$N_{D^0}^{\text{sv}}$	$445 \pm 22$	$445 \pm 22$
$f_{D^0}^{v_1 v_2}$	$0.41 \pm 0.22$	
$N_{D_s}$	$6835 \pm 166$	
$f_{D^+}$	$0.245 \pm 0.020$	
$N_{B \rightarrow D^* 3\pi X}$	$424 \pm 21$	$443 \pm 22$
$f_{D_s^+}$	$0.494 \pm 0.028$	$0.467 \pm 0.032$
$f_{D_{s0}^{*+}}$	$0_{-0.000}^{+0.010}$	$0_{-0.000}^{+0.042}$
$f_{D_{s1}^+}$	$0.384 \pm 0.044$	$0.444 \pm 0.064$
$f_{D_s^+ X}$	$0.836 \pm 0.077$	$0.647 \pm 0.107$
$f_{(D_s^+ X)_s}$	$0.159 \pm 0.034$	$0.138 \pm 0.040$
$N_{B_1 B_2}$	197	197 (fixed)
$N_{\text{not}D^*}$	243	243 (fixed)

Table 4.5 – Fit results for the three-dimensional fit. The constraints on the parameters  $f_{D_s^+}$ ,  $f_{D_{s0}^{*+}}$ ,  $f_{D_{s1}^+}$ ,  $f_{D_s^+ X}$  and  $f_{(D_s^+ X)_s}$  are applied taking into account their correlations. Table and results extracted from Ref. [3].

The  $3\pi$  mass distribution is shown in Figure 4.8 for candidates with  $M(D^{*-} 3\pi)$  between 5200 and 5350 MeV/ $c^2$ . The spectrum is dominated by the  $a_1(1260)^+$  resonance but a smaller peak due to a  $D_s^+ \rightarrow 3\pi$  component is clearly visible and needs to be subtracted.

To do so, a fit with the sum of a Gaussian function modelling the  $D_s^+$  mass peak, and an exponential describing the combinatorial background, is performed to extract this  $D_s^+$  contribution, which is estimated to be  $151 \pm 22$  candidates.

The normalisation yield for the Run1 dataset can be expressed as:

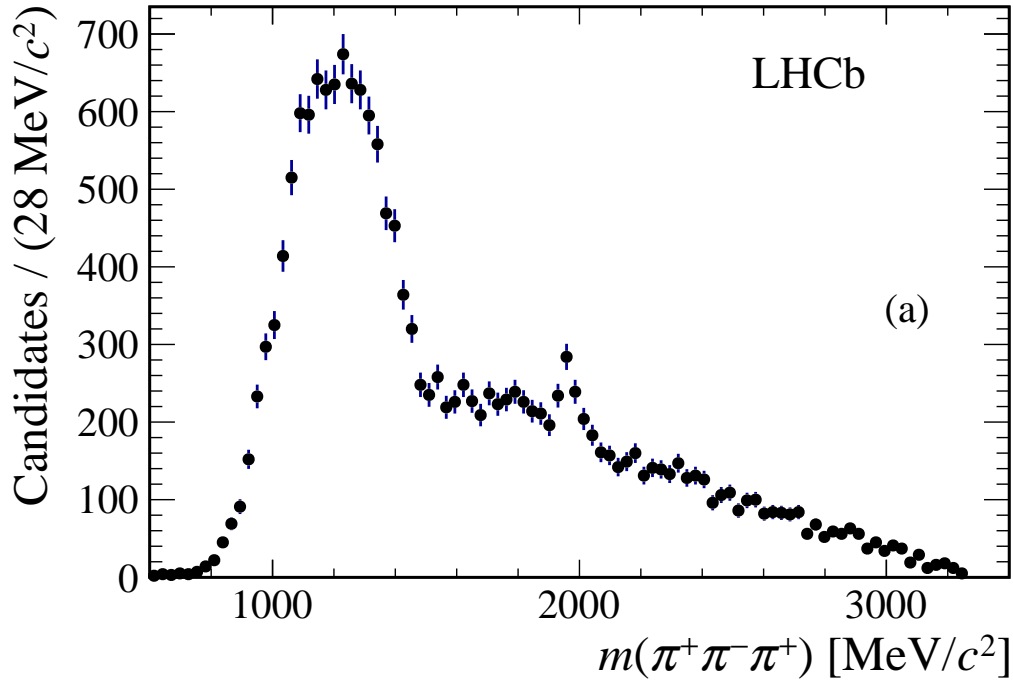
$$N_{\text{norm}} = 17\,660 \pm 143 \text{ (stat)} \pm 64 \text{ (syst)} \pm 22 \text{ (sub)}$$

where the third uncertainty is related to the subtraction of the  $B^0 \rightarrow D^{*-} D_s^+$  component.

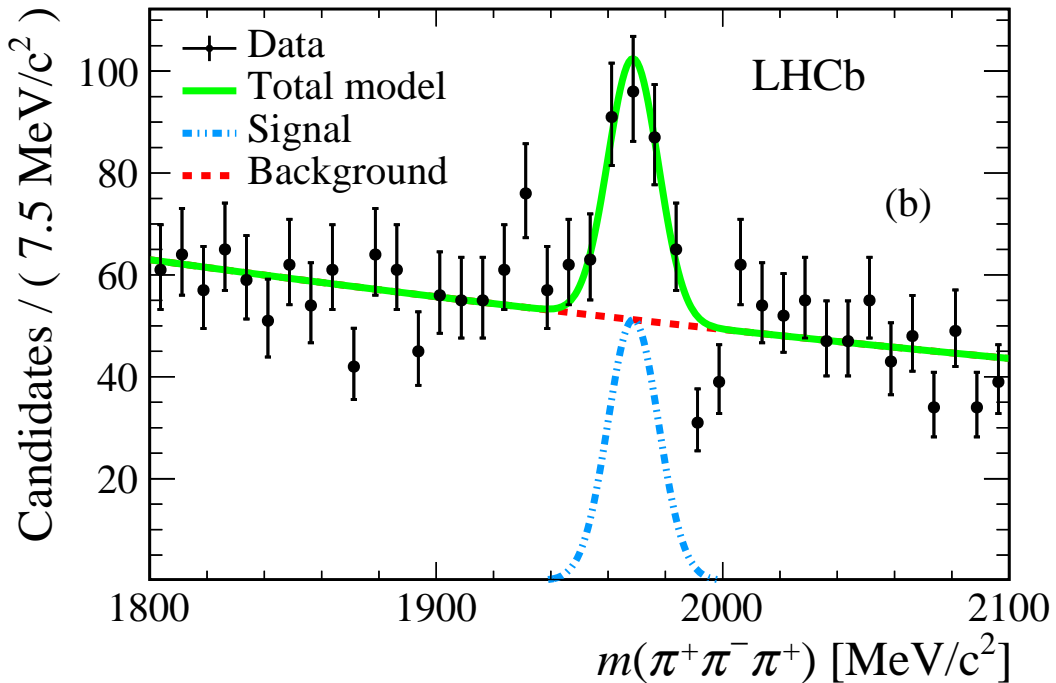
Finally, the extraction of  $\mathcal{K}(D^{*-})$  can be performed using Eq. 4.1 defined in Sec. 4.1. It is measured to be:

$$\mathcal{K}(D^{*-}) = 1.97 \pm 0.13 \text{ (stat)} \pm 0.18 \text{ (syst)}$$

The systematics uncertainties associated to its measurement are discussed in Sec. 4.5.



(a) Distribution of  $m(3\pi)$  after selection requiring  $m(D^{*-}3\pi)$  to be between 5200 and 5350  $\text{MeV}/c^2$ .



(b) Fit in the mass region around the  $D_s^+$ .

Figure 4.8 – Study of the  $3\pi$  mass for the extraction of the normalisation yield. Figures taken from [3].

## 4.5 Systematics

The detailed discussion on the systematic uncertainties associated to the measurement of  $\mathcal{R}(D^*)$  using the hadronic  $\tau$  reconstruction can be found in Ref [3, 102, 107]. Systematics can be divided in the following categories:

- the  $\tau$  decay model
- the modelling of the different components of the background
- potential biases in the fit used to extract the signal yield
- selection efficiencies, especially related to the trigger system
- particle identification efficiencies
- use of external branching fractions

The systematics related to the  $\tau$  decay model are discussed in Sec. 4.5.1 and a complete description of the assessment of the systematic uncertainty concerning the particle identification is shown in Sec. 4.5.2. Finally, a summary of the different systematic uncertainties is provided in Sec. 4.5.3.

### 4.5.1 $\tau$ decay model

The first uncertainty to consider concern the parameter  $f_{\tau \rightarrow 3\pi\nu_\tau}$ , the relative branching fraction of  $\tau \rightarrow 3\pi\nu_\tau$  with respect to the sum of the branching fractions of  $\tau \rightarrow 3\pi\nu_\tau$  and  $\tau \rightarrow 3\pi\pi^0\nu_\tau$ . The associated uncertainty to this ratio is at the level of 0.01 and a fit is performed using a Gaussian constraint of this ratio, evaluated to be  $0.78 \pm 0.01$ . Another fit is performed fixing the ratio to the value found by the previous fit. The quadratic difference of the uncertainties of the two fits on the signal yield is taken as the systematic uncertainty associated to the ratio  $f_{\tau \rightarrow 3\pi\nu_\tau}$ , measuring how precisely the signal composition is known. This results in a systematic uncertainty of 0.7%.

The  $B \rightarrow D^*$  form factors used to compute  $\mathcal{R}(D^*)$  and discussed in Chap. 2 have four free parameters extracted from data,  $R_1(1)$ ,  $R_2(1)$ ,  $\rho^2$  and  $R_0(1)$  as discussed in Ref. [49]. The parameters  $R_1(1)$ ,  $R_2(1)$ ,  $\rho^2$  are varied within their uncertainties taking into account their correlations and the parameter  $R_0(1)$  is assumed to be uncorrelated to the others and is also varied within its uncertainties. A total of 100 fits are performed and the standard deviation of the distribution of variation of the signal yield with respect to the one found in the nominal fit, measured to be 0.7% is taken as the associated systematic uncertainty.

The effect of the polarisation of the  $\tau$  was also studied for both  $\tau \rightarrow 3\pi\nu$  and  $\tau \rightarrow 3\pi\pi^0\nu$ . Studies on simulation samples found that due to dominant contribution of the  $a_1(1260)$  component, there is no correlation between the  $\tau$  polarisation and the mass of the  $3\pi$  in the  $3\pi$  channel and thus no systematic uncertainty is assigned. For the  $3\pi\pi^0$  channel, the systematic uncertainty is taken as the selection efficiency for the  $3\pi\pi^0$  channel multiplied by the ratio of the distributions of the angles describing the  $\tau$  polarisation produced

with the TAUOLA model, taking into account the polarisation in its modelling of the decay, with respect to a pure phase space model. This results in a 1.5% shift of the  $3\pi\pi^0$  efficiency which is scaled by the branching fraction of  $\tau \rightarrow 3\pi\pi^0$  to give a systematic uncertainty of 0.4%.

To take into account the contamination of other  $\tau$  hadronic decays in the result, a dedicated simulation producing inclusively hadronic  $\tau$  decay was used to study this effect. Only 1% of the events of this simulation sample involving other hadronic  $\tau$  decays than the two used in the analysis were able to pass the selection, which is taken as the related systematic uncertainty.

Finally, the feed-down coming from excited  $D^{**}\tau\nu_\tau$  decays is studied. The uncertainty on the fraction of  $D^{**}\tau\nu$  events ( $f_{D^{**}\tau\nu}$ ) is estimated to be 40% through the study of the upper limit of the number of  $D^{**}\tau\nu_\tau$  event passing the selection criteria which results in a systematic uncertainty of 2.3%. An additional 1.5% systematic uncertainty is assigned after the study of events coming from  $B_s^0 \rightarrow D_s^{**}(\rightarrow D^*K^0)\tau\nu_\tau$ .

The systematic uncertainties related to  $f_{\tau \rightarrow 3\pi\bar{\nu}_\tau}$ , the polarisation of the  $\tau$  and the contamination of other hadronic  $\tau$  decays do not depend on the particular decay  $B^0 \rightarrow D^{*-}\tau\bar{\nu}_\tau$  and will be therefore also assigned to the measurement of  $\mathcal{R}(\Lambda_c)$  presented in Chap. 5.

## 4.5.2 Particle identification

As the ratio of efficiencies of both signal and normalisation modes used to compute the final result is evaluated on simulation samples, a correction factor is required to take into account any disagreement on the PID efficiencies in data and simulation.

To do so, a data driven technique is used to estimate PID efficiencies for both signal ( $\tau \rightarrow 3\pi\nu_\tau$  and  $\tau \rightarrow 3\pi\pi^0\nu_\tau$ ) and normalisation modes. The ratio of these efficiencies will then be used to correct the result.

This data-driven technique relies on a calibration procedure which allows to select pure samples of  $K$  and  $\pi$  without using any PID selection, these samples will be referred as calibration samples. This is performed using the so-called `PIDCalib` package and the detailed procedure to select high-purity samples of a given type of particles through the use of the `sPlot` technique [108], is described in details in Ref. [109].

As PID efficiencies are affected by the occupancy of the detector and the kinematics of the event, a binning scheme has to be defined to map all the events in both calibration and simulation samples, in the following the number of hits in the SPD (`nSPDHits`), the pseudorapidity of the track ( $\eta$ ) and its momentum ( $p$ ) are used to construct the binning scheme.

To extract the data-driven efficiency of a particular PID cut for a simulation event, one simply needs to know to which bin belongs this simulation event and to take the ratio of the number of events of this bin for the calibration sample before and after applying the PID cut. In the following these data-driven efficiencies will be referred as weights as they will be used to reweight the ratio of PID efficiencies estimated on simulation samples.

The selection cuts to study with this method are as follows:

- $\text{ProbNN}_{\pi^i} > 0.6$  for the three pions coming from the  $\tau$  candidate,
- $\text{ProbNN}_{\pi^i} > 0.1$  for the pion coming from the  $D^*$ ,
- $\text{ProbNN}_k < 0.1$  for the pion coming from the  $\tau$  with charge opposite with respect to the other two.

For each pion, the binning scheme used in this study is as follows:

- 7 bins between 1.5 and 5 in  $\eta$
- 3 bins between 0 and 600 in nSPDHits
- in momentum, 3 bins are defined [1000, 5150, 9300, 15600] to match the momentum thresholds of the RICH detectors and 30 bins between 19000 and 100000  $\text{MeV}/c$

The use of nSPDHits as a binning variable to estimate the detector efficiency can be illustrated by the large decrease of PID efficiency in calibration data for the large nSPDHits bin, i.e. 400 to 600 hits, at high momenta, above 40  $\text{GeV}/c$  as shown in Figure 4.9.

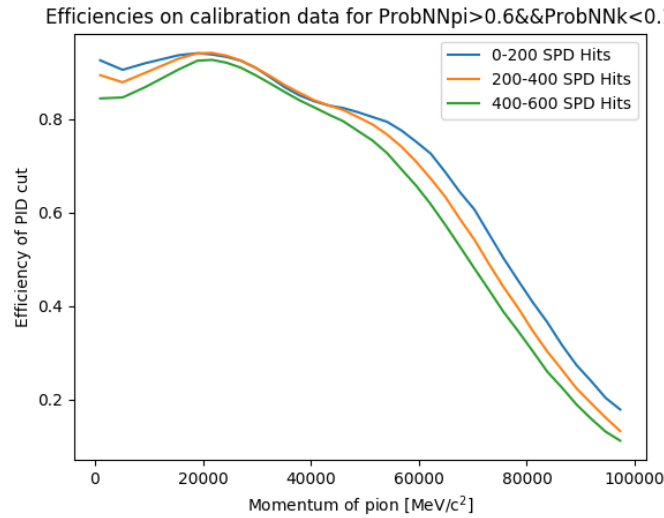
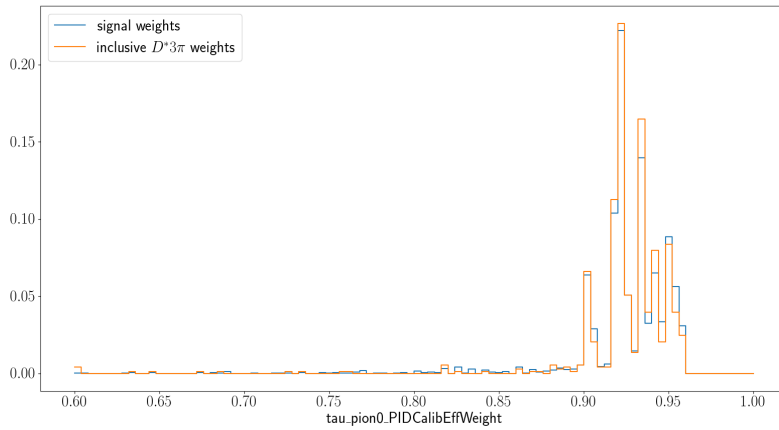


Figure 4.9 – Distribution of the PID efficiency as a function of pion momentum for 3 different nSPDHits bins.

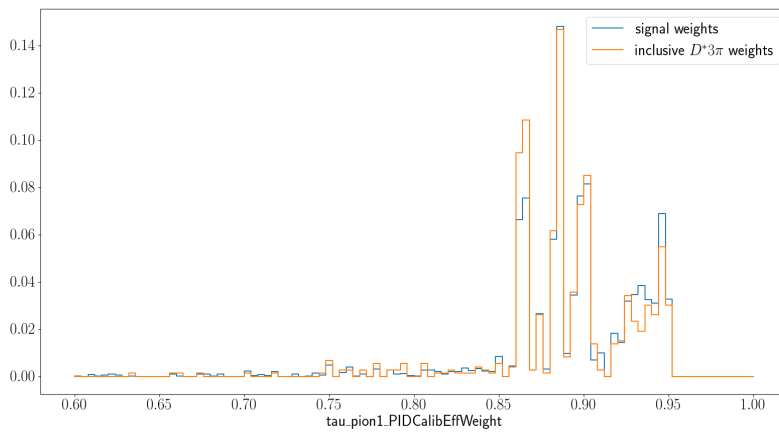
In addition, the nSPDHits distribution in the simulation samples is scaled by a factor 1.4 to reproduce the distribution measured in data.

The PID efficiency estimated on the calibration data samples for both one of the same charged pions and the opposite charged pion of the  $3\pi$  of the  $\tau$  can be seen in Fig. 4.10

In Fig. 4.11, the distributions of weights for both exclusive  $D^*3\pi$  and signal ( $3\pi$  component) simulation samples are shown, which is the product of the efficiencies computed for each of the pions of the event. The average of the two distribution give respectively the efficiency of the PID selection estimate on calibration data samples. As these two distributions are quite similar, the correcting ratio will be very close to 1.



(a)



(b)

Figure 4.10 – PID efficiency estimated on calibration data sample for both one of the same charged pions (a) and the opposite charged pion (b) are shown for both signal ( $3\pi$  component) in blue and  $D^*3\pi$  simulated samples for 2012 data taking conditions.

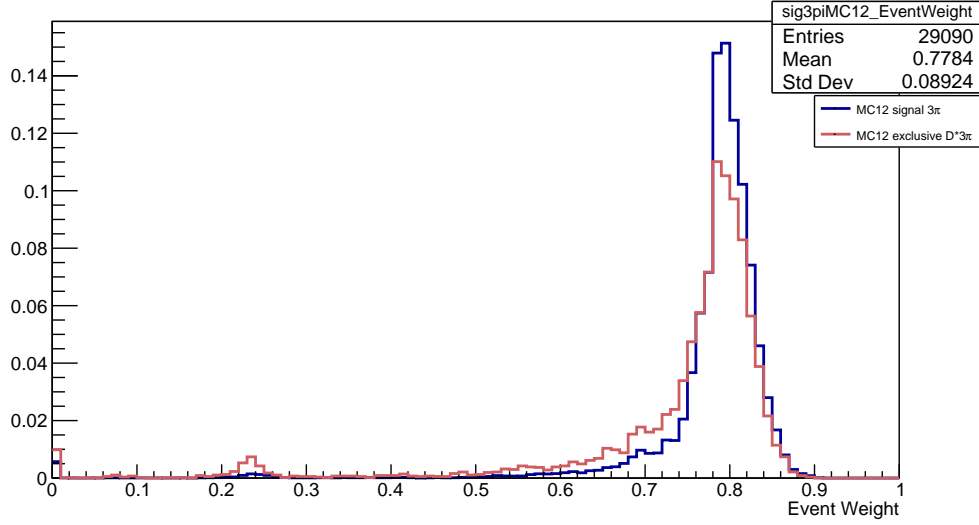


Figure 4.11 – Normalized distributions of the data-driven efficiencies for the PID selection for both exclusive  $D^*3\pi$  (red) and signal (blue) simulation samples for 2012 data taking conditions.

The correcting ratio can then be expressed as:

$$r_{PID} = \frac{\bar{w}_\tau}{\bar{w}_{D^*3\pi}} \quad (4.3)$$

where  $\bar{w}_X$  denotes the average of the PID efficiency distribution computed from calibration data samples for the  $X$  mode.

$\bar{w}_\tau$  is the weighted average of the two signal components by the product of their branching fraction and their efficiencies ( $\epsilon_{3\pi}$  and  $\epsilon_{3\pi\pi^0}$ ) and can then be described as:

$$\bar{w}_\tau = \frac{\bar{w}_{3\pi} \times \epsilon_{3\pi} \mathcal{B}(\tau \rightarrow 3\pi\nu) + \bar{w}_{3\pi\pi^0} \times \epsilon_{3\pi\pi^0} \mathcal{B}(\tau \rightarrow 3\pi\pi^0\nu)}{\epsilon_{3\pi} \mathcal{B}(\tau \rightarrow 3\pi\nu) + \epsilon_{3\pi\pi^0} \mathcal{B}(\tau \rightarrow 3\pi\pi^0\nu)} \quad (4.4)$$

To assess the systematic uncertainty coming from the choice of binning scheme in the reweighting procedure, the computation of  $r_{PID}$  is performed twice with respectively twice (fine binning) and half (coarse binning) the number of momentum bins with respect to the binning scheme describe above.

The systematic uncertainty is then taken as:

$$\sigma_{sys}(\bar{w}_X) = \frac{|\bar{w}_X^{fine} - \bar{w}_X^{nominal}| + |\bar{w}_X^{coarse} - \bar{w}_X^{nominal}|}{2}$$

The statistical uncertainty arises from the finite size of both the calibration sample and the simulation samples is also studied. The statistical uncertainty coming from the calibration sample size was found to be negligible and the uncertainty related to the simulation sample size was estimated using the standard deviation of the PID weight distribution.

A study was also made to assess the stability of the results with respect to the choice of nSPDHits binning scheme. Using twice the numbers of bins, a difference of  $r_{PID}$  of no more than 0.6%, which is taken as the uncertainty associated to the binning definition of nSPDHits.

This allow to compute  $r_{PID}$  for both 2011 and 2012 simulations samples and they were measured to be:

$$r_{PID}^{2011} = 1.0201 \pm 0.0073$$

and

$$r_{PID}^{2012} = 1.0606 \pm 0.0073$$

$r_{PID}$  is then defined as the weighted average of the two ratios for both 2011 and 2012 samples in the 1:2 ratio to reflect the relative sizes of the two datasets collected:

$$r_{PID} = 1.0475 \pm 0.0054$$

$r_{PID}$  was used to compute  $\mathcal{K}(D^{*-})$  and its associated systematic uncertainty was found to be 1.3%.

### 4.5.3 Summary of systematic uncertainties

Table 4.6 summarizes the systematic uncertainties on the measurement of the ratio  $\mathcal{B}(B^0 \rightarrow D^{*-}\tau^+\nu_\tau)/\mathcal{B}(B^0 \rightarrow D^{*-}3\pi)$ . The total uncertainty is 9.1%. For  $\mathcal{R}(D^{*-})$ , a 4.5% systematic uncertainty due to the knowledge of the external branching fractions is added.

## 4.6 $\mathcal{R}(D^*)$ result

To conclude,  $\mathcal{K}(D^{*-})$ , the ratio of branching fractions between  $B^0 \rightarrow D^{*-}\tau^+\nu_\tau$  and  $B^0 \rightarrow D^{*-}3\pi$  decays modes is measured to be

$$\mathcal{K}(D^{*-}) = 1.97 \pm 0.13 \text{ (stat)} \pm 0.18 \text{ (syst)},$$

where the first uncertainty is statistical and the second systematic.

Using the branching fraction  $\mathcal{B}(B^0 \rightarrow D^{*-}3\pi) = (7.214 \pm 0.28) \times 10^{-3}$  from the weighted average of the measurements presented in Ref. [4, 5, 6], a value of the branching fraction of  $B^0 \rightarrow D^{*-}\tau^+\nu_\tau$  is obtained

$$\mathcal{B}(B^0 \rightarrow D^{*-}\tau^+\nu_\tau) = (1.42 \pm 0.094 \text{ (stat)} \pm 0.129 \text{ (syst)} \pm 0.054) \times 10^{-2},$$

where the third uncertainty denotes the current uncertainty on the external branching fraction of  $B^0 \rightarrow D^{*-}3\pi$ . The precision of this measurement is comparable to that of the current world average of Ref. [110].

Contribution	Value in %
$\mathcal{B}(\tau^+ \rightarrow 3\pi\bar{\nu}_\tau)/\mathcal{B}(\tau^+ \rightarrow 3\pi(\pi^0)\bar{\nu}_\tau)$	0.7
Form factors (template shapes)	0.7
Form factors (efficiency)	1.0
$\tau$ polarization effects	0.4
Other $\tau$ decays	1.0
$B \rightarrow D^{**}\tau^+\nu_\tau$	2.3
$B_s^0 \rightarrow D_s^{**}\tau^+\nu_\tau$ feed-down	1.5
$D_s^+ \rightarrow 3\pi X$ decay model	2.5
$D_s^+$ , $D^0$ and $D^+$ template shape	2.9
$B \rightarrow D^{*-}D_s^+(X)$ and $B \rightarrow D^{*-}D^0(X)$ decay model	2.6
$D^{*-}3\pi X$ from $B$ decays	2.8
Combinatorial background (shape + normalization)	0.7
Bias due to empty bins in templates	1.3
Size of simulation samples	4.1
Trigger acceptance	1.2
Trigger efficiency	1.0
Online selection	2.0
Offline selection	2.0
Charged-isolation algorithm	1.0
Particle identification	1.3
Normalization channel	1.0
Signal efficiencies (size of simulation samples)	1.7
Normalization channel efficiency (size of simulation samples)	1.6
Normalization channel efficiency (modelling of $B^0 \rightarrow D^{*-}3\pi$ )	2.0
Total uncertainty	9.1

Table 4.6 – List of the individual systematic uncertainties for the measurement of the ratio  $\mathcal{B}(B^0 \rightarrow D^{*-}\tau^+\nu_\tau)/\mathcal{B}(B^0 \rightarrow D^{*-}3\pi)$ . Table extracted from Ref. [3].

The first measurement of  $\mathcal{R}(D^{*-})$  using three-pions of the  $\tau$  is finally obtained using the branching fraction of  $\mathcal{B}(B^0 \rightarrow D^{*-}\mu^+\nu_\mu) = (4.88 \pm 0.10) \times 10^{-2}$  from Ref. [7].

$$\mathcal{R}(D^{*-}) = 0.291 \pm 0.019 (\text{stat}) \pm 0.026 (\text{syst}) \pm 0.013 (\text{ext})$$

The result is in agreement with the SM expectation from Ref. [110] within  $0.95\sigma$  and consistent with previous measurements. It can be noted that the statistical uncertainty associated with this measurement is one of the smallest of the various  $\mathcal{R}(D^*)$  measurements and even if its value is found to be between the SM prediction and the World Average value, due to its precision, the disagreement of the new World Average value of  $\mathcal{R}(D^*)$  taking into account this measurement, shown in Fig. 4.12, is slightly enforced.

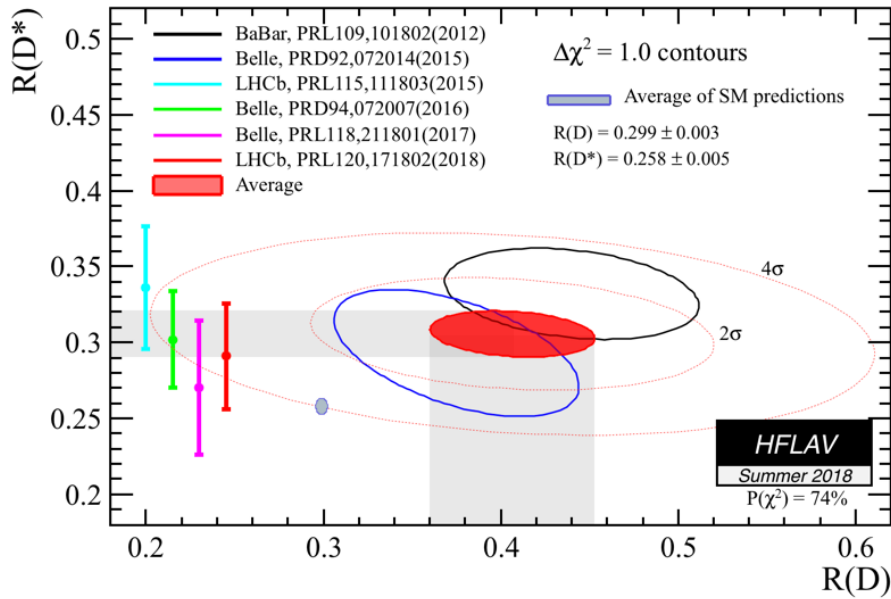


Figure 4.12 – Current status of the combination of both  $\mathcal{R}(D)$  and  $\mathcal{R}(D^*)$  measurements. Figure taken from Ref. [1].

An average of the LHCb measurements can also be performed using the  $\mathcal{R}(D^*)$  result of the analysis using the muonic decay of the  $\tau$  described in Ref. [67] and taking into account small correlations for  $B \rightarrow D^*$  form factors,  $\tau$  polarisation effects and  $D^{**}\tau\nu_\tau$  feed-down, the value is found to be:

$$\mathcal{R}(D^{*-}) = 0.310 \pm 0.0155 (\text{stat}) \pm 0.0219 (\text{syst})$$

where the statistical weight of the presented measurement is approximately 1.5 the weight of the measurement with the muonic decay of the  $\tau$ .

The use of the  $\tau$  reconstruction through the use of its decay into three charged pions can be used to study other semitauonic decays. The  $\mathcal{R}(\Lambda_c)$  analysis using the same strategy is thus presented in Chap. 5.



# Measurements of $\mathcal{B}(\Lambda_b^0 \rightarrow \Lambda_c^+ \tau \bar{\nu}_\tau)$ and $\mathcal{R}(\Lambda_c^+)$

## Contents

---

<b>5.1</b>	<b>Analysis method . . . . .</b>	<b>109</b>
5.1.1	Definition of the measurement . . . . .	109
5.1.2	Possible normalisation procedures . . . . .	110
5.1.3	Background channels classification . . . . .	112
5.1.4	Determination of the signal yield . . . . .	114
<b>5.2</b>	<b>Data and simulation samples . . . . .</b>	<b>114</b>
5.2.1	Data samples . . . . .	114
5.2.2	Simulation samples . . . . .	114
<b>5.3</b>	<b>Selection of the events . . . . .</b>	<b>115</b>
5.3.1	Online selection . . . . .	116
5.3.2	Offline preselection . . . . .	116
5.3.3	Event topology . . . . .	119
5.3.4	Additional cuts . . . . .	120
5.3.5	Selection of the normalisation events . . . . .	126
5.3.6	$\Lambda_c^+$ background removed using sideband subtraction . . . . .	126
5.3.7	$\Lambda_c^*$ feed-down . . . . .	129
<b>5.4</b>	<b>Isolation tools . . . . .</b>	<b>130</b>
5.4.1	Charged particles isolation using a BDT . . . . .	131
5.4.2	Neutrals isolation . . . . .	135
<b>5.5</b>	<b>Reconstruction techniques . . . . .</b>	<b>139</b>
5.5.1	Reconstructing $\Lambda_b^0 \rightarrow \Lambda_c^+ \tau^- \bar{\nu}_\tau$ events . . . . .	139
5.5.2	Signal reconstruction results using simulation samples . . . . .	140

5.5.3	Partial reconstruction of $\Lambda_b^0 \rightarrow \Lambda_c^+ D_s^-$ events . . . . .	141
<b>5.6</b>	<b>Estimation of the efficiencies</b> . . . . .	<b>149</b>
5.6.1	Trigger efficiencies . . . . .	149
5.6.2	Stripping efficiencies . . . . .	154
5.6.3	Selection efficiencies . . . . .	156
<b>5.7</b>	<b>Description and performances of the BDT</b> . . . . .	<b>157</b>
5.7.1	Introduction on Boosted Decision Trees for event classification	157
5.7.2	Definition of a Boosted Decision Tree algorithm . . . . .	158
5.7.3	Description of the BDT . . . . .	158
5.7.4	Validation of the BDT . . . . .	165
<b>5.8</b>	<b>Determination of the normalisation yield</b> . . . . .	<b>168</b>
5.8.1	Normalisation using the $\Lambda_b^0 \rightarrow \Lambda_c^+ \pi^- \pi^+ \pi^-$ exclusive peak . . .	168
<b>5.9</b>	<b>Double-charm backgrounds</b> . . . . .	<b>175</b>
5.9.1	Determination of the $\Lambda_b^0 \rightarrow \Lambda_c^+ D_s^- X$ background composition on data . . . . .	175
5.9.2	Data-driven control samples . . . . .	177
<b>5.10</b>	<b>Extraction of the signal yield</b> . . . . .	<b>182</b>
5.10.1	The fit model . . . . .	182
5.10.2	Computation of the constrained parameters of the fit . . . . .	183
5.10.3	Fit results . . . . .	186
5.10.4	Evidence of the observation of $\Lambda_b^0 \rightarrow \Lambda_c^+ \tau \nu_\tau$ decay . . . . .	188
<b>5.11</b>	<b>Systematics</b> . . . . .	<b>189</b>
5.11.1	$\tau$ decay model . . . . .	189
5.11.2	Systematics related to the fitting procedure . . . . .	189
5.11.3	Efficiencies, selection and trigger . . . . .	192
5.11.4	Normalisation channel . . . . .	192
5.11.5	$\Lambda_c^*$ feed-down . . . . .	193
5.11.6	Simulation statistics . . . . .	193
5.11.7	Systematics uncertainties summary . . . . .	193
<b>5.12</b>	<b>Results</b> . . . . .	<b>194</b>
5.12.1	Results regarding $\mathcal{R}(\Lambda_c)$ . . . . .	194
5.12.2	Observation of the decay $\Lambda_b^0 \rightarrow \Lambda_c^+ \tau^- \bar{\nu}_\tau$ . . . . .	194
5.12.3	Prospects . . . . .	194

---

This chapter describes the measurement of the branching fraction of the decay  $\Lambda_b^0 \rightarrow \Lambda_c^+ \tau^- \bar{\nu}_\tau$  and the strategy to compute  $\mathcal{R}(\Lambda_c)$ .

## 5.1 Analysis method

### 5.1.1 Definition of the measurement

The aim of this analysis is to measure both the branching fraction of the decay  $\Lambda_b^0 \rightarrow \Lambda_c^+ \tau^- \bar{\nu}_\tau$  and the ratio  $\mathcal{R}(\Lambda_c)$  defined as:

$$\mathcal{R}(\Lambda_c^+) = \frac{\mathcal{B}(\Lambda_b^0 \rightarrow \Lambda_c^+ \tau^- \bar{\nu}_\tau)}{\mathcal{B}(\Lambda_b^0 \rightarrow \Lambda_c^+ \mu^- \bar{\nu}_\mu)} \quad (5.1)$$

As the  $\tau$  is considered in its decay into three pions, it is much easier to control the systematics by performing the measurement of:

$$\mathcal{K}(\Lambda_c^+) = \frac{\mathcal{B}(\Lambda_b^0 \rightarrow \Lambda_c^+ \tau^- \bar{\nu}_\tau, \tau^- \rightarrow 3\pi\nu_\tau)}{\mathcal{B}(\Lambda_b^0 \rightarrow \Lambda_c^+ \pi^- \pi^+ \pi^-)} \quad (5.2)$$

where the numerator is the branching fraction of the decay of interest and the denominator is the normalisation channel, which shares the same final state with the signal and is linked to the initial dominant background of the analysis, i.e.  $\Lambda_b^0 \rightarrow \Lambda_c^+ 3\pi X$ .

The ratio in Eq. 5.2 can be expressed as:

$$\mathcal{K}(\Lambda_c^+) = \frac{\mathcal{B}(\Lambda_b^0 \rightarrow \Lambda_c^+ \tau^- \bar{\nu}_\tau)}{\mathcal{B}(\Lambda_b^0 \rightarrow \Lambda_c^+ \pi^- \pi^+ \pi^-)} = \frac{N_{sig}}{N_{norm}} \times \frac{\epsilon_{norm}}{\epsilon_{sig}} \times \frac{1}{\mathcal{B}(\tau^- \rightarrow \pi^- \pi^+ \pi^- (\pi^0)\nu_\tau)} \quad (5.3)$$

where  $N_{sig}$ ,  $\epsilon_{sig}$  and  $N_{norm}$ ,  $\epsilon_{norm}$  are respectively the number of reconstructed events and the selection efficiency of signal<sup>1</sup> and normalisation.  $N_{sig}$  is the result of the fit discussed in Sec. 5.10 and  $N_{norm}$  is measured using a dedicated fit on the exclusive peak of  $\Lambda_b^0 \rightarrow \Lambda_c^+ \pi^- \pi^+ \pi^-$ . Efficiencies  $\epsilon_{sig}$  and  $\epsilon_{norm}$  are evaluated on Monte-Carlo samples. As the  $\tau$  is reconstructed using either  $\tau^- \rightarrow \pi^- \pi^+ \pi^- \nu_\tau$  or  $\tau^- \rightarrow \pi^- \pi^+ \pi^- \pi^0 \nu_\tau$ ,  $\mathcal{B}(\tau^- \rightarrow \pi^- \pi^+ \pi^- (\pi^0)\nu_\tau)$  denotes the sum of the branching fractions of these two modes.

The decay chain for the signal is chosen as:

$$\begin{aligned} \Lambda_b^0 &\rightarrow \Lambda_c^+ \tau^- \bar{\nu}_\tau \\ &\hookrightarrow \pi^- \pi^+ \pi^- (\pi^0)\nu_\tau \\ &\hookrightarrow pK^- \pi^+ \end{aligned} \quad (5.4)$$

Due to the presence of neutrinos in the signal decay chain and the non-reconstructed  $\pi^0$  when present, the visible final state is only composed of a  $\Lambda_c^+$  and three charged pions. Through a fit of the three pions tracks, the  $\tau$  vertex is reconstructed and even though two neutrinos are present,  $E_\tau$  and  $E_{\Lambda_b^0}$  can be reconstructed thanks to the constraints

<sup>1</sup> $\epsilon_{sig}$  is the weighted average of the efficiencies of the two decay modes of the  $\tau$ ,  $\tau \rightarrow 3\pi\nu_\tau$  and  $\tau \rightarrow 3\pi\pi^0\nu_\tau$ .

given by the lines of flight of the  $\Lambda_c^+$  and the 3 pions. A method to reconstruct signal events is studied in Sec. 5.5, which also allows to reconstruct the  $\Lambda_b^0$  momentum.

The  $\Lambda_c^+$  is reconstructed through a fit to the tracks of the proton, kaon and pion.

In the following, the following naming conventions will then be used:

- signal mode: is referring to the decay  $\Lambda_b^0 \rightarrow \Lambda_c^+ \tau^- \bar{\nu}_\tau$  with the  $\tau$  decaying into three pions and the neutrinos with or without an additional  $\pi^0$ .
- normalisation mode: is stated as the decay  $\Lambda_b^0 \rightarrow \Lambda_c^+ \pi^- \pi^+ \pi^-$  where contributions of the type  $\Lambda_b^0 \rightarrow \Lambda_c^{*+} \pi^-$  or  $\Lambda_b^0 \rightarrow \Sigma_c^{(*)} \pi \pi$  are not taken into account due to their kinematics too far from the signal one.  $\Lambda_c^+ 3\pi$  normalisation events are thus mainly  $\Lambda_c^+ a_1(1260)^-$ .
- $3\pi$ : will always refer to the three charged pions system.

### 5.1.2 Possible normalisation procedures

After extracting  $\mathcal{K}(\Lambda_c)$ , the computation of  $\mathcal{B}(\Lambda_b^0 \rightarrow \Lambda_c^+ \tau^- \bar{\nu}_\tau)$  can be computed using the PDG value of  $\mathcal{B}(\Lambda_b^0 \rightarrow \Lambda_c^+ \pi^- \pi^+ \pi^-) = 0.77 \pm 0.11\%$  [7] as follows:

$$\mathcal{B}(\Lambda_b^0 \rightarrow \Lambda_c^+ \tau^- \bar{\nu}_\tau) = \mathcal{K}(\Lambda_c) \times \mathcal{B}(\Lambda_b^0 \rightarrow \Lambda_c^+ \pi^- \pi^+ \pi^-) \quad (5.5)$$

The computation of  $\mathcal{R}(\Lambda_c)$  is not as straightforward and several ways can be studied to do so:

**direct normalisation** : using directly the values of both  $\mathcal{B}(\Lambda_b^0 \rightarrow \Lambda_c^+ \pi^- \pi^+ \pi^-)$  and  $\mathcal{B}(\Lambda_b^0 \rightarrow \Lambda_c^+ \mu^- \bar{\nu}_\mu)$  from PDG,  $\mathcal{R}(\Lambda_c)$  is simply:

$$\mathcal{R}(\Lambda_c) = \mathcal{K}(\Lambda_c) \times \frac{\mathcal{B}(\Lambda_b^0 \rightarrow \Lambda_c^+ \pi^- \pi^+ \pi^-)}{\mathcal{B}(\Lambda_b^0 \rightarrow \Lambda_c^+ \mu^- \bar{\nu}_\mu)} \quad (5.6)$$

The downside of this method is the size of its uncertainty contributing to the total uncertainty of  $\mathcal{R}(\Lambda_c)$ ,  $\sim 27\%$ .

**normalisation using trigger efficiencies** The main problem of the method above is based on the use of two external measurements and each measurement uncertainty carries contribution coming from the production fraction of  $\Lambda_b^0$  baryons,  $f_{\Lambda_b^0}$ , and  $\mathcal{B}(\Lambda_c^+ \rightarrow p K^- \pi^+)$ . The following is a method using only data taken by the LHCb detector to overcome this limitation:

$$\mathcal{R}(\Lambda_c) = \mathcal{K}(\Lambda_c) \times \frac{N_{obs}(\Lambda_b^0 \rightarrow \Lambda_c^+ \pi^- \pi^+ \pi^-)}{N_{obs}(\Lambda_b^0 \rightarrow \Lambda_c^+ \mu^- \bar{\nu}_\mu)} \times \frac{\epsilon_{\Lambda_c^+ \mu^- \bar{\nu}_\mu}}{\epsilon_{\Lambda_c^+ 3\pi}} \quad (5.7)$$

In this case, efficiencies, especially trigger ones, have to be precisely determined using MC samples. Typically, one can expect a contribution coming from normalisation to the total uncertainty at the level of roughly 15%.

**normalisation using theoretical partial widths** : The goal of this method is to benefit from the precise measurement of  $\mathcal{B}(B^0 \rightarrow D^{*-}\pi^+\pi^-\pi^+)$ , the computation of  $\mathcal{R}(\Lambda_c)$  is then rewritten as:

$$\mathcal{R}(\Lambda_c) = \mathcal{K}(\Lambda_c) \times \mathcal{N}_1 \times \mathcal{N}_2 \times \mathcal{N}_3 \quad (5.8)$$

The  $\mathcal{N}_i$  factors are defined as follows:

$$\mathcal{N}_1 = \frac{\mathcal{B}(\Lambda_b^0 \rightarrow \Lambda_c^+ \pi^- \pi^+ \pi^-)}{\mathcal{B}(B^0 \rightarrow D^{*-} \pi^+ \pi^- \pi^+)} \quad (5.9)$$

$$\mathcal{N}_2 = \frac{\mathcal{B}(B^0 \rightarrow D^{*-} \pi^+ \pi^- \pi^+)}{\mathcal{B}(B^0 \rightarrow D^- \mu^+ \nu_\mu)} \quad (5.10)$$

$$\mathcal{N}_3 = \frac{\tau_{B^0}}{\tau_{\Lambda_b^0}} \times \frac{\Gamma(B^0 \rightarrow D^- \mu^+ \nu_\mu)}{\Gamma(\Lambda_b^0 \rightarrow \Lambda_c^+ \mu^- \bar{\nu}_\mu)} \quad (5.11)$$

$\mathcal{N}_1$  can be rewritten as

$$\mathcal{N}_1 = \frac{N_{obs}(\Lambda_b^0 \rightarrow \Lambda_c^+ \pi^- \pi^+ \pi^-)}{N_{obs}(B^0 \rightarrow D^{*-} \pi^+ \pi^- \pi^+)} \times \frac{\epsilon_{D^{*-}3\pi}}{\epsilon_{\Lambda_c^+3\pi}} \times \frac{f_d}{f_{\Lambda_b^0}} \times \frac{\mathcal{B}(D^{*+} \rightarrow K^- \pi^+ \pi^+)}{\mathcal{B}(\Lambda_c^+ \rightarrow p \pi^+ K^-)} \quad (5.12)$$

$\mathcal{N}_1$  can be estimated directly within LHCb with a good statistical uncertainty, up to a few percent thanks to the large samples of both  $\Lambda_b^0 \rightarrow \Lambda_c^+ \pi^- \pi^+ \pi^-$  and  $B^0 \rightarrow D^{*-} \pi^+ \pi^- \pi^+$  events. The ratio of beauty baryon and meson production fractions,  $f_{\Lambda_b^0}/f_d$  is taken from the combined usage of papers Ref. [111] and Ref. [112]. It has to be noted that the branching ratio  $\mathcal{B}(\Lambda_c^+ \rightarrow p K \pi)$  cancels in this ratio as it is used in the latter paper to compute the ratio of production fractions. The study of the efficiency of both  $\Lambda_b^0 \rightarrow \Lambda_c^+ 3\pi$  and  $B^0 \rightarrow D^{*-} 3\pi$  as a function of  $p_T$  is still required as the ratio of production fractions has a strong dependence over  $p_T$  as shown in Fig. 5.1

As  $\mathcal{N}_2$  is the ratio of two precisely measured branching fractions, it can be computed using directly the PDG values, with a uncertainty at the level of 5%. Finally, to get  $\mathcal{N}_3$ , one needs the ratio of partial widths computed using Lattice QCD, which can be estimated up to 9% uncertainty.

Using Lattice computations ([2], [60] and [113]) and measurements from both BaBar [57] and Belle [58] to extract the  $B \rightarrow D$  form factors, the ratio of partial decay widths is expected to be:

$$\frac{\Gamma(\Lambda_b^0 \rightarrow \Lambda_c^+ \mu^- \bar{\nu}_\mu)}{\Gamma(B^0 \rightarrow D^- \mu^+ \nu_\mu)} = 2.37 \pm 0.16$$

which leads to a total uncertainty coming from this normalisation procedure of 10-12%.

The current strategy is to rely on both direct normalisation and the inputs of Lattice QCD to use the ratio of partial widths to measure  $\mathcal{R}(\Lambda_c)$ .

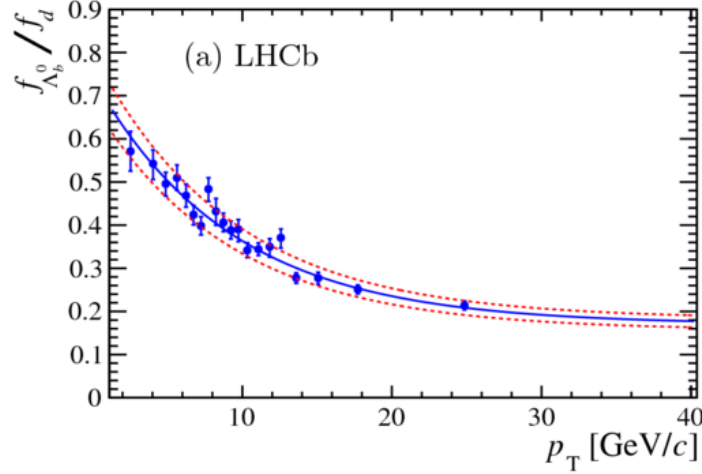


Figure 5.1 – Dependence of the ratio of production fraction  $f_{\Lambda_b^0}/f_d$  on the  $p_T$  of the  $b$ -hadron. Figure extracted from Ref. [111].

### 5.1.3 Background channels classification

Tab. 5.1 presents the different channels sharing the same final state as the signal with their expected branching fraction as most of the branching fraction of  $\Lambda_b^0$  to double charm hadrons are not yet measured. The estimation is based on comparisons with  $B^0$  decays.

At first, the background coming from  $\Lambda_b^0 \rightarrow \Lambda_c^+ 3\pi X$  completely dominates the signal. Fortunately thanks to the combination of the high boost of the  $b$  hadrons and the excellent performances of the VELO in terms of spatial resolution, the event topology, which can be defined as the relative positions of the different vertices in the event, can be precisely known. All secondary vertices, such as the  $\Lambda_c^+$  one or the reconstructed vertex of the three pions, will be downstream of the PV but their relative positions is an important information and a cut based on this information can be build to remove this background. This cut is referred in the following as an event topology cut and is studied in more depth in Sec. 5.3.

This cut on the event topology requires the  $3\pi$  vertex to be downstream with respect to the  $\Lambda_c^+$  one with a significance of at least  $5\sigma$  along the  $z$ -axis to forbid these three pions to come directly from the  $\Lambda_b^0$  vertex. This method is able to keep a good signal efficiency, reduces almost completely the  $\Lambda_b^0 \rightarrow \Lambda_c^+ 3\pi X$  background and can also be reversed to study its effect on normalisation events. The event selection is further refined with a set of cuts described in Sec. 5.3.

Events with the required topology are decay products of a particle with a lifetime long enough to create a secondary vertex displaced from the  $\Lambda_b^0$  one. Along with signal events where the pions come from the  $\tau^-$  lepton, background arises from  $\Lambda_b^0 \rightarrow \Lambda_c^+ D_s^{-(*)}$ ,  $\Lambda_b^0 \rightarrow \Lambda_c^+ \bar{D}^0 X$  and  $\Lambda_b^0 \rightarrow \Lambda_c^+ D^- X$  events where the charm hadron decays through  $D \rightarrow 3\pi(N)$ ,  $N$  denoting a unknown number of particles. The largest of these contributions comes from  $\Lambda_b^0 \rightarrow \Lambda_c^+ D_s^{(*)-}$  events with  $D_s^{(*)-}$  being either  $D_s^-$ ,  $D_s^{*-}$ ,  $D_s^-(2317)$  or  $D_s^-(2457)$ .

This background carries usually additional charged particles coming either from the  $\Lambda_b^0$

Decays modes	$\mathcal{B}$ (%)
<b>Signal channel</b>	
$\Lambda_b^0 \rightarrow \Lambda_c^+ \tau^- (\rightarrow \pi^- \pi^+ \pi^- (\pi^0) \nu_\tau) \bar{\nu}_\tau$	$0.173 \pm 0.005$
<b>Normalisation channel</b>	
$\Lambda_b^0 \rightarrow \Lambda_c^+ \pi^- \pi^+ \pi^-$	$0.77 \pm 0.11$
<b>Background channels</b>	
$\Lambda_b^0 \rightarrow \Lambda_c^+ \pi^- \pi^+ \pi^- X$	$\sim 7$
$\Lambda_b^0 \rightarrow \Lambda_c^+ D_s^- / D_s^{*-} / D_s^- (2317) / D_s^- (2457) (\rightarrow \pi^- \pi^+ \pi^- N)$	0.251
$\Lambda_b^0 \rightarrow \Lambda_c^+ K^- \bar{D}^{*0} (\rightarrow \bar{D}^0 (\rightarrow K^+ \pi^- \pi^+ \pi^- (\pi^0)) \pi^0 / \gamma)$	0.125
$\Lambda_b^0 \rightarrow \Lambda_c^+ K^- \bar{D}^{*0} (\rightarrow \bar{D}^0 (\rightarrow K^+ \pi^- \pi^+ \pi^- (\pi^0)) \gamma / \pi^0)$	0.12
$\Lambda_b^0 \rightarrow \Lambda_c^+ \bar{K}^0 D^{*-} (\rightarrow \bar{D}^0 (\rightarrow K^+ \pi^- \pi^+ \pi^- (\pi^0)) \pi^-)$	0.12
$\Lambda_b^0 \rightarrow \Lambda_c^+ \bar{K}^{*0} D^{*-} (\rightarrow \bar{D}^0 (\rightarrow K^+ \pi^- \pi^+ \pi^- (\pi^0)) \pi^-)$	0.06
$\Lambda_b^0 \rightarrow \Lambda_c^+ D^- (\rightarrow \pi^- \pi^+ \pi^- (N))$	0.046
$\Lambda_b^0 \rightarrow \Lambda_c^+ K^- \bar{D}^0 (\rightarrow K^+ \pi^- \pi^+ \pi^- (\pi^0))$	0.025
$\Lambda_b^0 \rightarrow \Lambda_c^+ \bar{K}^0 D^{*-} (\rightarrow D^- (\rightarrow \pi^- \pi^+ \pi^- (\pi^0)) \gamma / \pi^0)$	0.015
$\Lambda_b^0 \rightarrow \Lambda_c^+ D_s^- / D_s^{*-} / D_s^- (2317) / D_s^- (2457) (\rightarrow \pi^- \pi^+ \pi^-)$	0.012
$\Lambda_b^0 \rightarrow \Lambda_c^+ \bar{K}^{*0} D^{*-} (\rightarrow D^- (\rightarrow \pi^- \pi^+ \pi^- (\pi^0)) \gamma / \pi^0)$	0.008
$\Lambda_b^0 \rightarrow \Lambda_c^+ K^0 D^- (\rightarrow \pi^- \pi^+ \pi^- (N))$	0.005

Table 5.1 – Expected branching fractions for signal and background sources with  $\Lambda_c^+ \pi^- \pi^+ \pi^-$  as visible final state.

The signal branching fraction is the SM expectation, for other modes, expectations based on  $B^0$  decays are used with measured decays of  $D^{*-}$ ,  $D^-$ ,  $D^0$  extracting from PDG [7].

or the  $\tau^-$  vertex. It is then possible to use isolation algorithms to look for these additional tracks and veto each combination with a track found to be compatible with one of these vertices. Neutral isolation methods are also used to search for neutral energy in calorimeter cells located in a cone around the  $\Lambda_b^0$  or  $\tau^-$  direction. These tools have a more precise study in Sec. 5.4.

Moreover, there is no  $\nu$  emitted in these background events and a dedicated partial reconstruction can give meaningful results. These variables are then used in a Boosted Decision Tree (BDT) to better distinguish signal from the different background categories.

Description and results of the partial reconstruction method are explained in Sec. 5.5 and the tuning of the classifier and its performances are described in Sec. 5.7.

Several other sources of background exist, such as:

- combinatorial: such candidates are coming from events with a reconstructed  $\Lambda_c^+$  and three pions coming from a different process. It creates a smooth component in the  $M(\Lambda_c^+ 3\pi)$  distribution. Its contribution is estimated from the high-mass region of the  $M(\Lambda_c^+ 3\pi)$  distribution,  $M(\Lambda_c^+ 3\pi) > 5700 \text{ MeV}/c^2$ , with wrong-sign (WS),  $\Lambda_c^+ \pi^+ \pi^- \pi^+$ , events coming from a dedicated stripping line.
- misidentified kaons: this background arises from one of more kaons wrongly identified as pions are used to create the three pions candidate. In that case, events coming from  $\Lambda_b^0 \rightarrow \Lambda_c^+ D^- (\rightarrow \pi^- K^+ \pi^- (N))(X)$  can be selected. Its contribution

can be studied by assigning the kaon mass to the opposite charged pion with respect to the  $D^-$  and searching for a mass peak in the mass of the three pions candidates distribution.

- misidentified leptons: semileptonic decays of the  $D_s^-$  with the lepton being wrongly identified as a pion are another source of background events. They can be controlled through a dedicated subsample with correctly identified leptons.
- fake  $\Lambda_c^+$  events: the level of background below the  $\Lambda_c^+$  mass peak is not negligible and needs to be accounted for. Details of the procedure can be found in Sec. 5.3.6.

### 5.1.4 Determination of the signal yield

As a summary, this analysis is aiming at the measurement of both  $\mathcal{B}(\Lambda_b^0 \rightarrow \Lambda_c^+ \tau^- \bar{\nu}_\tau)$  and  $\mathcal{K}(\Lambda_c)$  using a similar strategy as the one used for  $\mathcal{R}(D^*)$  [107].

To do so, a three dimensional template fit to the squared momentum transferred to the  $\tau \bar{\nu}_\tau$  lepton pair distribution ( $q^2$ ), the output of the BDT and the decay time of the  $\tau$  lepton is used to extract the signal yield.

Control samples are used to constrain the background contributions in the fit. A fit to the  $\Lambda_c^+ 3\pi$  mass distribution is performed on a sample enriched in  $\Lambda_b^0 \rightarrow \Lambda_c^+ D_s^-$  events as described in Sec. 5.9 to extract the relative normalisations of the different  $D_s^+$  components and the  $D^0$  control sample is used to calibrate the normalisation of the  $D^0$  template as discussed in Sec. 5.10.

## 5.2 Data and simulation samples

### 5.2.1 Data samples

This analysis is based on the whole Run1 dataset, meaning data collected during 2011 ( $\sqrt{s} = 7$  TeV) and 2012 ( $\sqrt{s} = 8$  TeV) with integrated luminosity of respectively  $1 \text{ fb}^{-1}$  and  $2 \text{ fb}^{-1}$ .

Datasets collected with each polarity of the magnet, labelled as MagUp and MagDown, are merged and the two datasets for 2011 and 2012 data taking periods are considered together for the rest of the analysis. This also holds true for the simulation samples.

### 5.2.2 Simulation samples

This analysis is using several simulated samples to understand background composition and correctly model it. Each generated sample is required to have the six charged tracks considered in the analysis, *i.e.* kaon, proton, and pion coming from the  $\Lambda_c^+$  and the three pions from the  $\tau^-$ , within the LHCb acceptance.

A special cut was designed for the production of double charm simulated events, the largest requests of this analysis, to gain some CPU time. The six tracks described above have to pass the cut specified in Eq. 5.13 at the generator level, in order to not waste time at the Detector simulation level which is the most CPU intensive part of the simulation process. This requirement allows to gain roughly a factor 2 for the event CPU time.

$$p_T > 130 \text{ MeV}/c \ \&\& \ p > 1200 \text{ MeV}/c \quad (5.13)$$

The signal samples were both generated using the TAUOLA model [114] implemented in EvtGen[115], the main generator for  $B$  hadrons decays used in LHCb.

Thanks to the data collected by the BaBar collaboration [116], it is possible to tune the parameters of TAUOLA [117] to properly describe the  $\tau$  polarisation for  $\tau \rightarrow 3\pi\nu_\tau$ . Such tuning is not yet available for the decay with an additional  $\pi^0$ , therefore data collected by the CLEO collaboration [118] are used for the tuning.

To study the contamination in this analysis of decays of excited charm baryons, simulation samples of  $\Lambda_b^0 \rightarrow \Lambda_c^{*+}\tau^-\bar{\nu}_\tau$  and  $\Lambda_b^0 \rightarrow \Sigma_c^{(*)}\pi\tau^-\bar{\nu}_\tau$  with  $\Lambda_c^*$  and  $\Sigma_c^{(*)}$  decaying respectively as

$$\Lambda_b^0 \rightarrow \Lambda_c^{*+}\tau^-\bar{\nu}_\tau, \quad \Lambda_c^{*+} \rightarrow \Lambda_c^+\pi^-\pi^+$$

and

$$\Lambda_b^0 \rightarrow \Sigma_c^{(*)}\pi\tau^-\bar{\nu}_\tau, \quad \Sigma_c^{(*)} \rightarrow \Lambda_c^+\pi$$

are also produced, with  $\Sigma_c\pi$  referring either as  $\Sigma_c^{++}\pi^-$  or  $\Sigma_c^+\pi^0$ <sup>2</sup>. Simulation samples for normalisation were also produced with  $\Lambda_c^*$  contributions.

Simulated samples for double charm backgrounds are cocktails of all the decay modes giving at least three  $\pi$ .

The simulation production focusing on  $D^0$  decay modes takes into account decays of excited charm mesons, *i.e.*  $D^{*-}$ ,  $D^{*0}$  and  $D_{s1}$  states into  $D^0$  and also decays with an associated  $K^-$  or  $K^{*-}$ . The same strategy was applied for decays modes including a  $D^-$  with contributions from  $D^{*-}$  and associated production with either a  $K^0$  or a  $K^{*0}$ .

Finally, for  $D_s^-$  decays, the main background of the analysis, contributions from excited  $D_s$  states, *i.e.*  $D_s^-$ ,  $D_s(2317)^-$ ,  $D_s(2457)^-$  and  $D_s(2536)^-$ , are included.

Tab. 5.2 presents a summary of the different simulated samples created for this analysis.

## 5.3 Selection of the events

This section describes the selection of the events used in the analysis. It can be divided into three parts:

- an online selection based on the LHCb trigger system.
- an offline preselection, called stripping, to select signal candidates.

<sup>2</sup>These samples are not yet present in Tab. 5.2 as their processing is still ongoing.

Decay type	Statistics
$\Lambda_b^0 \rightarrow \Lambda_c^+ \tau^- \bar{\nu}_\tau$ ( $\tau^- \rightarrow 3\pi\nu_\tau$ ) Tauola BaBar tune	37,506
$\Lambda_b^0 \rightarrow \Lambda_c^+ \tau^- \bar{\nu}_\tau$ ( $\tau^- \rightarrow 3\pi\pi^0\nu_\tau$ ) Tauola	11,677
$\Lambda_b^0 \rightarrow \Lambda_c^+ \pi^- \pi^+ \pi^-$	30,666
$\Lambda_b^0 \rightarrow \Lambda_c^+ D_s^-$ ( $D_s^- \rightarrow 3\pi N$ )	610,197
$\Lambda_b^0 \rightarrow \Lambda_c^+ D^0$ ( $D^0 \rightarrow 3\pi N$ )	607,090
$\Lambda_b^0 \rightarrow \Lambda_c^+ D^-$ ( $D^- \rightarrow 3\pi N$ )	550,666

Table 5.2 – Summary of the simulation samples used in this analysis.

- a final selection based primarily on the event topology.

This selection is then used to process both data and simulation samples to create the templates used by the fit described in Sec. 5.10 to extract the number of signal events  $N_{sig}$ .

### 5.3.1 Online selection

At the L0 level, events are asked to either be selected by the dedicated Hadron trigger or being a TIS event, with TIS (and TOS) trigger categories being defined in Chap. 3.

At the software trigger level, events need to be selected by at least one of the following trigger lines:

- Topological trigger: these lines are designed to select B hadron decaying into 2, 3 or 4 particles.
- $\Lambda_c^+$  trigger: this trigger is looking inclusively in each event for a  $\Lambda_c^+$  decaying into  $pK\pi$  or  $pKK$ .
- Charm hadron trigger: this trigger line is dedicated to search for charm hadrons decaying into three hadrons.

Using the naming conventions of the LHCb trigger system, the trigger selection can then be expressed as:

- **L0**: L0Global\_TIS or L0HadronDecision\_TOS
- **Hlt1**: Hlt1TrackAllL0Decision\_TOS
- **Hlt2**: Hlt2Topo{2,3,4}BodyBBDTDecision\_TOS or  
Hlt2CharmHadLambdaC2{PiPK,KPK,KPPI}Decision\_TOS or  
Hlt2CharmHadD2HHHDecision\_TOS

### 5.3.2 Offline preselection

Stripping lines are preselections implemented directly in the analysis framework of LHCb.

Two different stripping lines are used for the selection of  $\Lambda_c^+ \tau \nu$  events:

- **StrippingLb2LcTauNuForB2XTauNu**: the main line to select  $\Lambda_c^+ \tau^-$  candidates
- **StrippingLb2LcTauNuWSForB2XTauNu**: a line dedicated to select  $\Lambda_c^+ \tau^+$  candidates which are used to study the combinatorial background

This selection is designed to have final state particles with good track quality,  $\tau$  and  $\Lambda_c^+$  vertices of good quality and sufficient displacement of both of these vertices from the PV. In addition, some requirements are also required on the particles identification (PID) for both  $\tau$  and  $\Lambda_c^+$  daughters. The complete set of cuts used in in both stripping lines is shown in Tab. 5.3, the different variables are defined as follows:

$\chi_{track}^2/ndof$  : the  $\chi^2$  per degrees of freedom of the fit of the long track which the particle is associated

$\chi_{track}^2 - prob$  : the  $\chi^2$  probability of the track fit. If this probability is low, the fit quality is too poor for the track to be selected

$Ghost_{prob}$  : the probability of a track to only be a random combination of hits

$IP_{\chi^2}(PV)$  : the  $\chi^2$  distance of a given particle to the PV.  $IP_{\chi^2}(PV) > 5$  means that the track is required to be displaced from the PV with a  $5\sigma$  significance.

**DOCA** : the distance of closest approach of all the tracks to be combined to form either the  $\Lambda_c^+$ ,  $\tau$  or  $\Lambda_b^0$  in the context of this analysis

**DIRA** : the cosine of the angle between the momentum of a given particle and the direction given by the position of the PV and the decay vertex of this particle

$\chi^2$  **vertex** : the  $\chi^2$  of the fit combining the tracks to form the vertex.

$\chi^2$  **vertex-PV distance** : the  $\chi^2$  distance between the decay vertex of the particle considered and the PV. The larger this distance is, the higher the probability of its decay vertex to be displaced from the PV is

$PID\alpha(x)$  :  $PID\alpha = \log \mathcal{L}(\alpha) - \log \mathcal{L}(\pi)$ , as defined in Sec. 3.2.2, is a measurement of the compatibility of a given track  $x$  to be identified as the particle  $\alpha$ ,  $\alpha$  being either  $K$ ,  $\mu$ ,  $p$  or  $e$

$\min(m(\pi\pi))$  : the minimum of the mass of the two  $\pi^-\pi^+$  pairs from the  $3\pi$  of the  $\tau$

Cut	Value
$\Lambda_b^0$	
DIRA	$> 0.995$
$\max(DOCA)$	$< 0.15$ mm
$m(\Lambda_c^+ 3\pi)$	$\in [2500, 5900]$ MeV/ $c^2$
$\Lambda_c^+$	
$\chi^2$ vertex	$< 30$
DIRA	$> 0.995$
$\max(DOCA)$	$< 0.5$ mm
$IP_{\chi^2}(PV)$	$> 10$
$\chi^2$ Vertex-PV distance	$> 36$
$p_T$	$> 1200$ MeV/ $c$
$m(pK^-\pi^+)$	$\in [2256.5, 2316.5]$ MeV/ $c^2$
$\tau$	
$\chi^2$ vertex	$< 25$
DIRA	$> 0.99$
$\max(DOCA)$	$< 0.15$ mm
At least two pions with $p_T$	$> 300$ MeV/ $c$
At least two pions with $IP_{\chi^2}(PV)$	$> 5$
$m(3\pi)$	$\in [400, 3500]$ MeV/ $c^2$
$\min(m(\pi\pi))$	$< 1670$ MeV/ $c^2$
$\pi$ from $\tau$	
$Ghost_{prob}$	$< 0.4$
$\chi_{track}^2/ndof$	$< 3$
$IP_{\chi^2}(PV)$	$> 4$
$p_T$	$> 250$ MeV/ $c$
PIDk( $\pi$ )	$< 8$
$\Lambda_c^+$ daughters	
$Ghost_{prob}$	$< 0.4$
$\chi_{track}^2/ndof$	$< 3$
$\chi_{track}^2$ -prob	$> 0.01$
$IP_{\chi^2}(PV)$	$> 10$
$p_T$	$> 250$ MeV/ $c$
$p$	$> 2000$ MeV/ $c$
PIDk( $K$ )	$> 3$
PIDk( $\pi$ )	$< 50$
PIDp( $p$ )	$> 5$

Table 5.3 – Cuts used in the stripping selection.

### 5.3.3 Event topology

#### 5.3.3.1 Topology of a signal event

In order to remove the background coming from prompt  $\Lambda_c^+ 3\pi X$  decays, the most useful tool is the event topology. As the three pions are coming directly from the  $\Lambda_b^0$ , the  $3\pi$  vertex should be closer from the  $\Lambda_b^0$  one with respect to a signal event where the  $\tau$  is able to transport them.

Two cuts can be define to take advantage of the event topology:

- **detachment** cut: the  $3\pi$  vertex has to be downstream with respect to the  $\Lambda_b^0$  one with a significance of at least  $4\sigma$
- **inversion** cut: the  $3\pi$  vertex is required to be downstream of the  $\Lambda_c^+$  one with a significance of at least  $5\sigma$

The significance is defined as

$$\sqrt{vtx_z(\Lambda_X)_{err} \oplus vtx_z(3\pi)_{err}}$$

with  $\Lambda_X$  referring to  $\Lambda_b^0$  for the detachment cut and  $\Lambda_c^+$  for the inversion one. The event topology for a signal decay is shown in Fig. 5.2 with the two cuts.

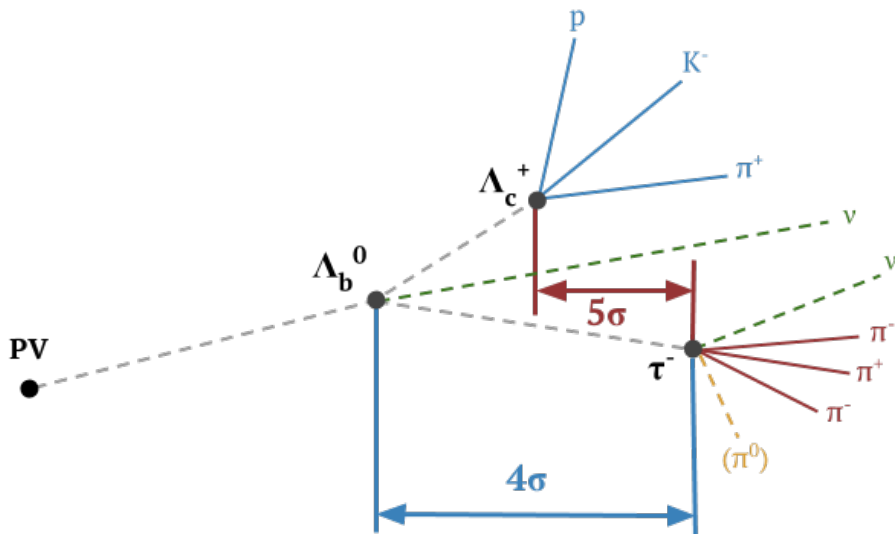


Figure 5.2 – Topology of a signal decay. The **detachment** cut is shown in blue and the **inversion** one in red.

#### 5.3.3.2 Choice of vertex cut

In the  $\mathcal{R}(D^*)$  analysis, the **detachment** cut was used as its selection efficiency on signal was roughly twice higher than the **inversion** one and was then used for the event selection. However, the downside of this cut is a more prominent contribution due to prompt

$3\pi$  events in the dataset after the event selection and a very large inclusive production of such events is required to account for this background in the final fit.

Due to the shorter lifetime of the  $\Lambda_c^+$ , the relative efficiency of the **inversion** cut with respect to the **detachment** one is higher, 63% for signal in MC 2012 sample to be compared with the one for the  $\mathcal{R}(D^*)$  analysis, which was roughly 50%.

To validate the use of the **inversion** cut in the event selection instead of the **detachment** one, in addition to the higher signal efficiency, one can study the rejection of prompt  $\Lambda_c^+$   $3\pi$   $X$  events using the exclusive  $\Lambda_b^0 \rightarrow \Lambda_c^+ 3\pi$  peak. Using the full selection described in Tab. 5.4,  $8396 \pm 101$  events in the  $\Lambda_c^+$   $3\pi$  peak are found in the 2012 dataset as shown in Fig. 5.4a,  $77 \pm 19$  with the detachment cut added and only  $8 \pm 13$  with the inversion one as seen respectively in Fig. 5.4b and Fig. 5.4c.

This validates the use of the **inversion** cut with its extra rejection of  $\Lambda_c^+$   $3\pi$  events, which completely removes the need of a  $3\pi$  prompt template in the final fit.

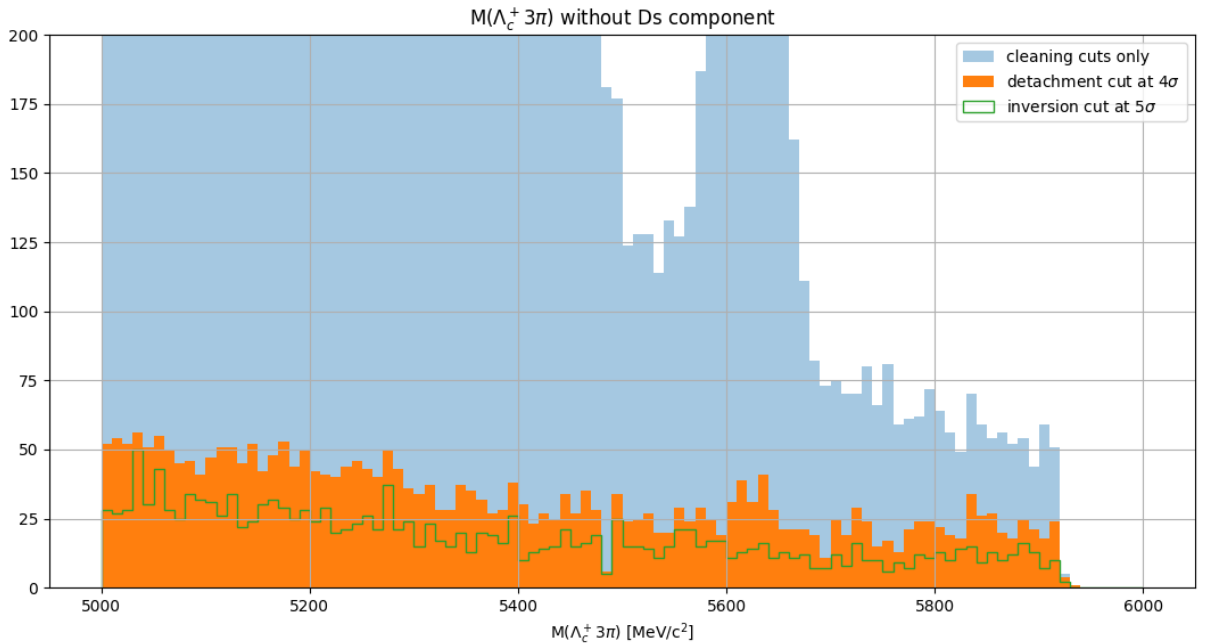
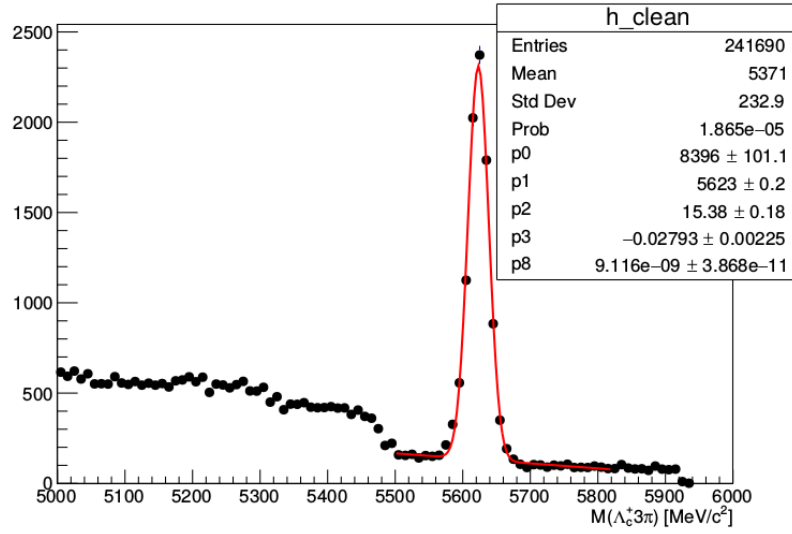
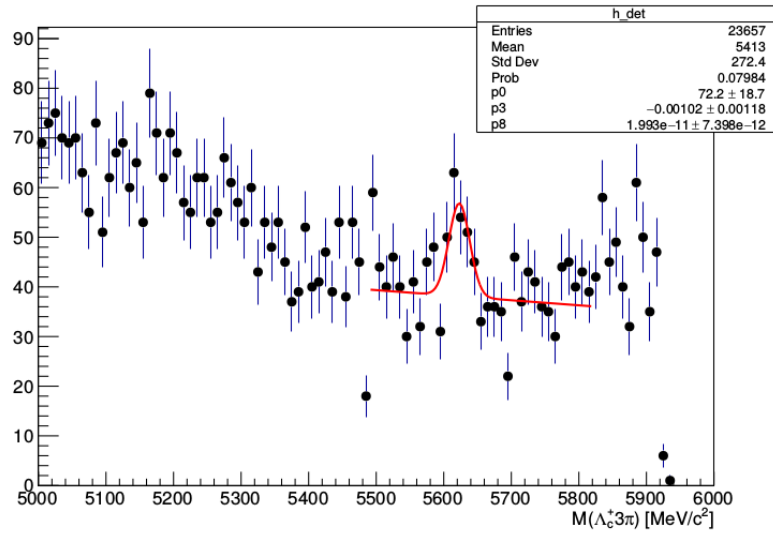
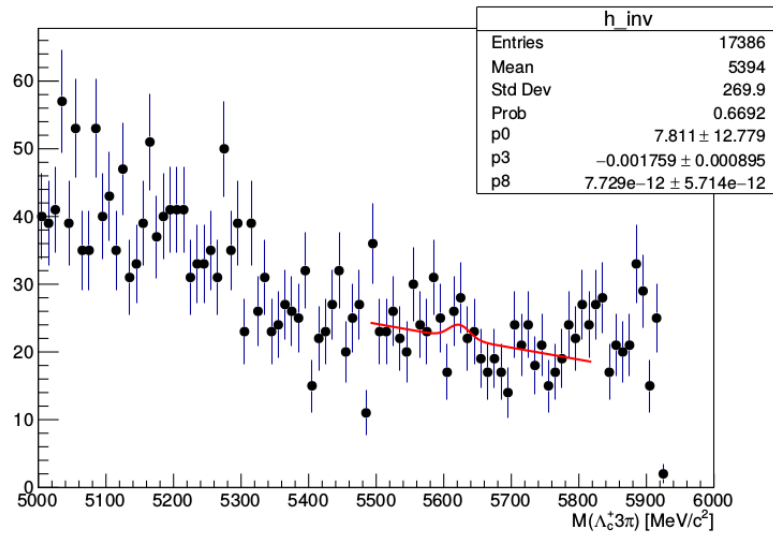


Figure 5.3 –  $M(\Lambda_c^+ 3\pi)$  with only cleaning cuts (blue), detachment cut added (orange) and inversion cut (green).

### 5.3.4 Additional cuts

In addition to the event topology requirement, other cuts are also used to remove background coming from the PV, interactions with the material and combinatorics. They are denoted as the  $\Lambda_b^0$  **selection** in Tab. 5.4.

In addition to this first set of cuts, additional cuts are required to better select the  $\Lambda_c^+$  and the three pions from the  $\tau^-$ . The same logic applies for both particles with the need


 (a) Fit of the  $\Lambda_b^0 \rightarrow \Lambda_c^+ 3\pi$  peak with the  $D_s^+$  component removed

 (b)  $M(\Lambda_c^+ 3\pi)$  distribution with detachment cut.

 (c)  $M(\Lambda_c^+ 3\pi)$  distribution with inversion cut.

of a good quality vertex and PID requirements for these six tracks. They are labelled as  $\Lambda_c^+$  and  $\tau^-$  selections in Tab. 5.4. As a naming convention of the rest of the document, if these additional cuts are considered without any topological cut, this set of cuts is designed as cleaning cuts. The selection of the  $\Lambda_c^+$  and the reduction of the background over its mass peak is further discussed in Sec. 5.3.6.

Among these cuts, some are designed to reject double charm background with the use of tools discussed in the following sections of this document, such as:

- the square root of the momentum transferred to the  $\tau$ - $\nu$  system,  $\sqrt{q^2}$ , which can be seen as the mass of the virtual W, is required to be positive
- the pion with an opposite charge with respect to the  $\tau^-$  is required to have  $\text{ProbNNk} < 0.1$  to suppress  $D^-$  events where this pion candidate is actually a misidentified kaon coming from a  $D^-$  decay
- the output of the BDT discussed in Sec. 5.4, labelled as isoBDT needs to be greater than 0.6

Distributions of the variables used in the event selection are shown for signal, both  $3\pi$  and  $3\pi\pi^0$ , and exclusive  $\Lambda_c^+$   $3\pi$  simulated samples with 2012 conditions in Fig. 5.5, Fig. 5.6 and Fig. 5.7.

Variable	Cut	
<b><math>\Lambda_b^0</math> selection</b>		
$[vtx_z(\Lambda_c^+) - vtx_z(\tau^-)]/\text{error}$	$< -5$	
BPVVDR( $\tau^-$ )	$\in [0.25, 5.2]$ mm	
PV( $\Lambda_c^+$ )	$= \text{PV}(\tau^-)$	
number of $\Lambda_b^0$ candidates	$= 1$	
<b><math>\Lambda_c^+</math> selection</b>		
$\chi^2[vtx(\Lambda_c^+)]$	$< 15$	
$\chi^2[IP_{PV}(\Lambda_c^+)]$	$> 15$	
ProbNNpi of $\pi$ from $\Lambda_c^+$	$> 0.6$	
ProbNNk of $K$ from $\Lambda_c^+$	$> 0.3$	
ProbNNp of $p$ from $\Lambda_c^+$	$> 0.35$	
ProbNNk of $p$ from $\Lambda_c^+$	$< 0.5$	
<b><math>\tau^-</math> selection</b>		
$\chi^2[vtx(\tau^-)]$	$< 10$	
$[vtx_z(\tau^-) - vtx_z(PV)]/\text{error}$	$> 10$	
$\chi^2[IP_{PV}(\pi)], \pi$ from $\tau^-$	$> 15$	
ProbNNpi of each $\pi$ from $\tau^-$	$> 0.6$	
$m(3\pi)$	$< 1600 \text{ MeV}/c^2$	
<b><math>\Lambda_c^+DX</math> background rejection</b>		
ProbNNk of $\pi^+$ from $\tau^-$	$< 0.1$	
$\sqrt{q^2}$	$> 0$	Sec. 5.5
Isolation	$\text{BDT}_{iso} > 0.6$	Sec. 5.4

Table 5.4 – The cuts used in the event selection, this set of cuts is denoted as **final** in the following.

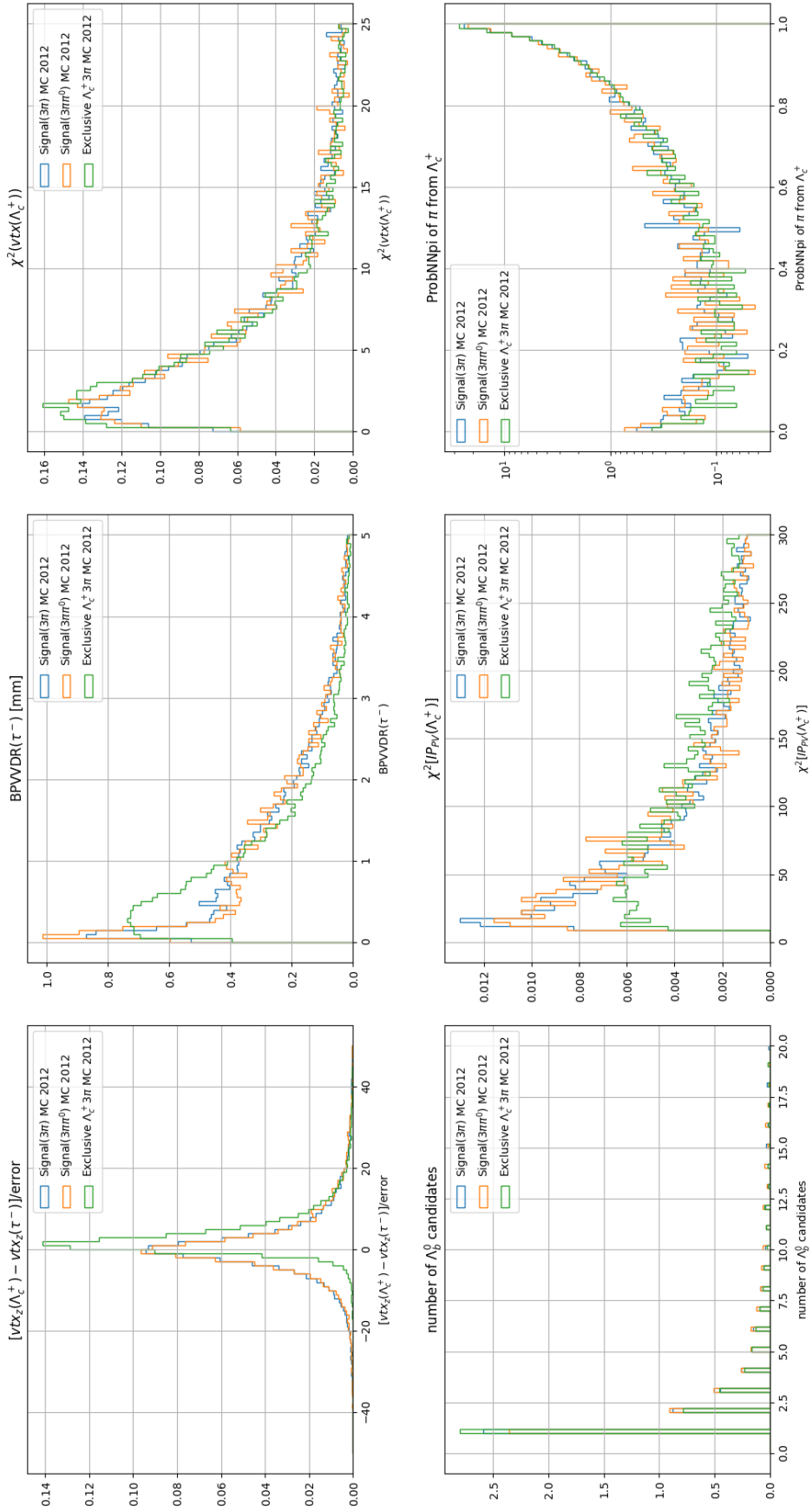


Figure 5.5 – Distributions of variables included in the event selection for signal (in blue), signal with additional  $\pi^0$  (in orange) and exclusive  $\Lambda_c^+ 3\pi$  2012 (in green) MC samples.

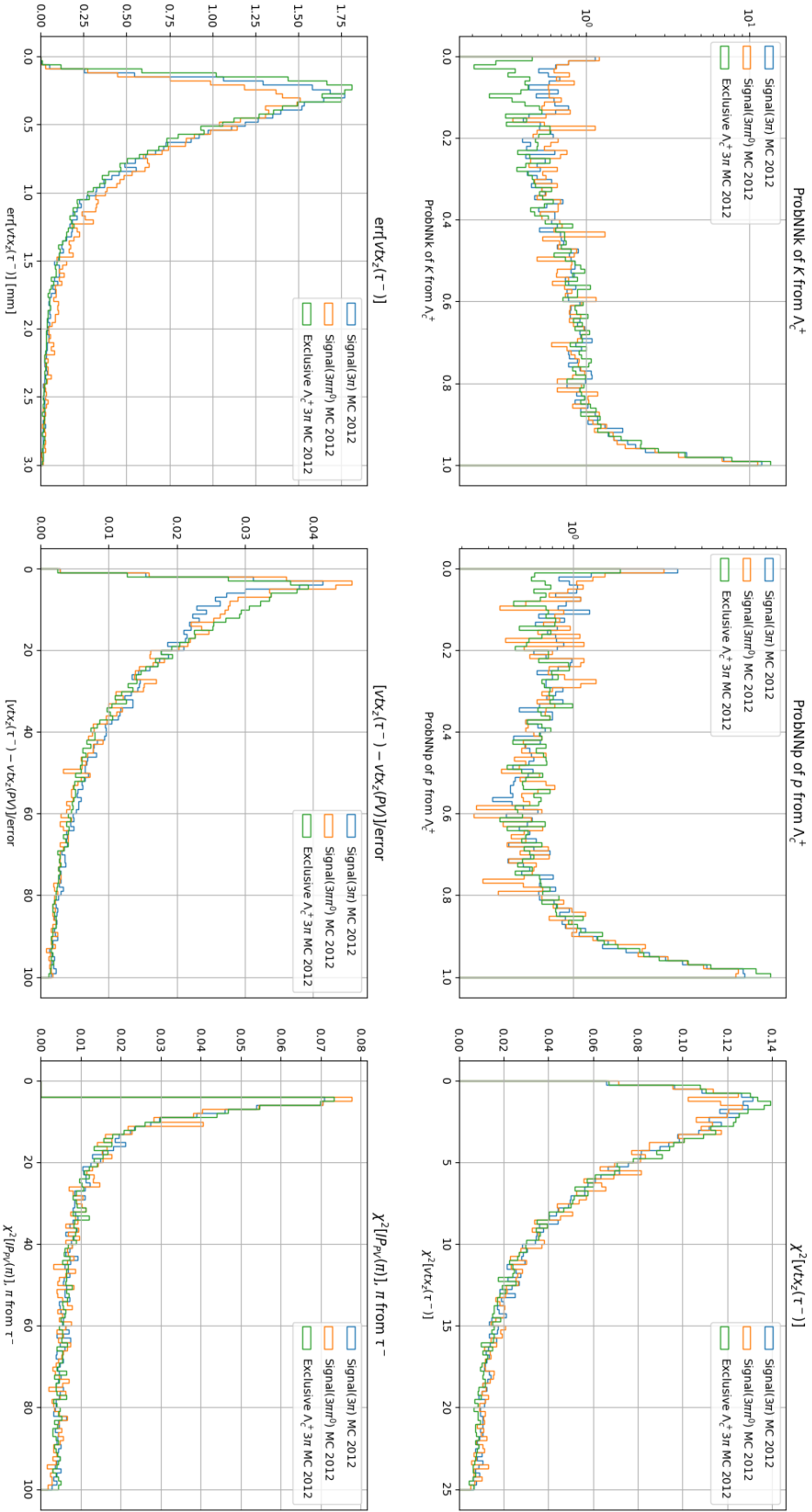


Figure 5.6 – Distributions of variables included in the event selection for signal (in blue), signal with additional  $\pi^0$  (in orange) and exclusive  $\Lambda_C^+ 3\pi$  2012 (in green) MC samples.

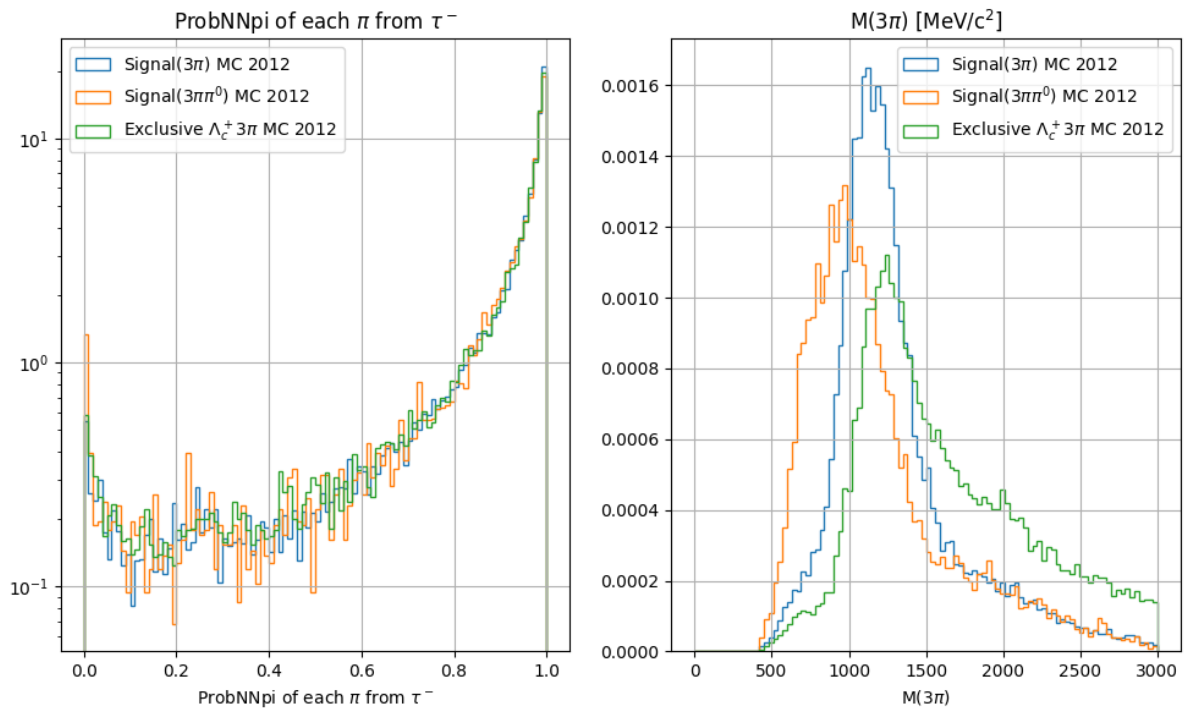


Figure 5.7 – Distributions of variables included in the event selection for signal (in blue), signal with additional  $\pi^0$  (in orange) and exclusive  $\Lambda_c^+ 3\pi$  2012 (in green) MC samples.

### 5.3.5 Selection of the normalisation events

In order to select the  $\Lambda_c^+$   $3\pi$  events of the normalisation channel, a so-called *normal topology* is required where the  $\Lambda_c^+$  vertex must be downstream with respect to the  $3\pi$  one with a significance of a least  $4\sigma$ . The selection for normalisation events, called `normal_final`, requires this topology cut and the full set of additional cuts described in Tab. 5.4

### 5.3.6 $\Lambda_c^+$ background removed using sideband subtraction

With the selection described in Sec. 5.3.4 and a previous definition of the PID requirement on the proton only asking for the ProbNNp of the proton to be higher than 0.2, the background under the  $\Lambda_c^+$  mass peak is still noticeable and must be taken into account. In this section, a study of this background and its rejection is presented. For reference, the distribution of the  $M(\Lambda_c^+)$  for data in Run1 using the selection described above is shown in Fig. 5.8.

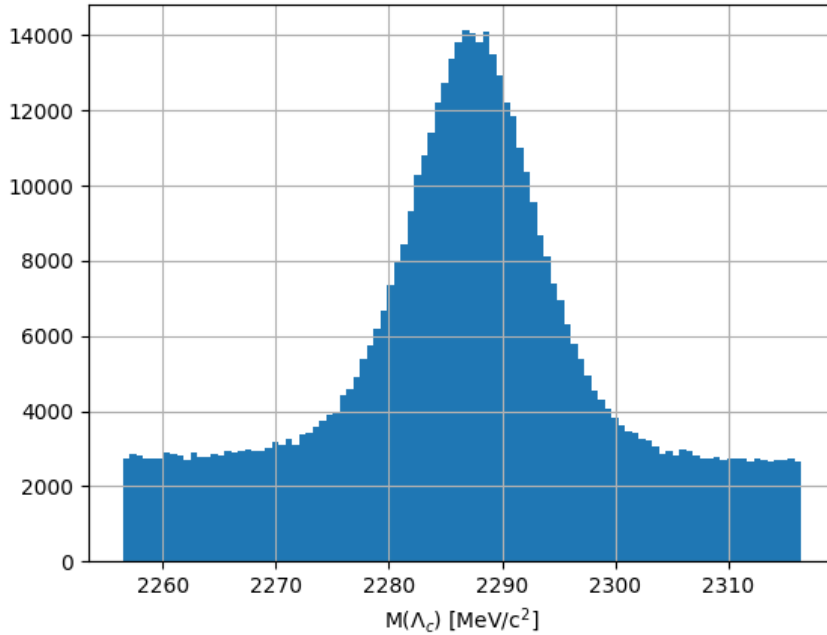


Figure 5.8 –  $M(\Lambda_c^+)$  distribution is shown for Run1 data after final selection but old PID requirement on the proton of the  $\Lambda_c^+$ .

The removal of this background relies on the sideband subtraction, with the sidebands defined as follows:

$$M(\Lambda_c^+) \in [2256.5, 2270] \text{ or } M(\Lambda_c^+) \in [2300, 2316.5] \quad (5.14)$$

with the mass expressed in  $\text{MeV}/c^2$ .

Unfortunately, the level of background to subtract is high enough with this selection to increase noticeably the statistical uncertainty on the number of signal events in the fit. It is then required to reduce the level of background below the  $\Lambda_c^+$  mass peak without significant drop of the signal efficiency. The following PID requirement:

- ProbNNp of the proton:  $> 0.35$
- ProbNNk of the proton:  $< 0.5$

reduce the background level by a factor 3 with a signal efficiency of 83% with respect to the selection where the only requirement on the PID of the proton is ProbNNp  $> 0.2$ . The comparison of these two PID requirements can be seen in Fig. 5.9.

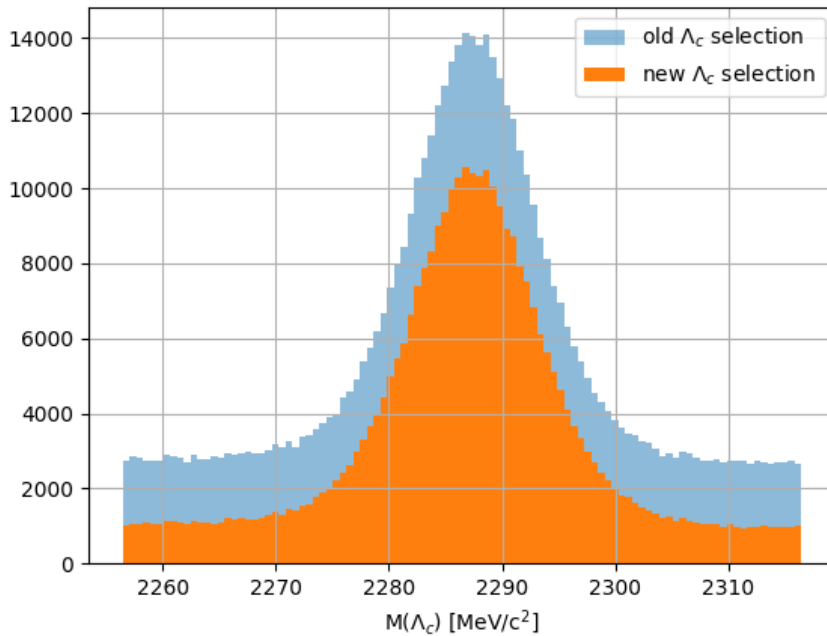
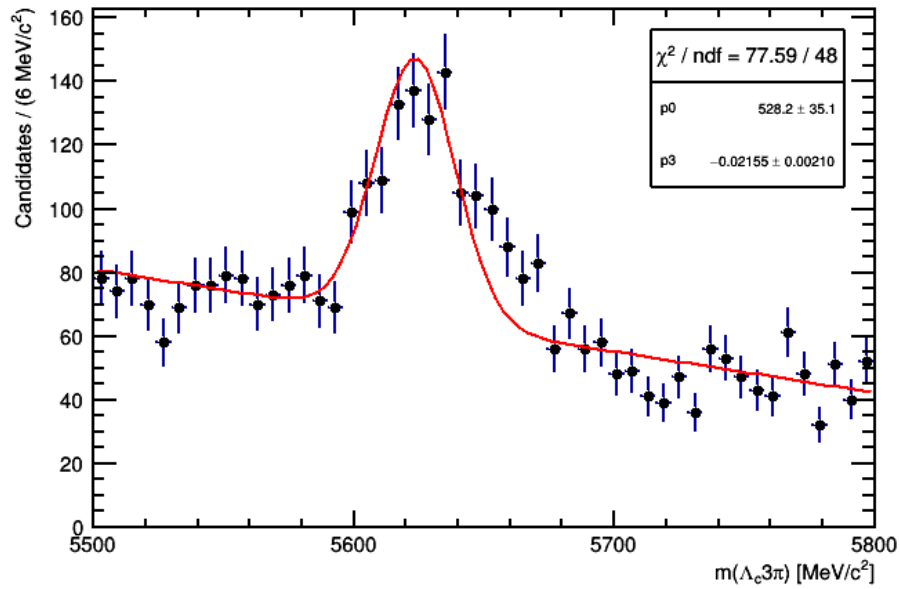


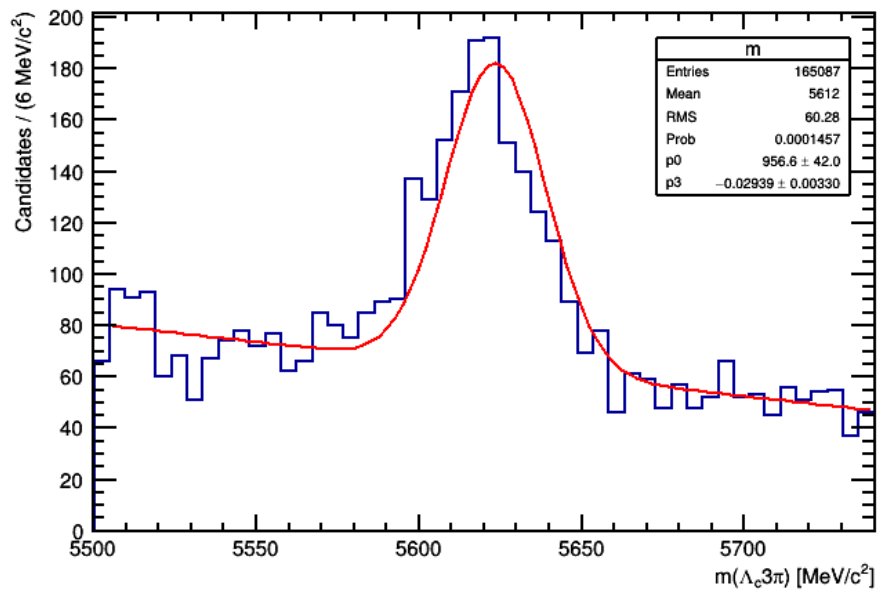
Figure 5.9 –  $M(\Lambda_c^+)$  distribution is shown for Run1 data after final selection and tighter  $\Lambda_c^+$  selection.

As the available mass range for the  $\Lambda_c^+$  given by the stripping is only of  $60 \text{ MeV}/c^2$ , a signal contamination in sidebands has also to be taken into account. This contamination of real  $\Lambda_c^+$  in the sidebands can be seen in Fig. 5.10 where the  $\Lambda_c^+ 3\pi$  mass is shown for both the lower and upper  $\Lambda_c^+$  sidebands. In both plots, a clear peak of  $\Lambda_b^0 \rightarrow \Lambda_c^+ 3\pi$  is visible which motivates the study of this effect.

To do so, one can use the exclusive  $\Lambda_b^0 \rightarrow \Lambda_c^+ 3\pi$  peak. It is indeed possible to count the number of events in the exclusive peak per bin of  $\Lambda_c^+$  mass, throughout the whole  $\Lambda_c^+$  mass range. The outcome of this analysis allows to draw the  $\Lambda_c^+$  mass distribution with only real  $\Lambda_c^+$  as seen in Fig. 5.11. The number of events in the sidebands in this plot is then a measure of the signal contamination which is evaluated to be 5.6%, even if it will cancel in both  $\mathcal{K}(\Lambda_c^+)$  and  $\mathcal{R}(\Lambda_c)$  ratios.



(a)



(b)

Figure 5.10 –  $\Lambda_c^+$   $3\pi$  mass distribution for the lower (a) and upper (b)  $\Lambda_c^+$  sidebands.

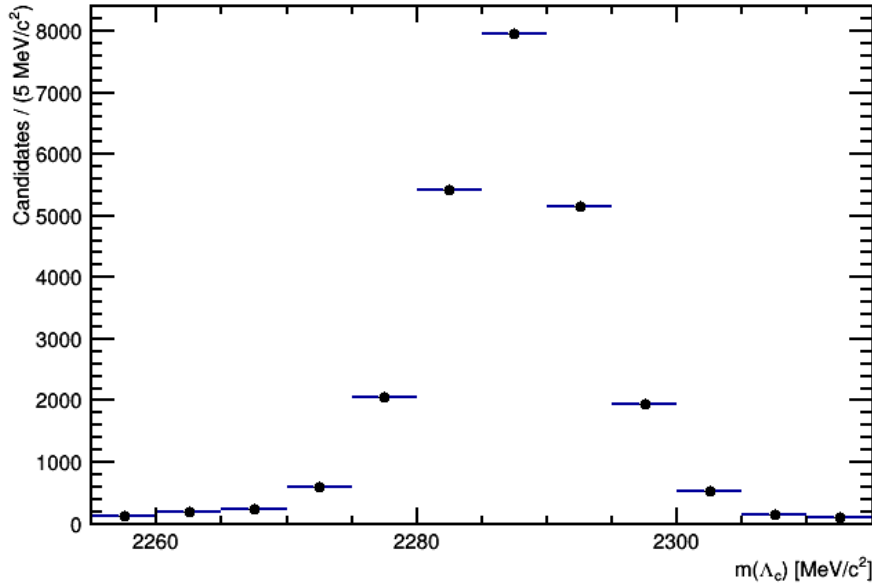


Figure 5.11 – Distribution of the  $\Lambda_c^+$  mass with events in the exclusive peak of  $\Lambda_b^0 \rightarrow \Lambda_c^+ 3\pi$ .

### 5.3.7 $\Lambda_c^*$ feed-down

$\Lambda_c^*$  contribution arises from  $\Lambda_c^{*+} \rightarrow \Lambda_c^+ \pi^- \pi^+$  and  $\Lambda_c^{*+} \rightarrow \Lambda_c^+ \pi^0 \pi^0$  decays. As the neutral decay is not detected, the reconstruction of  $\Lambda_c^*$  in its decay into two charged pions is used in the following to estimate the total feed-down.

The feed-down in data from both  $\Lambda_c(2625)$  and  $\Lambda_c(2593)$  is of 2100 events which corresponds to  $\sim 10\%$  of the number of events in the  $\Lambda_b^0 \rightarrow \Lambda_c^+ 3\pi$  exclusive peak and is shown in Fig. 5.12 with the difference of  $\Lambda_c^{*+} \pi^- \pi^+$  and  $\Lambda_c^+$  mass distributions.

The estimation of the ratio of the yields  $N(\Lambda_c^* 3\pi)/N(\Lambda_c^+ 3\pi)$  is presented here with  $\Lambda_c^* 3\pi$  being the sum of  $\Lambda_c(2593) 3\pi$  and  $\Lambda_c(2625) 3\pi$  contributions. Due to the current lack of  $\Lambda_c^* 3\pi$  simulation sample produced with either 2011 or 2012 conditions, this ratio is measured using 2016 data and simulation samples. This ratio is measured in 2016 data to be 0.138.

The selection for this study is slightly different in order to maximise the  $\Lambda_c^* 3\pi$  efficiency. The selection efficiency (without the acceptance part) is  $1.35 \times 10^{-3}$  for the  $\Lambda_c^+ 3\pi$  yield and  $0.475 \times 10^{-3}$  for the  $\Lambda_c^* 3\pi$  one. Thus, the ratio of the yields corrected by the efficiencies is 0.588.

Finally, to extract the  $\Lambda_c^*$  feed-down in  $\Lambda_c \tau \nu$  events, one needs to estimate the efficiency of  $\Lambda_c^* \tau \nu$  events to pass the selection used to create the templates for the fit.

This cannot be measured precisely as no simulation sample for  $\Lambda_c^* \tau \nu$  is available yet. Efficiency already measured on the  $\Lambda_c^* 3\pi$  sample are then used for this purpose.

If we take 0.9 as an estimate for the drop of efficiency due to the emission of the two

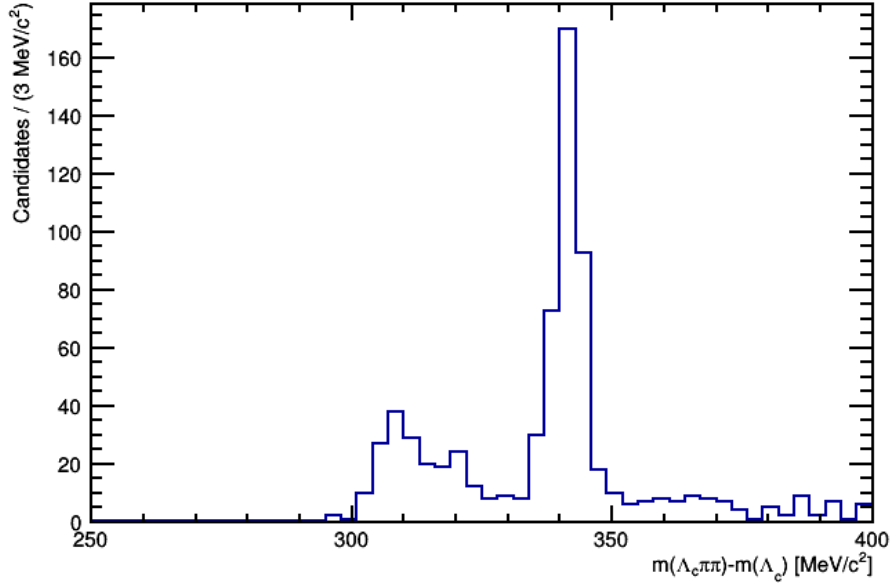


Figure 5.12 – Distribution of  $M(\Lambda_c^+ \pi^- \pi^+) - M(\Lambda_c^+)$  in 2012 data. The two peaks correspond to  $\Lambda_c(2593)$  and  $\Lambda_c(2625)$  resonances.

pions of the  $\Lambda_c^*$ , we then have: for the charged case:

$$\frac{N(\Lambda_c^* 3\pi)}{N(\Lambda_c^+ 3\pi)} \times \epsilon_{\Lambda_c^* 3\pi} \times \epsilon_{iso}^\pm \times w^\pm \times 0.9 = 2.07\%$$

for the neutral one:

$$\frac{N(\Lambda_c^* 3\pi)}{N(\Lambda_c^+ 3\pi)} \times \epsilon_{\Lambda_c^* 3\pi} \times \epsilon_{iso}^0 \times w^0 \times 0.9 = 10.7\%$$

with the efficiencies of the isolation selection estimated for charged ( $\epsilon_{iso}^\pm$ ) and neutral ( $\epsilon_{iso}^0$ ) decays modes of the  $\Lambda_c^*$  estimated to be respectively 0.1 and 0.5. The two weights,  $w^\pm$  and  $w^0$ , are introduced in the computation to take into account the relative branching fractions of the charged and neutral modes with  $w^\pm = \frac{1}{3}$  and  $w^0 = \frac{2}{3}$ .

The first estimation of  $\Lambda_c^* \tau \nu$  feed-down is then respectively 2.07% and 10.4% for charged and neutral decays of the  $\Lambda_c^*$ . The total feed-down is then estimated to be of 12.5% which is very similar to the  $D^{**}$  one in the hadronic  $\mathcal{R}(D^*)$  analysis.

## 5.4 Isolation tools

The event selection discussed in Sec. 5.3 is efficient to discriminate between signal events and events with  $3\pi$  coming from the  $\Lambda_b^0$  vertex or with particles misidentified as pions. The remaining background is mostly composed of double charm decays where the three pions are produced by a D meson –  $D_s^-$ ,  $D^-$  or  $D^0$  – often produced in association with other charged or neutral particles.

It is possible to remove this background searching for these additional particles produced in addition with the reconstructed candidate, in the following, they will be referred as non-isolated events. Two types of isolation algorithms are used in this analysis to reject this background, charged particle isolation is described in Sec. 5.4.1 and isolation against neutral particles is shown in Sec. 5.4.2.

### 5.4.1 Charged particles isolation using a BDT

To identify and reject non-isolated events, a two-stage Boosted Decision Tree (BDT) approach is chosen. In the context of this analysis, BDT are used as classifiers, meaning that labelled samples of both signal and background events are provided for the training of such algorithm to adjust its internal parameters. The output of the classifier is a score comprised between 0 and 1, with 0 meaning a background like event and 1 a signal-like one.

Applied on a sample with unknown content, such algorithms are then able to identify both background and signal events based on the information present in the training set. Such algorithms will be further discussed in Sec. 5.7.

To perform charged isolation, two different BDT need to be used, the first one for tracks, the second at the event level. They will be further referred as track-BDT and isoBDT in the following.

The track-BDT was first designed, developed and used in the measurement of the mixing frequency  $\Delta m_d$  using semileptonic B decays [119].

After the reconstruction of the signal candidate, remaining tracks of the event are divided in two categories:

- isolated tracks: these tracks cannot be attached to one of the vertices of the signal candidate decay chain. In Fig. 5.13, they are coloured in grey.
- non-isolated tracks: denoted in red in Fig. 5.13, they are the ones to be identified in order to veto background events

In a BDT-based algorithm, one wants to detect a signal, non-isolated tracks, from a background composed of isolated ones. Several MC samples were used for the training, such as inclusive  $b\bar{b}$  and  $c\bar{c}$  samples, and the output of each BDT can be computed for each track of a signal candidate.

At this point, the isolation is only provided at the track level, one needs to provide a method able to aggregate all the information available for each track of the event to decide whether or not the event should be vetoed. This is the work to be performed by the isoBDT.

The training of the isoBDT is performed using signal  $\tau \rightarrow 3\pi\nu_\tau$  simulation samples as the isolated sample. Using the truth matching information available in simulation, the non-isolated background sample is defined as follows:

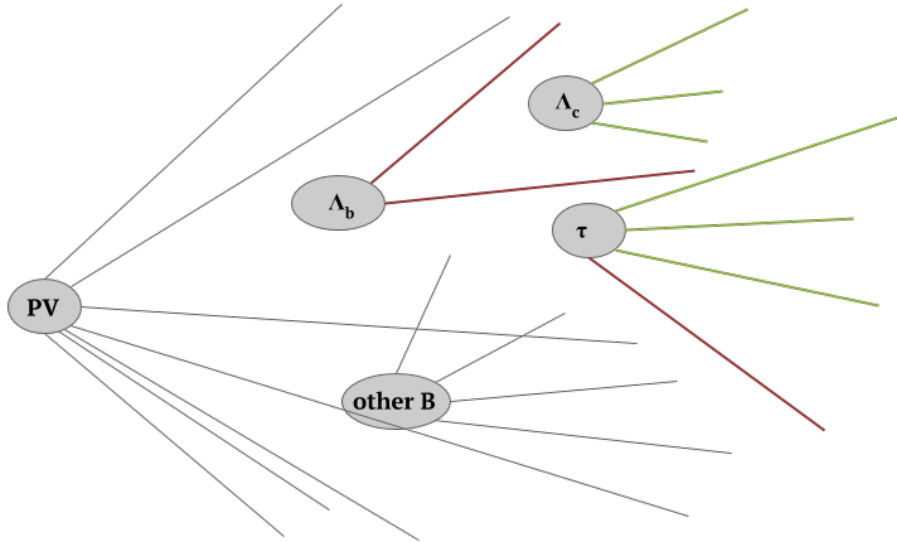


Figure 5.13 – Schema of the event where the tracks used to create the signal candidate are shown in green, isolated tracks in grey and non-isolated tracks in red.

- $\Lambda_c^+ D_s^-$  events where two additional charged pions are found in the decay chain, this background sub-sample is labelled as 5-tracks  $D_s^-$ .
- $\Lambda_c^+ D^0 X$  events with two extra charged kaons identified in the event. This subset is then called  $2K-D^0$ .

The  $M(\Lambda_c^+ 3\pi)$  distribution of the 5-tracks  $D_s^-$  component is shown in Fig. 5.14.

For each tracks of the signal candidate, three pions from the  $\tau$  and pion, kaon and proton from the  $\Lambda_c^+$ , the variables used are:

- IsoSumBDT
- IsoMinBDT
- PAIR\_M

The first two variables are output of two track-BDT trained with different configurations and the third is the mass of the combination of the particle considered with the non-isolated track having the lowest track-BDT value. The ratio of the  $p_T$  of the  $\Lambda_b^0$  to the sum of the  $p_T$  of the  $\Lambda_b^0$  and the  $p_T$ , denoted as ConeIso is also used.

The training and testing distributions of the BDT output for both signal and background are shown in Fig. 5.15, the list of variables with their importance score in Fig. 5.16 and the ROC curve, showing the background rejection over the signal efficiency, is presented in Fig. 5.17.

Requiring events used in the analysis to have an output of the isoBDT greater than 0.6 is able to greatly reject the non-isolated events as shown in Tab. 5.5. For instance, the isoBDT is able to have an efficiency on  $D^0$  events with two  $K$ , a source of background very similar to the signal if no isolation is used, at the level of  $\sim 7\%$ .

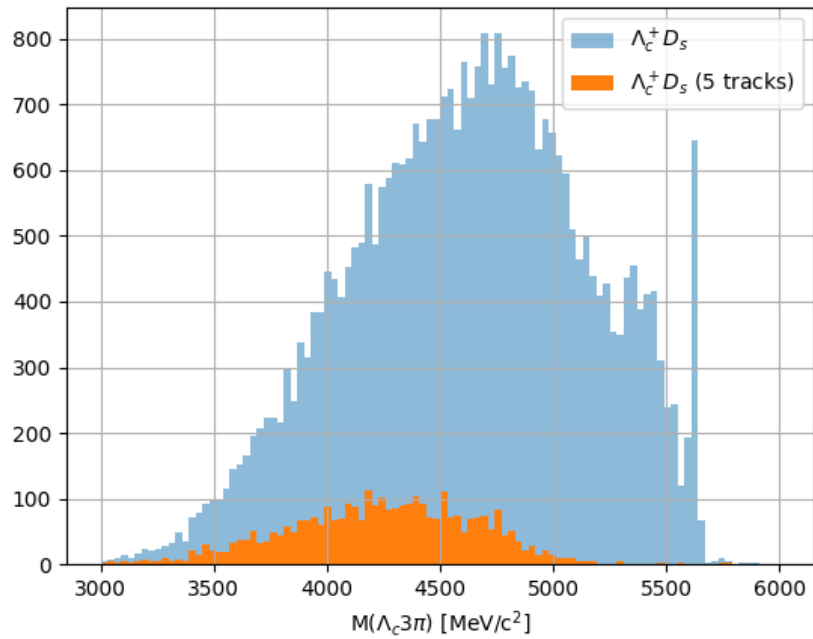


Figure 5.14 – Distribution of  $M(\Lambda_c^+ 3\pi)$  for the  $\Lambda_c^+ D_s^-$  2012 MC sample (in blue) and its 5-tracks  $D_s^-$  component (in orange).

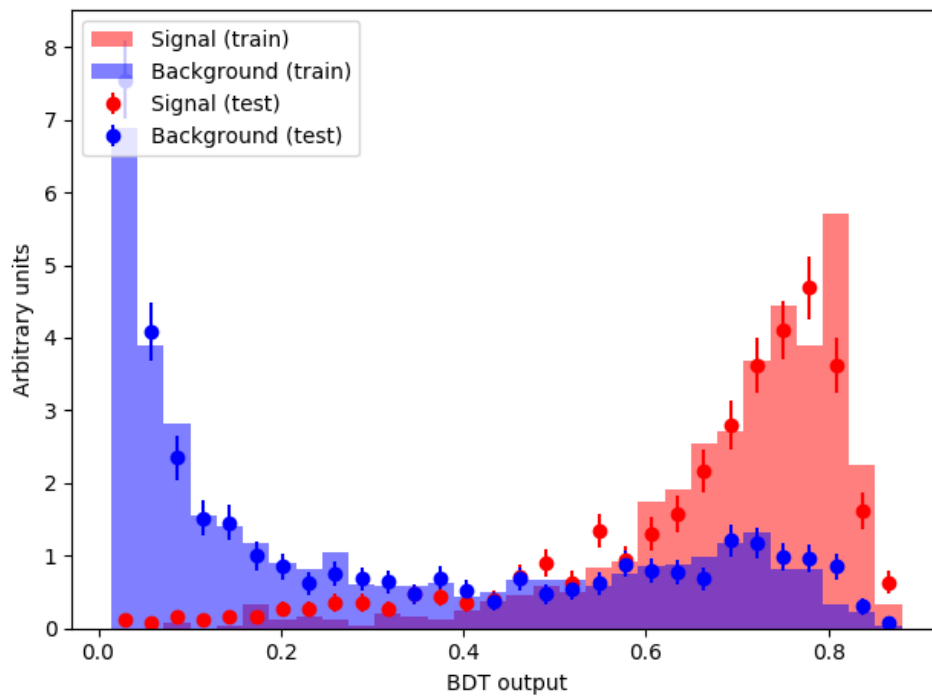


Figure 5.15 – Distributions for both signal (red) and background (blue) for testing and training samples.

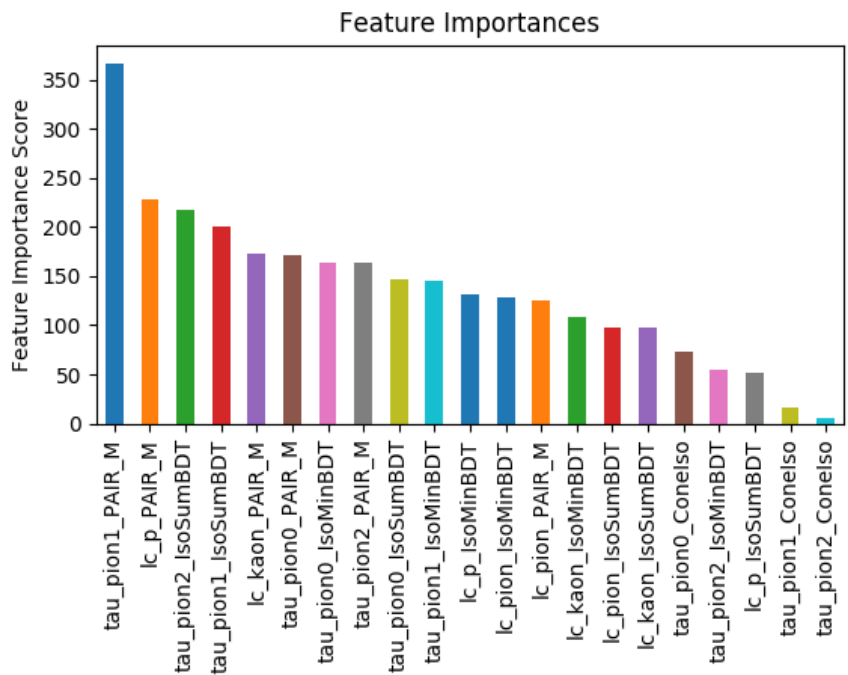


Figure 5.16 – Importance score for each variable used in the isolation BDT.

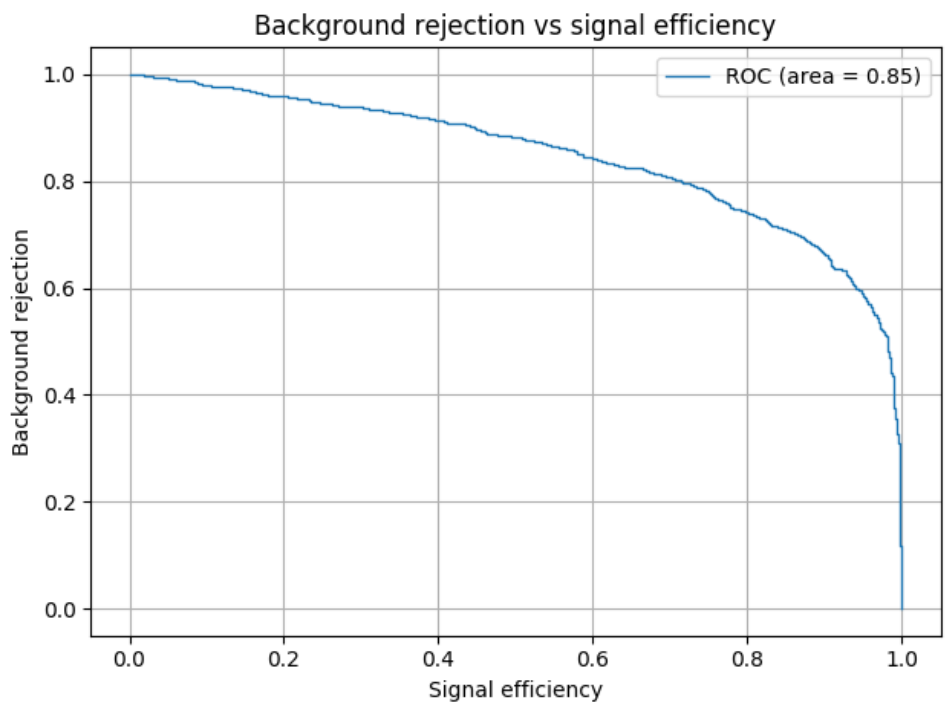


Figure 5.17 – Background rejection as a function of signal efficiency for the isolation BDT.

Dataset	$\epsilon_{isoBDT}$ (%)
Signal	79
5-tracks $D_s^-$	29
$2K-D^0$	7

Table 5.5 – Efficiencies on both signal and background simulation samples used to train the isoBDT.

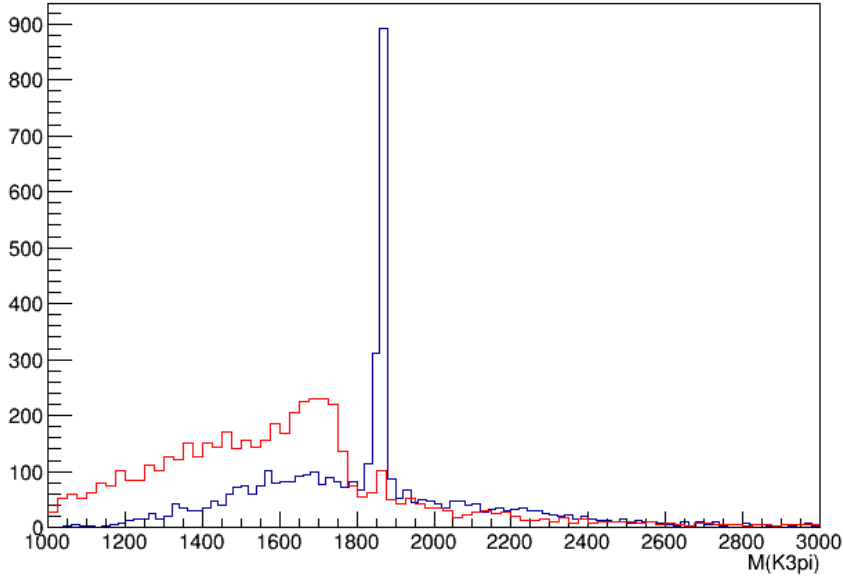


Figure 5.18 – Invariant mass of the system composed of the three pions and additional track compatible either with a pion (red) or a Kaon (blue).

#### 5.4.1.1 Charged isolation control samples

The method based on counting tracks at either  $A_c^+$  or  $3\pi$  vertices can be used to build control samples of non-isolated samples. In Fig. 5.18, the mass distribution of  $3\pi h$  is shown when an additional track compatible with pion or kaon hypothesis is found. Clear peaks corresponding to  $D^0 \rightarrow \pi^+\pi^-\pi^+K^-$  and  $D^0 \rightarrow \pi^+\pi^-\pi^+\pi^-$  can be seen. A control sample is then built by requiring a mass window of  $\pm 20 \text{ MeV}/c^2$  around the  $D^0$  mass.

#### 5.4.2 Neutrals isolation

Background candidates often decay to extra neutral particles ( $\gamma$ ,  $\pi^0$ , ...) and they can be vetoed using information provided by the calorimeter system. The neutral isolation algorithm looks for neutral energy in a cone, which radius  $\Delta R = \sqrt{\Delta\eta^2 + \Delta\phi^2}$  can be tuned between 0.1 and 0.5, around the  $3\pi$  direction.

A data-MC comparison of the  $P_z$  of the neutral particles selected by the algorithm is shown in Fig. 5.19, using the exclusive decay  $A_b^0 \rightarrow A_c^+ 3\pi$  with 2012 samples. Its dis-

tribution is also shown in Fig. 5.20 for both signal and  $\Lambda_c^+ D^0 X$  events, with a much higher peak at zero for the signal distribution, where all events are isolated, with respect to  $\Lambda_c^+ D^0 X$  events, which are non-isolated events, with a distribution featuring a long tail at high values. Another test is shown in Fig. 5.21, where the distribution of the  $\Lambda_c^+ 3\pi$  mass is shown without neutral isolation requirement and with a requirement of 8 GeV of neutral energy to be found in a cone around the  $3\pi$  axis with a drop of efficiency much more important on the exclusive  $\Lambda_b^0 \rightarrow \Lambda_c^+ 3\pi$  peak where all the events are isolated with respect to the broad component where the  $3\pi$  are often associated with at least one neutral particle.

The neutral isolation variables are used in the training of the BDT described in Sec. 5.7.

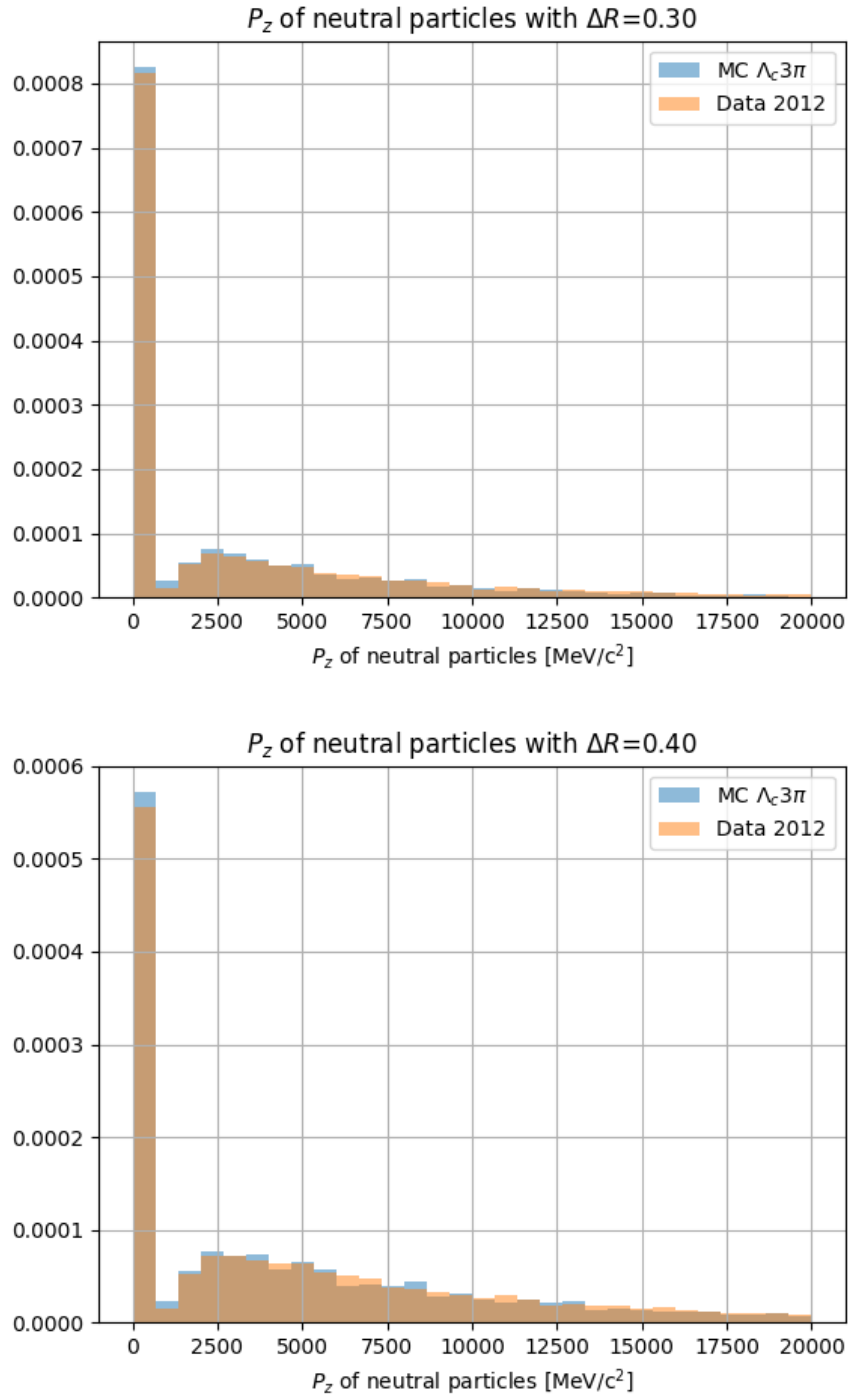


Figure 5.19 – Comparison of the  $P_z$  of the neutral particles selected by the neutral isolation. The exclusive  $\Lambda_c^+ 3\pi$  sample (in blue) is compared with the data sample (in orange) for cone sizes of 0.3 and 0.4.

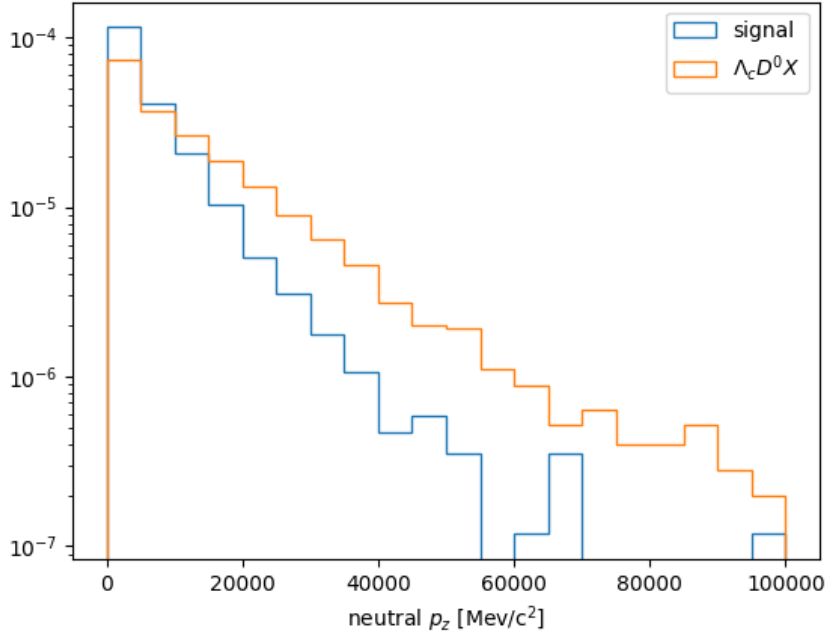


Figure 5.20 – Normalised distribution of the  $P_z$  of neutral particles with  $\Delta R = 0.4$  for both signal and  $\Lambda_c^+ D^0 X$  simulation datasets.

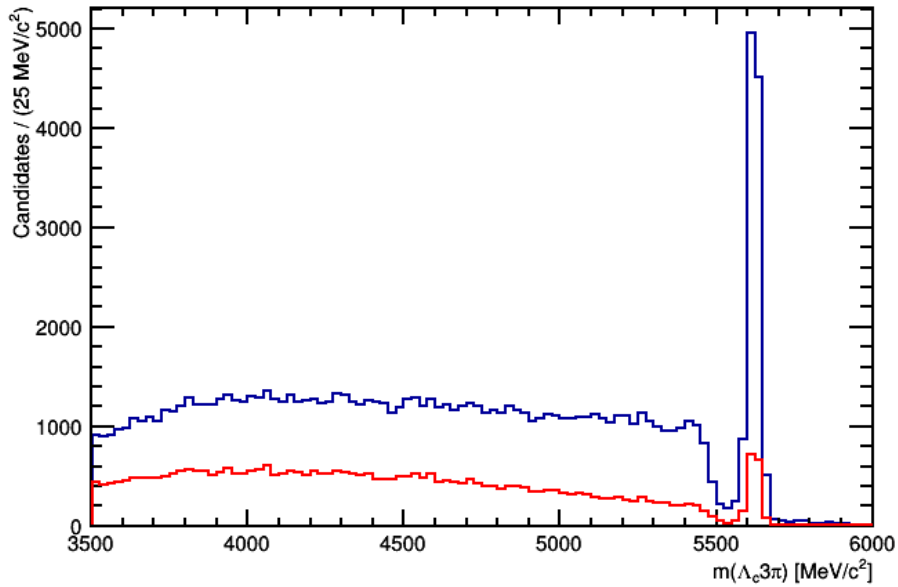


Figure 5.21 –  $\Lambda_c^+ 3\pi$  mass distribution in the 2012 simulation sample with no neutral isolation requirement (blue) and with a requirement of 8 GeV of neutral energy in a cone around the  $3\pi$  axis.

## 5.5 Reconstruction techniques

The full reconstruction of  $\Lambda_b^0 \rightarrow \Lambda_c^+ \tau^- \bar{\nu}_\tau (\rightarrow 3\pi(\pi^0)\nu_\tau)$  events using a missing energy technique is not directly possible due to the two missing neutrinos. However, if one adds constraints on both  $\tau$  and  $\Lambda_b^0$  masses, it becomes possible to reconstruct  $\Lambda_b^0$  and  $\tau$  momenta but also the  $\tau$  decay time. This section presents two reconstruction methods used in the analysis, one to fully reconstruct an event under the hypothesis of it being a signal one and a partial reconstruction method useful to reconstruct  $\Lambda_b^0 \rightarrow \Lambda_c^+ D_s^-$  events and thus, strengthening its rejection.

### 5.5.1 Reconstructing $\Lambda_b^0 \rightarrow \Lambda_c^+ \tau^- \bar{\nu}_\tau$ events

To fully reconstruct  $\Lambda_b^0 \rightarrow \Lambda_c^+ \tau^- \bar{\nu}_\tau$  events, the direction of the  $\tau$  is needed, given by the line joining both the 3 pions vertex and the  $\Lambda_b^0$  one.

The  $\tau$  momentum can be estimated, using the constraint that the 3 pions come from the  $\tau$  decay, up to a two-fold ambiguity, as follows:

$$|\vec{p}_\tau| = \frac{(m_{3\pi}^2 + m_\tau^2)|\vec{p}_{3\pi}|\cos\theta \pm \sqrt{(m_\tau^2 - m_{3\pi}^2) - 4m_\tau^2|\vec{p}_{3\pi}|^2\sin^2\theta}}{2(E_{3\pi}^2 - |\vec{p}_{3\pi}|^2\cos^2\theta)} \quad (5.15)$$

In Eq. 5.15,  $\theta$  is the angle between the directions of the  $\tau$  and the three pions.  $m_{3\pi}$ ,  $E_{3\pi}$  and  $|\vec{p}_{3\pi}|$  are respectively the invariant mass, energy and 3-momentum of the  $3\pi$  system, with  $m_\tau$  being the mass of the  $\tau$  lepton.

To resolve the two-fold ambiguity, one can tune  $\theta$  in order for both solutions to become only one using:

$$\theta_{\max} = \arcsin\left(\frac{m_\tau^2 - m_{3\pi}^2}{2m_\tau|\vec{p}_{3\pi}|}\right) \quad (5.16)$$

Using Eq. 5.16,  $|\vec{p}_\tau|$  becomes  $|\vec{p}_\tau(\theta_{\max})|$  and the same method can be reused to estimate the  $\Lambda_b^0$  momentum using the formula:

$$|\vec{p}_{\Lambda_b^0}| = \frac{(m_{\Lambda_c^+\tau}^2 + m_{\Lambda_b^0}^2)|\vec{p}_{3\Lambda_c^+\pi}|\cos\theta' \pm \sqrt{(m_{\Lambda_b^0}^2 - m_{\Lambda_c^+\tau}^2) - 4m_{\Lambda_b^0}^2|\vec{p}_{\Lambda_c^+\tau}|^2\sin^2\theta'}}{2(E_{\Lambda_c^+\tau}^2 - |\vec{p}_{\Lambda_c^+\tau}|^2\cos^2\theta')} \quad (5.17)$$

Here,  $\vec{p}_{\Lambda_c^+\tau}$  is defined as:

$$\vec{p}_{\Lambda_c^+\tau} = \vec{p}_{\Lambda_c^+} + \vec{p}_\tau(\theta_{\max}) \quad (5.18)$$

One then only needs to reconstruct  $|\vec{p}_{\Lambda_b^0}|$  to use the  $\theta'$  value leading to a single solution:

$$\theta'_{\max} = \arcsin\left(\frac{m_{\Lambda_b^0}^2 - m_{\Lambda_c^+\tau}^2}{2m_{\Lambda_b^0}|\vec{p}_{\Lambda_c^+\tau}|}\right) \quad (5.19)$$

Having both momenta of  $\tau$  and  $\Lambda_b^0$  reconstructed, one can then compute the mass of the virtual  $W$  boson ( $M_W$ ) and the momentum transferred to the  $\tau$ - $\nu$  system defined as:

$$q^2 = p_W^2 = (p_{\Lambda_b^0} - p_{\Lambda_c^+})^2 \quad (5.20)$$

This variable is used in the final fit described in Sec. 5.10 to extract the signal yield. The shape of its distribution could also be the subject of further studies to test several New Physics scenarios.

Finally, the extraction of the  $\tau$  decay time can be obtained using the reconstructed  $\vec{p}_\tau$  by first recovering the Lorentz factors:

$$\beta = \frac{|\vec{p}_\tau|}{E_\tau} \quad (5.21)$$

$$\gamma = \frac{1}{\sqrt{1 - \beta^2}} \quad (5.22)$$

where  $E_\tau$  is the energy of the  $\tau$ . Using both  $\Lambda_b^0$  and  $\tau$  vertices and their coordinates denoted as  $\Lambda_{b,x,y,z}^0$  and  $\tau_{x,y,z}$ , one can then compute the distance of flight of the  $\tau$  and its decay time:

$$L = \sqrt{(\tau_x - \Lambda_{b,x}^0)^2 + (\tau_y - \Lambda_{b,y}^0)^2 + (\tau_z - \Lambda_{b,z}^0)^2} \quad (5.23)$$

$$t_\tau = \frac{Lc}{\beta\gamma} \quad (5.24)$$

## 5.5.2 Signal reconstruction results using simulation samples

### 5.5.2.1 Signal $\Lambda_b^0 \rightarrow \Lambda_c^+ \tau (\rightarrow 3\pi\nu_\tau) \bar{\nu}_\tau$ simulation samples

Results using the 2012 signal,  $\Lambda_b^0 \rightarrow \Lambda_c^+ \tau (\rightarrow 3\pi\nu_\tau) \bar{\nu}_\tau$ , sample are presented. Events need to pass the final selection described in Sec. 5.3. The resolution on the  $\Lambda_b^0$  momentum can be seen on Fig. 5.22, the  $q^2$  one is shown in Fig. 5.23, both resolutions show no significant bias. Finally, the  $\tau$  decay time is also presented in Fig. 5.24.

### 5.5.2.2 $\Lambda_b^0 \rightarrow \Lambda_c^+ D_s^-$ simulation samples

Results using the 2012  $\Lambda_c^+ D_s^-$  background sample,  $\Lambda_b^0 \rightarrow \Lambda_c^+ D_s^- (\rightarrow 3\pi N)$ , sample are presented. The resolution on the  $\Lambda_b^0$  momentum can be seen on Fig. 5.25, the  $q^2$  one is shown in Fig. 5.27. Finally, the  $\tau$  decay time is also presented in Fig. 5.28.

As for the results on the signal samples, no clear sign of bias is visible on the resolution plots for both the reconstructed  $\Lambda_b^0$  momentum and the  $q^2$ . As both  $D_s^{*-}$  and  $D_s^{**}$  events in addition to  $D_s^-$  ones are present in the simulation sample, one can compare the result of the partial reconstruction for each sub-component as shown for the  $q^2$  in Fig. 5.26, again no clear bias is visible.

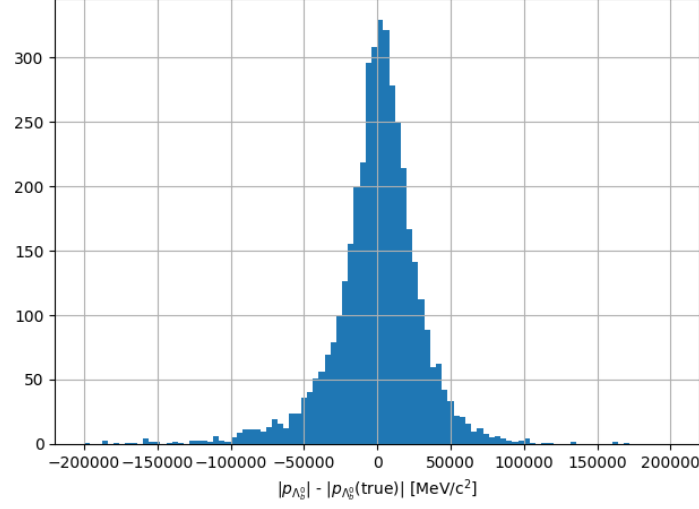


Figure 5.22 – Resolution on the reconstructed  $\Lambda_b^0$  momentum ( $|p_{\Lambda_b^0}| - |p_{\Lambda_b^0}(true)|$  using the signal reconstruction technique.)

### 5.5.3 Partial reconstruction of $\Lambda_b^0 \rightarrow \Lambda_c^+ D_s^-$ events

One can write the momentum conservation equation for events coming from  $\Lambda_b^0 \rightarrow \Lambda_c^+ D_s^-$  decays as follows:

$$|\vec{p}_{\Lambda_b^0}| \vec{u}_{\Lambda_b^0} = p_{\Lambda_c^+}^{\vec{}} + |p_{D_s^-}^{\vec{}}| u_{D_s^-}^{\vec{}} \quad (5.25)$$

In Eq. 5.25,  $p_{\Lambda_b^0}^{\vec{}}$ ,  $p_{D_s^-}^{\vec{}}$  and  $p_{\Lambda_c^+}^{\vec{}}$  are the momenta of the particles involved in the decay and  $u_{\Lambda_b^0}^{\vec{}}$ ,  $u_{D_s^-}^{\vec{}}$  are their unit vectors. Using simple vectorial algebra, two methods are available to compute the values of  $p_{\Lambda_b^0}^{\vec{}}$  and  $p_{D_s^-}^{\vec{}}$ , they will be referred as *vectorial* and *scalar* approaches in the rest of the section and denote with respectively a subscript v or s.  $\Lambda_b^0$  and  $D_s^-$  momenta can be expressed as:

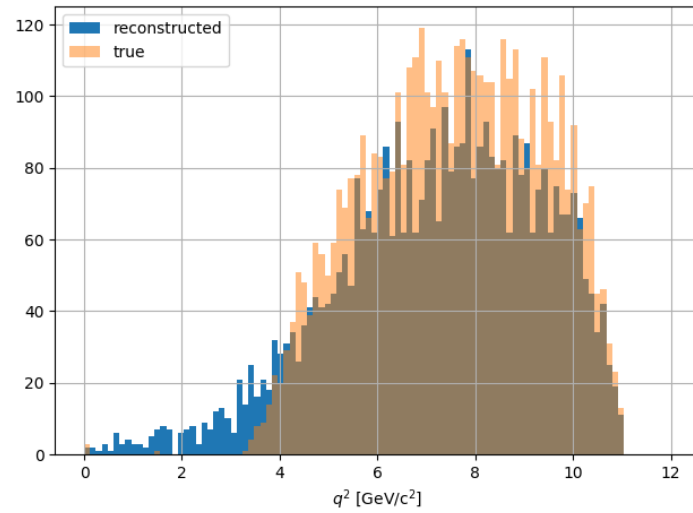
$$P_{\Lambda_b^0, v} = \frac{|p_{\Lambda_c^+}^{\vec{}} \times u_{D_s^-}^{\vec{}}|}{|u_{\Lambda_b^0}^{\vec{}} \times u_{D_s^-}^{\vec{}}|} \quad (5.26)$$

$$P_{\Lambda_b^0, s} = \frac{u_{\Lambda_c^+}^{\vec{}} \cdot u_{\Lambda_b^0}^{\vec{}} - (p_{\Lambda_c^+}^{\vec{}} \cdot u_{D_s^-}^{\vec{}})(u_{\Lambda_b^0}^{\vec{}} \cdot u_{D_s^-}^{\vec{}})}{1 - (u_{\Lambda_b^0}^{\vec{}} \cdot u_{D_s^-}^{\vec{}})^2} \quad (5.27)$$

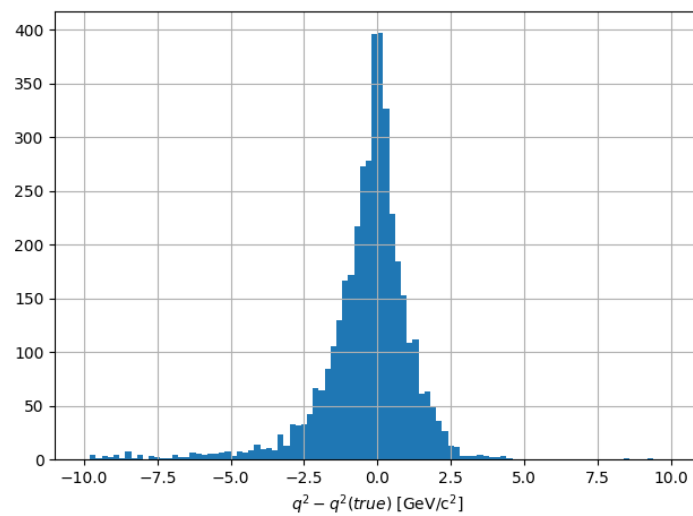
$$P_{D_s^-, v} = \frac{|p_{\Lambda_c^+}^{\vec{}} \times u_{\Lambda_b^0}^{\vec{}}|}{|u_{D_s^-}^{\vec{}} \times u_{\Lambda_b^0}^{\vec{}}|} \quad (5.28)$$

$$P_{D_s^-, s} = \frac{(p_{\Lambda_c^+}^{\vec{}} \cdot u_{\Lambda_b^0}^{\vec{}})(u_{\Lambda_b^0}^{\vec{}} \cdot u_{D_s^-}^{\vec{}}) - p_{\Lambda_c^+}^{\vec{}} \cdot u_{D_s^-}^{\vec{}}}{1 - (u_{\Lambda_b^0}^{\vec{}} \cdot u_{D_s^-}^{\vec{}})^2} \quad (5.29)$$

To reconstruct  $\Lambda_b^0$  and  $D_s^-$  momenta, one thus uses:

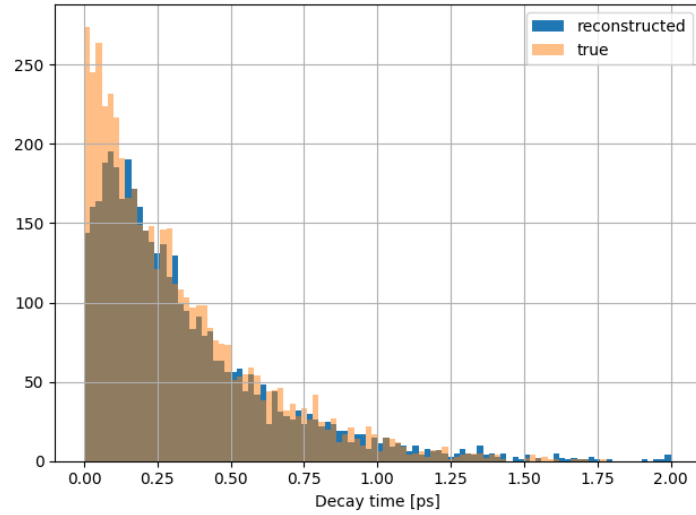


(a)

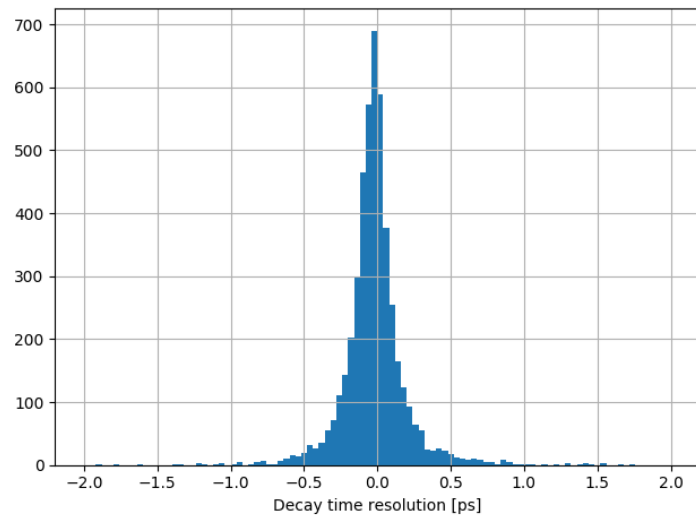


(b)

Figure 5.23 – Reconstructed  $q^2$  (blue) to be compared with the true  $q^2$  (red) distribution for signal  $\Lambda_B^0 \rightarrow \Lambda_C^+ \tau^- (\rightarrow 3\pi\nu_\tau) \bar{\nu}_\tau$  simulation sample (a) and the associated resolution on  $q^2$ :  $(q^2 - q^2(\text{true}))$  (b).



(a)



(b)

Figure 5.24 – Reconstructed  $\tau$  decay time (blue) to be compared with the true one (orange) for signal  $\Lambda_b^0 \rightarrow \Lambda_c^+ \tau^- (\rightarrow 3\pi\nu_\tau) \bar{\nu}_\tau$  simulation sample (a) and the associated resolution on the  $\tau$  decay time (b).

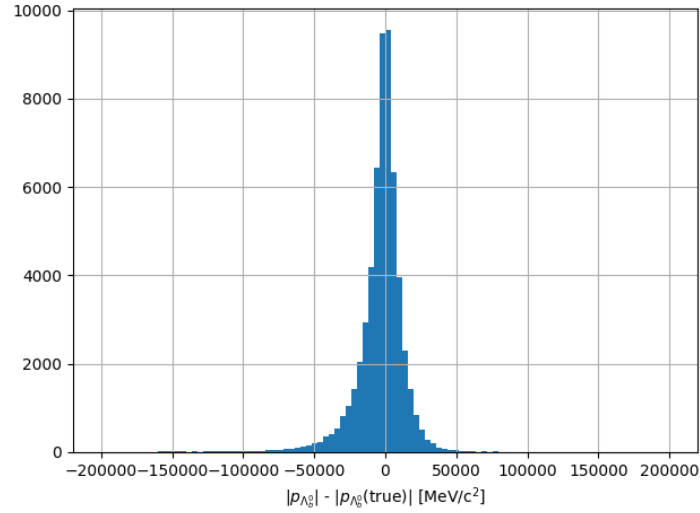


Figure 5.25 – Resolution on the reconstructed  $\Lambda_b^0$  momentum ( $|p_{\Lambda_b^0}| - |p_{\Lambda_b^0}(true)|$ ) using the signal reconstruction technique.

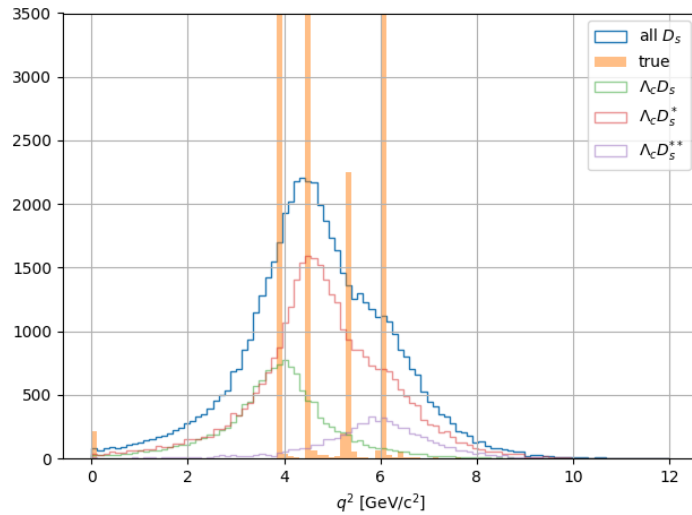
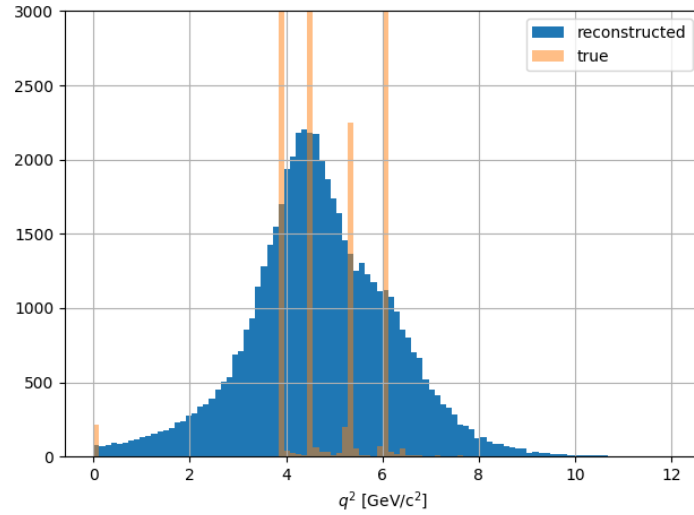
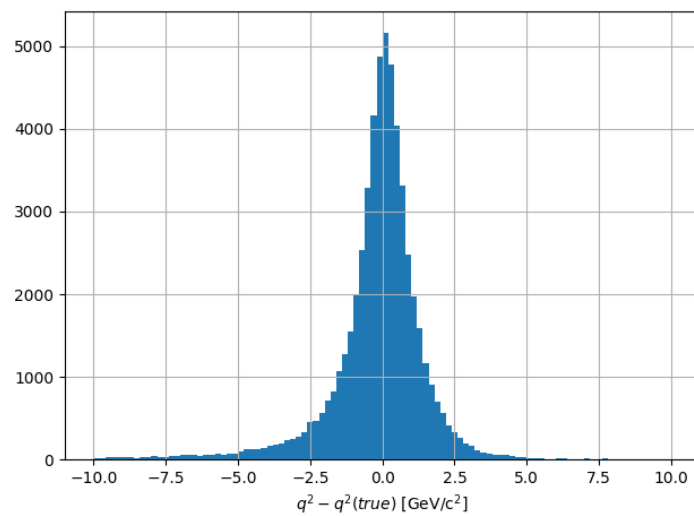


Figure 5.26 – Reconstructed  $q^2$  (blue) to be compared with the true  $q^2$  (red) distribution for  $\Lambda_b^0 \rightarrow \Lambda_c^+ D_s^- (\rightarrow 3\pi N)$  background simulation sample. The  $q^2$  distribution is also splitted in  $D_s$  (green),  $D_s^*$  (red) and  $D_s^{**}$  (purple) contributions.

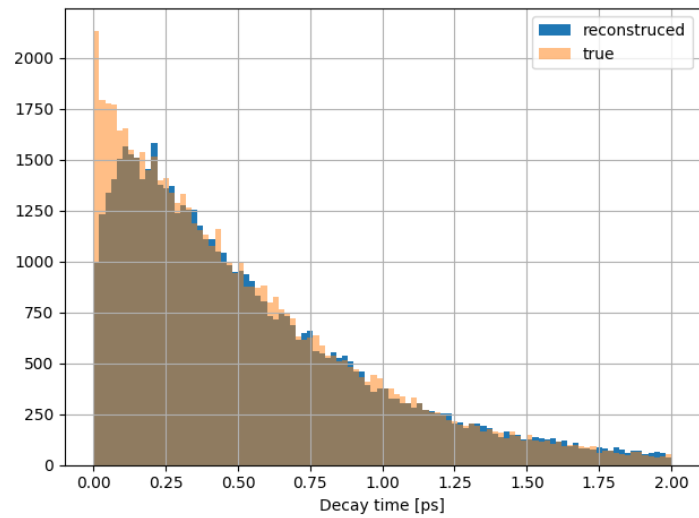


(a)

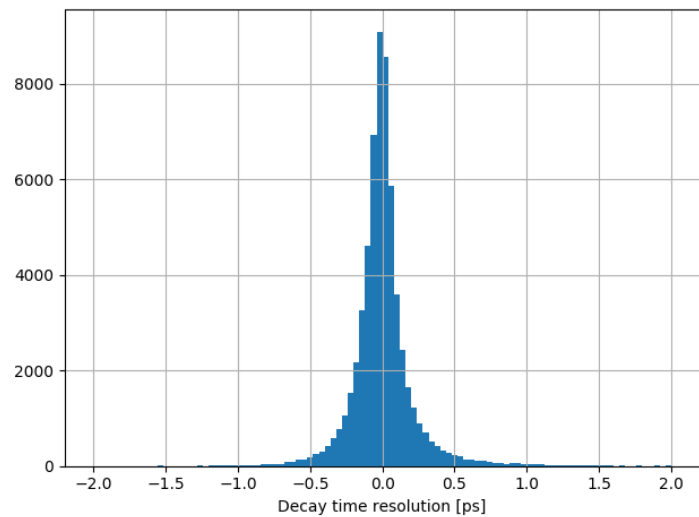


(b)

Figure 5.27 – Reconstructed  $q^2$  (blue) to be compared with the true  $q^2$  (red) distribution for  $\Lambda_b^0 \rightarrow \Lambda_c^+ D_s^- (\rightarrow 3\pi N)$  background simulation sample (a) and the corresponding resolution on the  $q^2$ :  $(q^2 - q^2(\text{true}))$  (b).



(a)



(b)

Figure 5.28 – Reconstructed  $\tau$  decay time (blue) to be compared with the true one (orange) for  $\Lambda_b^0 \rightarrow \Lambda_c^+ D_s^- (\rightarrow 3\pi N)$  background simulation sample (a) and its resolution (b).

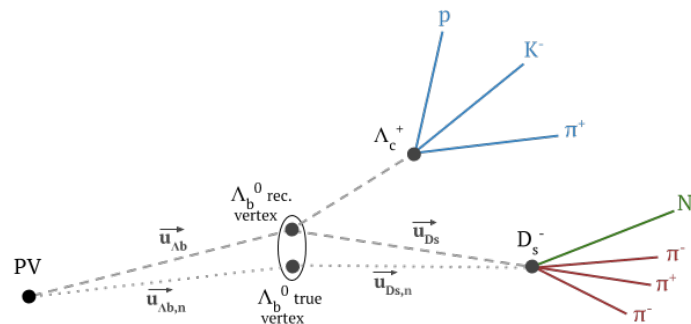


Figure 5.29 – Scheme of the decay  $\Lambda_b^0 \rightarrow \Lambda_c^+ D_s^- (\rightarrow \pi^- \pi^+ \pi^- N)$ .

- $\vec{p}_{\Lambda_c^+}$  which is fully reconstructed
- $\vec{u}_{\Lambda_b^0}$  giving the direction of the line joining  $\Lambda_b^0$  and primary vertices
- $\vec{u}_{D_s^-}$  which is the direction of the  $D_s^-$  neglecting potential neutral particles, denoted as  $N$  in Fig. 5.29

To take into account the neutral component of the  $D_s^-$  momentum, one can extend this method by applying a correction to the  $\Lambda_b^0$  vertex position. This correction is obtained as a function of the mass of the three charged pions ( $m(3\pi)$ ), using a  $\Lambda_b^0 \rightarrow \Lambda_c^+ D_s^-$  simulation sample, with  $D_s^-$  selected to decay into  $3\pi\pi^0$ .

Fig. 5.30 presents the profile of the correction to add to the  $\Lambda_b^0$  vertex position along the  $z$ -axis:  $-d_z$  ( $-d_z = vtx_z(\Lambda_b^0) - vtx_z(\Lambda_b^0)^{true}$ ) as a function of  $m(3\pi)$ .

A parabolic function is chosen to fit this profile, and the dependence of  $-d_z$  can be expressed as:

$$-d_z = 0.578 + (5.823 \times 10^{-4}) \times m(3\pi) + (1.489 \times 10^{-7}) \times m(3\pi)^2 \quad (5.30)$$

with  $d_z$  expressed in mm and  $m(3\pi)$  in MeV/ $c^2$ .

The effect of this correction on the resolution of the  $\Lambda_b^0$  vertex is shown in Fig. 5.31. Although the effect is fairly small, the  $\Lambda_b^0$  vertex resolution gets smaller after the correction is applied

Using this correction, it is then possible to recompute the  $\Lambda_b^0$  vertex position and compute new unit vectors called  $\vec{u}_{D_s^-}$  and  $\vec{u}_{\Lambda_b^0}$ . Using equations 5.26 to 5.29, new momentum values can be expressed for both  $\Lambda_b^0$  and  $D_s^-$  by plugging in these new vector units. These new momentum variables are then called  $P_{\Lambda_b^0, vn}$ ,  $P_{\Lambda_b^0, sn}$ ,  $P_{D_s^-, vn}$  and  $P_{D_s^-, sn}$ .  $D_s^-$  masses in these various schemes can also be computed and are denoted  $m_{D_s^-, v, s, vn, sn}^2$ .

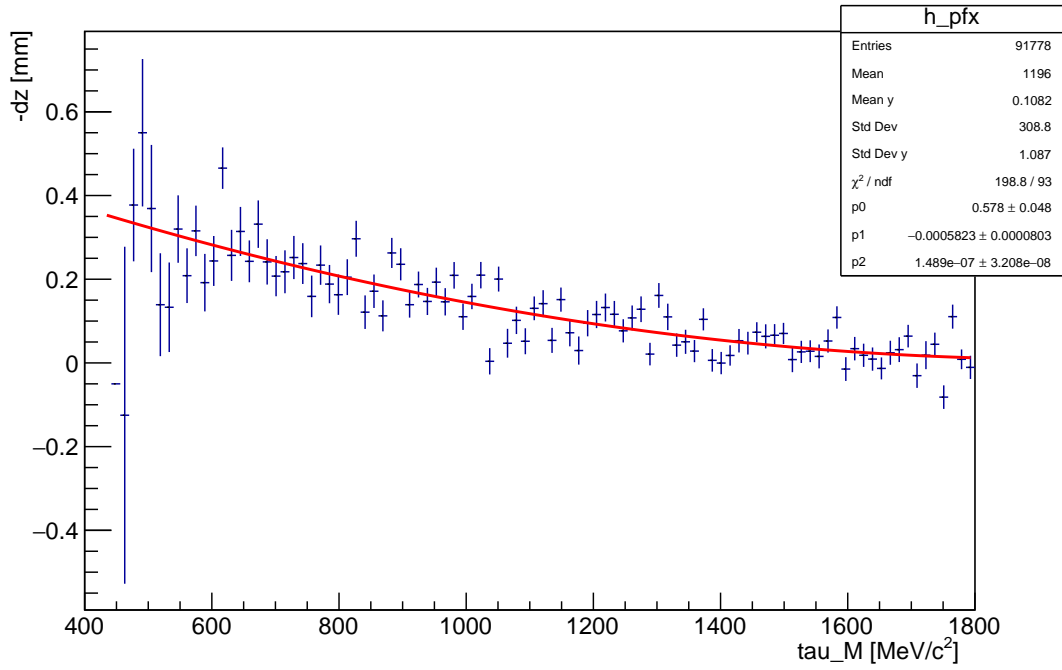


Figure 5.30 – The profile of the correction  $-d_z$  as a function of  $m(3\pi)$ . A parabola is chosen as the fit model.

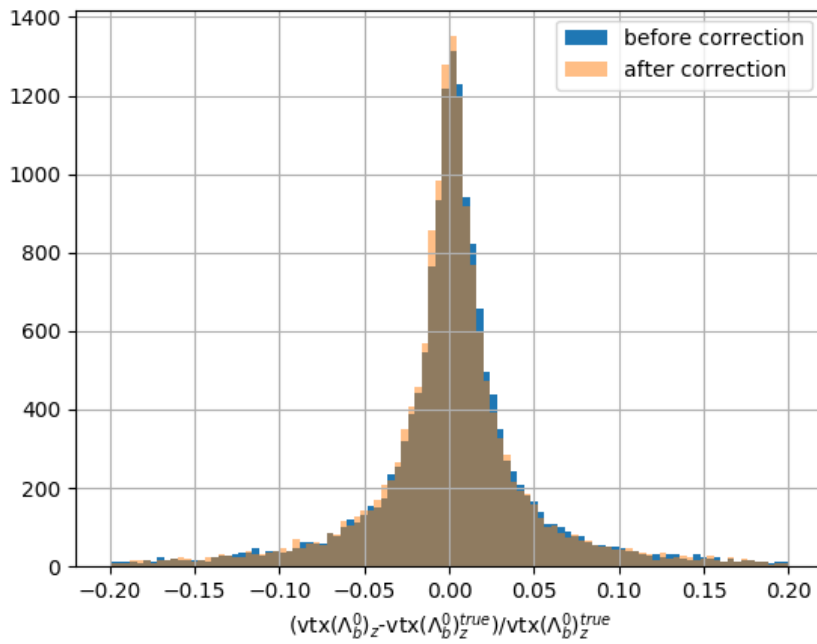


Figure 5.31 – Resolution on the  $\Lambda_b^0$  vertex ( $z$  component) on  $\Lambda_b^0 \rightarrow \Lambda_c^+ D_s^-$  simulation sample, before and after the correction  $-d_z$  is applied.

## 5.6 Estimation of the efficiencies

Efficiencies need to be precisely known for both normalisation and signal modes. The main goal is to know for each step of the selection the ratio of signal and normalisation efficiencies and the associated uncertainties as precisely as possible as the efficiency ratio is used to compute  $\mathcal{K}(\Lambda_c^+)$  and thus  $\mathcal{R}(\Lambda_c)$ .

As they are estimated using simulation samples, in addition to the computation of the efficiencies, this section also presents several studies for data and simulation disagreement, performed using the exclusive peak  $\Lambda_b^0 \rightarrow \Lambda_c^+ 3\pi$ .

Efficiencies for both modes need to be split according to the various selection steps of the analysis, such as:

$$\epsilon_{analysis} = \epsilon_{sel} \times \epsilon_{stripping} \times \epsilon_{trigger} \times \epsilon_{acc} \quad (5.31)$$

The acceptance efficiency ( $\epsilon_{acc}$ ) is taken from the simulation procedure. The trigger efficiency is evaluated using the TISTOS method which estimates the trigger efficiency by using the events belonging to both TIS and TOS trigger categories.

### 5.6.1 Trigger efficiencies

Trigger efficiencies are computed for both L0 and HLT2 trigger levels and MC/Data disagreement are studied and correction factors are defined.

#### 5.6.1.1 L0 trigger efficiencies

To study the L0Hadron effects in this analysis, the TISTOS method described in [94], is used.

L0 trigger efficiencies are then defined as:

$$\epsilon_{\text{L0Hadron\_TOS}} = \frac{N_{events}(\text{L0Hadron\_TOS} \ \& \ \text{LOGlobal\_TIS})}{N_{events}(\text{LOGlobal\_TIS})} \quad (5.32)$$

$$\epsilon_{\text{LOGlobal\_TIS}} = \frac{N_{events}\text{L0Hadron\_TOS}\&\&\text{LOGlobal\_TIS}}{N_{events}\text{L0Hadron\_TOS}} \quad (5.33)$$

L0Hadron properties are sensitive to any neutral energy produced with the  $\Lambda_c^+ 3\pi$  system. As no additional energy is present in the main component of the signal channel  $\Lambda_c^+ \tau \nu_\tau$ , exclusive channels are selected to perform the study in both MC and data samples. Two channels can be considered,  $\Lambda_b^0 \rightarrow \Lambda_c^+ 3\pi$  and  $\Lambda_b^0 \rightarrow \Lambda_c^+ D_s^- (\rightarrow 3\pi)$ . The first one benefits from large statistics but only covers the normal topology case whether the second one is well suited for both normal and inverted topologies<sup>3</sup> but the statistics is limited.

<sup>3</sup>Event topology is discussed in depth in Sec. 5.3.

The selection for this study consists in the cuts presented in Tab. 5.4 with the isolation requirements described in Sec. 5.3 and the trigger requirement defined at the beginning of this section.

Tab. 5.6 presents the efficiencies of each available sample.

Table 5.6 – L0Hadron efficiencies computed for several exclusive samples in data and simulation for 2012 conditions.

Sample	Data/MC	Nb of events	Vertex topology	Efficiency (%)
$\Lambda_c^+ 3\pi$	Data	4326	Normal	33.6
$\Lambda_c^+ 3\pi$	MC	1206	Normal	56.0
$\Lambda_c^+ \tau \nu_\tau$	MC	471	Normal	53.1
$\Lambda_c^+ \tau \nu_\tau$	MC	917	Inverted	39.8

The L0Hadron efficiency is strongly correlated to the  $3\pi$  transverse momentum. Fig. 5.32, show the efficiency of the L0Hadron trigger as a function of the transverse momentum of the  $3\pi$  for  $\Lambda_b^0 \rightarrow \Lambda_c^+ 3\pi$  in both simulation and data samples in 2012 conditions for normal event topology.

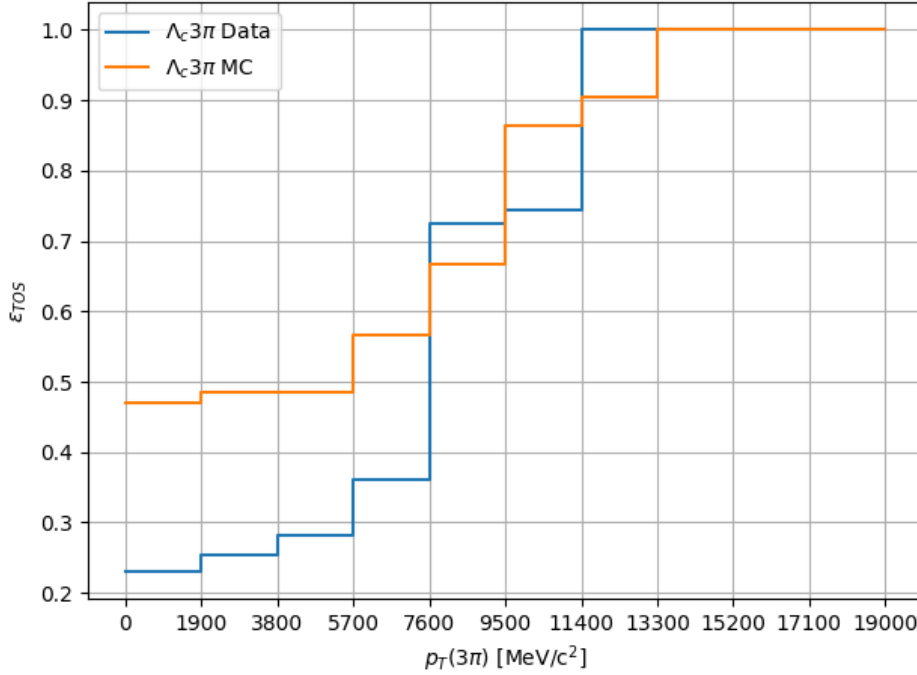


Figure 5.32 – Efficiency of the L0Hadron trigger as a function of  $p_T(3\pi)$  measured using  $\Lambda_b^0 \rightarrow \Lambda_c^+ 3\pi$  in normal topology. Blue and orange curves are respectively data and simulation efficiencies in 2012 conditions.

The ratio of these two distributions shown in Fig. 5.33 is fitted using a polynomial function to compute the weights used to correct the overestimate of the L0Hadron efficiency in simulation samples. There is a strong overestimate of the L0 efficiency in the simulation at low  $p_T(3\pi)$  and the ratio still leaves a 10% correction to take into account.

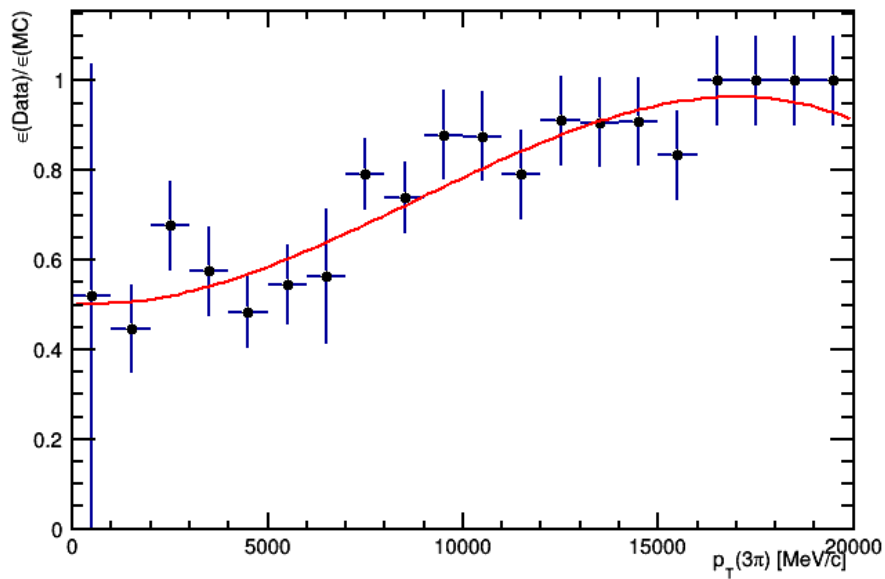


Figure 5.33 – Distribution of the efficiency correction as a function of  $p_T(3\pi)$  to be applied on simulation samples to match the data L0Hadron trigger efficiency.

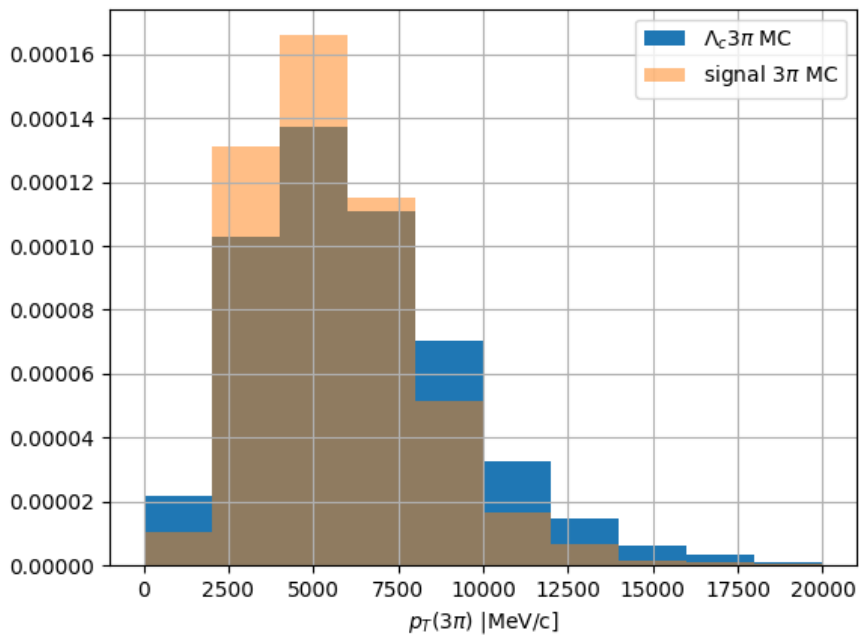


Figure 5.34 – Normalised distributions of  $p_T(3\pi)$  for both signal and normalisation 2012 simulation samples.

### 5.6.1.2 Effects of the SPD multiplicity

The L0 trigger efficiency for both L0Hadron\_T0S and L0Global\_TIS events is dependent on the number of hits in the SPD detector. This study is performed on the exclusive peak of  $\Lambda_b^0 \rightarrow \Lambda_c^+ 3\pi$  in both data and simulation samples.

First, the agreement on the distribution of hits in the SPD is performed between simulation and data samples. Thus, the number of hits in the SPD in simulation needs to be scaled by a factor 1.4 to reproduce the distribution in data. This is presented in Fig. 5.35.

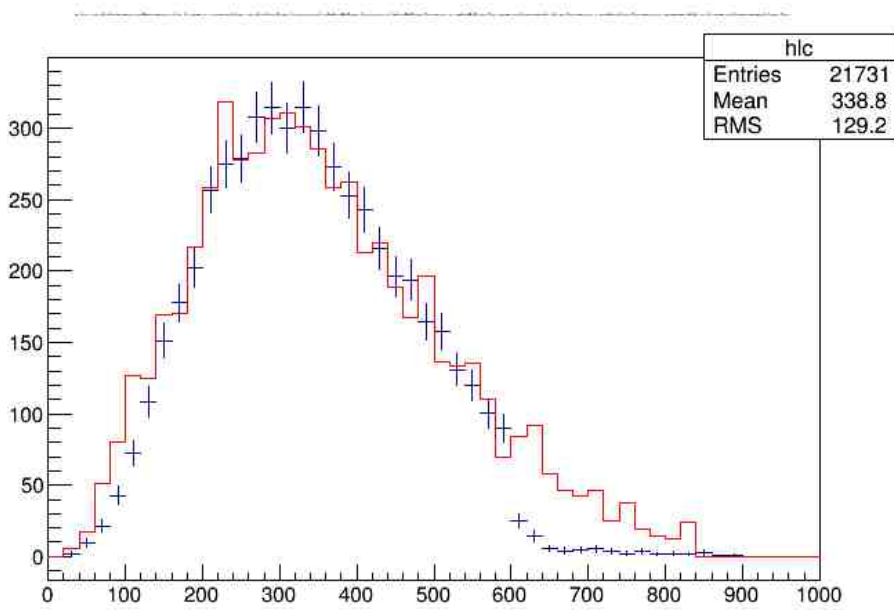


Figure 5.35 – Comparison between the number of hits in the SPD for data (blue) and simulation (red) for events in the exclusive peak of  $\Lambda_b^0 \rightarrow \Lambda_c^+ 3\pi$ .

The distribution for simulation is scaled by a factor 1.4 in order to match the data one.

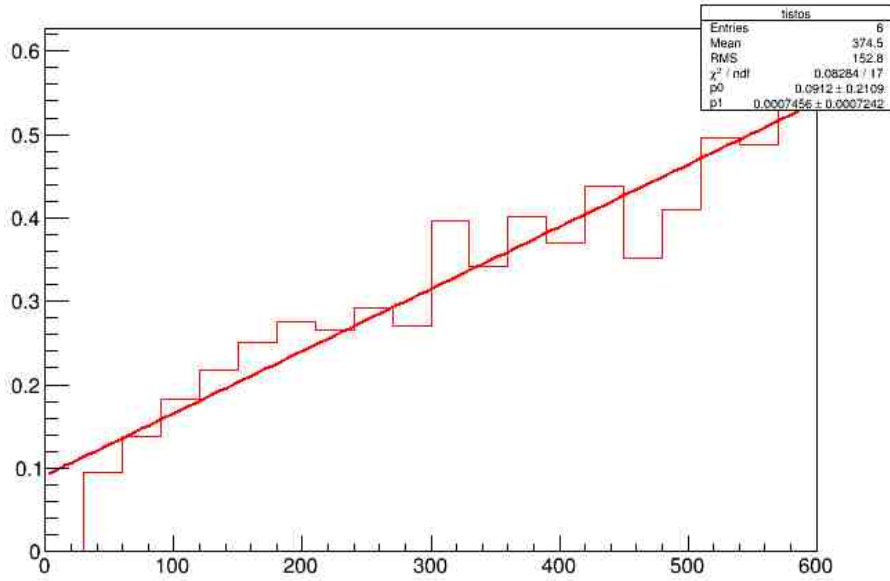


Figure 5.36 – L0TIS efficiency as a function of the number of hits in the SPD for events in the exclusive peak of  $\Lambda_b^0 \rightarrow \Lambda_c^+ 3\pi$  in data.

### 5.6.1.3 HLT2 efficiencies

Simulation samples used in this analysis are filtered at the stripping level requiring events to pass a topological Hlt2 trigger line or one of the CharmHadron ones. This preselection of trigger-lines is tighten using the lines specified in Sec. 5.3.1 and can be divided in two categories, Hlt2 trigger topological trigger lines which will be referred as trigger **Topo** and a set of lines dedicated for the  $\Lambda_c^+$  candidate which defines a **Lc** trigger.

As the trigger study is performed on samples after the stripping processing, one can measure:

$$\epsilon_{\text{not OR}} = \frac{N_{\text{events}}(\text{not (Lc or Topo)})}{N_{\text{events}}} \quad (5.34)$$

$$\epsilon_{\text{Lc|Topo}} = \frac{N_{\text{events}}(\text{Lc \& Topo})}{N_{\text{events}}(\text{Topo})} \quad (5.35)$$

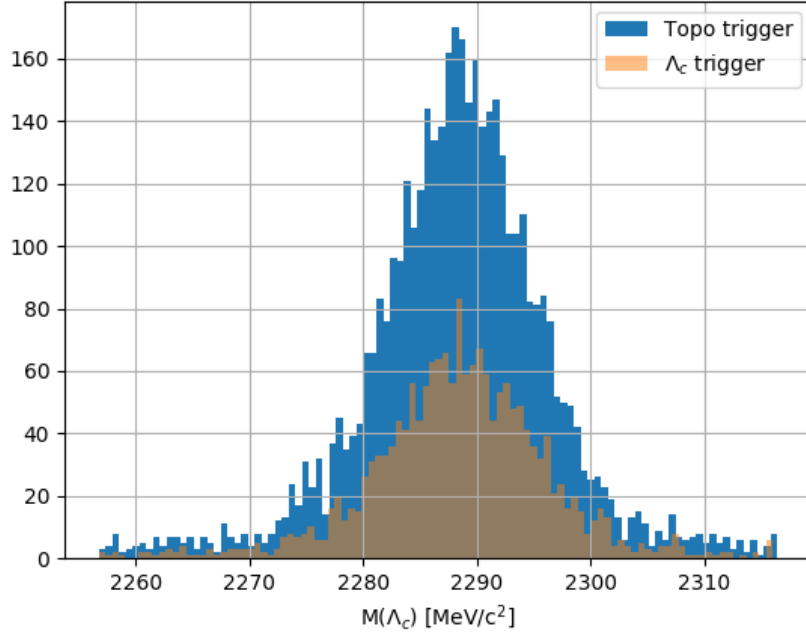
$$\epsilon_{\text{Topo|Lc}} = \frac{N_{\text{events}}(\text{Topo \& Lc})}{N_{\text{events}}(\text{Lc})} \quad (5.36)$$

The number of events which does not pass our trigger selection, is measured to be 1156 events out of 17684 in 2012 data and 264 out of 5282 for  $\Lambda_c^+ 3\pi$  events. This means that  $\epsilon_{\text{not OR}}$  is 6.5% in 2012 in data and 4.9% in simulation.

Table 5.7 – Efficiencies on  $\Lambda_c^+$   $3\pi$  events for both MC and data after stripping and selection cuts.

Year	Trigger line	Hlt2 efficiency (%)
2012 (data)	Topo	92.6
	Lc	32.4
2012 (MC)	Topo	97.7
	Lc	45.1

The efficiency of the Lc trigger part is overestimated in simulation but this effect is limited due to the fact that the Topo trigger part accounts for the majority of triggered events and benefits from a better estimation in simulation.


 Figure 5.37 –  $pK\pi$  mass distribution for both Topo (blue) and Lc (orange) trigger configurations for 2012 conditions.

Hlt2 efficiencies are studied as defined in Eq. 5.34, Eq. 5.35 and Eq. 5.36 as a function of the square momentum transferred to the  $\tau\nu_\tau$  system  $q^2$ . Efficiencies for both Topo, Lc trigger configurations and their union, denoted as OR is shown in Fig. 5.38.

## 5.6.2 Stripping efficiencies

The stripping efficiency is evaluated for both signal ( $3\pi$  and  $3\pi\pi^0$ ) and normalisation for each year of data taking in Tab. 5.8. The signal efficiency is the average of efficiencies for each signal mode weighted by its branching fraction.

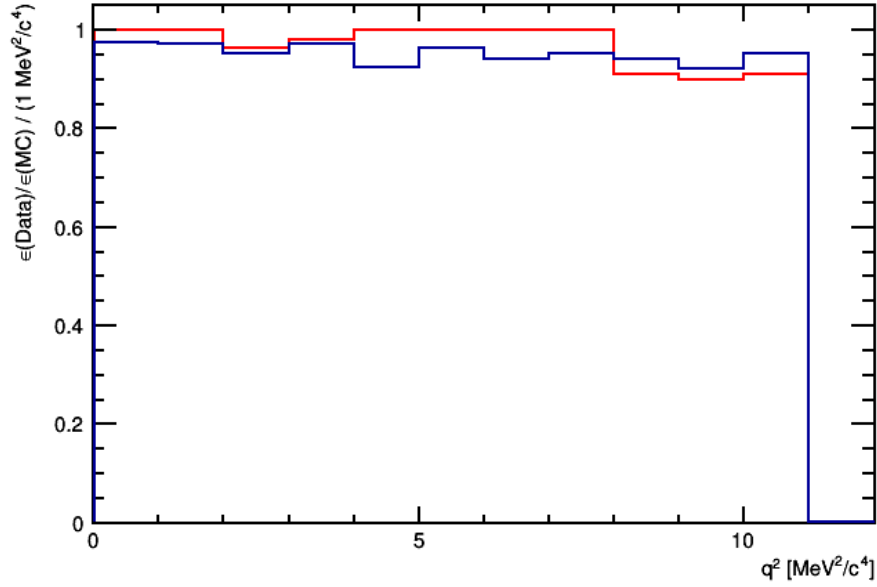


Figure 5.38 – Efficiency for the Topo trigger measured on events triggered by the  $\Lambda_c^+$  trigger as a function of  $q^2$  for 2012 signal MC sample.

Year	$\epsilon_{\tau 3\pi}(\%)$	$\epsilon_{\tau 3\pi\pi^0}(\%)$	$\epsilon_{sig}(\%)$	$\epsilon_{norm}(\%)$	$\epsilon_{sig}/\epsilon_{norm}$
2011	0.40	0.35	0.38	0.67	0.572
2012	0.36	0.33	0.35	0.59	0.593

Table 5.8 – Stripping efficiencies for both signal and normalisation channels for each year of data taking.

### 5.6.3 Selection efficiencies

To check any discrepancy between data and simulation samples concerning selection efficiencies, a detailed comparison of the efficiency of each cut applied performed on the exclusive peak of  $\Lambda_b^0 \rightarrow \Lambda_c^+ 3\pi$  is performed and shown in Tab. 5.9. It shows that each cut is well described by the simulation with a typical error of 1.5%.

Table 5.9 – Detailed comparison of selection efficiencies on the  $\Lambda_b^0 \rightarrow \Lambda_c^+ 3\pi$  exclusive peak in both data and simulation samples for 2012 conditions.

cut	Data	MC
$\text{BPVVDR}(\tau) \in [0.25, 5.2] \text{ mm}$	$100 \pm 0.03$	94.4
$\chi^2[\text{vt}x(\Lambda_c^+)] < 15$	93.8	93.5
$\chi^2[\text{IP}_{PV}(\Lambda_c^+)] > 15$	99.6	99.1
$\chi^2[\text{vt}x(\tau)] < 10$	88.8	87.4
$\text{ProbNNp}(\text{p}) > 0.2$	89.5	90.7
$\text{ProbNNp}(\text{K}) > 0.3$	89.8	91.8
$PV_\tau = PV_{\Lambda_c^+}$	95.3	94.2
number of $\Lambda_b^0$ candidates = 1	79.2	79.6
$\text{ProbNNp}(\pi) > 0.6$	73.3	73.9
all cuts	36.9	35.3

The Tab. 5.10 presents a summary of the efficiencies for each part of the selection of events for both signal and normalisation channels.

Category	$\Lambda_b^0 \rightarrow \Lambda_c^+ 3\pi$	Signal	
		$\tau \rightarrow 3\pi$	$\tau \rightarrow 3\pi\pi^0$
Acceptance (%)	15.61	16.15	15.57
Filter (%)	0.607	0.375	0.334
Reduction (%)	32.5	32.6	26.8
Cleaning (%)	65.3	65.8	68.1
Charged isolation (%)	72.6	71.6	65.0
M(W) cut (%)	-	85.3	87.3
Vertex selection (%)	-	31.4	29.6
m( $3\pi$ ) cut (%)	-	98.7	100
ProbNNpi from $\Lambda_c^+$ (%)	95.6	95.8	94.1
Trigger (%)	96.8	89.0	90.0
$\Lambda_c^+$ feed-down removal (%)	91.9	-	-
$\Lambda_c^+$ mass window (%)	96.8	96.3	96.3
$\Lambda_c^+$ side band subtraction (%)	96.6	96.2	96.2
$\Lambda_c^+$ Gaussian Fit (%)	96.5	-	-
Overall efficiency	$10.44 \times 10^{-5}$	$1.63 \times 10^{-5}$	$0.999 \times 10^{-5}$

Table 5.10 – Detailed description of the efficiencies of the different selections applied for both signal and normalisation channels.

## 5.7 Description and performances of the BDT

As described before, the main background to be rejected after applying the event selection, especially the vertex detachment requirement, is coming from double charm decays with the major contribution being  $\Lambda_b^0 \rightarrow \Lambda_c^+ D_s^-$  events.

This analysis is relying on the `XGBoost` library [120] to create the Boosted Decision Tree (BDT) which will be used to distinguish signal from  $\Lambda_c^+ D_s^-$  events. `scikit-learn` [121] and `matplotlib` [122] libraries are also used for the tuning of the hyperparameters and the visualisation of the performances of the BDT.

### 5.7.1 Introduction on Boosted Decision Trees for event classification

#### 5.7.1.1 Classification using Machine Learning techniques

Boosted Decision Trees (BDT) are a subclass of Machine Learning (ML) algorithms. The common features of this wide category of algorithms is the possibility to detect statistical patterns in a provided dataset, "learning" information from the data, and apply this knowledge on a different dataset.

These algorithms are now widely spread in a wide variety of fields such as computer vision, spam emails filtering or handwriting recognition. In High Energy Physics, these algorithms are also very helpful for particle identification, tracking and event classification, which is the main subject of this section.

An ML algorithm dedicated for event classification, also referred as classifier, is designed to compute as an output a score for a given event, measuring how signal-like or background-like the event is. For the rest of this section, a score of 0 means a perfect background-like event whereas a score of 1 indicates a pure signal-like event.

Such algorithm needs to be provided a dataset of labelled data, meaning that background and signal are identified as such, to be able to apply the learned classification on a given dataset. The following steps can be identified to tune such algorithm:

- a subset of the labelled dataset is first provided to the algorithm. This is the training step: the internal parameters of the algorithm are tuned depending on the statistical patterns present in the dataset, also known as training sample.
- the other part of the labelled dataset is used to apply the algorithm on it, this is the test step. This step is crucial for the algorithm generalisation capability preventing it to be too sensible to the training sample features.
- the algorithm is then applied to the dataset of interest provided for each event a score on how likely it is to belong either to the background or signal category.

Several classification ML algorithms are available such as Support Vector Machines (SVC), Neural Networks (NN) or Boosted Decision Trees (BDTs) which will be further

discussed.

## 5.7.2 Definition of a Boosted Decision Tree algorithm

A Boosted Decision Tree can be described as an aggregate of Decision Trees (DT). Such Decision Trees, as illustrated in Fig. 5.39, are composed of nodes and decisions, *i.e.* rectangular cuts on the variables of the training dataset, linking them. The initial node, the root node with all the available training sample is split iteratively in new nodes. The cut chosen for each splitting is set to optimize the purity of the splitted dataset.

When the algorithm cannot further optimise the purity, it stops at the terminal nodes, the leaves, with the each subset being labelled either as a signal or background category depending on its content.

Relying only on decision trees to classify events is often not satisfying as they have the tendency to be overly sensitive to the training sample features and poorly perform on a new dataset.

The method to give satisfactory results using Decision Trees relies on two techniques:

- using an ensemble of DT instead of a single one, the score considered is then the average of the outputs of all the DTs.
- differentiate the training for each DT using a method called *boosting*. The misclassified events by the  $i$ -th DT are weighted higher than the ones classified correctly and the  $i + 1$ -th DT is trained on this weighted sample. In that way, DTs are only targeting on the events misclassified, they are ‘specialized’ in a sense. Boosting algorithms differ on the method to weight the dataset from one DT to another.

The first implementation of a boosting algorithm was designed in 1995 and is called the Adaptive Boosting (AdaBoost) [123]. In this analysis, the boosting algorithm is called Gradient Boosting and its implementation is presented in depth in [120].

## 5.7.3 Description of the BDT

This section describes the variables used to define the BDT, the simulation samples used to perform its training and performances.

### 5.7.3.1 The variables used in the BDT

To train the classifier, a set of 15 variables is chosen, they are related to partial reconstruction, isolation techniques, the three  $\pi$  system internal dynamics and kinematics.

**Partial reconstruction (6 variables)** As described in Sec. 5.5, two methods to reconstruct events are applied in two scenarios:

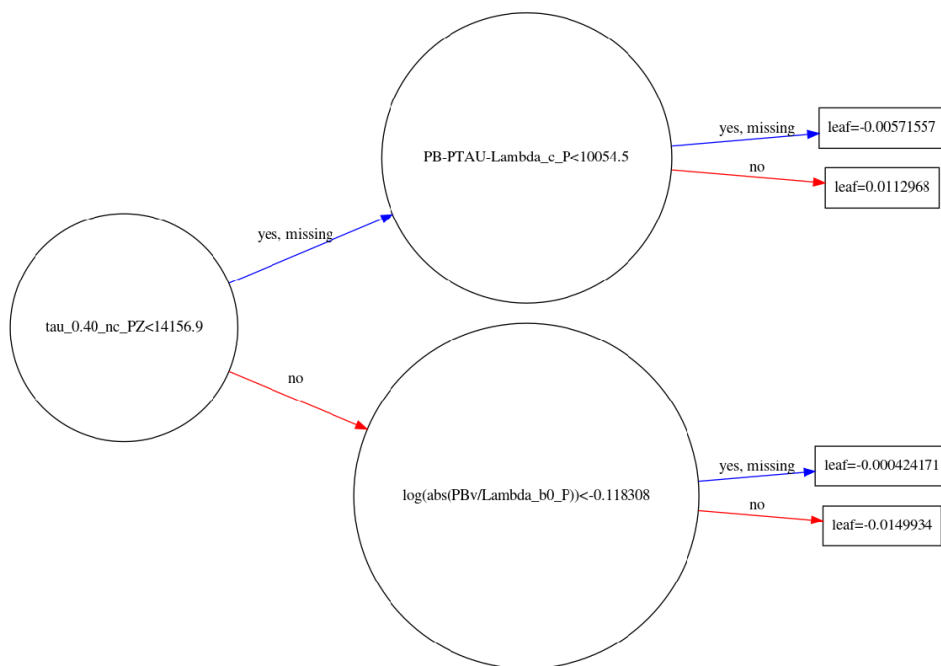


Figure 5.39 – A schematic view of one of the decision trees used in the BDT described in the following of this section. The initial node at the left is called the root node. Within each node is shown the particular variable used to split the dataset and the related cut value. On the extreme right are the external nodes, with their associated score. The score is related to the probability of being a signal-like event ( $p_{sig}$ ) by  $p_{sig} = \frac{1}{1+e^{-score}}$ .

- Reconstruction as a signal event:  
 One variable is coming from the reconstruction of the event under the signal hypothesis combining both  $\Lambda_b^0$  and  $\tau$  reconstructed momenta (see Sec. 5.5.1):
  1.  $|\vec{p}_{\Lambda_b^0}| - |\vec{p}_\tau| - |\vec{p}_{\Lambda_c^+}|$ : the energy of the neutrino emitted at the  $\Lambda_b^0$  vertex computed using the reconstructed momenta of both  $\Lambda_b^0$  and  $\tau$  as described in Sec. 5.5.1
- Reconstruction as a background event:  
 Events are reconstructed under the assumption of a  $\Lambda_b^0 \rightarrow \Lambda_c^+ D_s^-$  decay (See Sec. 5.5.3). From this reconstruction method, six variables are included in the BDT.
  2. `PBSn`: the  $\Lambda_b^0$  momentum reconstructed using the scalar product method after applying a correction to the  $\Lambda_b^0$  vertex position
  3. `log(abs(PBv/Lambda_b0_P)`: the ratio between the reconstructed  $\Lambda_b^0$  momentum and the visible one
  4. `log(abs((PBSn-PBvn)/PBvn))`: the normalized difference between both estimators of the  $\Lambda_b^0$  momentum
  5. `mN2v`: the squared mass of the reconstructed neutral vector
  6. `sqrt(abs(mDs2vn))`: the reconstructed mass of the  $D_{(s)}^{(*,**)}$  system

**Neutral and charged isolation (4 variables)** In most cases, the  $3\pi$  coming from a  $D_s^-$  decay are accompanied by a neutral energy component. This neutral energy can be looked for in cones around the  $3\pi$  system with various aperture as described in Sec. 5.4.2. Three variables carrying information about isolation of neutral particles are included in the BDT.

7. `tau_0_40_nc_mult`: the multiplicity of neutral particles in a cone with an aperture of 0.4, meaning that  $\Delta R = \sqrt{\Delta\phi^2 + \Delta\eta^2}$  between the considered neutral energy deposit and the  $\tau$  direction has to be below 0.4
8. `tau_0_40_nc_PZ`: the sum of the neutral energy contained in the cone of aperture 0.4

Even if a veto of non-isolated events using charged isolation at both  $\Lambda_b^0$  and  $\tau$  is included in the event selection, two variables are nevertheless used in the BDT:

9. `tau_0_20_cc_mult`: the multiplicity of charged particles in a cone of aperture 0.2
10. `tau_0_20_cc_PZ`: the energy located in a cone of aperture 0.2 centred around the  $3\pi$  vector

**The  $3\pi$  system dynamics (2 variables)** The dynamics of the  $3\pi$  system does not involve the same intermediate resonances for signal and background. If the  $3\pi$  system for the signal comes from a  $a_1$  decay, there are important contributions from  $\eta \rightarrow \pi^+ \pi^- \pi^0$

and  $\eta' \rightarrow \eta\pi^+\pi^-$  for  $D_s^-$  background events. As  $a_1 \rightarrow \rho\pi$ , the maximum of the two  $\pi^-\pi^+$  pairs will peak at the  $\rho$  mass for signal events whereas the  $\pi^-\pi^+$  mass distribution for  $D_s^-$  events is bound to be between 278 MeV/ $c^2$  and 400 MeV/ $c^2$ , meaning that  $m(\pi^-\pi^+)$  will have a stronger component at low mass for  $D_s^-$  events.

11.  $\min[m(\pi^+, \pi^-)]$
12.  $\max[m(\pi^+, \pi^-)]$

**Kinematics (3 variables)** Finally, kinematics variables are included in the BDT to reject other types of background events. `Lambda_b0_M` is especially useful to reject events where the  $D_s^-$  decays into  $\tau^-$  and events where the 3 pions do not all come from the same vertex.

13. `Lambda_b0_L0KI_BPVVDR`: the  $\rho$ -distance between the primary vertex and the  $\Lambda_b^0$  one
14. `tau_PE`: the energy of the  $3\pi$  system
15. `Lambda_b0_M`: the mass of the six tracks system

The BDT is trained on a simulation signal sample, combining both 2011 and 2012 data taking conditions, where the  $\tau$  decays in three charged pions.

The background sample is composed of all the available  $\Lambda_b^0 \rightarrow \Lambda_c^+ D_s^- X$  events from 2011 and 2012 simulation productions and a fraction of the  $\Lambda_b^0 \rightarrow \Lambda_c^+ D^- X$  and  $\Lambda_b^0 \rightarrow \Lambda_c^+ \bar{D}^0 X$  productions. A first implementation only using  $\Lambda_c^+ D_s^+$  events as background for the training showed that a significant amount of  $\Lambda_c^+ D_s^-$  and  $\Lambda_c^+ \bar{D}^0$  events ended up in the high BDT region, where the signal lies. The comparison between this first BDT and the one presented in this document is shown in Fig. 5.42. The BDT shapes for both signal and  $\Lambda_c^+ D_s^-$  samples are very similar but the peak at high BDT, indicating signal-like events, is removed in both  $\Lambda_c^+ D^0$  and  $\Lambda_c^+ D^-$  samples. This means that at the cost of a small degradation of the performances of the BDT for signal and  $\Lambda_c^+ D_s^-$  events, both  $\Lambda_c^+ D^0$  and  $\Lambda_c^+ D^-$  are much more distinguishable from signal ones which is crucial for the fit described in Sec. 5.10 to give optimal results.

Events in both samples are asked to pass the event selection described in Sec. 5.3, two additional cuts ( $M(\Lambda_c^+ 3\pi) < 5600$  MeV/ $c^2$  and  $M(3\pi) < 1800$  MeV/ $c^2$ ). They are then randomly splitted in half for training and testing of the BDT.

Distributions of variables included in the BDT for both signal and background are shown in Fig. 5.40 and the correlation matrices for both signal and background are presented in Fig. 5.41.

### 5.7.3.2 Performances and tuning of the parameters

To ensure that the BDT is not overtrained, distributions of its output for signal and background for both testing and training samples are shown in Fig. 5.43.

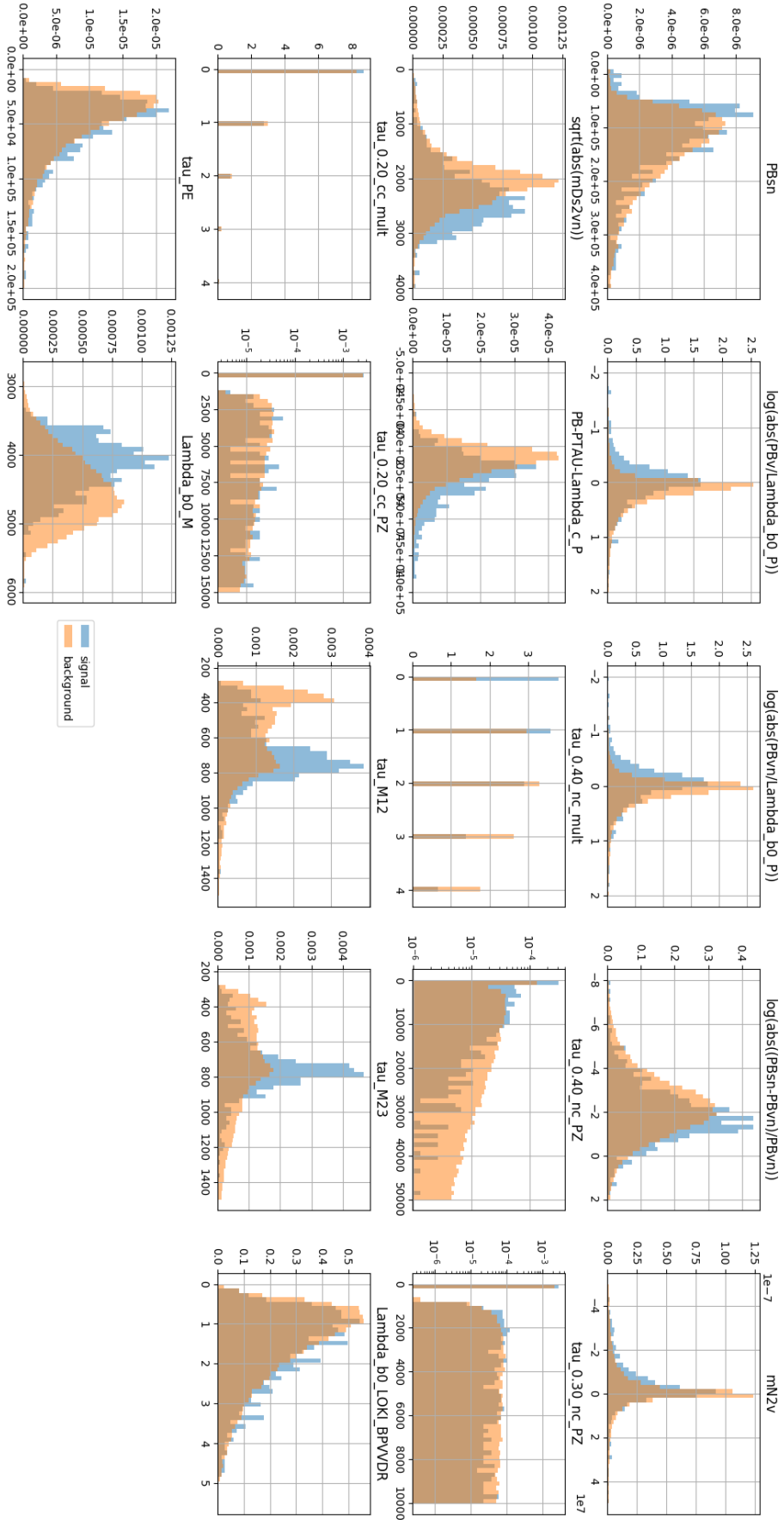


Figure 5.40 – Distributions of variables included in the BDT for signal (in blue) and background (in orange).

## 5.7. DESCRIPTION AND PERFORMANCES OF THE BDT

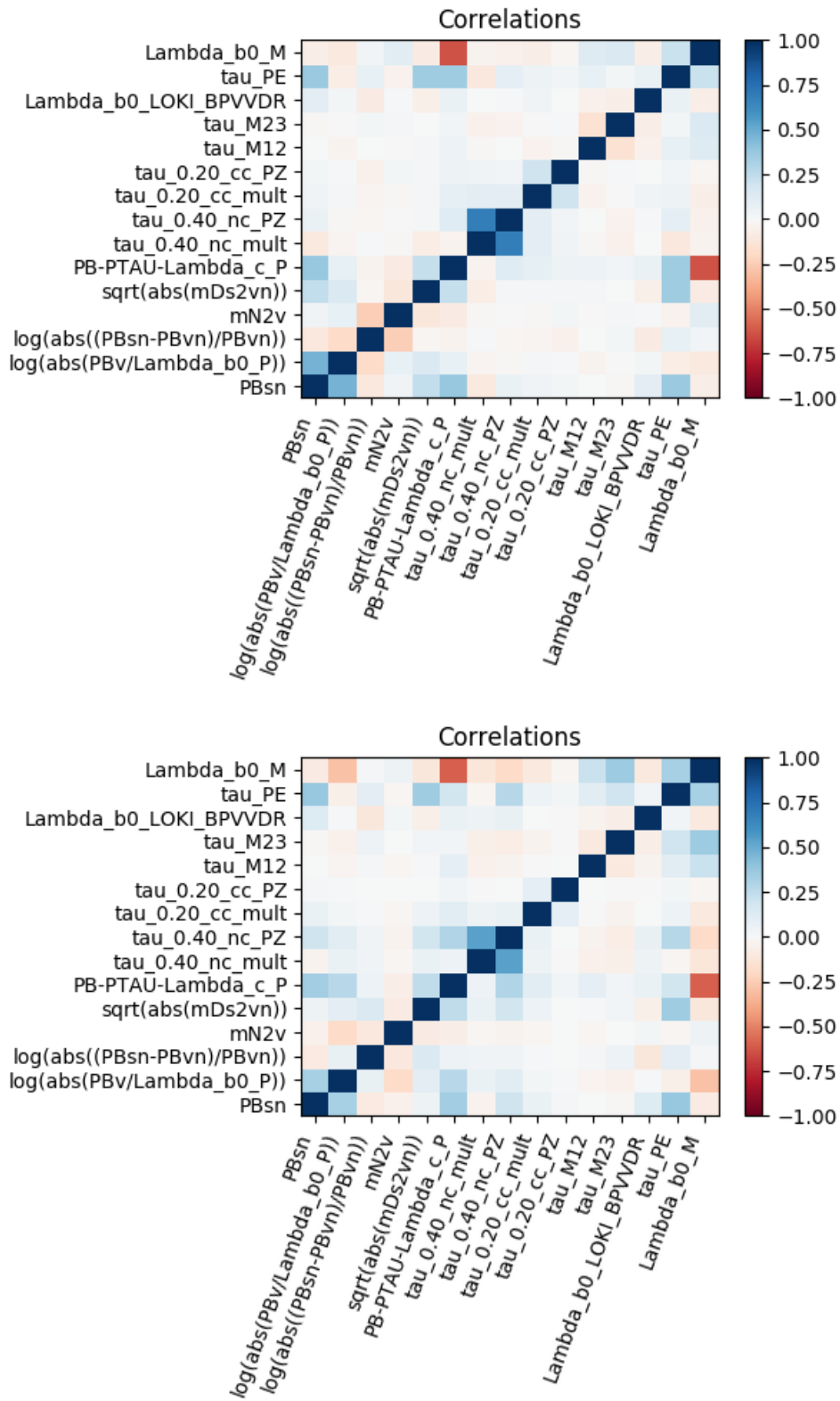


Figure 5.41 – Correlation Matrices for the input variables for both signal and background samples.

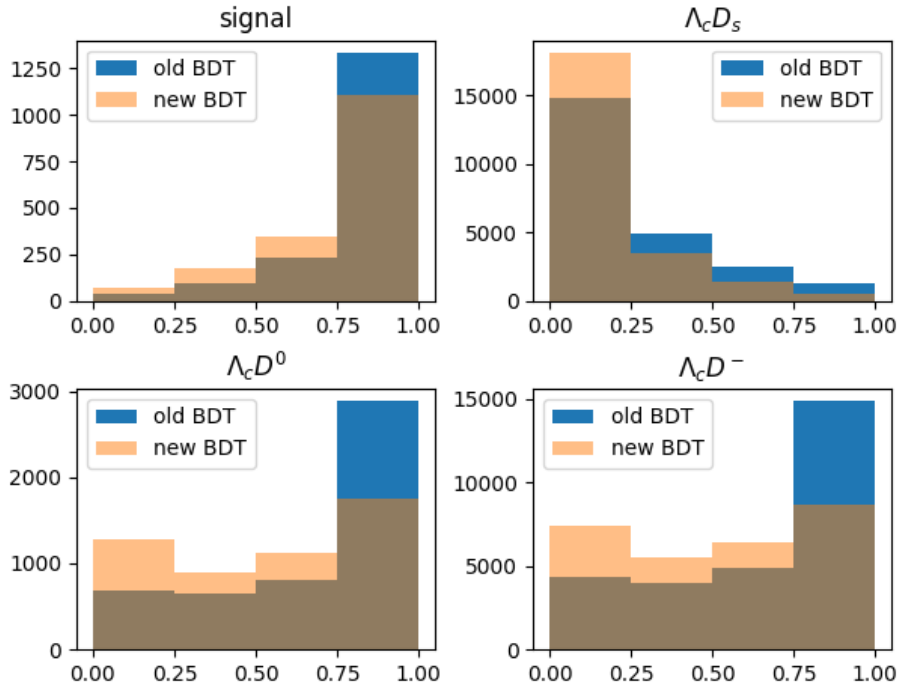


Figure 5.42 – Comparison of the output distributions of the first implementation of the BDT and the current one. The difference is the introduction of  $\Lambda_c^+ D_s^-$  and  $\Lambda_c^+ \bar{D}^0$  simulation events in the background dataset for the training.

The list of parameters used in the XGBoost implementation of a BDT and their tuning is as follows:

- learning\_rate: 0.01
- n\_estimators: 1000
- max\_depth: 2
- min\_child\_weight: 4
- subsample: 0.8
- colsample\_bytree: 0.8
- scale\_pos\_weight: 24.71

The learning rate corresponds to a weight added to each new decision tree during the training of the BDT. A low value of the learning rate, below 1, reduces the importance of an individual tree. n\_estimators is the number of trees considered in the BDT, max\_depth corresponds to the maximal number of layer of nodes in each decision tree. As max\_depth is set to 2, only two different cuts are considered per decision tree. These settings are meant to give robust results and to reduce the possibilities of overtraining. The same applies for the value of min\_child\_weight, which states the minimum of entries to have in an external node.

subsample and colsample\_bytree are parameters enabling the possibility to perform sub-

sampling in the construction of the decision trees, each decision tree is built using a randomly chosen subsample of the training dataset. By doing so, the final BDT is more robust.

The parameter `scale_pos_weight` is the balance between signal and background samples and is set to the ratio of number of events in signal and background training samples.

The ROC<sup>4</sup> curve is shown in Fig. 5.44, an area under the ROC curve of 0.92 is found which means that the BDT is performing well, and the importance score of each variable of the BDT is presented in Fig. 5.45.

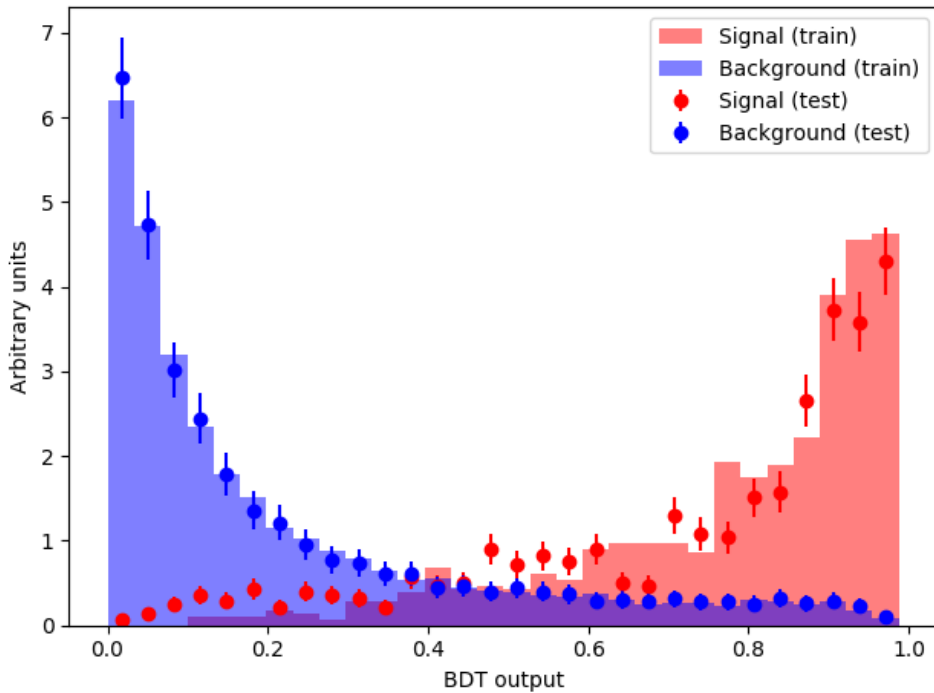


Figure 5.43 – The BDT output for both signal and background in training and testing samples.

With the parameters mentioned above, the signal efficiency estimated on a 2012 MC sample is 88% and 8% for the  $\Lambda_c^+ D_s^-$  sample with a cut on the BDT output at 0.5.

#### 5.7.4 Validation of the BDT

To check the validity of the BDT implementation, especially any simulation/data discrepancies that could bias its output, the normalised distribution of the output of the BDT for the events found in the  $\Lambda_b^0 \rightarrow \Lambda_c^+ 3\pi$  peak is shown in Fig. 5.46 using the normal-final selection. For the data distribution, the  $\Lambda_c^+$  background has been removed using the sideband subtraction method described in Sec. 5.3.6, both distributions agree reasonably well with each other.

<sup>4</sup>ROC stands for Receiver Operating Characteristic, which is a standard method to estimate the performances of a binary classifier.

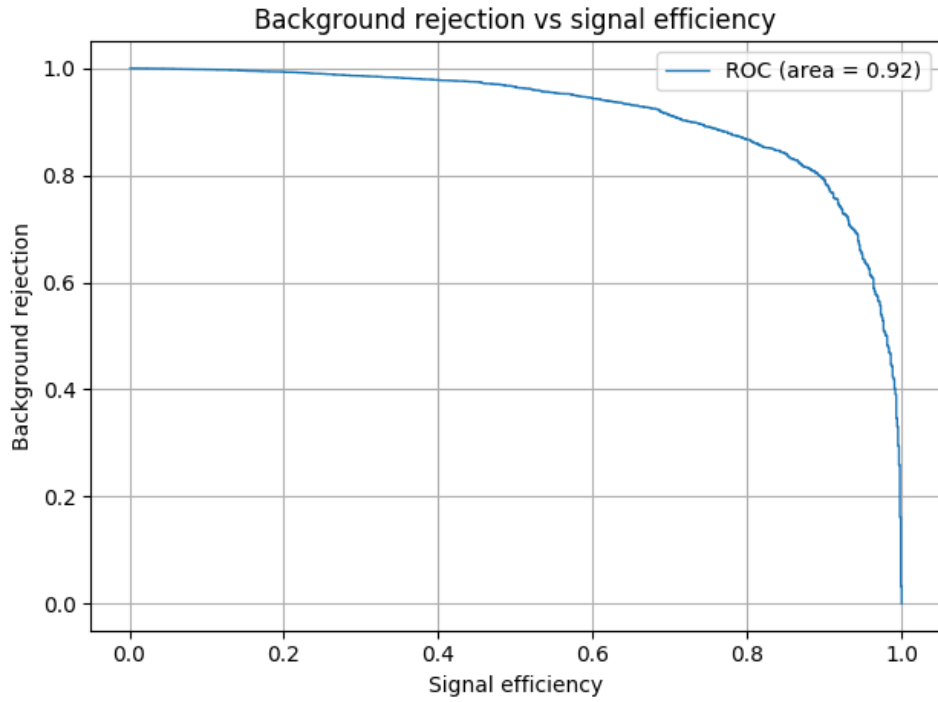


Figure 5.44 – The BDT rejection vs signal efficiency.

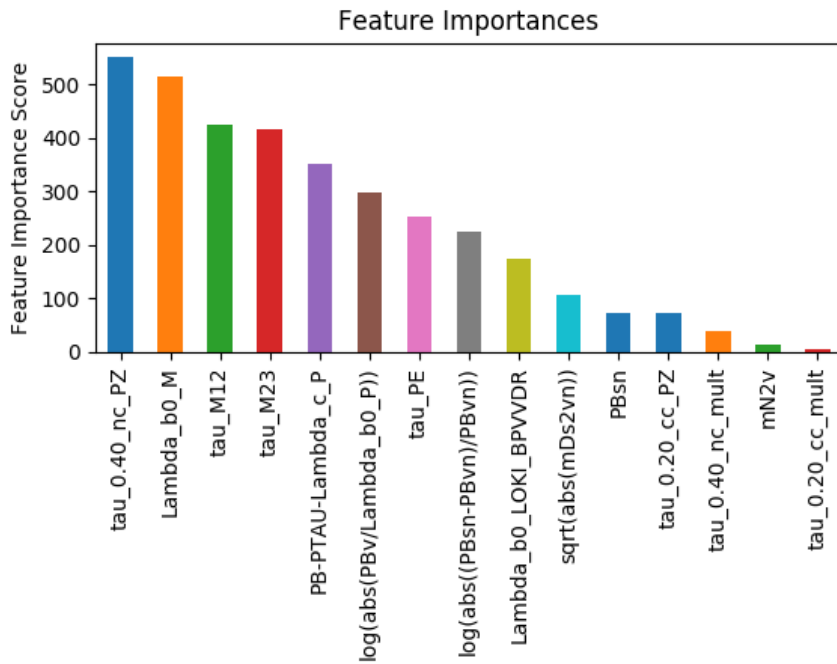


Figure 5.45 – Importance score for each variable of the BDT.

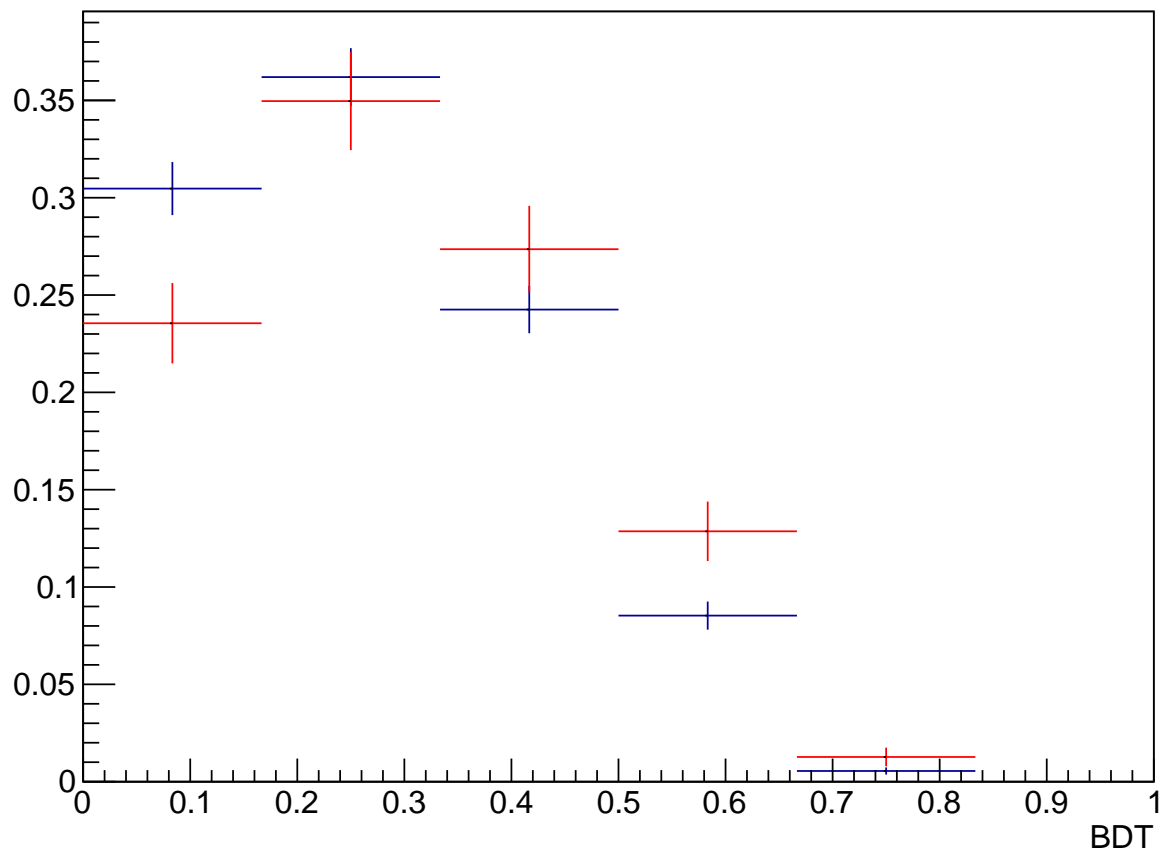


Figure 5.46 – Distribution of the output of the BDT for events in the  $\Lambda_c^+ 3\pi$  mass peak for both Run1 data (blue) and simulation sample (red).

## 5.8 Determination of the normalisation yield

This sections presents the work needed to measure the normalisation yield and the relevant ratios required to compute  $\mathcal{R}(\Lambda_c)$ .

### 5.8.1 Normalisation using the $\Lambda_b^0 \rightarrow \Lambda_c^+ \pi^- \pi^+ \pi^-$ exclusive peak

The normalisation mode for this analysis is  $\Lambda_b^0 \rightarrow \Lambda_c^+ \pi^- \pi^+ \pi^-$  and the determination of its yield in Run1 data is crucial for both the measurement of the  $\mathcal{B}$  of  $\Lambda_b^0 \rightarrow \Lambda_c^+ \tau^- \bar{\nu}_\tau$  and the computation of  $\mathcal{R}(\Lambda_c)$ , even if additional factors, discussed in the next parts of this section are also needed.

The selection used for the normalisation mode, as described in Sec. 5.3, consists in a cut on the event topology where the  $\Lambda_c^+$  is asked to be upstream from the  $\tau$  with a significance of  $4\sigma$  and the additional cleaning cuts, which is referred as the `normal_final` selection.

#### 5.8.1.1 Normalisation yield extraction

The precise determination of the normalisation yield is performed using a fit in the  $[5500 \text{ MeV}/c^2, 5800 \text{ MeV}/c^2]$  range on the  $M(\Lambda_c^+ 3\pi)$  distribution. The  $\Lambda_b^0 \rightarrow \Lambda_c^+ 3\pi$  peak is described by a Gaussian and the combinatorial background is modelled using an exponential function. The fit on the Run1 dataset is shown in Fig. 5.47.

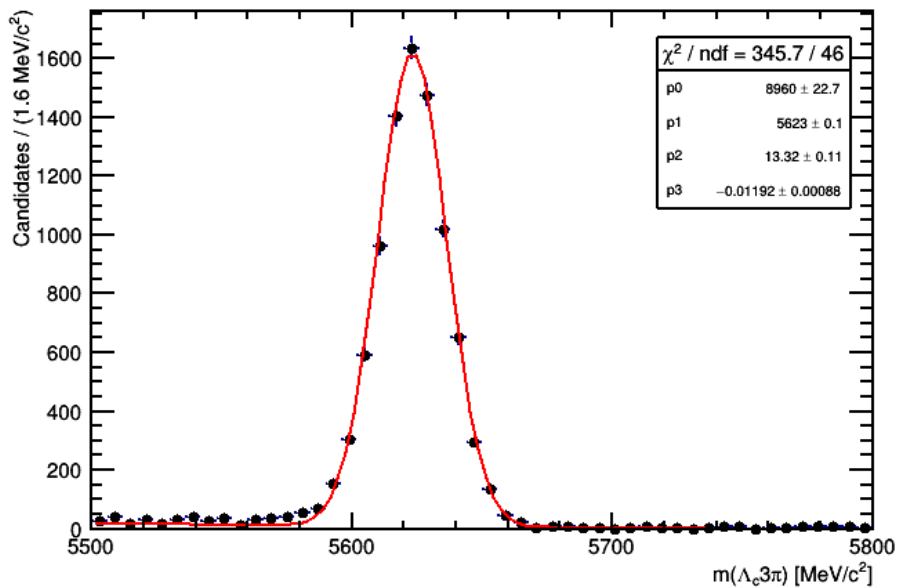


Figure 5.47 – Fit to the  $\Lambda_c^+ 3\pi$  mass distribution using the Run1 dataset after the `normal_final` selection.

## 5.8. DETERMINATION OF THE NORMALISATION YIELD

The normalisation yield extracted from the fit is measured to be in the Run1 dataset:

$$N_{norm} = 9520 \pm 120 (stat)$$

A contribution from  $\Lambda_b^0 \rightarrow \Lambda_c^+ D_s^- (\rightarrow 3\pi)$  can also clearly be seen in Fig. 5.48, where the  $3\pi$  mass distribution is shown with the same normal-final selection used in the normalisation fit. Another contribution comes from  $\Sigma_c \pi$  decays, the normalisation yield will soon be subtracted from these contributions.

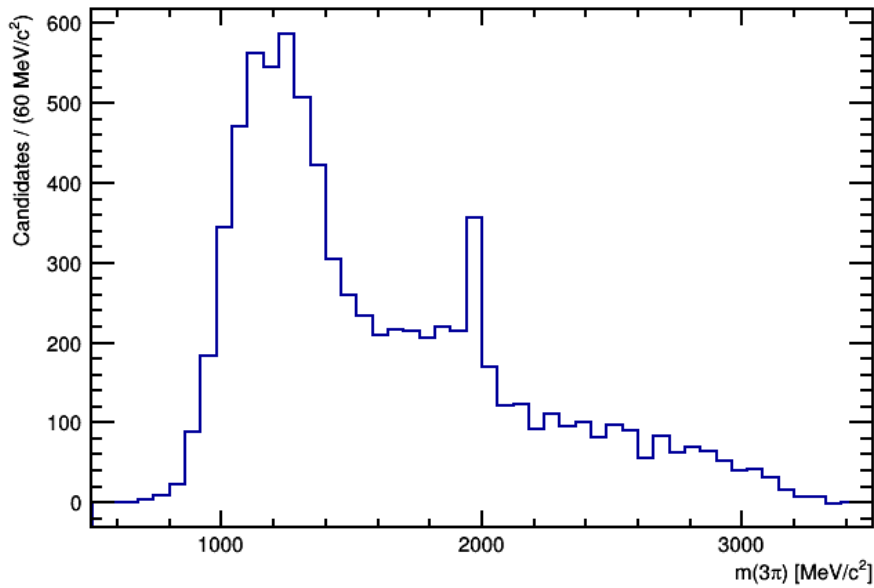


Figure 5.48 – The  $3\pi$  mass distribution in the Run1 dataset with the normal-final selection.

### 5.8.1.2 Data simulation study on the event topology cut for normalisation events

Normalisation events are selected using the `normal_final` selection discussed in Sec. 5.3. The extraction of the normalisation yield is still lacking some elements but the agreement on the event topology cut is discussed in this section.

In Fig. 5.49, the  $\Lambda_c^+$   $3\pi$  peak is fitted using a selection without the cut on the event topology. The fit is done again after applying the complete `normal_final` selection as presented in Fig. 5.50. This allows to compute the efficiency of the cut on the event topology, the results are presented in Tab. 5.11 and the effect of the discrepancy between data and simulation is  $\sim 10\%$ .

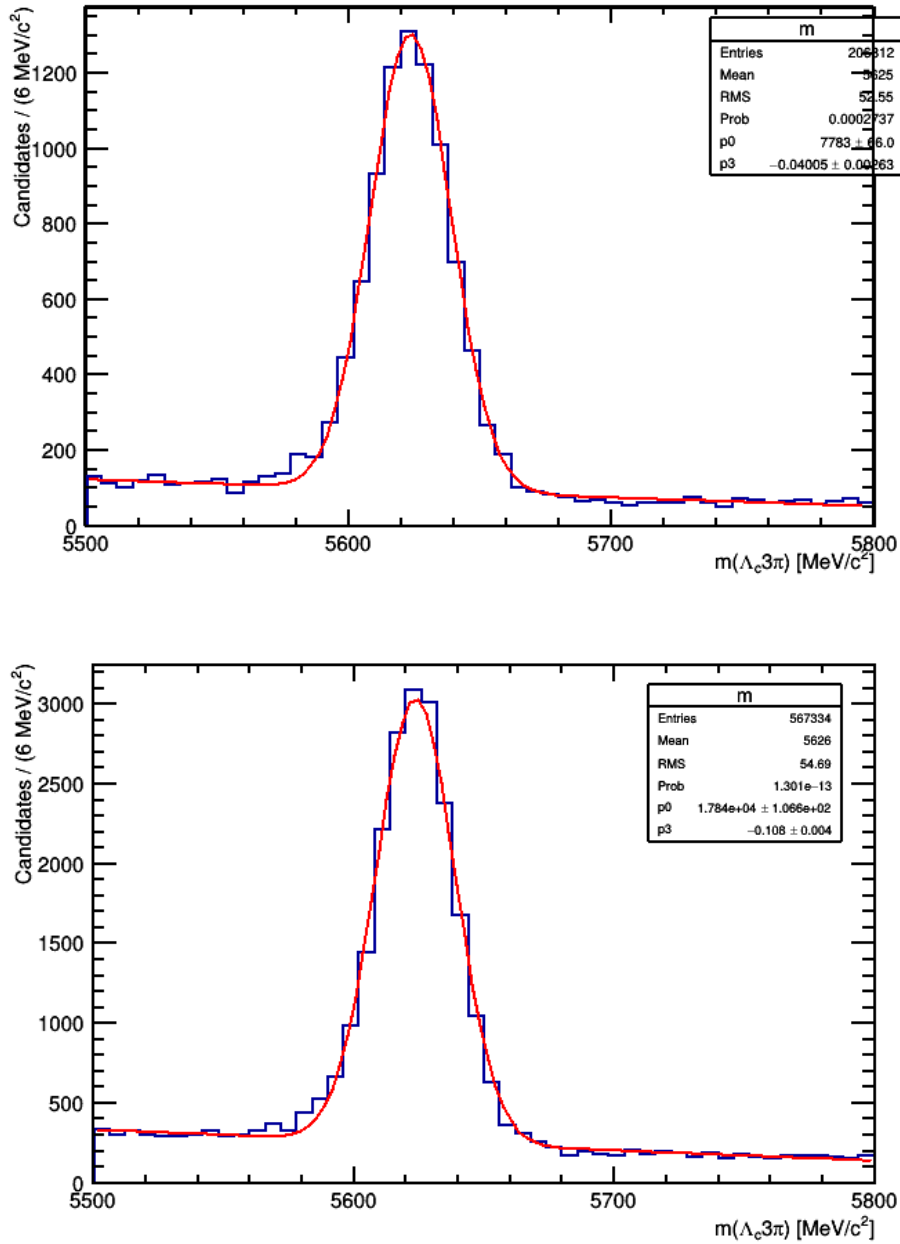


Figure 5.49 –  $\Lambda_c^+ 3\pi$  mass distribution for 2011 (top) and 2012 (bottom) data samples without the cut on the event topology.

Table 5.11 – Number of events and efficiency after the event topology cut on the events in the  $\Lambda_c^+ 3\pi$  peak.

	2011	2012
Number of events (without the event topology cut)	7762 ± 66	17684 ± 106
Number of events (with the complete <code>normal_final</code> selection)	1756 ± 31	3853 ± 51
Data efficiency (%)	22.6	21.8
Simulation efficiency (%)	-	25.1%

## 5.8. DETERMINATION OF THE NORMALISATION YIELD

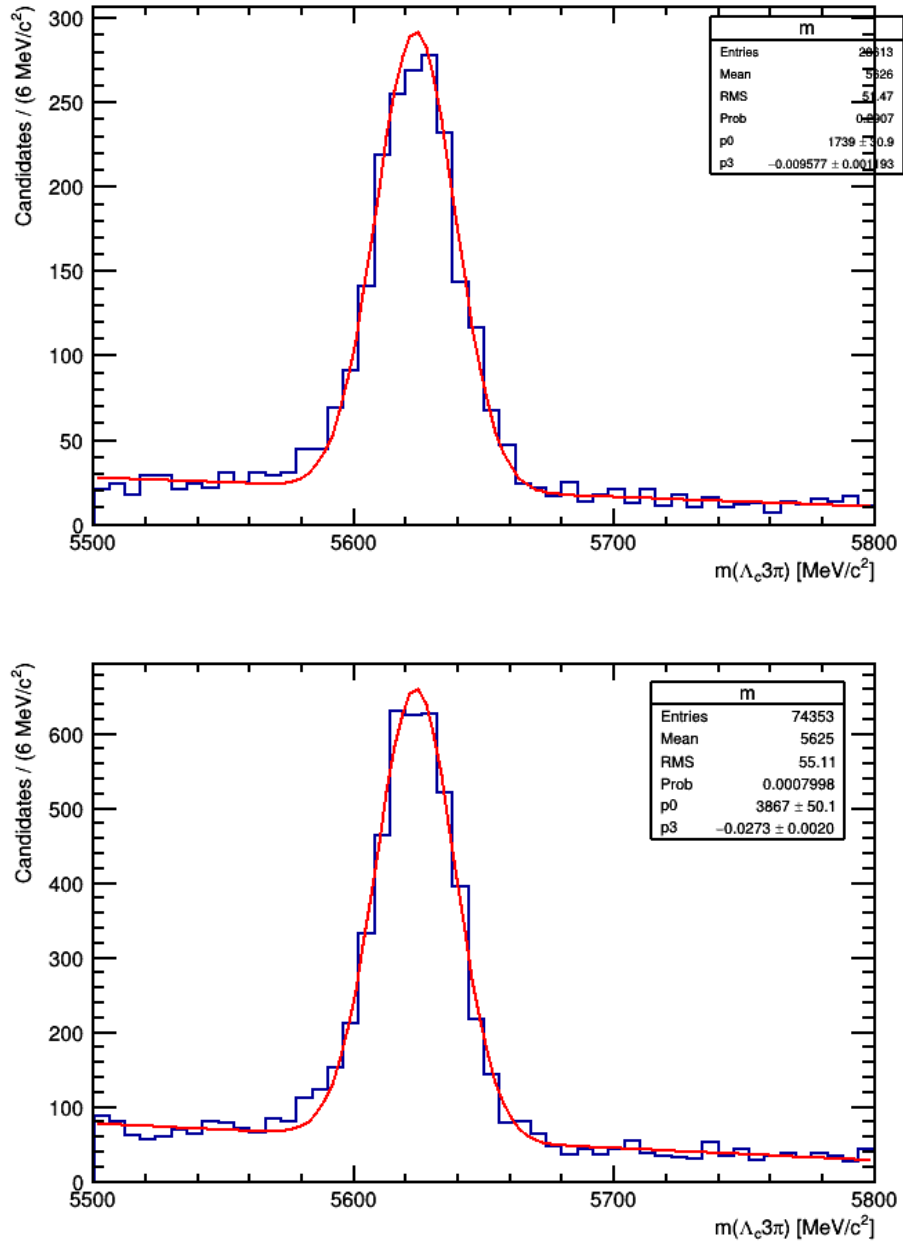


Figure 5.50 –  $\Lambda_c^+ 3\pi$  mass distribution for 2011 (top) and 2012 (bottom) data samples with the `normal_final` selection applied.

### 5.8.1.3 ratio of $\Lambda_b^0 \rightarrow \Lambda_c^+ \pi^- \pi^+ \pi^-$ and $B^0 \rightarrow D^{*-} \pi^+ \pi^- \pi^+$ yields

To be able to use the same external branching fractions used in the hadronic  $\mathcal{R}(D^*)$  analysis, one needs to precisely know the ratio:

$$\frac{\mathcal{B}(\Lambda_b^0 \rightarrow \Lambda_c^+ 3\pi)}{\mathcal{B}(B^0 \rightarrow D^* 3\pi)} \quad (5.37)$$

where the  $3\pi$  come from a  $a_1$  resonance.

To extract directly this ratio from data, samples of both simulation and data taking in 2012 conditions are used and the selection of events is as follows:

- events need to be TOS at the L0 trigger level and pass one of the topological trigger line at the Hlt2 trigger level (referred as **Topo** in Sec. 5.3.1)
- **ProbNNpi** of each  $\pi$  from  $\tau^- > 0.6$
- $\chi^2[vtx(\tau^-)] < 10$

The efficiency of this selection, estimated on dedicated simulation samples is respectively 57.5% for  $D^* 3\pi$  events and 63.1% for  $\Lambda_c^+ 3\pi$  ones.

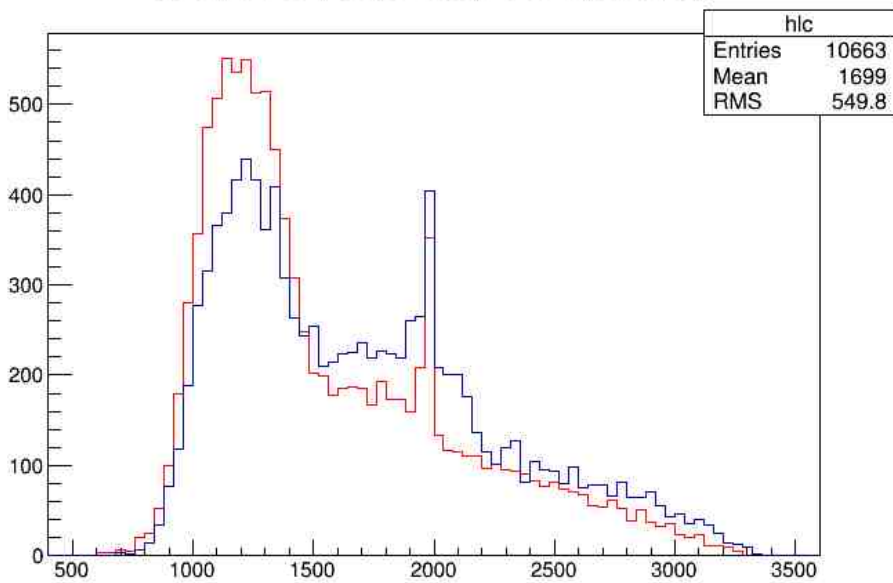


Figure 5.51 – Comparison of  $M(3\pi)$  distribution for  $\Lambda_c^+ 3\pi$  (blue) and  $D^* 3\pi$  (red) channels.

Although this selection is able to select both channels, one can see a bump around  $2 \text{ GeV}/c^2$  in the  $M(3\pi)$  distribution of  $\Lambda_c^+ 3\pi$  events in Fig. 5.51 which indicates the presence of events coming from  $\Lambda_c^* \rightarrow \Lambda_c^+ \pi\pi$  decays.

After vetoing these events and applying a sideband subtraction, the agreement is much better as shown in Fig. 5.52. Yet, as shown in Fig. 5.53,  $\Sigma_c$  contributions are found as  $\Sigma_c^{(*)} \rightarrow \Lambda_c^+ \pi$  decays are contributing. In both distributions, two clear peaks at  $160 \text{ MeV}/c^2$

## 5.8. DETERMINATION OF THE NORMALISATION YIELD

and  $230 \text{ MeV}/c^2$  are contributions from  $\Sigma_c(2455)^{++}$  and  $\Sigma_c(2520)^{++}$  in the top plot shown in Fig. 5.53 and  $\Sigma_c(2455)^0$  and  $\Sigma_c(2520)^0$  in the bottom one.

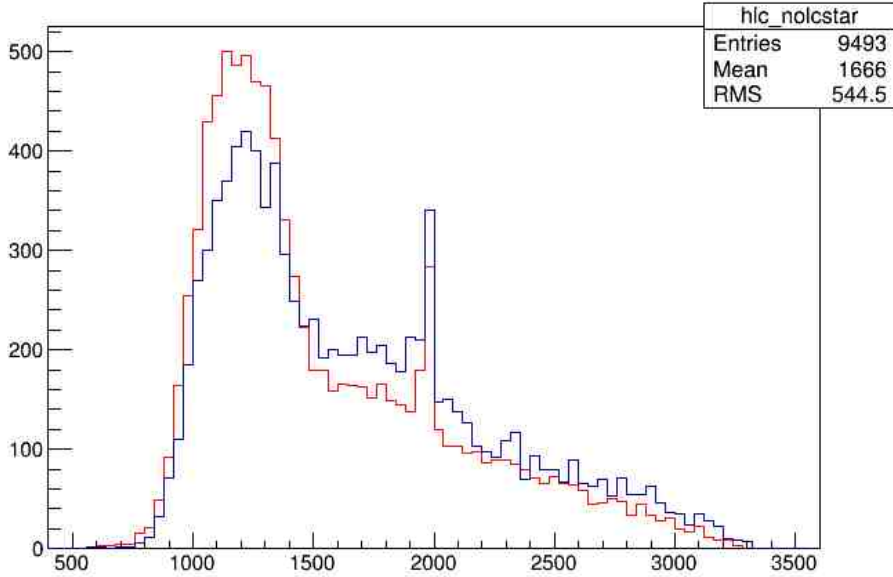


Figure 5.52 – Comparison of  $M(3\pi)$  distribution for  $\Lambda_c^+ 3\pi$  (blue) and  $D^* 3\pi$  (red) channels after  $\Lambda_c^*$  component is removed from  $\Lambda_c^+ 3\pi$  distribution.

After removing these components, the comparison of  $\Lambda_c^+ 3\pi$  and  $D^* 3\pi$  mass distributions is in much better agreement as shown in Fig. 5.54

Before taking into account selection efficiencies, the ratio of  $\Lambda_c^+ 3\pi$  over  $D^* 3\pi$  events is:

$$\frac{N_{events}(\Lambda_c^+ 3\pi)}{N_{events}(D^* 3\pi)} = 0.48 \pm 3\% \text{ (stat)} \pm 3\% \text{ (syst)} \quad (5.38)$$

with a 3% statistical uncertainty and a uncertainty associated to the subtraction of  $\Lambda_c^{*+} \pi^-$  events of 3%.

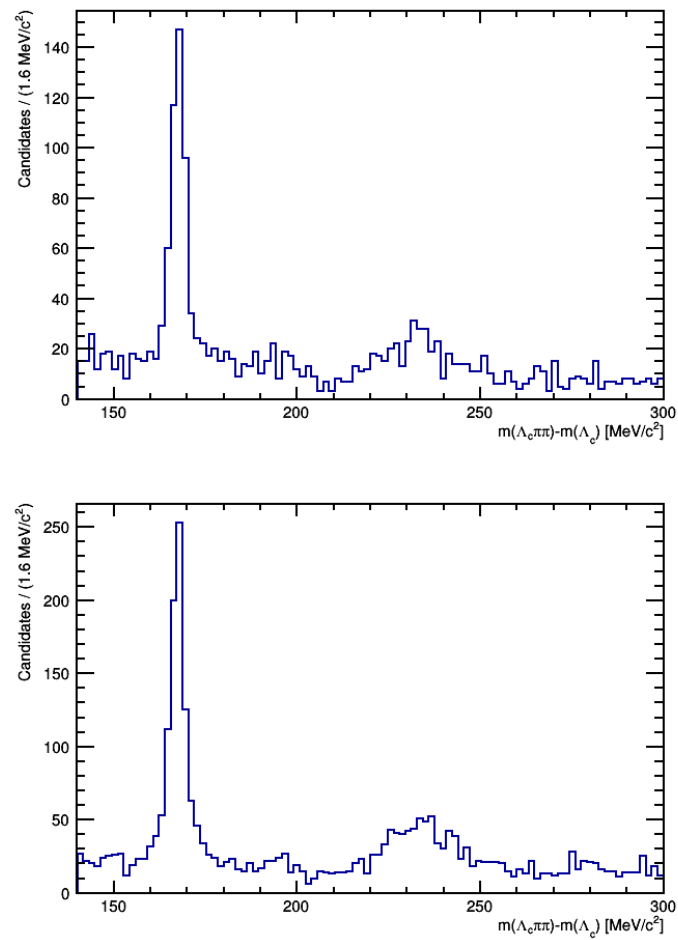


Figure 5.53 – Distribution of  $M(\Lambda_c^+ \pi^+) - M(\Lambda_c^+)$  (top) and  $M(\Lambda_c^+ \pi^-) - M(\Lambda_c^+)$  (bottom).

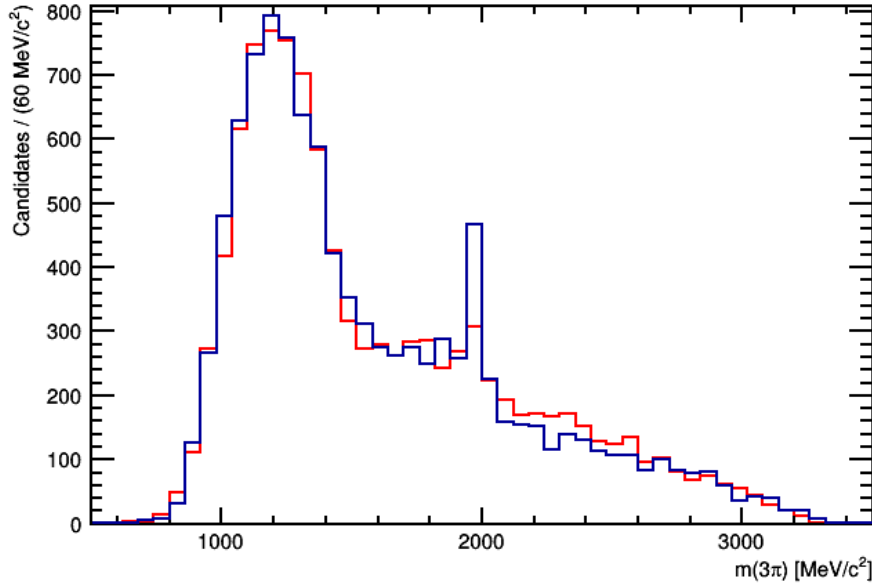


Figure 5.54 – Comparison of  $M(3\pi)$  distribution for  $\Lambda_c^+ 3\pi$  (blue) and  $D^* 3\pi$  (red) channels after the removal of  $\Lambda_c^*$  and  $\Sigma_c$  contributions to the  $\Lambda_c^+ 3\pi$  mass distribution.

## 5.9 Double-charm backgrounds

### 5.9.1 Determination of the $\Lambda_b^0 \rightarrow \Lambda_c^+ D_s^- X$ background composition on data

#### 5.9.1.1 Determination of the $D_s^-$ decay model

The  $D_s^-$  decay model described in this section comes from the work done for the  $\mathcal{R}(D^*)$  analysis [107]. To achieve a better background modelling, an enriched sample of  $D_s^-$  decays was extracted directly from the data using a BDT dedicated to discriminate double charm events from  $B^0 \rightarrow D^* \tau \nu$ . Then a simultaneous fit to  $\min(M(\pi^+ \pi^-))$ ,  $\max(M(\pi^+ \pi^-))$ ,  $M(\pi^- \pi^-)$  and  $M(\pi^- \pi^+ \pi^-)$  is performed using a model obtained from simulation samples.

The fit model is taking into account three types of  $D_s^-$  decays:

- $D_s^-$  decays with at least one pion coming from a  $\eta$  or  $\eta'$  which are then subdivided into  $\eta\pi$ ,  $\eta\rho$ ,  $\eta'\pi$  and  $\eta'\rho$  final states.
- $D_s^-$  decays with at least one pion coming from an intermediate resonance (IS) other than  $\eta$  or  $\eta'$ . These events are then classified in two final states categories:  $\text{IS}\pi$  and  $\text{IS}\rho$ . These decays are dominated by IS being either  $\omega$  or  $\phi$  resonances.
- $D_s^-$  decays with no pion coming from an intermediate resonance (noIS). These decays can be subdivided as follows:  $K^0 3\pi$ ,  $\eta 3\pi$ ,  $\eta' 3\pi$ ,  $\omega 3\pi$ ,  $\phi 3\pi$ ,  $\tau(\rightarrow 3\pi)\nu_\tau$  and non-resonant  $3\pi$ . These contributions are denoted as  $\alpha$  in Eq. 5.39

The model used is described in the following with the dependence on the fit variables omitted for clarity:

$$\begin{aligned}
 \mathcal{P} = & (1 - f_{bkg}) \left[ f_\eta [f_{\eta\rho} \mathcal{P}_{\eta\rho} + (1 - f_{\eta\rho}) \mathcal{P}_{\eta\pi}] + f_{\eta'} (f_{\eta'\rho} \mathcal{P}_{\eta'\rho} (1 - f_{\eta'\rho}) \mathcal{P}_{\eta'\pi}) \right. \\
 & \left. + (1 - f_\eta - f_{\eta'}) [(1 - f_{noIS}) (f_{IS\rho} \mathcal{P}_{IS\rho} + (1 - f_{IS\rho}) \mathcal{P}_{IS\pi}) + f_{noIS} \sum_\alpha f_{noIS\alpha} \mathcal{P}_{noIS\alpha}] \right] \\
 & + f_{bkg} \mathcal{P}_{bkg}
 \end{aligned} \tag{5.39}$$

In this parametrisation,  $f_{bkg}$  takes into account background events not originating from  $D_s^-$  decays and  $f_{noISK^0} + f_{noIS\eta} + f_{noIS\eta'} + f_{noIS\omega} + f_{noIS\phi} + f_{noIS\tau} + f_{noISnr} = 1$ .

As branching fractions for  $D_s^- \rightarrow \eta'\pi$  and  $D_s^- \rightarrow \tau\nu$  are well measured, corresponding parameters in the model are constrained.

The fit results can be translated in weights to apply to simulation samples in order to match the  $D_s^-$  decay model obtained extracted from the data. Tab. 5.12 gives the contribution of each category of  $D_s^-$  decays and the weights to be applied.

Table 5.12 – Results of the fit to the  $D_s^-$  decay model. Relative contribution and weights to be applied are reported for each category of decays.

parameter	$D_s^-$ decay	Relative contribution	Correction weight
$f_\eta$	$\eta\pi^- + X_n$	$0.156 \pm 0.0097$	
$f_{\eta\rho}$	$\eta\rho^-$	$0.70 \pm 0.090$	$0.88 \pm 0.13$
$(1 - f_{\eta\rho})$	$\eta\pi$		$0.75 \pm 0.23$
$f_{\eta'}$	$\eta'\pi^- + X_n$	$0.3168 \pm 0.015$	
$f_{\eta'\rho}$	$\eta'\rho^-$	$0.565 \pm 0.043$	$0.71 \pm 0.063$
$(1 - f_{\eta'\rho})$	$\eta'\pi$		$0.808 \pm 0.088$
$f_{IS\rho}$	$(\phi + \omega)\rho^-$	$0.2088 \pm 0.106$	$0.28 \pm 0.14$
$(1 - f_{IS\rho})$	$(\phi + \omega)\pi^-$		$1.588 \pm 0.208$
$f_{noIS}$	$M3\pi$	$0.6075 \pm 0.043$	
$f_{noIS\eta}$	$\eta3\pi$	$0.3299 \pm 0.0616$	$1.81 \pm 0.36$
$f_{noIS\eta'}$	$\eta'3\pi$	$0.2617 \pm 0.0283$	$5.39 \pm 0.66$
$f_{noIS\omega}$	$\omega3\pi$	$0.1306 \pm 0.0377$	$5.19 \pm 1.53$
$f_{noISK^0}$	$K^03\pi$		$1.025 \pm 0.7$
$f_{noIS\phi}$	$\phi3\pi$	$0.0901$	$0.97$
$f_{noIS\tau}$	$\tau(\rightarrow 3\pi + X_n)\nu$	$0.0392$	$0.97$
$f_{noISnr}$	$X_{nr}3\pi$	$0.1258 \pm 0.016$	$6.69 \pm 0.94$
$f_{bkg}$		$0.2299 \pm 0.0153$	

## 5.9.2 Data-driven control samples

### 5.9.2.1 $\Lambda_c^+ D_s^- X$ sample

A pure sample of  $\Lambda_b^0 \rightarrow \Lambda_c^+ D_s^- X$  events can be selected using the events in the mass peak of  $D_s^- \rightarrow \pi^- \pi^+ \pi^-$ . Three kinds of events are selected that way:

- $\Lambda_b^0 \rightarrow \Lambda_c^+ D_s^-$  present in the exclusive  $D_s^-$  peak
- $\Lambda_b^0 \rightarrow \Lambda_c^+ D_s^{-(**,*)}$  events where at least one additional particle is missing. These events have a  $q^2$  shifted to higher values.
- $D_s^-$  decays associated with an excited  $\Lambda_c^*$ , *i.e.*  $\Lambda_b^0 \rightarrow \Lambda_c^{+*} D_s^{-(**(*))}$

Fig. 5.56 presents the comparison between data and the  $\Lambda_c^+ D_s^-$  simulation sample. To test the data/MC agreement, a 1D fit is performed on  $M(\Lambda_c^+ 3\pi)$ , with a model described as:

$$\mathcal{P}_{model} = f_{WS} \mathcal{P}_{WS} + \frac{(1 - f_{WS})}{k} \sum_i f_i \mathcal{P}_i \quad (5.40)$$

$f_{WS}$  is the fraction of events passing the wrong-sign stripping line, used to describe the combinatorial background events. This parameter is fixed in the fit.  $\mathbf{f}_i$ , where  $i = \{D_s^{*-}, D_s^-, D_{s0}^{*-}, D_{s1}^{\prime-}, \Lambda_c^{*+} D_s^-, \Lambda_c^{*+} D_s^{*-}, \Lambda_c^* D_s^{**}\}$ , are the relative yields of  $\Lambda_b^0 \rightarrow \Lambda_c^+ D_s^-$ ,  $\Lambda_b^0 \rightarrow \Lambda_c^+ D_{s0}^{*-}$ ,  $\Lambda_b^0 \rightarrow \Lambda_c^+ D_{s1}^{\prime-}$ ,  $\Lambda_b^0 \rightarrow \Lambda_c^{*+} D_s^-$ ,  $\Lambda_b^0 \rightarrow \Lambda_c^{*+} D_s^{*-}$  and  $\Lambda_b^0 \rightarrow \Lambda_c^{*+} D_s^{**}$  with respect to the number of  $\Lambda_b^0 \rightarrow \Lambda_c^+ D_s^{*-}$  candidates. These parameters are floating in the fit and  $f_{D_s^{*-}} = 1$  by definition.

All templates are coming from a dedicated simulation samples except  $\Lambda_c^*$  contributions directly extracted from data. This will be changed as soon as a simulation sample for these modes is available.

The fit results are shown in Fig. 5.56 with projections to  $q^2$ ,  $3\pi$  decay time and the output of the BDT and in Tab. 5.13, with the correlation matrix shown in Tab. 5.14.

Table 5.13 – Fit results for the  $\Lambda_c^+ D_s^- X$  control sample

Parameter	Simulation	Fit result	Ratio Data/MC
$f_{WS}$		0.011	
$f_{D_s^-}$	0.51	$0.736 \pm 0.100$	$1.45 \pm 0.20$
$f_{D_{s0}^{*-}}$	0.08	$0.564 \pm 0.140$	$7.46 \pm 1.85$
$f_{D_{s1}^{\prime-}}$	0.44	$0.539 \pm 0.110$	$1.23 \pm 0.25$
$f_{\Lambda_c^* D_s^-}$	0.15	$0.0 \pm 0.137$	$0.0 \pm 0.21$
$f_{\Lambda_c^* D_s^*}$	0.33	$0.0 \pm 0.137$	$0.0 \pm 0.13$
$f_{\Lambda_c^* D_s^{**}}$	0.24	$0.229 \pm 0.050$	$0.97 \pm 0.21$

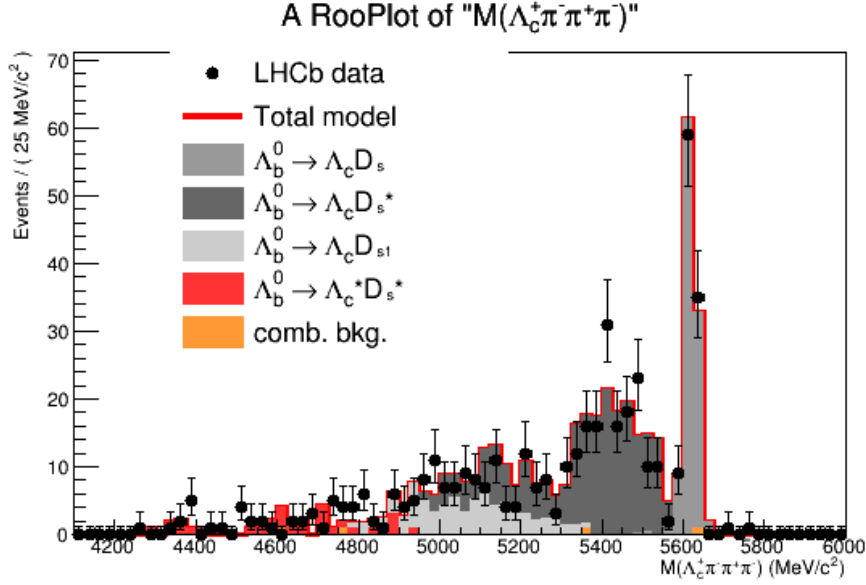

 Figure 5.55 – Fit to the  $M(\Lambda_c^+ 3\pi)$  distribution to extract the fractions of the  $D_s^+$  components.

 Table 5.14 – Correlation between the fit parameters from a fit to the  $D^* 3\pi$  invariant mass distribution of  $D_s^+ \rightarrow 3\pi$  events.

	$f_{D_{s1}^-}$	$f_{D_s^-}$	$f_{\Lambda_c^* D_s^{**}}$	$f_{\Lambda_c^* D_s^-}$	$f_{D_{s0}^{*-}}$	$f_{\Lambda_c^* D_s^{**}}$
$f_{D_{s1}^-}$	1.000	0.246	0.043	0.000	-0.259	-0.002
$f_{D_s^-}$	0.246	1.000	0.309	0.000	0.394	0.000
$f_{\Lambda_c^* D_s^{**}}$	0.043	0.309	1.000	0.000	0.321	0.000
$f_{\Lambda_c^* D_s^-}$	0.000	0.000	0.000	1.000	-0.002	0.000
$f_{D_{s0}^{*-}}$	-0.259	0.394	0.321	-0.002	1.000	-0.000
$f_{\Lambda_c^* D_s^*}$	-0.002	0.000	0.000	0.000	-0.000	1.000

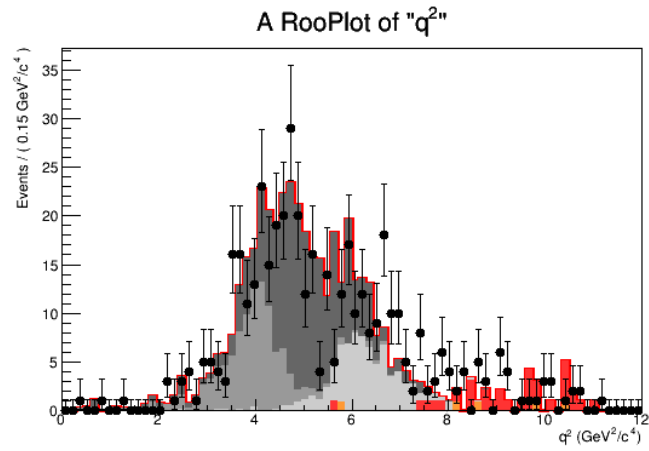
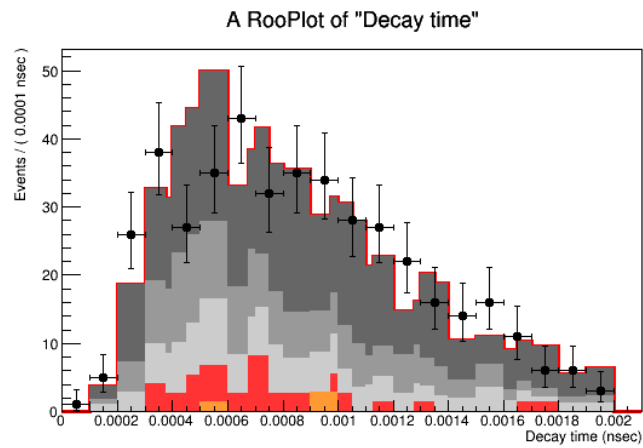
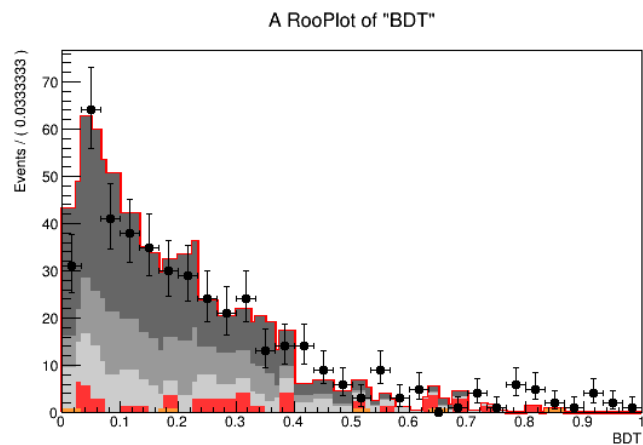
### 5.9.2.2 $\Lambda_c^+ D^0 X$ sample

It is possible to select  $D^0 \rightarrow K\pi\pi\pi$  events using the isolation tools described in Sec. 5.4. These events are selected using a signal candidate and an extra track with opposite charge with respect to the  $3\pi$  system pointing to the  $3\pi$  vertex. Thus a control sample of  $\Lambda_b^0 \rightarrow \Lambda_c^+ D^0 X$  can be extracted from both data and simulation.

Distributions of  $M(K3\pi)$ ,  $q^2$ ,  $\tau$  decay time and output of the BDT are shown in Fig. 5.57 for both data and dedicated  $\Lambda_c^+ D^0 X$  cocktail simulation sample.

### 5.9.2.3 $\Lambda_c^+ D^- X$ sample

In the cuts listed in Sec. 5.3, the cut on the ProbNNk ( $< 0.1$ ) of the opposite charged pion with respect to the charge of the  $3\pi$  system removes  $\Lambda_b^0 \rightarrow \Lambda_c^+ D^- X$  events. A control

(a) Fit projection on the  $q^2$  variable.(b) Fit projection on the  $\tau$  lifetime.

(c) Fit projection on the output of the BDT.

Figure 5.56 – Projections of the  $D_s^+$  control sample fit to the  $\Lambda_c^+ 3\pi$  mass on the variables used in the fit to extract the signal yield.

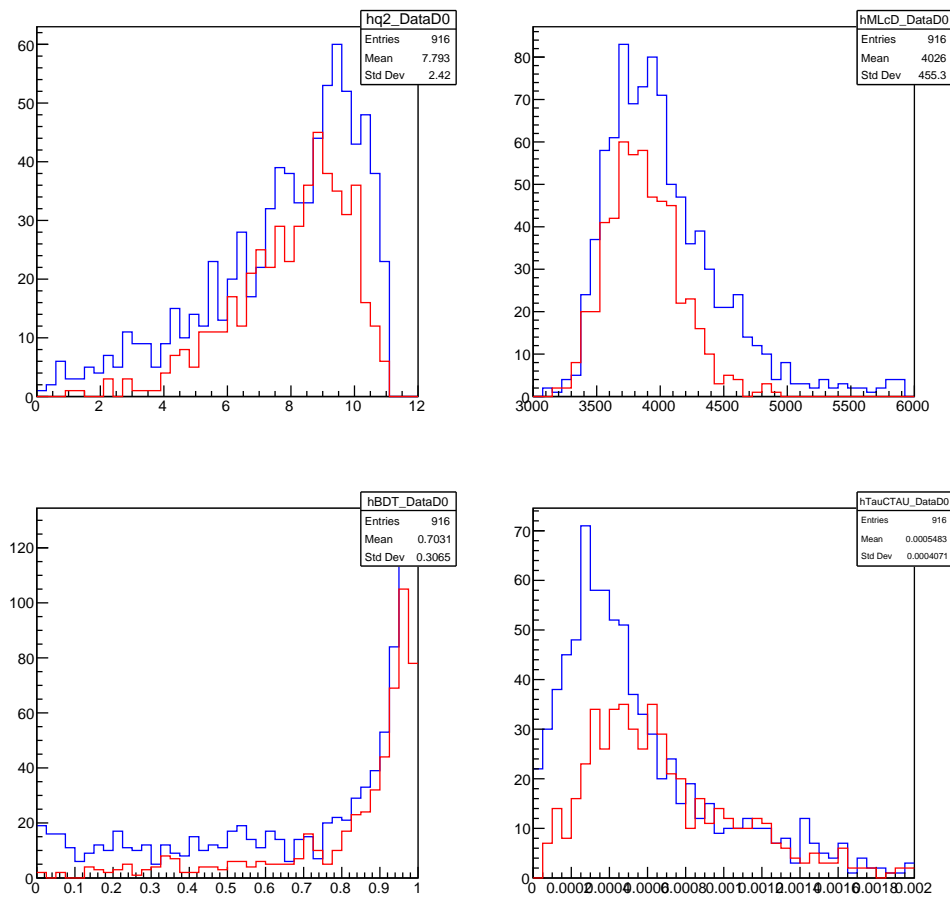


Figure 5.57 –  $q^2$  (top left),  $M(\Lambda_b^0)$  (top right), BDT (bottom left) and  $\tau$  decay time (bottom right) for both data and simulation for the  $D^0$  control sample.

## 5.9. DOUBLE-CHARM BACKGROUNDS

sample of  $D^-$  events is then selected around the  $D^- \rightarrow K\pi\pi$  exclusive peak by reversing this PID requirement.

The same study performed for the  $D^0$  control sample is used and  $M(\Lambda_c^+ K\pi\pi)$ ,  $q^2$  and output of the BDT distributions are shown in Fig. 5.58.

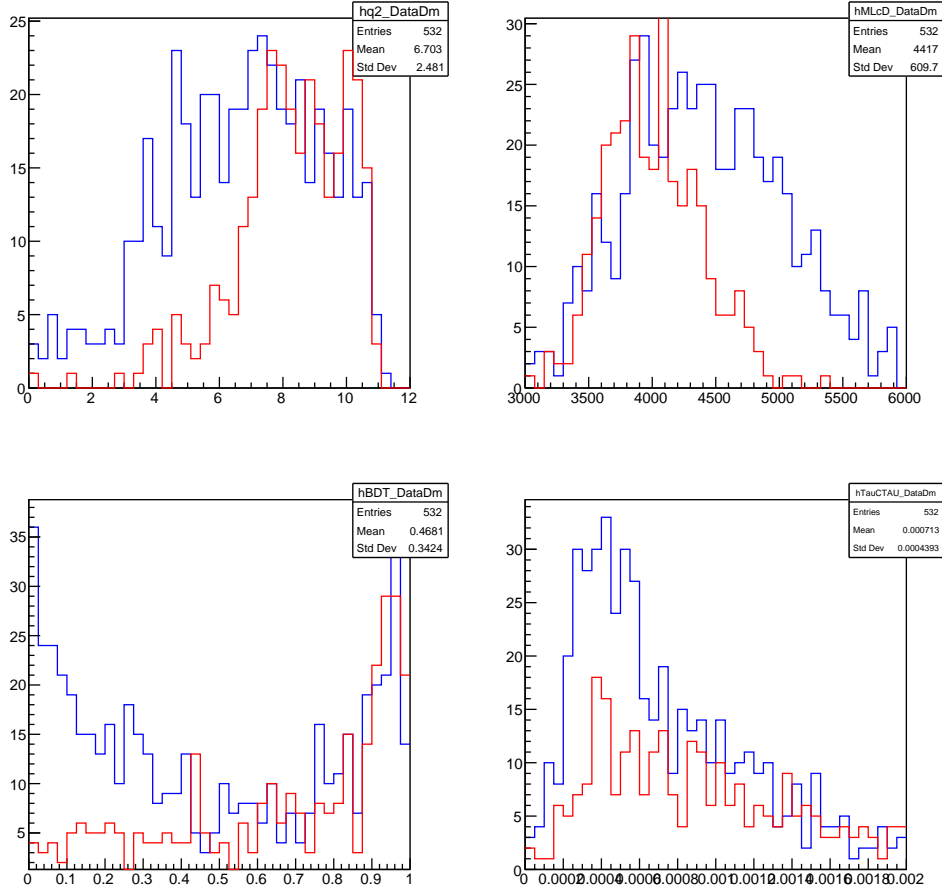


Figure 5.58 –  $q^2$  (top left),  $M(\Lambda_b^0)$  (top right), BDT (bottom left) and  $\tau$  decay time (bottom right) for both data and simulation for the  $D^-$  control sample.

## 5.10 Extraction of the signal yield

### 5.10.1 The fit model

The yield of signal mode,  $\Lambda_b^0 \rightarrow \Lambda_c^+ \tau^- \bar{\nu}_\tau$ , is extracted using a 3-dimensional template fit in bins of  $q^2$ ,  $3\pi$  decay time and output of the BDT distribution using the `HistFactory` toolkit [124]. Templates for each signal and background modes are created using:

- 6 bins in  $q^2$  with  $[0 < q^2 < 11]$  ( $\text{GeV}^2/c^4$ )
- 6 bins in  $3\pi$  decay time,  $[0.00 < \tau < 0.002]$  (ns), with the last bin taking into account all events with a  $\tau$  lifetime higher than 0.002 ns.
- 6 bins in BDT,  $[0 < BDT < 1]$

This bin scheme is the best compromise between a low number of bins with high statistics and coarse description of the fit components and a high number of bins with detailed description of the shapes of the different fit components but a large number of low-populated bins which could lead to potential bias and instabilities.

Some parameters of the fit are constrained using the fit of the  $D_s^-$  mass distribution discussed in Sec. 5.9.1.1, which means that a Gaussian constraint of  $\pm 1\sigma$  is applied around their central values.

The components of the model used in the fit are presented in Tab. 5.15.

Table 5.15 – Description of the fit components and their corresponding normalisation parameters.

Component	Normalisation
$\Lambda_b^0 \rightarrow \Lambda_c^+ \tau^- (\rightarrow 3\pi\nu)\nu$	$N_{sig} \times f_{\tau \rightarrow 3\pi\nu}$
$\Lambda_b^0 \rightarrow \Lambda_c^+ \tau^- (\rightarrow 3\pi\pi^0\nu)\nu$	$N_{sig} \times (1 - f_{\tau \rightarrow 3\pi\nu})$
$\Lambda_b^0 \rightarrow \Lambda_c^+ D^0 X$ same vertex	$N_{D^0}^{same}$
$\Lambda_b^0 \rightarrow \Lambda_c^+ D^0 X$ different vertices	$f_{D^0}^{v_1-v_2} N_{D^0}^{same}$
$\Lambda_b^0 \rightarrow \Lambda_c^+ D^- X$	$N_{D^-}$
$\Lambda_b^0 \rightarrow \Lambda_c^+ D_s^-$	$N_{D_s}$
$\Lambda_b^0 \rightarrow \Lambda_c^+ D_s^{*-}$	$N_{D_s} \times f_{D_s^*}$
$\Lambda_b^0 \rightarrow \Lambda_c^+ D_{s0}^{*-}$	$N_{D_s} \times f_{D_{s0}^*}$
$\Lambda_b^0 \rightarrow \Lambda_c^+ D_{s1}^{\prime-}$	$N_{D_s} \times f_{D_{s1}^{\prime}}$
Combinatoric $\Lambda_b^0$	$N_{B_1-B_2}$
Combinatoric $\Lambda_c^+$	$N_{\Lambda_c^+}^{bkg}$

- $N_{sig}$  is a parameter left free in the fit to account for the number of signal events. It is multiplied by a random number in the range  $[0.2, 5.0]$  to keep the analysis blinded. The blinding procedure of this analysis is described at the end of this section.
- $f_{\tau \rightarrow 3\pi\nu}$  is the relative  $\mathcal{B}$  of  $\tau \rightarrow 3\pi\nu$ , *i.e.*  $\mathcal{B}(\tau \rightarrow 3\pi\nu)/(\mathcal{B}(\tau \rightarrow 3\pi\nu) + \mathcal{B}(\tau \rightarrow 3\pi\pi^0\nu))$  and is fixed in the fit.

- $\mathbf{N}_{D^0}^{\text{same}}$  is the number of  $\Lambda_b^0 \rightarrow \Lambda_c^+ D^0 X$  events where the three pions come from the  $D^0$  vertex. Its value is taken from the number of events with a kaon found by the isolation tools, which allows to recover the  $D^0 \rightarrow K3\pi$  exclusive peak as discussed in Sec. 5.4. A 5% Gaussian constraint is applied to this parameter, to take into account the uncertainties of  $\mathcal{B}(D^0 \rightarrow K3\pi)$  and  $\mathcal{B}(D^0 \rightarrow K3\pi X)$ . More details are given in Sec. 5.10.2.
- $\mathbf{f}_{D^0}^{v_1-v_2}$  is the ratio of  $\Lambda_b^0 \rightarrow \Lambda_c^+ D^0 X$  events where at least one pion comes from the  $D^0$  vertex and another pion from another vertex with respect to  $\mathbf{N}_{D^0}^{\text{same}}$ .
- $\mathbf{N}_{D^-}$  is the number of  $D^-$  events, which is left free in the fit.
- $\mathbf{N}_{D_s^-}$  is the number of  $D_s^-$  events, which is left free in the fit.
- $\mathbf{f}_{D_s^-}$ ,  $\mathbf{f}_{D_{s0}^{*-}}$ ,  $\mathbf{f}_{D_{s1}^{\prime-}}$  are the ratios of  $\Lambda_b^0 \rightarrow \Lambda_c^+ D_s^-$ ,  $\Lambda_b^0 \rightarrow \Lambda_c^+ D_{s0}^{*-}$  and  $\Lambda_b^0 \rightarrow \Lambda_c^+ D_{s1}^{\prime-}$  events with respect to  $\Lambda_b^0 \rightarrow \Lambda_c^+ D_s^{*-}$  events. These ratios are constrained parameters resulting from the  $D_s^-$  decay model discussed in Sec. 5.9.1.1 corrected by efficiency.
- $\mathbf{N}_{B_1-B_2}$  is the number of combinatorial events where the  $\Lambda_c^+$  and  $3\pi$  come from different decays. Its value is fixed using the number of wrong-sign events in the region above the  $\Lambda_b^0$  mass defined as  $M(\Lambda_c^+ 3\pi) > 5700 \text{ MeV}/c^2$ .
- $\mathbf{N}_{\Lambda_c^+}^{\text{bkg}}$  is the number of background events under the  $\Lambda_c^+$  mass peak.

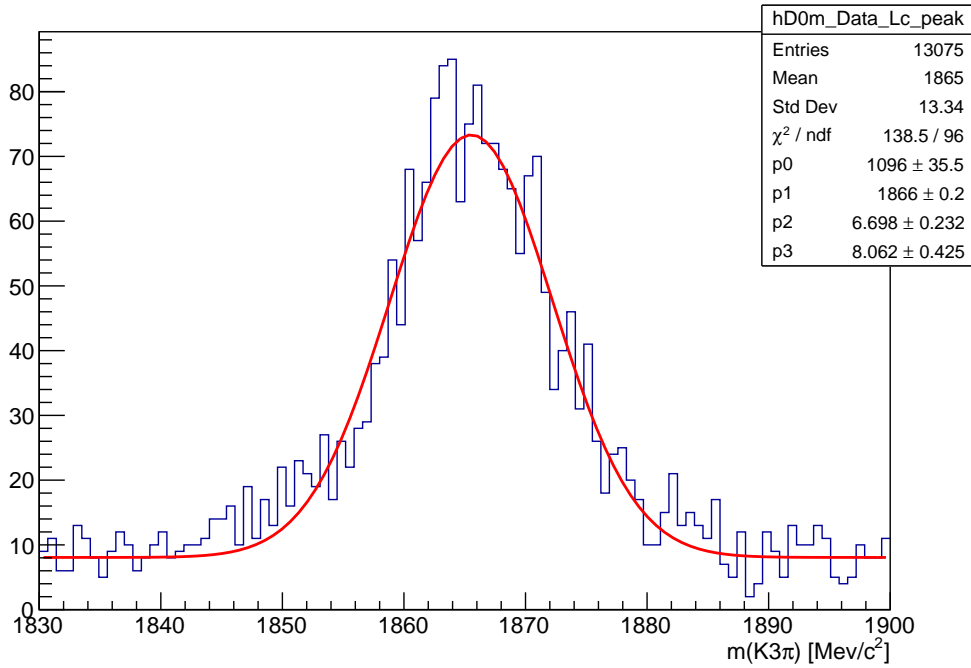
The blinding of the analysis is done by multiplying the number of signal events by a random number generated between 0.2 and 5. Plots are also only presenting the pulls of the fit and the overall model to compare with data.

### 5.10.2 Computation of the constrained parameters of the fit

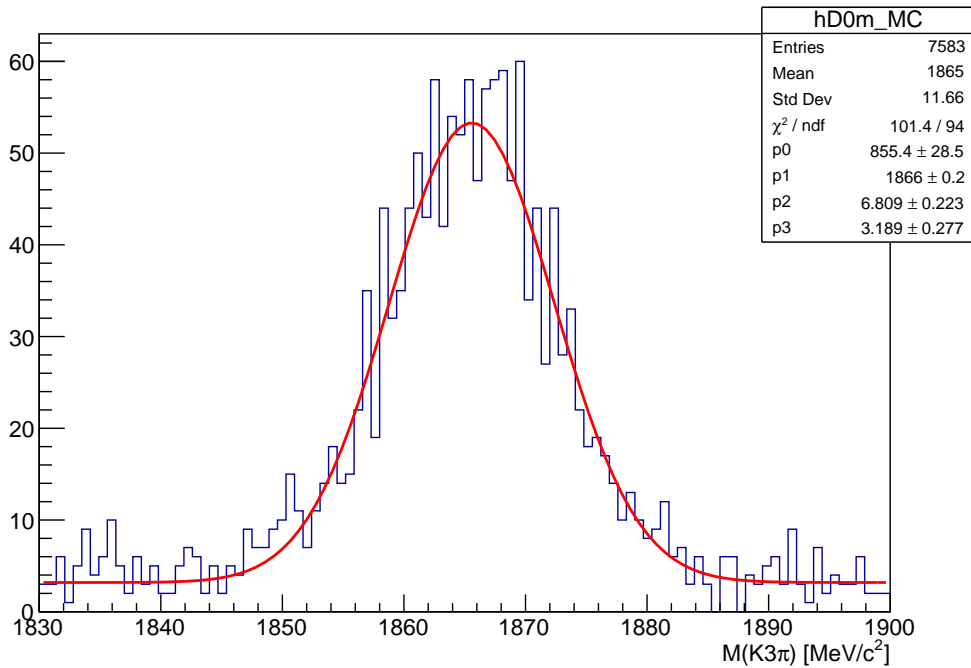
In addition to the  $D_s^-$  fractions taken from the fit discussed in Sec. 5.9, two other factors are constrained, the  $D^0$  yield and the number of combinatorial events.

The number of events in the  $\Lambda_c^+ D^0$  simulation sample is scaled by the ratio of the number of events in the  $D^0 \rightarrow K3\pi$  mass peak found in Data and simulation samples. The mass is reconstructed using charged isolation algorithms looking for extra tracks in the underlying event. The  $K3\pi$  peak is fitted in data using a Gaussian after removing the  $\Lambda_c^+$  background using sideband subtraction. Fig. 5.59a and Fig. 5.59b respectively present the fit to the  $K3\pi$  mass distribution for both Run1 data and simulation samples. The scaled factor is found to be 0.226 and a 5% uncertainty is considered on the scale  $D^0$  yield in the fit to account for its uncertainty.

The events passing both the Wrong-Sign (WS) stripping line and the event selection are used to model the combinatorial background where the  $\Lambda_c^+$  and the 3 pions do not come from the same B hadron. In the region above  $5700 \text{ MeV}/c^2$  of the  $\Lambda_c^+ 3\pi$  mass distribution, no event can come from a  $\Lambda_b^0$  decay, and thus, is only made of combinatorial background. The number of events in the WS sample is then scale by the ratio of the number of events with  $M(\Lambda_c^+ 3\pi) > 5700 \text{ MeV}/c^2$  found in data and WS samples which is measured to be



(a)  $M(K3\pi)$  distribution in the  $\Lambda_c^+$  mass region before sideband subtraction for Run1 data.



(b)  $M(K3\pi)$  distribution for the Run1  $\Lambda_c^+ D_s^+$  simulation sample.

Figure 5.59 – The fit to the  $K3\pi$  mass for both Run1 data in the  $\Lambda_c^+$  mass peak region (a) and for simulation (b).

0 which indicates how effective the rejection of the combinatorial background is through the subtraction of the  $\Lambda_c^+$  sidebands.

### 5.10.3 Fit results

Results of the nominal HistFactory fit are shown in Tab. 5.16. The projections of the fit results are respectively presented for  $q^2$ , the  $\tau$  decay time and the output of the BDT in Fig. 5.61, Fig 5.60 and Fig. 5.62.

Parameter	Fit result	Constraint value
$N_{sig}$	$1359 \pm 168$ (12.4%)	
$f_{\tau \rightarrow 3\pi\nu}$		0.78
$N_{D^-}$	$641 \pm 64$	
$N_{D^0}^{same}$	$62 \pm 3$	$109 \pm 5$
$f_{D^0}^{v_1-v_2}$	$5.40 \pm 0.97$	
$N_{D_s}$	$1596 \pm 62$	
$f_{D_s}$	$0.632 \pm 0.097$	$0.736 \pm 0.100$
$f_{D_{s0}^*}$	$0.295 \pm 0.081$	$0.564 \pm 0.140$
$f_{D_{s1}^*}$	$0.529 \pm 0.082$	$0.539 \pm 0.110$
$N_{B_1-B_2}$		0.
$N_{\Lambda_c^+}^{bkg}$		581
$\chi^2$	212	
reduced $\chi^2$ ( $ndof = 186$ )	1.14	

Table 5.16 – Fit results with  $N_{sig}$  blinded

error on $N_{sig}$ (precision)	Parameter status
168 ( <b>12.4%</b> )	nominal fit
168 ( <b>12.2%</b> )	$f_{D^0}^{v_1-v_2}$ fixed
165 ( <b>12.0%</b> )	$N_{D^0}^{same}$ fixed
145 ( <b>10.5%</b> )	$N_{D^-}$ fixed

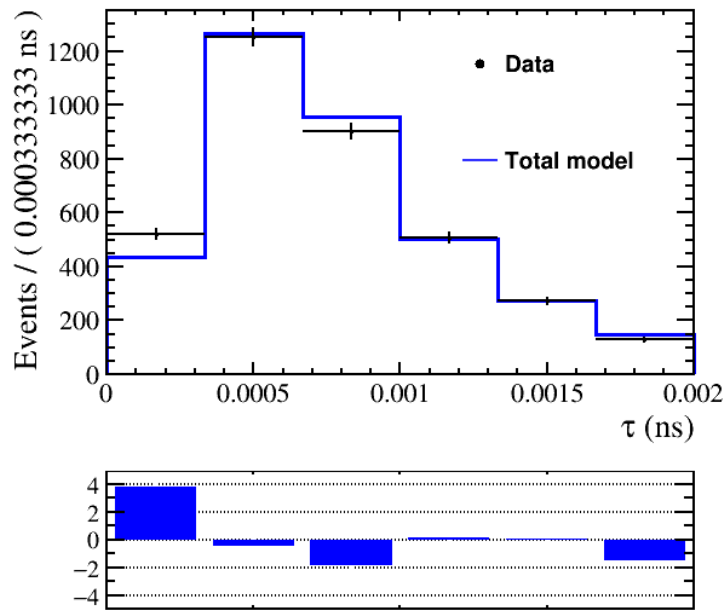
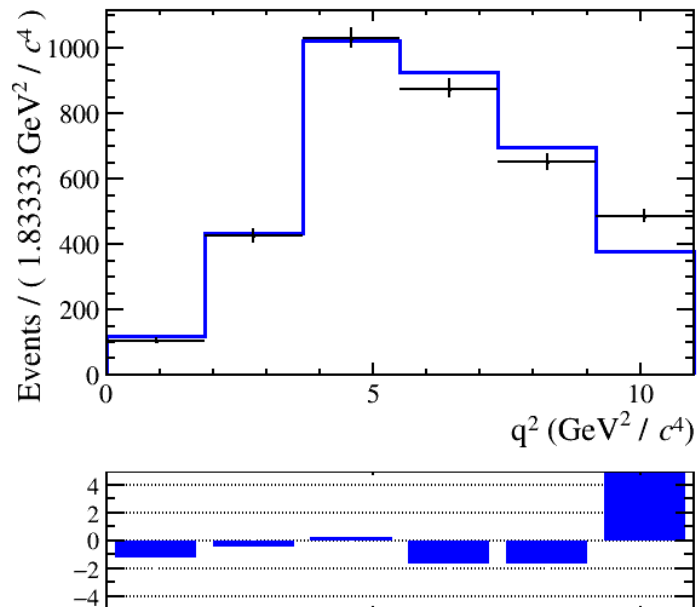
Table 5.17 – Number of signal events and its uncertainty for the nominal fit and fit setup iteratively fixing a parameter.

In Tab. 5.17 are reported the value of  $N_{sig}$  and its uncertainty for various fit configurations which is used to determine the statistical uncertainty on the signal yield.

The fit reduced  $\chi^2$ ,  $\chi^2/nDOF$ , is also computed including the Monte-Carlo statistics, with the nominal fit, its value is found to be  $\chi^2/nDOF = 0.956$ , indicating a good agreement between the fit model and the data.

#### 5.10.3.1 Determination of the statistical uncertainty on the signal yield

The statistical uncertainty of the signal yield is determined by fixing the  $D^-$  and  $D^0$  decay model parameters to their fit values. The quadratic difference between the signal yield uncertainty in the nominal fit and this fit with fixed parameters is then referred as the systematic uncertainty coming from the knowledge of the  $D^-$  and  $D^0$  decay model.

Figure 5.60 –  $3\pi$  decay time distribution for the nominal fit.Figure 5.61 –  $q^2$  distribution for the nominal fit.

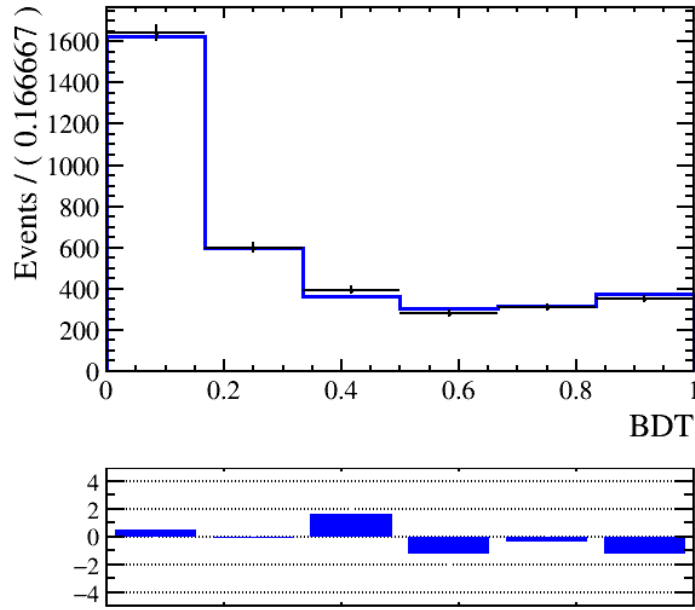


Figure 5.62 – BDT distribution for the nominal fit.

The result of the fit with fixed  $D^0$  and  $D^-$  parameters is  $N_{sig} = 1376 \pm 145(10.5\%)$  which leads to a statistical uncertainty of 10.5% and a systematic uncertainty due to  $D^-$  and  $D^0$  decay model of 6.6%.

#### 5.10.4 Evidence of the observation of $\Lambda_b^0 \rightarrow \Lambda_c^+ \tau \nu_\tau$ decay

Although the extraction of both  $\mathcal{B}(\Lambda_b^0 \rightarrow \Lambda_c^+ \tau \bar{\nu}_\tau)$  and  $\mathcal{R}(\Lambda_c)$  are the final results of this analysis, it is also possible to state the observation of the  $\Lambda_b^0 \rightarrow \Lambda_c^+ \tau \bar{\nu}_\tau$  decay without unblinding the fit results.

To do so, the fit is performed using with a fixed number of signal events set to zero. The  $\chi^2$  of this fit is measured to be 259 whereas the  $\chi^2$  of the nominal fit is measured to be 212. The  $\chi^2$  difference ( $\Delta\chi^2$ ) allows to reject the hypothesis of no signal with a significance of  $\sqrt{\Delta\chi^2} = 6.9$  thus obtaining the evidence of the observation of the decay  $\Lambda_b^0 \rightarrow \Lambda_c^+ \tau \bar{\nu}_\tau$  with a statistical significance of  $6.9\sigma$  when considering only statistical effects.

## 5.11 Systematics

The different systematics related to the measurement of both  $\mathcal{K}\Lambda_c^+$  and  $\mathcal{R}(\Lambda_c)$  are discussed in this section. Some systematics uncertainties have been mentioned earlier in this document but this section is meant to provide a detailed summary of each systematic uncertainty. All systematics are reported at the end of the section in Tab. 5.19.

As the analysis is still ongoing, a few sources of systematic have not been yet considered such as the correction of the PID selection efficiencies as described in Sec. 3.2.2. These studies will be performed in a near future and are nevertheless described in the following of this section.

### 5.11.1 $\tau$ decay model

#### 5.11.1.1 $\tau$ polarisation effects and hadronic contamination

As mentioned in Sec. 4.5.1, as the  $\tau$  decay does not depend on the  $B$  hadron decay, the results on the  $\tau$  decay model concerning the effect of the  $\tau$  polarisation and the contamination from other hadronic  $\tau$  decay, such as  $\tau \rightarrow 3\pi\pi^0\pi^0$  are taken from the  $\mathcal{R}(D^*)$  analysis.

Systematic uncertainties of 0.4% and 1.0% are thus respectively associated to the  $\tau$  polarisation and the hadronic contamination.

#### 5.11.1.2 Signal composition systematic uncertainty

One parameter of the fit model is the fraction of  $\tau \rightarrow 3\pi\nu$  signal events with respect to the total ( $\tau \rightarrow 3\pi\nu + \tau \rightarrow 3\pi\pi^0\nu$ ) which is fixed to 0.78. A uncertainty of 1% is assigned to this fraction due to the knowledge of  $\mathcal{B}(\tau \rightarrow 3\pi\nu)$ ,  $\mathcal{B}(\tau \rightarrow 3\pi\pi^0\nu)$  and their respective efficiencies.

A fit is performed with this fraction using a Gaussian constraint of  $0.78 \pm 0.01$ . This fit is then repeated with the fraction fixed at the value found by the previous fit. The squared difference between the raw uncertainty from these two fits is taken as the systematic uncertainty due to the signal composition, which is 3.0%.

### 5.11.2 Systematics related to the fitting procedure

The estimation of systematic and statistical uncertainties follows the same procedure as the hadronic  $\mathcal{R}(D^*)$  analysis. As the fit model is constrained by the knowledge of the Double charm background components provided by external measurements, these parameters are fixed at their nominal fit values to extract the statistical uncertainty on the fit. The systematic uncertainties are then computed as the difference between the nominal fit result and the fit result with fixed parameters.

### 5.11.2.1 $D_s^-$ decay model systematic uncertainty

In Sec. 5.9.1.1, the  $D_s^-$  decay model is presented. The fit performed during the hadronic  $\mathcal{R}(D^*)$  analysis gives weights according to each component of the internal composition of  $D_s^- \rightarrow \pi^- \pi^+ \pi^- X$  decays.

These weights are then used to correct the composition of the  $\Lambda_c^+ D_s^-$  simulation samples. The uncertainties of the fit will then be used to generate several alternative  $D_s^-$  templates for each  $D_s^-$  component in the 3D fit by varying the baseline template using both uncertainties and correlations between the  $D_s^-$  sub-components.

Using these new templates, the fit will be performed again and the distribution of the difference in the signal yield with respect to the nominal fit, divided by the nominal fit

$$\frac{N_{sig}^{alternative} - N_{sig}^{nominal}}{N_{sig}^{nominal}}$$

will be constructed, its standard deviation will be taken as the systematic uncertainty.

For now, a 2.5% systematic uncertainty is associated with the  $D_s^-$  decay model to match the uncertainty found in the  $\mathcal{R}(D^*)$  analysis.

### 5.11.2.2 Interpolation technique for template shape systematic uncertainties

The variables used in the fit,  $q^2$ ,  $\tau$  lifetime and BDT output, can have non negligible correlation with other variables, mainly kinematics, which can affect the shape of the templates and thus, the fit results.

Based on the work made for the hadronic  $\mathcal{R}(D^*)$  analysis, a set of 4 variables is chosen to study their effects on the fit.

They are:

- the  $\Lambda_c^+ 3\pi$  mass as it is observed to be highly correlated with the  $q^2$ , its variation need then to be taken into account.
- the  $3\pi$  mass which also affects the  $q^2$  distribution resolution. Events with a low  $3\pi$  mass tend to have a worse resolution and this affects directly the  $q^2$  one.
- the minimum of the  $\pi^- \pi^+$  mass. Both minimum and maximum of  $m(\pi^- \pi^+)$  enter the BDT as shown in Sec. 5.7 and thus, affect the shape of its output.
- the maximum of the  $\pi^- \pi^+$  mass for the same reason as above.

To study the effects of these variables, sets of weighted alternate templates are created for each background category of the model, i.e.  $D_s^-$ ,  $D^0$ ,  $D^-$  and combinatorial.

The distributions of each variable described above is varied using a quadratic interpolation

method and (linear) weights are applied on the templates, which are described as follows:

$$\begin{aligned}
 \omega_{M(\Lambda_c^+ 3\pi)} &= 1 + 2\alpha_{M(\Lambda_c^+ 3\pi)} \left( \frac{M(\Lambda_c^+ 3\pi) - 2700}{6000 - 2700} - \frac{1}{2} \right) \\
 \omega_{M(3\pi)} &= 1 + 2\alpha_{M(3\pi)} \left( \frac{M(3\pi) - 3m_\pi}{5700 - 3m_\pi} - \frac{1}{2} \right) \\
 \omega_{\min(M(\pi^-\pi^+))} &= 1 + 2\alpha_{\min(M(\pi^-\pi^+))} \left( \frac{\min(M(\pi^-\pi^+)) - 2m_\pi}{1000 - 2m_\pi} - \frac{1}{2} \right) \\
 \omega_{\max(M(\pi^-\pi^+))} &= 1 + 2\alpha_{\max(M(\pi^-\pi^+))} \left( \frac{\max(M(\pi^-\pi^+)) - 2m_\pi}{1400 - 2m_\pi} - \frac{1}{2} \right)
 \end{aligned} \tag{5.41}$$

Using Eq. 5.41, for each background component and for each variable studied, two alternate templates are create with the  $\alpha_i$  taking the values  $\pm 1$ .

Then, the fit is performed with each  $\alpha_i$  taken as a nuisance parameter allowing the interpolation between nominal and alternative templates using a quadratic interpolation method. All  $\alpha_i$  are allowed to float in the range  $[-1, +1]$  with a Gaussian constraint  $\sigma = 1$  included.

**$D_s^- D^0$  and  $D_s^-$  templates uncertainty** For the  $D_s^-$  template, only the variation on  $M(\Lambda_c^+ 3\pi)$  is taken into account as the effects of the other variables are already taken into account in the systematic uncertainty associated with the  $D_s^-$  decay model.

Tab. 5.18 presents the signal yield, its error and relative uncertainty with alphas considered for each background component.

Background component	$N_{sig}$	Relative uncertainty (%)
$D_s^-$	$1359 \pm 168$	12.4
$D_s^{*-}$	$1341 \pm 168$	12.5
$D_s^{*0}$	$1360 \pm 168$	12.4
$D_{s1}^{\prime-}$	$1366 \pm 161$	12.4
$\Lambda_c^+ bkg$	$1390 \pm 190$	13.7
$B_1 - B_2$	$1359 \pm 168$	12.4
$D^-$	$1526 \pm 172$	11.5
$D^{0v_1-v_2}$	$1404 \pm 253$	18.2
$D^{0same}$	$1390 \pm 170$	12.2

Table 5.18 – Signal yield and its uncertainty for each fit component its shape being varied using the  $\alpha$  parameters. For the  $D_s^-$  components only the  $\alpha$  corresponding to the variation along  $M(\Lambda_c^+ 3\pi)$  is considered.

The quadratic difference of the fit uncertainty with the shape varied of a particular background component with respect to the nominal fit gives the uncertainty related to the shape of this template. A fit is then performed with all shapes being allowed to vary, in order to take properly into account all the correlations between these alpha parameters.

The fit converges nicely, with a difference in log-likelihood,  $\Delta LL$ , of -8 and a very good  $\chi^2$ . The difference in signal yield between this fit (1512) and the nominal one (1359), *i.e.* a relative change of 11% is taken as the systematic uncertainty related to the shape parameters.

### 5.11.3 Efficiencies, selection and trigger

As the measured quantity is  $\mathcal{K}(\Lambda_c^+)$ , most of the selection efficiencies cancel in the ratio and only the remaining uncertainty has to be taken into account.

The peak of the exclusive decay  $\Lambda_b^0 \rightarrow \Lambda_c^+ \tau \nu_\tau$  is also used to study and correct for any disagreement between data and simulation samples.

#### 5.11.3.1 Trigger efficiency

The trigger efficiency, especially the L0Hadron part, is studied with respect to both the  $\tau$  lifetime and  $m(\Lambda_c^+ 3\pi)$ . Using the TISTOS method described in Sec. 5.6 to compute the trigger efficiencies and the exclusive peak of  $\Lambda_b^0 \rightarrow \Lambda_c^+ 3\pi$ , one can extract the correction to account for data and simulation disagreement on the trigger efficiency. The correction is been measured to  $+11.6 \pm 1\%$  and must be applied to  $(70 \pm 1)\%$  of the events.

#### 5.11.3.2 Systematic associated with TOS-nonTOS ratio

As shown in Sec. 5.6, the number of hits in the SPD sub-detector, `nSPDHits` is badly reproduced in simulation. As the TIS trigger efficiency is very correlated with `nSPDHits`, the ratio of TOS and nonTOS events has to be corrected. A systematic uncertainty of 1% is associated with this procedure.

#### 5.11.3.3 Other data/simulation adjustments

In addition to the trigger effects mentioned above, PID, the vertex requirement and isolation discrepancies between data and simulation are studied. This lead to a systematic uncertainty of 3.4%, excluding PID for the moment.

### 5.11.4 Normalisation channel

For the computation of  $\mathcal{K}(\Lambda_c^+)$ , feed-down from the  $\Lambda_c^* \pi$  events was removed from  $\Lambda_c^+ 3\pi$  signal peak, as well as  $\Lambda_c^+ D_s^+$  events where the  $D_s^+$  decayed to  $3\pi$ . The attached systematic uncertainty in this subtraction is estimated to be 3%, based on the agreement between the  $3\pi$  mass distribution of  $\Lambda_c^+ 3\pi$  and  $D^* 3\pi$  events.

### 5.11.5 $\Lambda_c^*$ feed-down

The nominal fit includes 12.5% of  $\Lambda_c^*$  feed-down. This fraction was varied by  $\pm 50\%$ . As a result, the fit yield changed by 2.5%, which is the value assigned to the uncertainty regarding this feed-down.

### 5.11.6 Simulation statistics

The systematic due to the finite size of simulation samples used to extract the shapes of the different background categories in the fit is computed using a bootstrapping procedure. The fit is performed 200 times with resampled simulation samples and the width of the signal yield distribution found with these resampled dataset is taken as the associated systematic. As the width is found to be 100 and the nominal fit gives 1350 signal events, the systematic is found to be 7.4%.

### 5.11.7 Systematics uncertainties summary

Tab. 5.19 presents a summary of all the uncertainty sources associated with the evaluation of  $\mathcal{K}(\Lambda_c^+)$ .

Contribution	Value (%)
$\tau$ polarization effects	0.4
Other $\tau$ decays	1.0
$3\pi\pi^0/3\pi$	1.6
$\Lambda_c^*\tau\nu$ contribution	2.5
Normalisation channel (feed-down subtraction)	3.0
$D_s^+ \rightarrow 3\pi X$ decay model	2.5
$D_s^+$ , $D^0$ and $D^+$ templates shape	11.3
$\Lambda_b^0 \rightarrow \Lambda_c^+ D^- X$ and $\Lambda_b^0 \rightarrow \Lambda_c^+ D^0 X$	6.6
Combinatorial background	0.5
L0Hadron trigger efficiency	1.0
Stripping	2.0
Data/simulation agreement relative to vertex and isolation	2.5
Efficiencies (Simulation statistics)	1.5
Simulation statistics	7.4
Total internal error	16.2
Total External error	12.0

Table 5.19 – List of all the sources of systematic uncertainties with their values in % for the  $\mathcal{R}(\Lambda_c)$  measurement. LHCb Unofficial.

## 5.12 Results

### 5.12.1 Results regarding $\mathcal{R}(\Lambda_c)$

The  $\mathcal{K}(\Lambda_c^+)$  observable, define in Eq. 5.2, in Sec. 5.1 is computed from the observed yields of signal and normalisation, and from the relative efficiencies.

The central value of  $\mathcal{R}(\Lambda_c)$  is kept blinded due to the upcoming publication of the LHCb publication based upon this work. The result can be therefore quoted as:

$$\mathcal{R}(\Lambda_c^+) = \frac{\mathcal{B}(\Lambda_b^0 \rightarrow \Lambda_c^+ \tau^- \bar{\nu}_\tau)}{\mathcal{B}(\Lambda_b^0 \rightarrow \Lambda_c^+ \mu^- \bar{\nu}_\mu)} = XXX \times (1 \pm 0.105(\text{stat}) \pm 0.162(\text{syst}) \pm 0.12(\text{ext})) \quad (5.42)$$

where the first uncertainty is statistical, the second corresponds to the total internal systematic uncertainty as described in Sec. 5.11 and the third takes into account the uncertainty on the  $\mathcal{B}$  of  $B^0 \rightarrow D^{*-} 3\pi$  (4.3%) and the uncertainty coming from the ratio  $\frac{\Gamma(\Lambda_b^0 \rightarrow \Lambda_c^+ \mu^+ \nu_\mu)}{\Gamma(\Lambda_b^0 \rightarrow \Lambda_c^+ \tau^+ \nu_\tau)}$  (6.8%) as discussed in Sec. 5.1.

### 5.12.2 Observation of the decay $\Lambda_b^0 \rightarrow \Lambda_c^+ \tau^- \bar{\nu}_\tau$

The observation of the decay  $\Lambda_b^0 \rightarrow \Lambda_c^+ \tau^- \bar{\nu}_\tau$  is demonstrated with a purely statistical significance of  $6.9 \sigma$  as shown in Sec. 5.10.4 through the difference in  $\chi^2$  between the nominal fit and a fit performed with the no signal hypothesis. This result takes into account the limited statistics of the simulation sample.

To include the systematic uncertainties in the computation of the  $\chi^2$  difference, a fit is performed with both all alpha parameters and signal yield left free to float and another with the signal yield forced to 0. This is a conservative method since it allows the background shapes variation to be independent in the two fits, while they are of course correlated. The  $\Delta\chi^2$  is found to be 32, corresponding to a significance of  $5.7 \sigma$  once the systematic uncertainties are taken into account.

Thanks to this computation of the  $\Delta\chi^2$  taking into account the systematic effects using the alpha parameters, the first observation of the decay  $\Lambda_b^0 \rightarrow \Lambda_c^+ \tau^- \bar{\nu}_\tau$  can be claimed with a statistical significance of  $5.7 \sigma$ .

### 5.12.3 Prospects

The result of this analysis is based on the data collected during the Run1 of the LHC, which represent  $3 \text{ fb}^{-1}$ . During Run2, the LHCb detector collected  $0.33 \text{ fb}^{-1}$  in 2015,  $1.67 \text{ fb}^{-1}$  in 2016,  $1.61 \text{ fb}^{-1}$  in 2017 and  $1.8 \text{ fb}^{-1}$  in 2018 with a cross-section  $\sigma(pp \rightarrow b\bar{b}X)$  roughly two times higher with respect to Run1 due to the increase of the energy in the centre-of-mass frame from 8 TeV to 13 TeV. In addition, the trigger efficiency is also roughly two times higher thanks to many improvements.

This allow to expect a decrease of the statistical uncertainty by a factor 1.9 using the data collected during Run1 and in the first half of the Run2 (2015 & 2016) and 2.9 by performing the analysis on both Run1 and the full Run2 dataset (2015-2018). This results in an expected statistical uncertainty of 5.5% for the first case and 3.6% for the latter with expected systematic uncertainty expected to be respectively 10% and 8% as both constraints on the double charmed background using external inputs and the use of additional simulation samples will help to decrease the total systematic uncertainty.



# Conclusion

Semitaquonic decays have been demonstrated as excellent probes of potential Lepton Flavour Universality violation and a novel technique for the  $\tau$  reconstruction was successfully used to measure  $\mathcal{R}(D^*)$ .

The measurement of  $\mathcal{R}(D^*)$  with the  $\tau$  reconstructed in its  $3\pi$  decay modes, based on the  $3 \text{ fb}^{-1}$  sample of LHC data taken at 7 and 8 TeV centre-of-mass energy, is reported in this thesis with a dedicated study of particle identification efficiencies and related systematic uncertainty. Using the signal yield extracted from the 3D templates-based fit and external measurements of  $\mathcal{B}(B^0 \rightarrow D^{*-}3\pi)$  and  $\mathcal{B}(B^0 \rightarrow D^{*-}\mu^+\nu_\mu)$ ,  $\mathcal{R}(D^*)$  is measured to be:

$$\mathcal{R}(D^{*-}) = 0.291 \pm 0.019 (\text{stat}) \pm 0.026 (\text{syst}) \pm 0.013 (\text{ext})$$

The LHCb combination of this result with the  $\mathcal{R}(D^*)$  muonic measurement reported in Ref. [67] is found to be:

$$\mathcal{R}(D^{*-}) = 0.310 \pm 0.0155 (\text{stat}) \pm 0.0219 (\text{syst})$$

This leads to a substantial improvement in the precision of the World Average value and increases slightly its discrepancy with SM expectation.

The analysis of  $\mathcal{R}(\Lambda_c)$ , the main work of this thesis, is reported in great detail. Using the same Run1 sample, the observation of the decay  $\Lambda_b^0 \rightarrow \Lambda_c^+ \tau \bar{\nu}_\tau$  has been demonstrated for the first time, with a significance of  $5.7 \sigma$ , measured as the difference in  $\chi^2$  between the nominal fit and a fit performed with the no signal hypothesis. This significance takes into account systematic uncertainties and the limited statistics of the simulation sample.

The statistical uncertainty related to  $\mathcal{R}(\Lambda_c)$  has been measured to be 10.5%. Given the fact that a tighter signal selection has been applied here to  $\Lambda_c^+ \tau \bar{\nu}_\tau$  sample compared to the  $D^{*-}$  channel due to a lack of a large prompt background sample, this demonstrates that  $\mathcal{R}(\Lambda_c)$  can in the future be measured with the same statistical precision than  $\mathcal{R}(D^*)$ , a very encouraging result. The internal systematic uncertainties are presently dominated by the limited knowledge of  $\Lambda_b^0$  decays to  $\Lambda_c^+ D^- X$  decays at the global level of 16.2%. A significant reduction can be expected in the future with the addition of more data and external constraints on the  $D^-$  background. The systematic uncertainty due to external

---

branching ratios can be brought down to 12% by the use of solid theoretical external input which enables to bridge the absolute branching ratio of the decay  $\Lambda_b^0 \rightarrow \Lambda_c^+ 3\pi$  to the well measured decay rate of  $B^0 \rightarrow D^* 3\pi$ .

The signal yield extracted from the fit is for the moment reported in a blinded way as follows:

$$\mathcal{R}(\Lambda_c^+) = \frac{\mathcal{B}(\Lambda_b^0 \rightarrow \Lambda_c^+ \tau^- \bar{\nu}_\tau)}{\mathcal{B}(\Lambda_b^0 \rightarrow \Lambda_c^+ \mu^- \bar{\nu}_\mu)} = XXX \times (1 \pm 0.105(\text{stat}) \pm 0.162(\text{syst}) \pm 0.12(\text{ext})) \quad (5.43)$$

Based on the work reported in this thesis, the LHCb collaboration plans to publish soon a measurement of  $\mathcal{R}(\Lambda_c)$  based using data collected during both Run1 and Run2, where both statistical and systematic uncertainties should be reduced by a significant amount. This result will enable a very sensitive test of Lepton Universality in semitauonic decays.

# Bibliography

- [1] HFLAV. *Average of  $R(D)$  and  $R(D^*)$  for Summer 2018*. URL: <https://hflav-eos.web.cern.ch/hflav-eos/semi/summer18/RDRDs.html>, (Cited on pages 10, 15, 45, 50, 82, 105)
- [2] William Detmold, Christoph Lehner, and Stefan Meinel.  $\Lambda_b \rightarrow p\ell^-\bar{\nu}_\ell$  and  $\Lambda_b \rightarrow \Lambda_c\ell^-\bar{\nu}_\ell$  form factors from lattice QCD with relativistic heavy quarks. *Phys. Rev.*, D92.3 (2015), p. 034503. DOI: [10.1103/PhysRevD.92.034503](https://doi.org/10.1103/PhysRevD.92.034503). arXiv: [1503.01421](https://arxiv.org/abs/1503.01421) [[hep-lat](#)] (Cited on pages 10, 38, 46, 111)
- [3] R. Aaij et al. Test of lepton flavor universality by the measurement of the  $B^0 \rightarrow D^{*-}\tau^+\nu_\tau$  branching fraction using three-prong  $\tau$  decays. *Phys. Rev.*, D97 (2018), p. 072013. DOI: [10.1103/PhysRevD.97.072013](https://doi.org/10.1103/PhysRevD.97.072013). arXiv: [1711.02505](https://arxiv.org/abs/1711.02505) [[hep-ex](#)] (Cited on pages 13–15, 47, 81, 83, 84, 86, 88–90, 93–98, 104)
- [4] R Aaij et al. Study of  $B^0 \rightarrow D^{*-}\pi^+\pi^-\pi^+$  and  $B^0 \rightarrow D^{*-}K^+\pi^-\pi^+$  decays. *Phys. Rev.*, D87.9 (2013), p. 092001. DOI: [10.1103/PhysRevD.87.092001](https://doi.org/10.1103/PhysRevD.87.092001). arXiv: [1303.6861](https://arxiv.org/abs/1303.6861) [[hep-ex](#)] (Cited on pages 15, 82, 103)
- [5] G. Majumder et al. Observation of  $B^0 \rightarrow D^{*-}(5\pi)^+$ ,  $B^+ \rightarrow D^{*-}(4\pi)^{++}$  and  $B^+ \rightarrow \bar{D}^{*0}(5\pi)^+$ . *Phys. Rev. D*, 70 (11 Dec. 2004), p. 111103. DOI: [10.1103/PhysRevD.70.111103](https://doi.org/10.1103/PhysRevD.70.111103). URL: <https://link.aps.org/doi/10.1103/PhysRevD.70.111103> (Cited on pages 15, 82, 103)
- [6] J. P. Lees et al. Measurement of the  $B^0 \rightarrow D^{*-}\pi^+\pi^-\pi^+$  branching fraction. *Phys. Rev.*, D94.9 (2016), p. 091101. DOI: [10.1103/PhysRevD.94.091101](https://doi.org/10.1103/PhysRevD.94.091101). arXiv: [1609.06802](https://arxiv.org/abs/1609.06802) [[hep-ex](#)] (Cited on pages 15, 82, 103)
- [7] C. Patrignani et al. Review of Particle Physics. *Chin. Phys.*, C40.10 (2016), p. 100001. DOI: [10.1088/1674-1137/40/10/100001](https://doi.org/10.1088/1674-1137/40/10/100001) (Cited on pages 15, 25, 31, 105, 110, 113)
- [8] R. Aaij et al. Measurement of the ratio of the  $\mathcal{B}(B^0 \rightarrow D^{*-}\tau^+\nu_\tau)$  and  $\mathcal{B}(B^0 \rightarrow D^{*-}\mu^+\nu_\mu)$  branching fractions using three-prong  $\tau$ -lepton decays. *Phys. Rev. Lett.*, 120 (2018), p. 171802. DOI: [10.1103/PhysRevLett.120.171802](https://doi.org/10.1103/PhysRevLett.120.171802). arXiv: [1708.08856](https://arxiv.org/abs/1708.08856) [[hep-ex](#)] (Cited on pages 15, 47, 81)
- [9] R. P. Feynman. Mathematical Formulation of the Quantum Theory of Electromagnetic Interaction. *Physical Review*, 80 (Nov. 1950), pp. 440–457. DOI: [10.1103/PhysRev.80.440](https://doi.org/10.1103/PhysRev.80.440) (Cited on page 23)
- [10] Julian Schwinger. On Quantum-Electrodynamics and the Magnetic Moment of the Electron. *Phys. Rev.*, 73 (4 Feb. 1948), pp. 416–417. DOI: [10.1103/PhysRev.73.416](https://doi.org/10.1103/PhysRev.73.416)

## BIBLIOGRAPHY

---

- 73.416. URL: <https://link.aps.org/doi/10.1103/PhysRev.73.416> (Cited on page 23)
- [11] S. Tomonaga. On a Relativistically Invariant Formulation of the Quantum Theory of Wave Fields. *Progress of Theoretical Physics*, 1 (Aug. 1946), pp. 27–42. DOI: [10.1143/PTP.1.27](https://doi.org/10.1143/PTP.1.27) (Cited on page 23)
- [12] H. Fritzsch, M. Gell-Mann, and H. Leutwyler. Advantages of the color octet gluon picture. *Physics Letters B*, 47.4 (1973), pp. 365–368. ISSN: 0370-2693. DOI: [https://doi.org/10.1016/0370-2693\(73\)90625-4](https://doi.org/10.1016/0370-2693(73)90625-4). URL: <http://www.sciencedirect.com/science/article/pii/0370269373906254> (Cited on page 24)
- [13] D. J. Gross and F. Wilczek. Ultraviolet Behavior of Non-Abelian Gauge Theories. *Physical Review Letters*, 30 (June 1973), pp. 1343–1346. DOI: [10.1103/PhysRevLett.30.1343](https://doi.org/10.1103/PhysRevLett.30.1343) (Cited on page 24)
- [14] H. D. Politzer. Reliable Perturbative Results for Strong Interactions? *Physical Review Letters*, 30 (June 1973), pp. 1346–1349. DOI: [10.1103/PhysRevLett.30.1346](https://doi.org/10.1103/PhysRevLett.30.1346) (Cited on page 24)
- [15] R. Aaij et al. Observation of the resonant character of the  $Z(4430)^-$  state. *Phys. Rev. Lett.*, 112 (2014), p. 222002. DOI: [10.1103/PhysRevLett.112.222002](https://doi.org/10.1103/PhysRevLett.112.222002). arXiv: [1404.1903](https://arxiv.org/abs/1404.1903) [hep-ex] (Cited on page 24)
- [16] R. Aaij et al. Evidence for exotic hadron contributions to  $\Lambda_b^0 \rightarrow J/\psi p \pi^-$  decays. *Phys. Rev. Lett.*, 117 (2016), p. 082003. DOI: [10.1103/PhysRevLett.117.082003](https://doi.org/10.1103/PhysRevLett.117.082003). arXiv: [1606.06999](https://arxiv.org/abs/1606.06999) [hep-ex] (Cited on page 24)
- [17] Sheldon L. Glashow. Partial-symmetries of weak interactions. *Nuclear Physics*, 22.4 (1961), pp. 579–588. ISSN: 0029-5582. DOI: [https://doi.org/10.1016/0029-5582\(61\)90469-2](https://doi.org/10.1016/0029-5582(61)90469-2). URL: <http://www.sciencedirect.com/science/article/pii/0029558261904692> (Cited on pages 25, 30)
- [18] Abdus Salam. Weak and Electromagnetic Interactions. *Conf. Proc.*, C680519 (1968), pp. 367–377 (Cited on pages 25, 30)
- [19] Steven Weinberg. A Model of Leptons. *Phys. Rev. Lett.*, 19 (21 Nov. 1967), pp. 1264–1266. DOI: [10.1103/PhysRevLett.19.1264](https://doi.org/10.1103/PhysRevLett.19.1264). URL: <https://link.aps.org/doi/10.1103/PhysRevLett.19.1264> (Cited on pages 25, 30)
- [20] E. Fermi. Versuch einer Theorie der  $\beta$ -Strahlen. I. *Zeitschrift für Physik*, 88.3 (Mar. 1934), pp. 161–177. ISSN: 0044-3328. DOI: [10.1007/BF01351864](https://doi.org/10.1007/BF01351864). URL: <https://doi.org/10.1007/BF01351864> (Cited on page 25)
- [21] E. Noether. Invariant variation problems. *Transport Theory and Statistical Physics*, 1 (Jan. 1971), pp. 186–207. DOI: [10.1080/00411457108231446](https://doi.org/10.1080/00411457108231446). eprint: [physics/0503066](https://arxiv.org/abs/physics/0503066) (Cited on page 25)
- [22] David J Griffiths. *Introduction to elementary particles; 2nd rev. version*. Physics textbook. New York, NY: Wiley, 2008. URL: <https://cds.cern.ch/record/111880> (Cited on pages 26, 28)
- [23] J. P. Lees et al. Observation of Time Reversal Violation in the  $B^0$  Meson System. *Phys. Rev. Lett.*, 109 (2012), p. 211801. DOI: [10.1103/PhysRevLett.109.211801](https://doi.org/10.1103/PhysRevLett.109.211801). arXiv: [1207.5832](https://arxiv.org/abs/1207.5832) [hep-ex] (Cited on page 26)
- [24] T. D. Lee and C. N. Yang. Question of Parity Conservation in Weak Interactions. *Phys. Rev.*, 104 (1 Oct. 1956), pp. 254–258. DOI: [10.1103/PhysRev.104.254](https://doi.org/10.1103/PhysRev.104.254). URL: <https://link.aps.org/doi/10.1103/PhysRev.104.254> (Cited on page 27)

- 
- [25] M. Goldhaber, L. Grodzins, and A. W. Sunyar. Helicity of Neutrinos. *Phys. Rev.*, 109 (3 Feb. 1958), pp. 1015–1017. DOI: [10.1103/PhysRev.109.1015](https://doi.org/10.1103/PhysRev.109.1015). URL: <https://link.aps.org/doi/10.1103/PhysRev.109.1015> (Cited on page 27)
- [26] J. H. Christenson, J. W. Cronin, V. L. Fitch, and R. Turlay. Evidence for the  $2\pi$  Decay of the  $K_2^0$  Meson. *Phys. Rev. Lett.*, 13 (4 July 1964), pp. 138–140. DOI: [10.1103/PhysRevLett.13.138](https://doi.org/10.1103/PhysRevLett.13.138). URL: <https://link.aps.org/doi/10.1103/PhysRevLett.13.138> (Cited on page 27)
- [27] F. Englert and R. Brout. Broken Symmetry and the Mass of Gauge Vector Mesons. *Phys. Rev. Lett.*, 13 (9 Aug. 1964), pp. 321–323. DOI: [10.1103/PhysRevLett.13.321](https://doi.org/10.1103/PhysRevLett.13.321). URL: <https://link.aps.org/doi/10.1103/PhysRevLett.13.321> (Cited on page 30)
- [28] Peter W. Higgs. Broken Symmetries and the Masses of Gauge Bosons. *Phys. Rev. Lett.*, 13 (16 Oct. 1964), pp. 508–509. DOI: [10.1103/PhysRevLett.13.508](https://doi.org/10.1103/PhysRevLett.13.508). URL: <https://link.aps.org/doi/10.1103/PhysRevLett.13.508> (Cited on page 30)
- [29] Peter W. Higgs. Spontaneous Symmetry Breakdown without Massless Bosons. *Phys. Rev.*, 145 (4 May 1966), pp. 1156–1163. DOI: [10.1103/PhysRev.145.1156](https://doi.org/10.1103/PhysRev.145.1156). URL: <https://link.aps.org/doi/10.1103/PhysRev.145.1156> (Cited on page 30)
- [30] G. S. Guralnik, C. R. Hagen, and T. W. B. Kibble. Global Conservation Laws and Massless Particles. *Phys. Rev. Lett.*, 13 (20 Nov. 1964), pp. 585–587. DOI: [10.1103/PhysRevLett.13.585](https://doi.org/10.1103/PhysRevLett.13.585). URL: <https://link.aps.org/doi/10.1103/PhysRevLett.13.585> (Cited on page 30)
- [31] Georges Aad, Tatevik Abajyan, Brad Abbott, and Abdallah. Observation of a new particle in the search for the Standard Model Higgs boson with the ATLAS detector at the LHC. *Phys.Lett.*, B716 (Sept. 17, 2012), pp. 1–29. DOI: [10.1016/j.physletb.2012.08.020](https://doi.org/10.1016/j.physletb.2012.08.020) (Cited on pages 32, 55)
- [32] Serguei Chatrchyan, Vardan Khachatryan, and Albert M. Sirunyan. Observation of a new boson at a mass of 125 GeV with the CMS experiment at the LHC. *Phys.Lett.*, B716 (Aug. 17, 2012), pp. 30–61. DOI: [10.1016/j.physletb.2012.08.021](https://doi.org/10.1016/j.physletb.2012.08.021) (Cited on pages 32, 55)
- [33] G. Aad, T. Abajyan, B. Abbott, J. Abdallah, and L. Zwalinski. Evidence for the spin-0 nature of the Higgs boson using ATLAS data. *Physics Letters B*, 726.1 (2013), pp. 120–144. ISSN: 0370-2693. DOI: <https://doi.org/10.1016/j.physletb.2013.08.026>. URL: <http://www.sciencedirect.com/science/article/pii/S0370269313006527> (Cited on page 32)
- [34] Makoto Kobayashi and Toshihide Maskawa. CP-Violation in the Renormalizable Theory of Weak Interaction. *Progress of Theoretical Physics*, 49.2 (1973), pp. 652–657. DOI: [10.1143/PTP.49.652](https://doi.org/10.1143/PTP.49.652). eprint: [/oup/backfile/content\\_public/journal/ptp/49/2/10.1143/ptp.49.652/2/49-2-652.pdf](http://oup/backfile/content_public/journal/ptp/49/2/10.1143/ptp.49.652/2/49-2-652.pdf). URL: <http://dx.doi.org/10.1143/PTP.49.652> (Cited on page 33)
- [35] Lincoln Wolfenstein. Parametrization of the Kobayashi-Maskawa Matrix. *Phys. Rev. Lett.*, 51 (21 Nov. 1983), pp. 1945–1947. DOI: [10.1103/PhysRevLett.51.1945](https://doi.org/10.1103/PhysRevLett.51.1945). URL: <https://link.aps.org/doi/10.1103/PhysRevLett.51.1945> (Cited on page 33)

## BIBLIOGRAPHY

---

- [36] J. Charles et al. Current status of the Standard Model CKM fit and constraints on  $\Delta F = 2$  New Physics. *Phys. Rev.*, D91.7 (2015), p. 073007. DOI: [10.1103/PhysRevD.91.073007](https://doi.org/10.1103/PhysRevD.91.073007). arXiv: [1501.05013](https://arxiv.org/abs/1501.05013) [[hep-ph](#)] (Cited on page 34)
- [37] K. G. Begeman, A. H. Broeils, and R. H. Sanders. Extended rotation curves of spiral galaxies - Dark haloes and modified dynamics. *MNRAS*, 249 (Apr. 1991), pp. 523–537. DOI: [10.1093/mnras/249.3.523](https://doi.org/10.1093/mnras/249.3.523) (Cited on page 34)
- [38] P. A. R. Ade et al. Planck 2015 results. XIII. Cosmological parameters. *Astron. Astrophys.*, 594 (2016), A13. DOI: [10.1051/0004-6361/201525830](https://doi.org/10.1051/0004-6361/201525830). arXiv: [1502.01589](https://arxiv.org/abs/1502.01589) [[astro-ph.CO](#)] (Cited on page 34)
- [39] A. D. Sakharov. SPECIAL ISSUE: Violation of CP in variance, C asymmetry, and baryon asymmetry of the universe. *Soviet Physics Uspekhi*, 34 (May 1991), pp. 392–393. DOI: [10.1070/PU1991v034n05ABEH002497](https://doi.org/10.1070/PU1991v034n05ABEH002497) (Cited on page 34)
- [40] R. Aaij et al. Measurement of the  $B_s^0 \rightarrow \mu^+\mu^-$  branching fraction and search for  $B^0 \rightarrow \mu^+\mu^-$  decays at the LHCb experiment. *Phys. Rev. Lett.*, 111 (2013), p. 101805. DOI: [10.1103/PhysRevLett.111.101805](https://doi.org/10.1103/PhysRevLett.111.101805). arXiv: [1307.5024](https://arxiv.org/abs/1307.5024) [[hep-ex](#)] (Cited on page 37)
- [41] S. Schael et al. Precision electroweak measurements on the  $Z$  resonance. *Phys. Rept.*, 427 (2006), pp. 257–454. DOI: [10.1016/j.physrep.2005.12.006](https://doi.org/10.1016/j.physrep.2005.12.006). arXiv: [hep-ex/0509008](https://arxiv.org/abs/hep-ex/0509008) [[hep-ex](#)] (Cited on page 38)
- [42] Matthias Neubert. Heavy quark effective theory. *Subnucl. Ser.*, 34 (1997), pp. 98–165. arXiv: [hep-ph/9610266](https://arxiv.org/abs/hep-ph/9610266) [[hep-ph](#)] (Cited on pages 38, 42)
- [43] Christoph Bobeth, Gudrun Hiller, and Giorgi Piranishvili. Angular distributions of  $\bar{B} \rightarrow \bar{K}\ell^+\ell^-$  decays. *JHEP*, 12 (2007), p. 040. DOI: [10.1088/1126-6708/2007/12/040](https://doi.org/10.1088/1126-6708/2007/12/040). arXiv: [0709.4174](https://arxiv.org/abs/0709.4174) [[hep-ph](#)] (Cited on page 40)
- [44] R. Aaij et al. Test of lepton universality using  $B^+ \rightarrow K^+\ell^+\ell^-$  decays. *Phys. Rev. Lett.*, 113 (2014), p. 151601. DOI: [10.1103/PhysRevLett.113.151601](https://doi.org/10.1103/PhysRevLett.113.151601). arXiv: [1406.6482](https://arxiv.org/abs/1406.6482) [[hep-ex](#)] (Cited on page 40)
- [45] J. P. Lees et al. Measurement of Branching Fractions and Rate Asymmetries in the Rare Decays  $B \rightarrow K^{(*)}l^+l^-$ . *Phys. Rev.*, D86 (2012), p. 032012. DOI: [10.1103/PhysRevD.86.032012](https://doi.org/10.1103/PhysRevD.86.032012). arXiv: [1204.3933](https://arxiv.org/abs/1204.3933) [[hep-ex](#)] (Cited on pages 40, 41)
- [46] J.-T. Wei et al. Measurement of the Differential Branching Fraction and Forward-Backward Asymmetry for  $B \rightarrow K^{(*)}l^+l^-$ . *Phys. Rev. Lett.*, 103 (17 Oct. 2009), p. 171801. DOI: [10.1103/PhysRevLett.103.171801](https://doi.org/10.1103/PhysRevLett.103.171801). URL: <https://link.aps.org/doi/10.1103/PhysRevLett.103.171801> (Cited on pages 40, 41)
- [47] R. Aaij et al. Test of lepton universality with  $B^0 \rightarrow K^{*0}\ell^+\ell^-$  decays. *JHEP*, 08 (2017), p. 055. DOI: [10.1007/JHEP08\(2017\)055](https://doi.org/10.1007/JHEP08(2017)055). arXiv: [1705.05802](https://arxiv.org/abs/1705.05802) [[hep-ex](#)] (Cited on pages 40, 41)
- [48] Alexander Lenz. Lifetimes and heavy quark expansion. *Int. J. Mod. Phys.*, A30.10 (2015). [[63\(2014\)](#)], p. 1543005. DOI: [10.1142/S0217751X15430058](https://doi.org/10.1142/S0217751X15430058). arXiv: [1405.3601](https://arxiv.org/abs/1405.3601) [[hep-ph](#)] (Cited on page 42)
- [49] Svjetlana Fajfer, Jernej F. Kamenik, and Ivan Nisandzic. On the B to D\* tau nu Sensitivity to New Physics (Mar. 2012). eprint: [1203.2654](https://arxiv.org/abs/1203.2654) (Cited on pages 42–45, 98)
- [50] Irinel Caprini, Laurent Lellouch, and Matthias Neubert. Dispersive bounds on the shape of  $\bar{B} \rightarrow D^{(*)}$  lepton anti-neutrino form-factors. *Nucl. Phys.*, B530 (1998),

- pp. 153–181. DOI: [10.1016/S0550-3213\(98\)00350-2](https://doi.org/10.1016/S0550-3213(98)00350-2). arXiv: [hep-ph/9712417](https://arxiv.org/abs/hep-ph/9712417) [[hep-ph](#)] (Cited on page 44)
- [51] W. Dungel et al. Measurement of the form factors of the decay  $B^0 \rightarrow D^{*-}\ell^+\nu$  and determination of the CKM matrix element  $|V_{cb}|$ . *Phys. Rev.*, D82 (2010), p. 112007. DOI: [10.1103/PhysRevD.82.112007](https://doi.org/10.1103/PhysRevD.82.112007). arXiv: [1010.5620](https://arxiv.org/abs/1010.5620) [[hep-ex](#)] (Cited on page 45)
- [52] A. Abdesselam et al. Precise determination of the CKM matrix element  $|V_{cb}|$  with  $\bar{B}^0 \rightarrow D^{*+}\ell^-\bar{\nu}_\ell$  decays with hadronic tagging at Belle (2017). arXiv: [1702.01521](https://arxiv.org/abs/1702.01521) [[hep-ex](#)] (Cited on pages 45, 46)
- [53] C. Glenn Boyd, Benjamin Grinstein, and Richard F. Lebed. Precision corrections to dispersive bounds on form-factors. *Phys. Rev.*, D56 (1997), pp. 6895–6911. DOI: [10.1103/PhysRevD.56.6895](https://doi.org/10.1103/PhysRevD.56.6895). arXiv: [hep-ph/9705252](https://arxiv.org/abs/hep-ph/9705252) [[hep-ph](#)] (Cited on page 45)
- [54] Florian U. Bernlochner, Zoltan Ligeti, Michele Papucci, and Dean J. Robinson. Combined analysis of semileptonic  $B$  decays to  $D$  and  $D^*$ :  $R(D^{(*)})$ ,  $|V_{cb}|$ , and new physics. *Phys. Rev. D*, 95, (Mar. 2017), p. 115008. eprint: [1703.05330](https://arxiv.org/abs/1703.05330) (Cited on page 46)
- [55] Dante Bigi, Paolo Gambino, and Stefan Schacht.  $R(D^*)$ ,  $|V_{cb}|$ , and the Heavy Quark Symmetry relations between form factors (July 2017). eprint: [1707.09509](https://arxiv.org/abs/1707.09509) (Cited on pages 46, 48)
- [56] Sneha Jaiswal, Soumitra Nandi, and Sunando Kumar Patra. Extraction of  $|V_{cb}|$  from  $B \rightarrow D^{(*)}\ell\nu_\ell$  and the Standard Model predictions of  $R(D^{(*)})$  (July 2017). eprint: [1707.09977](https://arxiv.org/abs/1707.09977) (Cited on page 46)
- [57] Bernard Aubert et al. Measurement of  $|V_{cb}|$  and the Form-Factor Slope in anti- $B \rightarrow D^+ \ell^- \bar{\nu}_\ell$  anti- $\nu$  Decays in Events Tagged by a Fully Reconstructed B Meson. *Phys. Rev. Lett.*, 104 (2010), p. 011802. DOI: [10.1103/PhysRevLett.104.011802](https://doi.org/10.1103/PhysRevLett.104.011802). arXiv: [0904.4063](https://arxiv.org/abs/0904.4063) [[hep-ex](#)] (Cited on pages 46, 111)
- [58] R. Glattauer et al. Measurement of the decay  $B \rightarrow D\ell\nu_\ell$  in fully reconstructed events and determination of the Cabibbo-Kobayashi-Maskawa matrix element  $|V_{cb}|$ . *Phys. Rev.*, D93.3 (2016), p. 032006. DOI: [10.1103/PhysRevD.93.032006](https://doi.org/10.1103/PhysRevD.93.032006). arXiv: [1510.03657](https://arxiv.org/abs/1510.03657) [[hep-ex](#)] (Cited on pages 46, 111)
- [59] Jon A. Bailey et al.  $B \rightarrow D^+ \ell^- \bar{\nu}_\ell$  form factors at nonzero recoil and  $|V_{cb}|$  from 2+1-flavor lattice QCD. *Phys. Rev.*, D92.3 (2015), p. 034506. DOI: [10.1103/PhysRevD.92.034506](https://doi.org/10.1103/PhysRevD.92.034506). arXiv: [1503.07237](https://arxiv.org/abs/1503.07237) [[hep-lat](#)] (Cited on page 46)
- [60] Heechang Na, Chris M. Bouchard, G. Peter Lepage, Chris Monahan, and Junko Shigemitsu.  $B \rightarrow D\ell\nu$  form factors at nonzero recoil and extraction of  $|V_{cb}|$ . *Phys. Rev.*, D92.5 (2015). [Erratum: *Phys. Rev.*D93,no.11,119906(2016)], p. 054510. DOI: [10.1103/PhysRevD.93.119906](https://doi.org/10.1103/PhysRevD.93.119906), [10.1103/PhysRevD.92.054510](https://doi.org/10.1103/PhysRevD.92.054510). arXiv: [1505.03925](https://arxiv.org/abs/1505.03925) [[hep-lat](#)] (Cited on pages 46, 111)
- [61] Dante Bigi and Paolo Gambino. Revisiting  $B \rightarrow D\ell\nu$ . *Phys. Rev.*, D94.9 (2016), p. 094008. DOI: [10.1103/PhysRevD.94.094008](https://doi.org/10.1103/PhysRevD.94.094008). arXiv: [1606.08030](https://arxiv.org/abs/1606.08030) [[hep-ph](#)] (Cited on page 46)
- [62] J. P. Lees et al. Evidence for an excess of  $\bar{B} \rightarrow D^{(*)}\tau^-\bar{\nu}_\tau$  decays. *Phys. Rev. Lett.*, 109 (2012), p. 101802. DOI: [10.1103/PhysRevLett.109.101802](https://doi.org/10.1103/PhysRevLett.109.101802). arXiv: [1205.5442](https://arxiv.org/abs/1205.5442) [[hep-ex](#)] (Cited on pages 47, 51)

## BIBLIOGRAPHY

---

- [63] J. P. Lees et al. Measurement of an Excess of  $\bar{B} \rightarrow D^{(*)}\tau^{-}\bar{\nu}_{\tau}$  Decays and Implications for Charged Higgs Bosons. *Phys. Rev.*, D88.7 (2013), p. 072012. DOI: [10.1103/PhysRevD.88.072012](https://doi.org/10.1103/PhysRevD.88.072012). arXiv: [1303.0571](https://arxiv.org/abs/1303.0571) [[hep-ex](#)] (Cited on page 47)
- [64] Belle Collaboration et al. Measurement of the branching ratio of  $\bar{B} \rightarrow D^{(*)}\tau^{-}\bar{\nu}_{\tau}$  relative to  $\bar{B} \rightarrow D^{(*)}\ell^{-}\bar{\nu}_{\ell}$  decays with hadronic tagging at Belle. *Phys. Rev. D*, 92, (July 2015), p. 072014. eprint: [1507.03233](https://arxiv.org/abs/1507.03233) (Cited on page 47)
- [65] S. Hirose et al. Measurement of the  $\tau$  lepton polarization and  $R(D^{*})$  in the decay  $\bar{B} \rightarrow D^{*}\tau^{-}\bar{\nu}_{\tau}$ . *Phys. Rev. Lett.*, 118, (Dec. 2016), p. 211801. eprint: [1612.00529](https://arxiv.org/abs/1612.00529) (Cited on page 47)
- [66] S. Hirose et al. Measurement of the  $\tau$  lepton polarization and  $R(D^{*})$  in the decay  $\bar{B} \rightarrow D^{*}\tau^{-}\bar{\nu}_{\tau}$  with one-prong hadronic  $\tau$  decays at Belle. *Phys. Rev. D*, 97, (Sept. 2017), p. 012004. eprint: [1709.00129](https://arxiv.org/abs/1709.00129) (Cited on page 47)
- [67] R. Aaij et al. Measurement of the ratio of branching fractions  $\mathcal{B}(\bar{B}^0 \rightarrow D^{*+}\tau^{-}\bar{\nu}_{\tau})/\mathcal{B}(\bar{B}^0 \rightarrow D^{*+}\mu^{-}\bar{\nu}_{\mu})$ . *Phys. Rev. Lett.*, 115 (2015), p. 111803. DOI: [10.1103/PhysRevLett.115.111803](https://doi.org/10.1103/PhysRevLett.115.111803). arXiv: [1506.08614](https://arxiv.org/abs/1506.08614) [[hep-ex](#)] (Cited on pages 47, 49, 82, 105, 197)
- [68] R. Aaij et al. Measurement of the ratio of branching fractions  $\mathcal{B}(B_c^+ \rightarrow J/\psi\tau^+\nu_{\tau})/\mathcal{B}(B_c^+ \rightarrow J/\psi\mu^+\nu_{\mu})$ . *Phys. Rev. Lett.*, 120 (2018), p. 121801. DOI: [10.1103/PhysRevLett.120.121801](https://doi.org/10.1103/PhysRevLett.120.121801). arXiv: [1711.05623](https://arxiv.org/abs/1711.05623) [[hep-ex](#)] (Cited on page 48)
- [69] Damir Becirevic, Nejc Kosnik, and Andrey Tayduganov. Testing the Standard Model in  $B \rightarrow D\tau\bar{\nu}$  decay with minimal theory input (2013). URL: <http://arxiv.org/abs/1301.4037> (Cited on page 50)
- [70] Damir Bečirević, Nejc Košnik, Olcyr Sumensari, and Renata Zukanovich Funchal. Palatable Leptoquark Scenarios for Lepton Flavor Violation in Exclusive  $b \rightarrow s\ell_1\ell_2$  modes (Aug. 2016). URL: <http://arxiv.org/abs/1608.07583> (Cited on pages 50, 51)
- [71] Alakabha Datta, Saeed Kamali, Stefan Meinel, and Ahmed Rashed. Phenomenology of  $\Lambda_b \rightarrow \Lambda_c\tau\bar{\nu}_{\tau}$  using lattice QCD calculations (Feb. 2017). URL: <http://arxiv.org/abs/1702.02243> (Cited on pages 50, 51)
- [72] Minoru Tanaka. Charged Higgs Effects on Exclusive Semi-tauonic  $B$  Decays. *Z.Phys. C*, 67 (1995), pp. 321–326. eprint: [hep-ph/9411405](https://arxiv.org/abs/hep-ph/9411405) (Cited on page 51)
- [73] Sofiane M. Boucenna, Alejandro Celis, Javier Fuentes-Martín, Avelino Vicente, and Javier Virto. Non-abelian gauge extensions for B-decay anomalies. *Physics Letters, Section B: Nuclear, Elementary Particle and High-Energy Physics*, 760 (2016), pp. 214–219. DOI: [10.1016/j.physletb.2016.06.067](https://doi.org/10.1016/j.physletb.2016.06.067) (Cited on page 51)
- [74] ATLAS Collaboration. A search for high-mass resonances decaying to  $\tau\nu$  in  $pp$  collisions at  $\sqrt{s} = 13$  TeV with the ATLAS detector. *arXiv:1801.06992* [[hep-ex](#)], (Jan. 22, 2018). arXiv: [1801.06992](https://arxiv.org/abs/1801.06992). URL: <http://arxiv.org/abs/1801.06992> (Cited on page 52)
- [75] K. Aamodt et al. The ALICE experiment at the CERN LHC. *JINST*, 3 (2008), S08002. DOI: [10.1088/1748-0221/3/08/S08002](https://doi.org/10.1088/1748-0221/3/08/S08002) (Cited on page 54)
- [76] The ATLAS Collaboration et al. The ATLAS Experiment at the CERN Large Hadron Collider. *Journal of Instrumentation*, 3.08 (2008), S08003. URL: <http://stacks.iop.org/1748-0221/3/i=08/a=S08003> (Cited on page 55)

- [77] S. Chatrchyan et al. The CMS Experiment at the CERN LHC. *JINST*, 3 (2008), S08004. DOI: [10.1088/1748-0221/3/08/S08004](https://doi.org/10.1088/1748-0221/3/08/S08004) (Cited on page 55)
- [78] Georges Aad et al. Search for squarks and gluinos with the ATLAS detector in final states with jets and missing transverse momentum using  $\sqrt{s} = 8$  TeV proton–proton collision data. *JHEP*, 09 (2014), p. 176. DOI: [10.1007/JHEP09\(2014\)176](https://doi.org/10.1007/JHEP09(2014)176). arXiv: [1405.7875](https://arxiv.org/abs/1405.7875) [[hep-ex](#)] (Cited on page 55)
- [79] Vardan Khachatryan et al. Search for dark matter, extra dimensions, and unparticles in monojet events in proton–proton collisions at  $\sqrt{s} = 8$  TeV. *Eur. Phys. J.*, C75.5 (2015), p. 235. DOI: [10.1140/epjc/s10052-015-3451-4](https://doi.org/10.1140/epjc/s10052-015-3451-4). arXiv: [1408.3583](https://arxiv.org/abs/1408.3583) [[hep-ex](#)] (Cited on page 55)
- [80] The LHCb Collaboration, Augusto Alves Jr, L M Andrade Filho, A F Barbosa, I Bediaga, and G Cernicchiaro. The LHCb Detector at the LHC. *Journal of Instrumentation*, 3.08 (2008), S08005. URL: <http://stacks.iop.org/1748-0221/3/i=08/a=S08005> (Cited on page 55)
- [81] O. Adriani et al. The LHCf detector at the CERN Large Hadron Collider. *JINST*, 3 (2008), S08006. DOI: [10.1088/1748-0221/3/08/S08006](https://doi.org/10.1088/1748-0221/3/08/S08006) (Cited on page 55)
- [82] Alessia Tricomi and LHCf Collaboration. “Latest results of the LHCf experiment at LHC”. Sissa Medialab, Nov. 2, 2017, p. 025. DOI: [10.22323/1.314.0025](https://doi.org/10.22323/1.314.0025). URL: <https://pos.sissa.it/314/025> (Cited on page 55)
- [83] G. Anelli et al. The TOTEM experiment at the CERN Large Hadron Collider. *JINST*, 3 (2008), S08007. DOI: [10.1088/1748-0221/3/08/S08007](https://doi.org/10.1088/1748-0221/3/08/S08007) (Cited on page 55)
- [84] F. Ferro and TOTEM Collaboration. Measurements, status and plans of the TOTEM experiment at the LHC. *Journal of Physics: Conference Series*, 934.1 (2017), p. 012025. ISSN: 1742-6596. DOI: [10.1088/1742-6596/934/1/012025](https://doi.org/10.1088/1742-6596/934/1/012025). URL: <http://stacks.iop.org/1742-6596/934/i=1/a=012025> (Cited on page 55)
- [85] J. L. Pinfold. The MoEDAL Experiment at the LHC – a New Light on the Terascale Frontier. *J. Phys. Conf. Ser.*, 631.1 (2015), p. 012014. DOI: [10.1088/1742-6596/631/1/012014](https://doi.org/10.1088/1742-6596/631/1/012014) (Cited on page 55)
- [86] Acharya et al. Search for magnetic monopoles with the MoEDAL forward trapping detector in 2.11 fb<sup>-1</sup> of 13 TeV proton-proton collisions at the LHC (), p. 10 (Cited on page 55)
- [87] R. Aaij et al. LHCb detector performance. *Int. J. Mod. Phys.*, A30 (2015), p. 1530022. DOI: [10.1142/S0217751X15300227](https://doi.org/10.1142/S0217751X15300227). arXiv: [1412.6352](https://arxiv.org/abs/1412.6352) [[hep-ex](#)] (Cited on pages 57, 64, 74, 75, 78)
- [88] A. Arefev et al. Beam test results of the LHCb electromagnetic calorimeter (2008) (Cited on page 71)
- [89] R. Aaij et al. Performance of the LHCb calorimeters (2014). in preparation (Cited on page 71)
- [90] Vladimir Vava Gligorov and Mike Williams. Efficient, reliable and fast high-level triggering using a bonsai boosted decision tree (Oct. 25, 2012). URL: <http://xxx.lanl.gov/abs/1210.6861> (visited on 07/17/2018) (Cited on page 79)
- [91] M. Williams, V. Gligorov, C. Thomas, H. Dijkstra, J. Nardulli, and P. Spradlin. The HLT2 Topological Lines (2011) (Cited on page 79)

## BIBLIOGRAPHY

---

- [92] Albert Puig. *The LHCb trigger in 2011 and 2012*. Tech. rep. LHCb-PUB-2014-046. CERN-LHCb-PUB-2014-046. Geneva: CERN, Nov. 2014. URL: <https://cds.cern.ch/record/1970930> (Cited on page 79)
- [93] Sean Benson, V. V. Gligorov, Mika Anton Vesterinen, and John Michael Williams. The LHCb Turbo Stream. *J. Phys. Conf. Ser.*, 664.8 (2015), p. 082004. DOI: [10.1088/1742-6596/664/8/082004](https://doi.org/10.1088/1742-6596/664/8/082004) (Cited on page 79)
- [94] S Tolk, J Albrecht, F Dettori, and A Pellegrino. *Data driven trigger efficiency determination at LHCb*. Tech. rep. LHCb-PUB-2014-039. CERN-LHCb-PUB-2014-039. Geneva: CERN, May 2014. URL: <https://cds.cern.ch/record/1701134> (Cited on pages 80, 149)
- [95] *The Gaudi project*. URL: <https://gaudi.web.cern.ch/gaudi/> (Cited on page 80)
- [96] I. Antcheva, M. Ballintijn, B. Bellenot, M. Biskup, R. Brun, N. Buncic, Ph Canal, D. Casadei, O. Couet, V. Fine, L. Franco, G. Ganis, A. Gheata, D. Gonzalez Maline, M. Goto, J. Iwaszkiewicz, A. Kreshuk, D. Marcos Segura, R. Maunder, L. Moneta, A. Naumann, E. Offermann, V. Onuchin, S. Panacek, F. Rademakers, P. Russo, and M. Tadel. ROOT — A C++ framework for petabyte data storage, statistical analysis and visualization. *Computer Physics Communications*, 180.12 (2009), pp. 2499–2512. ISSN: 0010-4655. DOI: <https://doi.org/10.1016/j.cpc.2009.08.005>. URL: <http://www.sciencedirect.com/science/article/pii/S0010465509002550> (Cited on page 80)
- [97] M. Clemencic, G. Corti, S. Easo, C. R. Jones, S. Miglioranza, M. Pappagallo, P. Robbe, and the LHCb Collaboration. The LHCb Simulation Application, Gauss: Design, Evolution and Experience. *Journal of Physics: Conference Series*, 331.3 (2011), p. 032023. ISSN: 1742-6596. DOI: [10.1088/1742-6596/331/3/032023](https://doi.org/10.1088/1742-6596/331/3/032023). URL: <http://stacks.iop.org/1742-6596/331/i=3/a=032023> (visited on 07/16/2018) (Cited on page 80)
- [98] Torbjörn Sjöstrand, Stephen Mrenna, and Peter Skands. A brief introduction to PYTHIA 8.1. *Computer Physics Communications*, 178.11 (June 1, 2008), pp. 852–867. ISSN: 0010-4655. DOI: [10.1016/j.cpc.2008.01.036](https://doi.org/10.1016/j.cpc.2008.01.036). URL: <http://www.sciencedirect.com/science/article/pii/S0010465508000441> (visited on 07/16/2018) (Cited on page 80)
- [99] David J. Lange. The EvtGen particle decay simulation package. *Nuclear Instruments and Methods in Physics Research Section A: Accelerators, Spectrometers, Detectors and Associated Equipment*, BEAUTY2000, Proceedings of the 7th Int. Conf. on B-Physics at Hadron Machines 462.1 (Apr. 11, 2001), pp. 152–155. ISSN: 0168-9002. DOI: [10.1016/S0168-9002\(01\)00089-4](https://doi.org/10.1016/S0168-9002(01)00089-4). URL: <http://www.sciencedirect.com/science/article/pii/S0168900201000894> (visited on 07/16/2018) (Cited on page 80)
- [100] Piotr Golonka and Zbigniew Was. PHOTOS Monte Carlo: A Precision tool for QED corrections in  $Z$  and  $W$  decays. *Eur. Phys. J.*, C45 (2006), pp. 97–107. DOI: [10.1140/epjc/s2005-02396-4](https://doi.org/10.1140/epjc/s2005-02396-4). arXiv: [hep-ph/0506026](https://arxiv.org/abs/hep-ph/0506026) [hep-ph] (Cited on page 80)
- [101] S. Agostinelli et al. Geant4—a simulation toolkit. *Nuclear Instruments and Methods in Physics Research Section A: Accelerators, Spectrometers, Detectors and Associated Equipment*, 506.3 (July 1, 2003), pp. 250–303. ISSN: 0168-9002. DOI: [10.1016/S0168-9002\(03\)01368-8](https://doi.org/10.1016/S0168-9002(03)01368-8). URL: <http://www.sciencedirect.com/>

- [science/article/pii/S0168900203013688](https://cds.cern.ch/record/2316034) (visited on 07/16/2018) (Cited on page 80)
- [102] Benedetto Gianluca Siddi and Concezio Bozzi. *Measurement of the ration of the  $B^0 \rightarrow D^{*-} \tau^+ \nu_\tau$  and  $B^0 \rightarrow D^{*-} \mu^+ \nu_\mu$  branching fractions using thee-prong  $\tau$  decays.* Presented 28 Feb 2018. Feb. 2018. URL: <https://cds.cern.ch/record/2316034> (Cited on pages 85, 98)
- [103] I. M. Nugent, T. Przedzinski, P. Roig, O. Shekhovtsova, and Z. Was. Resonance chiral Lagrangian currents and experimental data for  $\tau^- \rightarrow \pi^- \pi^- \pi^+ \nu_\tau$ . *Phys. Rev.*, D88 (2013), p. 093012. DOI: [10.1103/PhysRevD.88.093012](https://doi.org/10.1103/PhysRevD.88.093012). arXiv: [1310.1053](https://arxiv.org/abs/1310.1053) [[hep-ph](#)] (Cited on page 86)
- [104] Florian U Bernlochner and Zoltan Ligeti. Semileptonic B ( s ) decays to excited charmed mesons with e , , and searching for new physics with R ( D \*\*) ( ) (Cited on page 91)
- [105] Kyle S. Cranmer. Kernel estimation in high-energy physics. *Comput. Phys. Commun.*, 136 (2001), pp. 198–207. DOI: [10.1016/S0010-4655\(00\)00243-5](https://doi.org/10.1016/S0010-4655(00)00243-5). arXiv: [hep-ex/0011057](https://arxiv.org/abs/hep-ex/0011057) [[hep-ex](#)] (Cited on page 92)
- [106] Tomasz Skwarnicki. *A study of the radiative CASCADE transitions between the Upsilon-Prime and Upsilon resonances.* PhD thesis. Cracow, INP, 1986. URL: <http://www-library.desy.de/cgi-bin/showprep.pl?DESY-F31-86-02> (Cited on page 92)
- [107] Federico Betti, Concezio Bozzi, Victor Renaudin, Antonio Romero Vidal, Benedetto Gianluca Siddi, and Guy Henri Maurice Wormser. Measurement of  $B(B^0 \rightarrow D^{*-} \tau^+ \nu_\tau)$  and  $R(D^*)$  with  $\tau$  three-prong pionic decays (Aug. 2015). URL: <https://cds.cern.ch/record/2040543> (Cited on pages 98, 114, 175)
- [108] Muriel Pivk and Francois R. Le Diberder. sPlot: A statistical tool to unfold data distributions. *Nucl.Instrum.Meth.*, A555 (2005), pp. 356–369. DOI: [10.1016/j.nima.2005.08.106](https://doi.org/10.1016/j.nima.2005.08.106). arXiv: [physics/0402083](https://arxiv.org/abs/physics/0402083) [[physics.data-an](#)] (Cited on page 99)
- [109] Lucio Anderlini, Andrea Contu, Christopher Rob Jones, Sneha Sirirshkumar Malde, Dominik Muller, Stephen Ogilvy, Juan Martin Otalora Goicochea, Alex Pearce, Ivan Polyakov, Wenbin Qian, Barbara Sciascia, Ricardo Vazquez Gomez, and Yanxi Zhang. *The PIDCalib package* (Cited on page 99)
- [110] Y. Amhis et al. Averages of  $b$ -hadron,  $c$ -hadron, and  $\tau$ -lepton properties as of summer 2014 (2014). arXiv: [1412.7515](https://arxiv.org/abs/1412.7515) [[hep-ex](#)] (Cited on pages 103, 105)
- [111] R. Aaij et al. Study of the kinematic dependences of  $\Lambda_b^0$  production in  $pp$  collisions and a measurement of the  $\Lambda_b^0 \rightarrow \Lambda_c^+ \pi^-$  branching fraction. *JHEP*, 08 (2014), p. 143. DOI: [10.1007/JHEP08\(2014\)143](https://doi.org/10.1007/JHEP08(2014)143). arXiv: [1405.6842](https://arxiv.org/abs/1405.6842) [[hep-ex](#)] (Cited on pages 111, 112)
- [112] R. Aaij et al. Measurement of  $b$  hadron production fractions in 7 TeV  $pp$  collisions. *Phys. Rev.*, D85 (2012), p. 032008. DOI: [10.1103/PhysRevD.85.032008](https://doi.org/10.1103/PhysRevD.85.032008). arXiv: [1111.2357](https://arxiv.org/abs/1111.2357) [[hep-ex](#)] (Cited on page 111)
- [113] Fermilab Lattice, MILC Collaborations, MILC : Jon A. Bailey, A. Bazavov, C. Bernard, C. M. Bouchard, C. DeTar, Daping Du, A. X. El-Khadra, J. Foley, E. D. Freeland, E. Gámiz, Steven Gottlieb, U. M. Heller, J. Komijani, A. S. Kronfeld, J. Laiho, L. Levkova, P. B. Mackenzie, E. T. Neil, Si-Wei Qiu, J. Simone, R. Sugar, D. Toussaint, R. S. Van de Water, and Ran Zhou. The  $B \rightarrow D \ell \nu$  form factors at

## BIBLIOGRAPHY

---

- nonzero recoil and  $|V_{cb}|$  from 2 + 1-flavor lattice QCD. *Phys. Rev. D*, 92, (Mar. 2015), p. 034506. eprint: [1503.07237](https://arxiv.org/abs/1503.07237) (Cited on page 111)
- [114] M. Chrzaszcz, T. Przedzinski, Z. Was, and J. Zaremba. TAUOLA of tau lepton decays— framework for hadronic currents, matrix elements and anomalous decays (2016). arXiv: [1609.04617 \[hep-ph\]](https://arxiv.org/abs/1609.04617) (Cited on page 115)
- [115] Anders Ryd, David Lange, Natalia Kuznetsova, Sophie Versille, Marcello Rotondo, David P. Kirkby, Frank K. Wuerthwein, and Akimasa Ishikawa. EvtGen: A Monte Carlo Generator for B-Physics (2005) (Cited on page 115)
- [116] B. Aubert et al. Exclusive Branching-Fraction Measurements of Semileptonic  $\tau$  Decays into Three Charged Hadrons, into  $\varphi\pi^-\nu_\tau$ , and into  $\varphi K^-\nu_\tau$ . *Phys. Rev. Lett.*, 100 (1 Jan. 2008), p. 011801. DOI: [10.1103/PhysRevLett.100.011801](https://doi.org/10.1103/PhysRevLett.100.011801). URL: <https://link.aps.org/doi/10.1103/PhysRevLett.100.011801> (Cited on page 115)
- [117] Ian M. Nugent. Invariant mass spectra of  $\tau^- \rightarrow h^-h^-h^+\nu_\tau$  decays. *Nucl. Phys. Proc. Suppl.*, 253-255 (2014), pp. 38–41. DOI: [10.1016/j.nuclphysbps.2014.09.010](https://doi.org/10.1016/j.nuclphysbps.2014.09.010). arXiv: [1301.7105 \[hep-ex\]](https://arxiv.org/abs/1301.7105) (Cited on page 115)
- [118] D. M. Asner et al. Hadronic structure in the decay tau-  $\rightarrow$  tau-neutrino pi- pi0 and the sign of the tau-neutrino helicity. *Phys. Rev.*, D61 (2000), p. 012002. DOI: [10.1103/PhysRevD.61.012002](https://doi.org/10.1103/PhysRevD.61.012002). arXiv: [hep-ex/9902022 \[hep-ex\]](https://arxiv.org/abs/hep-ex/9902022) (Cited on page 115)
- [119] C. Bozzi, M. Calvi, M. Fiore, M. Frosini, L. Grillo, S. Hansmann-Menzemer, B. Khanji, M. Kolpin, K. Kreplin, A. Lupato, J. van Tilburg, S. Vecchi, M. Vesterinen, and J. de Vries. *Measurement of the mixing frequency  $\Delta m_d$  using semileptonic  $B^0$  decays* (Cited on page 131)
- [120] Tianqi Chen and Carlos Guestrin. XGBoost: A Scalable Tree Boosting System. *arXiv:1603.02754 [cs]*, (2016), pp. 785–794. DOI: [10.1145/2939672.2939785](https://doi.org/10.1145/2939672.2939785). arXiv: [1603.02754](https://arxiv.org/abs/1603.02754). URL: <http://arxiv.org/abs/1603.02754> (Cited on pages 157, 158)
- [121] J. D. Hunter. Matplotlib: A 2D Graphics Environment. *Computing in Science Engineering*, 9.3 (May 2007), pp. 90–95. ISSN: 1521-9615. DOI: [10.1109/MCSE.2007.55](https://doi.org/10.1109/MCSE.2007.55) (Cited on page 157)
- [122] Fabian Pedregosa, Gaël Varoquaux, Alexandre Gramfort, Vincent Michel, Bertrand Thirion, Olivier Grisel, Mathieu Blondel, Peter Prettenhofer, Ron Weiss, Vincent Dubourg, Jake Vanderplas, Alexandre Passos, David Cournapeau, Matthieu Brucher, Matthieu Perrot, and Édouard Duchesnay. Scikit-learn: Machine Learning in Python. *Journal of Machine Learning Research*, 12 (Oct 2011), pp. 2825–2830. ISSN: ISSN 1533-7928. URL: <http://jmlr.org/papers/v12/pedregosa11a.html> (Cited on page 157)
- [123] Yoav Freund and Robert E Schapire. A Decision-Theoretic Generalization of On-Line Learning and an Application to Boosting. *Journal of Computer and System Sciences*, 55.1 (Aug. 1997), pp. 119–139. ISSN: 0022-0000. DOI: [10.1006/jcss.1997.1504](https://doi.org/10.1006/jcss.1997.1504). URL: <http://www.sciencedirect.com/science/article/pii/S002200009791504X> (Cited on page 158)
- [124] Kyle Cranmer, George Lewis, Lorenzo Moneta, Akira Shibata, and Wouter Verkerke. HistFactory: A tool for creating statistical models for use with RooFit and RooStats (2012) (Cited on page 182)

# Acknowledgements

C'est bientôt la fin de ce manuscrit et après avoir tant parlé du travail réalisé, voici venu le moment de tous vous remercier, vous qui l'avez rendu possible. Ces trois années furent riches en découvertes, en apprentissages et en visites de nouveaux endroits et si cela s'est bien passé, c'est grâce à vous.

First of all, I would like to thank all the members of my jury, Yannis Karyotakis and Francesco Forti, my referees, who took both the time to read my thesis and discuss its content giving insightful comments, Svjetlana Fajfer and Patrick Owen who accepted to evaluate my work and the LAL director, Achille Stocchi, for giving me the opportunity to pursue my thesis in such a wonderful place.

Avant de commencer cette thèse, le tau était pour moi un “gros électron” et je dois remercier Guy Wormser, mon directeur de thèse, pour m'avoir fait confiance et permis d'en apprendre tellement plus sur cette petite particule. Tu as été présent et disponible tout au long de ces trois années pour discuter physique et répondre à mes questions, encore merci !

J'aimerais aussi remercier toutes les personnes qui ont constitué le groupe LHCb du LAL pendant ma thèse pour leur accueil et leur soutien constant. J'ai eu la chance de travailler quotidiennement aux côtés de Vitalii et Frédéric et je leur suis très reconnaissant de l'atmosphère toujours paisible et sereine de notre bureau. Je ne serais peut-être pas en train d'écrire ces lignes si Patrick et Marie-Hélène ne m'avaient pas permis de faire un stage il y a quelques années et j'aimerais les remercier tous les deux pour leurs précieux conseils, c'est toujours extrêmement enrichissant de discuter avec vous. Yasmine, j'aimerais te remercier pour m'avoir permis d'expliquer la désintégration du  $D^0$  à des lycéens mais surtout pour toutes nos discussions au cours de ces trois ans, et j'espère que cela va continuer, d'une manière ou d'une autre ! L'équipe LHCb a eu bien des visages et des noms en trois ans et je tiens aussi à remercier Jacques, Francesco, Laure, Michael, Yiming, Joao, Emilie, Simone, Yanxi, Benoit, Martino, Alexis, Renato, Frederic, Sergei, Jibo, Andrii, Fabrice et Elisabeth pour les nombreuses discussions à Orsay, au CERN et ailleurs, je vous souhaite à tous beaucoup de réussite dans vos projets respectifs.

Si j'ai pu mener à bien ce travail, c'est aussi grâce au personnel des services administratifs du laboratoire, que je souhaite remercier ici chaleureusement, tout particulièrement Sylvie Teulet et Catherine Bourge.

---

I owe much gratitude to the LHCb collaboration as a whole with special thoughts for the hadronic  $\mathcal{R}(D^*)$  proponents, Antonio, Benedetto, Federico and Concezzio for all the help they provided and the conveners of the semileptonic working group Greg and Lucia who were extremely supportive during the latest developments of the analysis, I also need to mention Brian for all its help setting up the fit framework. For their help during my time as a Simulation liaison, I would also like to thank Gloria, Svende and Vladimir, I learned so much with you. I received also great help from Vava to prepare for the future and the Starterkit team, especially Alex and Chris, kindly answered all my snake-related questions, thanks again!

Je souhaite aussi remercier les personnes qui m'ont mises pas à pas sur le chemin de la thèse, les différents professeurs et professeures que j'ai eu le plaisir de rencontrer au cours des dernières années ainsi qu'Alexandra et Javier qui m'ont permis de découvrir la recherche en physique des saveurs et d'y prendre goût.

Valentin, Delphine, nos déjeuners au CESFO ont été autant de moments de respiration que j'ai été extrêmement heureux de prolonger lors de nos soirées avec Sylviane et Greg. Charles, Maxime, Hannah, Thibault, Léo, Nina, Hélène et Jan, je voulais vous redire ici à quel point je suis heureux et chanceux de vous avoir dans ma vie et je repense avec joie aux moments passés à Nantes, Orsay, Paris et Genève, je n'ai qu'un souhait, que ça continue !

Pour tout ce que vous m'avez appris et pour toujours avoir été là à chaque pas, à chaque étape, j'aimerais vous dire un grand merci Papa et Maman. Merci de m'avoir donné la confiance et la sérénité d'entamer ces longues études. Merci aussi à mes deux frères Félix et Oscar pour avoir été un soutien constant. Je voudrais aussi dire toute ma gratitude à Fabrice et Maryline, la vie à la fac a été tellement plus douce grâce à vous.

Avant de remercier la personne qui m'a le plus soutenu pendant cette folle aventure, j'aimerais exprimer ma gratitude envers Agnetha Fältskog, Anni-Frid Lyngstad, Benny Andersson et Björn Ulvaeus pour l'ensemble de leur oeuvre qui m'a tout particulièrement accompagné pendant l'écriture du présent manuscrit.

Sans toi, ça n'aurait peut-être même pas existé et ça n'a de toute façon de sens qu'avec toi, ma belle Mathilde. Tu m'as épaulé, supporté, soutenu, tu m'as changé les idées quand j'en avais besoin, tu m'as permis de me concentrer uniquement sur mon travail chaque fois que le temps me manquait et tout particulièrement pendant la rédaction, en un mot, tu as été absolument extraordinaire et je t'en suis infiniment reconnaissant. J'ai hâte de continuer notre grande aventure, ensemble, main dans la main, et t'aider aussi à réaliser tes rêves comme tu as su si bien le faire pour moi.

**Titre :** Test de l'universalité de la saveur des leptons à travers l'étude des désintégrations semitaoniques de  $\Lambda_b^0$  avec les désintégrations en trois pions du lepton  $\tau$  dans l'expérience LHCb au CERN

**Mots clés :** Physique du  $B$ , LHCb, Physique des saveurs, Physique des particules, Physique au delà du Modèle Standard

**Résumé :** L'étude de l'universalité de la saveur des leptons est actuellement un sujet prometteur pour tester la présence de contributions de nouvelle physique dans des processus décrits par le Modèle Standard. Les mesures de désintégrations semitaoniques sont particulièrement intéressantes car de possibles couplages de nouvelle physique au lepton  $\tau$  pourraient être accrus par rapport aux deux autres leptons du fait de sa masse. Les mesures expérimentales des rapports de branchement des désintégrations  $B \rightarrow D^* \tau \nu_\tau$  et  $B \rightarrow D \tau \nu_\tau$  sont présentement en tension avec les prédictions théoriques à la hauteur de  $3.78 \sigma$ . De nouvelles mesures ainsi que l'étude de nouveaux canaux sont ainsi indispensables pour comprendre l'origine de ce désaccord.

Le travail présenté dans cette thèse décrit l'utilisation d'une nouvelle technique pour reconstruire le lepton  $\tau$  via sa désintégration en trois pions et son usage pour mesurer des rapports de rapports de branchements pour deux désintégrations  $B^0 \rightarrow D^{*-} \tau^+ \nu_\tau$  et  $\Lambda_b^0 \rightarrow \Lambda_c^+ \tau^- \bar{\nu}_\tau$  par rapport aux mêmes désintégrations impliquant des muons. Ces rapports sont respective-

ment dénommés  $\mathcal{R}(D^*)$  et  $\mathcal{R}(\Lambda_c)$ .

$\mathcal{R}(D^*)$  est mesuré en utilisant les  $3 \text{ fb}^{-1}$  de collisions proton-proton collectées par le détecteur LHCb pendant le Run1 du LHC à une énergie dans le centre de masse de 7 et 8 TeV via la reconstruction du  $\tau$  en trois pions. Le résultat obtenu

$$\mathcal{R}(D^{*-}) = 0.291 \pm 0.019_{(\text{stat})} \pm 0.026_{(\text{syst})} \pm 0.013_{(\text{ext})}$$

est compatible avec la prédiction du Modèle Standard à  $1 \sigma$  près tout en étant cohérent avec les mesures précédemment effectuées. Sa précision permet aussi de conforter le désaccord entre la combinaison des mesures et la prédiction théorique.

Ces mêmes données sont aussi analysées dans cette thèse afin d'étudier la désintégration  $\Lambda_b^0 \rightarrow \Lambda_c^+ \tau^- \bar{\nu}_\tau$  observée pour la première fois avec une signification de  $5.7 \sigma$ . Les incertitudes statistiques et systématiques sont aussi estimées et  $\mathcal{R}(\Lambda_c)$  peut s'écrire

$$\mathcal{R}(\Lambda_c^+) = X \times (1 \pm 0.105_{(\text{stat})} \pm 0.162_{(\text{syst})} \pm 0.12_{(\text{ext})})$$

avec la valeur centrale encore masquée à ce jour.

**Title :** Probing Lepton Flavour Universality through semitaonic  $\Lambda_b^0$  decays using three-pions  $\tau$ -lepton decays with the LHCb experiment at CERN

**Keywords :**  $B$  Physics, LHCb, Flavour Physics, Particle Physics, Physics Beyond the Standard Model

**Abstract :** Probing Lepton Flavour Universality has been recently a very promising topic to test for the presence of New Physics contributions in Standard Model processes. Measurements involving semitaonic decays are interesting as potential New Physics couplings to the  $\tau$ -lepton could be enhanced with respect to the two other leptons due to its mass. Experimental measurements of  $B \rightarrow D^* \tau \nu_\tau$  and  $B \rightarrow D \tau \nu_\tau$  branching fractions are currently in tension with theoretical predictions at the  $3.78 \sigma$  level. Both precise measurements and analyses of new channels are thus required to understand the source of this disagreement.

The work presented in this thesis describes the use of a new technique to reconstruct  $\tau$ -lepton using its decay into three pions and its use to measure ratios of branching fractions for two decays  $B^0 \rightarrow D^{*-} \tau^+ \nu_\tau$  and  $\Lambda_b^0 \rightarrow \Lambda_c^+ \tau^- \bar{\nu}_\tau$  with respect to the same decays involving a muon, these ratios are referred as  $\mathcal{R}(D^{*-})$  and  $\mathcal{R}(\Lambda_c^+)$ .

Using the  $3 \text{ fb}^{-1}$  of proton-proton collisions recorded

by the LHCb detector during the LHC Run1 at a centre-of-mass energy of 7 and 8 TeV,  $\mathcal{R}(D^*)$  was measured using the three-pions reconstruction for the  $\tau$  to be

$$\mathcal{R}(D^{*-}) = 0.291 \pm 0.019_{(\text{stat})} \pm 0.026_{(\text{syst})} \pm 0.013_{(\text{ext})}$$

This result is compatible with the Standard Model expectation at the  $1 \sigma$  level and is consistent with previous measurements. Its precision is able to slightly enforce the disagreement between the combination of the measurements with the theoretical prediction.

The same dataset is also analysed in this thesis to study the  $\Lambda_b^0 \rightarrow \Lambda_c^+ \tau^- \bar{\nu}_\tau$  decay which is observed for the first time with a significance of  $5.7 \sigma$ . Both statistical and systematic uncertainties were estimated and  $\mathcal{R}(\Lambda_c)$  can then be expressed as

$$\mathcal{R}(\Lambda_c^+) = X \times (1 \pm 0.105_{(\text{stat})} \pm 0.162_{(\text{syst})} \pm 0.12_{(\text{ext})})$$

with its central value remaining blind at the moment.



